

DESIGN, SYNTHESIS, AND CHARACTERIZATION OF DIRHODIUM(II,II)  
COMPLEXES AS SENSITIZERS: TANDEM EXPERIMENTAL AND  
THEORETICAL STUDIES

A Dissertation

by

AGUSTIN MILLET

Submitted to the Office of Graduate and Professional Studies of  
Texas A&M University  
in partial fulfillment of the requirements for the degree of

DOCTOR OF PHILOSOPHY

Chair of Committee,	Kim R. Dunbar
Committee Members,	Marcetta Darensbourg
	Jean-Philippe Pellois
	Ricardo Eusebi
Head of Department,	Simon North

December 2019

Major Subject: Chemistry

Copyright 2019 Agustin Millet

## ABSTRACT

This dissertation focuses on the design, synthesis, and characterization of dirhodium complexes as sensitizers for dye-sensitized solar cells, as photoactivated chemotherapeutic drugs, and as photocatalysts for H<sub>2</sub> production with low-energy light. Thorough experimental and computational studies of their structural and photophysical properties were performed in order to evaluate their suitability for a variety of applications.

Coordination of partial-paddlewheel complexes through the axial positions in a step-wise manner led to the synthesis of a new class of dirhodium complexes, namely *cis*-[Rh<sub>2</sub>(AcO)<sub>2</sub>(qxnp)(MeCN)<sub>3</sub>][BF<sub>4</sub>]<sub>2</sub> and *cis*-[Rh<sub>2</sub>(AcO)<sub>2</sub>(qxnp)<sub>2</sub>][BF<sub>4</sub>]<sub>2</sub> (where qxnp = 2-(1,8-naphthyridin-2-yl)quinoxaline). These complexes display appropriate molar absorption coefficients for photoactivated chemotherapy and equatorial solvent molecules that can be photoreleased upon irradiation. The resulting aqua complexes were shown to be able to bind to ds-DNA upon visible light irradiation opening a door to a new class of compounds with potential anticancer properties.

Changing the acetate bridging ligands for a more electron rich formamidinate ligand led to the synthesis of a series of three new axially-blocked complexes of the form *cis*-[Rh<sub>2</sub>(DTolF)<sub>2</sub>(L)<sub>2</sub>][BF<sub>4</sub>]<sub>2</sub> (DTolF = N,N'-di-p-tolylformamidinate and L = axially blocking ligand) with improved photophysical properties when compared to the axially free analogues. These complexes display panchromatic absorption profiles and relatively long-lived excited states necessary for electron-transfer reactions. These represent the first

class of dirhodium complexes capable of accepting an electron from p-phenylenediamine with low energy light which makes them ideal candidates for p-type sensitization.

A step-wise reaction of qxnp and the partially solvated complex *cis*-[Rh<sub>2</sub>(DTolF)<sub>2</sub>(MeCN)<sub>6</sub>][BF<sub>4</sub>]<sub>2</sub> led to the synthesis of the first examples of *trans* dirhodium formamidinate complexes reported in the literature, *trans*-[Rh<sub>2</sub>(DTolF)<sub>2</sub>(qxnp)(MeCN)<sub>3</sub>][BF<sub>4</sub>]<sub>2</sub> and *trans*-[Rh<sub>2</sub>(DTolF)<sub>2</sub>(qxnp)<sub>2</sub>][BF<sub>4</sub>]<sub>2</sub>. The latter displays a red-shifted absorption spectrum when compared to the *cis* analogue and can also partake in electron transfer reactions upon irradiation with low energy light. This new synthetic methodology could facilitate the synthesis of a new class of supramolecular architectures with interesting photophysical properties.

Asymmetric complexes were also synthesized from the reaction of *cis*-[Rh<sub>2</sub>(DTolF)<sub>2</sub>(MeCN)<sub>6</sub>][BF<sub>4</sub>]<sub>2</sub>, qxnp, and np (1,8-naphthyridine). The complexes obtained are able to photocatalyze H<sub>2</sub> production upon 655 nm excitation which is a vast improvement over previously published dirhodium complexes.

The research presented in this dissertation expands on the current dirhodium chemistry literature as sensitizers for a variety of applications.

## DEDICATION

To my mother and brother for their unconditional love, constant support, and encouragement.

## ACKNOWLEDGEMENTS

I would like to thank my advisor, Professor Kim R. Dunbar for her guidance, mentoring and support all these years and particularly for taking a chance on me when I joined the group in 2015. I learned synthetic inorganic chemistry in her labs and thanks to her I get to call myself an inorganic chemist. I specially appreciate the freedom that she gave me very early on to pursue my research ideas and her encouragement to see them to fruition. Her passion for science was truly an inspiration and a driving force that kept me going and allowed me to produce science of which I am very proud of.

I would also like to specially thank our collaborator Professor Claudia Turro for her invaluable feedback and support that helped me become a better scientist. Also, for inviting me to her laboratories to learn about inorganic photochemistry and for helping me during my job application process.

Thank you to all of my committee members Professors Jean-Philippe Pellois, Marcetta Y. Darensbourg, and Ricardo Eusebi for their feedback, support, and interest on my projects. In particular, thank you to Prof. Pellois for his valuable input on the biological aspect of some of projects and for allowing me to use the facilities in his laboratories to perform experiments. Also, to Dr. Lisa M. Pérez for her feedback, help, and input on all the computational calculations that I performed that helped me better understand the systems I was working with.

Thanks also go to my past and present lab mates from the Dunbar group, Ellen Song, Eryn G. White, Ryan P. Coll, David Kempe, Brian S. Dolinar, Sayan Saha, An Vu,

Codi Sanders, Jill Ellenbarger, Toby Woods, Francisco Birk, Silvia Gómez-Coca, Dimitrios Alexandropoulos, Vignesh K. Radhakrishnan, Mukesh K. Singh, Kelsey Schulte, Haomiao Xie, and Junjie Huang. In particular, I would like to thank Ellen Song for her willingness to collaborate, her passion for science, and her valuable friendship in and out of the lab. Also, to my friends from outside of Dunbar group Carolyn Gunthardt, Ben Eickenhorst, and Michael Vyoral for keeping me sane throughout this process.

I would like to thank also my friends from back home Yamila Anahí Pérez-Sirkin, Luciano H. Di Stefano, and Christian A. Gomez for their friendship, advice, and help during my time at Texas A&M University.

Finally, I would like to thank my family. To my sisters Sofia Rodriguez and Macarena N. Millet Olivieri whom I love deeply and to my step-siblings Daniela and Facundo Rodriguez. To my mother, María E. Servera, and her husband, Oscar D. Rodriguez, for all of the sacrifices that they made to get me where I am today. Also, for instilling in me the values I carry today and for inspiring me to pursue my dreams. To my brother Ezequiel Millet for loving me unconditionally, for always being there for me whenever I needed him, and for encouraging me to exercise and better myself. To him and my mother I dedicate this dissertation.

## CONTRIBUTORS AND FUNDING SOURCES

### Contributors

This work was supervised by a dissertation committee consisting of Professor Kim R. Dunbar of the Department of Chemistry as committee chair and Professors Marcetta Darensbourg and Jean-Philippe Pellois of the Department of Chemistry, and Ricardo Eusebi of the Department of Physics and Astronomy as committee members.

The DNA-binding data studied in Chapter II were performed in collaboration with Professor Jean-Philippe Pellois in the Department of Biochemistry and Biophysics at Texas A&M University with help from Ellen Song from the Dunbar group. The photoaquation experiments were performed by Austin Lanquist from the Turro group at The Ohio State University (OSU). X-ray crystal data was solved and refined by Dr. Brian S. Dolinar from the Dunbar group.

The work presented in Chapter III was published in collaboration with Dr. Claudia Turro in the Department of Chemistry and Biochemistry at The Ohio State University Whittemore, T. J.; Millet, A.; Sayre, H. J.; Xue, C.; Dolinar, B. S.; White, E. G.; Dunbar, K. R.; Turro, C., *J. Am. Chem. Soc.* **2018**, *140* (15), 5161.

In chapter IV, time-resolved experiments presented in Chapter III were performed by Dr. Congcong Xue from the Turro group at OSU. <sup>1</sup>H NMR time-dependent studies were carried out with the help of Ellen Song from the Dunbar group.

The time-resolved experiments presented in Chapter V as well as the determination of the TON for H<sub>2</sub> production were performed by Dr. Congcong Xue from the Turro group at OSU.

The computational calculations were performed with software and computer time provided by Dr. L. M. Pérez at the Super Computing Facility and the Laboratory for Molecular Simulation at Texas A&M University. The use of the TAMU/LBMS-Applications Laboratory (Laboratory of Biological Mass Spectroscopy) is also acknowledged.

All other work conducted for the dissertation was completed by the student independently.

### **Funding Sources**

This graduate work was supported through funds from the National Science Foundation under Grant Number 419791-00001, U.S. Department of Energy, Office of Science Grant Number DE-SC001072, and the Welch Foundation Grant Number A-1449.

This research used resources of the Advanced Photon Source, a U.S. Department of Energy (DOE) Office of Science User Facility operated for the DOE Office of Science by Argonne National Laboratory under Contract No. DE-AC02-06CH11357. ChemMatCARS Sector 15 is supported by the National Science Foundation under Grant Number NSF/CHE-1346572.

The X-ray diffractometers and crystallographic computing systems in the X-ray Diffraction Laboratory at the Department of Chemistry at TAMU were purchased with



funds provided by the National Science Foundation (CHE-9807975, CHE-0079822 and CHE-0215838).

## TABLE OF CONTENTS

	Page
ABSTRACT .....	ii
DEDICATION .....	iv
ACKNOWLEDGEMENTS .....	v
CONTRIBUTORS AND FUNDING SOURCES.....	vii
TABLE OF CONTENTS .....	x
LIST OF FIGURES.....	xiii
LIST OF TABLES .....	xxiii
CHAPTER I INTRODUCTION .....	1
General Introduction .....	1
Dirhodium Complexes as PCT and PDT drugs .....	6
Dirhodium Complexes as Photocatalysts and Sensitizers for DSSCs and DSPECs....	15
Dissertation Objectives and Outline.....	26
CHAPTER II EFFECT OF THE EQUATORIAL POSITION ON THE PHOTOINDUCED BIOLOGICAL ACTIVITY OF DIRHODIUM(II,II) COMPLEXESWITH A SINLGE AXIAL BLOCKING LIGAND .....	28
Introduction .....	28
Experimental Section .....	32
Materials .....	32
Instrumentation and methods .....	34
Results and Discussion.....	37
Synthesis and Characterization .....	37
X-ray crystal structures .....	40
Electronic Absorption Spectroscopy .....	43
Electronic Structure Calculations .....	45
Photoaquation Experiments.....	51
DNA binding experiments.....	52
Conclusions .....	56

CHAPTER III TUNABLE RHODIUM(II,II) LIGHT ABSORBERS AS EXCITED STATE ELECTRON DONORS AND ACCEPTORS ACCESIBLE WITH RED/NEAR-IR IRRADIATION .....	57
Introduction .....	57
Experimental Section .....	63
Materials .....	63
Instrumentation and Methods .....	67
Results and Discussion.....	71
Synthesis and Characterization .....	71
X-ray Crystal Structures .....	74
Electrochemistry and Electronic Absorption Spectroscopy .....	79
Electronic Structure Calculations .....	83
Time-Resolved Spectroscopy .....	90
Excited State Charge Transfer.....	97
Conclusions .....	102
CHAPTER IV SYNTHETIC STRATEGIES FOR TRAPPING THE ELUSIVE <i>TRANS</i> -DIRHODIUM(II,II) FORMAMIDINATE ISOMER AND THE EFFECTS OF ISOMERISM ON THE PHOTOPHYSICAL PROPERTIES.....	104
Introduction .....	104
Experimental Section .....	108
Materials .....	108
Instrumentation and methods .....	111
Results and Discussion.....	116
Synthesis.....	116
X-ray Crystal Structures .....	121
Electrochemistry and Electronic Absorption Spectroscopy .....	126
Electronic Structure Calculations .....	129
Kinetic Studies .....	143
Time-Resolved Spectroscopy .....	146
Conclusions .....	150
CHAPTER V ASYMMETRIC DIRHODIUM COMPLEXES AS PHOTOCATALYSTS FOR H <sub>2</sub> PRODCUTION WITH LOW-ENERGY LIGHT.....	152
Introduction .....	152
Experimental Section .....	156
Materials .....	156
Instrumentation and methods .....	158
Results and Discussion.....	162
Synthesis and Characterization .....	162
X-ray crystal structures .....	163

Electrochemistry and Electronic Absorption Spectroscopy .....	167
Ground State Protonation .....	170
Electrocatalytic H <sub>2</sub> Production .....	174
Electronic Structure Calculations .....	175
Time-Resolved Spectroscopy .....	185
Photocatalytic Activity .....	188
Conclusions .....	190
CHAPTER VI CONCLUSIONS AND FUTURE DIRECTIONS .....	192
REFERENCES .....	208

## LIST OF FIGURES

	Page
Figure I.1 Schematic representation of the MO diagram for dinuclear complexes with monodentate ligands. ....	3
Figure I.2 Schematic representation of the MO diagram for dinuclear complexes supporting four equivalent formamidinate bridging ligands. ....	4
Figure I.3 General Jablonski diagram for the excitation of a sensitizer for photodynamic therapeutic (PDT) and dye-sensitized solar cell (DSSC) applications. ....	5
Figure I.4 Generalized Jablonski diagram for photoactivated chemotherapeutic (PCT) drugs. ....	6
Figure I.5 Mechanism of action of cis-platin as an anticancer drug. ....	7
Figure I.6 Pt based drugs approved for cancer treatment by the FDA (cisplatin, carboplatin, and oxaliplatin) other countries (nedaplatin, lobaplatin, and heptaplatin). ....	8
Figure I.7 Cytotoxic axially-blocked dirhodium complexes as inhibitors of DNA transcription <i>in vitro</i> for cancer treatment. ....	10
Figure I.8 Treatment scheme for PDT and PCT drugs. ....	11
Figure I.9 Molecular structures of porfimer sodium and $\delta$ -aminolevulinic acid. ....	13
Figure I.10 Examples of Pt(IV) pro-drugs as PCT agents. ....	14
Figure I.11 Mechanisms of action of the pro-drug Pt(IV) complexes for PCT application. ....	14
Figure I.12 Schematic representation of the formation of the aqua dirhodium complex <i>cis</i> -[Rh <sub>2</sub> (AcO) <sub>2</sub> (MeCN) <sub>4</sub> (H <sub>2</sub> O) <sub>2</sub> ][BF <sub>4</sub> ] <sub>2</sub> upon irradiation. ....	15
Figure I.13 Molecular structures of cationic dirhodium complexes for PCT applications. ....	15
Figure I.14 Schematic representation of the mechanism of action of an n-type sensitized solar cell, where $E_F$ is the Fermi level of the semiconductor and $V_{OC}$ is the open circuit potential of the device. ....	18

Figure I.15 Molecular structures of three different types of dyes for n-type semiconductor sensitization: N3 (ruthenium(II) dye), SM315 (Zn(II) phthalocyanine dye), and ADEKA (organic dye) with their respective IPCEs. ....	20
Figure I.16 Structure of the complexes <i>cis</i> -[Rh <sub>2</sub> (μ-form) <sub>2</sub> (μ-npCOO) <sub>2</sub> ][BF <sub>4</sub> ] <sub>2</sub> (where form = <i>p</i> -ditolylformamidinate or <i>p</i> -difluorobenzylformamidinate, and npCOO <sup>-</sup> = 1,8-naphthyridine-2-carboxylate) on the left and photo-induced electron transfer cycle on the right where MV <sup>2+</sup> (methyl viologen) is the substrate and BNAH (1-benzyl-1,4-dihydropyridine-3-carboxamide) is the sacrificial donor. ....	21
Figure I.17 Schematic representation of the mechanism of action of an n-type sensitized photoelectrosynthesis cell. ....	22
Figure I.18 Schematic representation of the chromophore-catalyst assembly [(4,4'-PO <sub>3</sub> H <sub>2</sub> ) <sub>2</sub> bpy) <sub>2</sub> Ru(4-Mebpy-4'-bimpy)Ru(tpy)(OH <sub>2</sub> )] <sup>4+</sup> in a DSPEC device for water splitting. ....	24
Figure I.19 Photocatalytic cycle schemes for single and multi-component assemblies for H <sub>2</sub> production. ....	25
Figure I.20 Molecular structure representation of the mixed valence dirhodium photocatalyst Rh <sub>2</sub> <sup>0,II</sup> (tfepma) <sub>2</sub> (CNAd) <sub>2</sub> Cl <sub>2</sub> . ....	26
Figure II.1 Schematic representations of the molecular structures of compounds II.1–3. ....	32
Figure II.2 Synthetic scheme for the syntheses of II.2 and II.3 from the starting material. ....	38
Figure II.3 Aromatic region of the <sup>1</sup> H NMR spectrum for II.2. ....	39
Figure II.4 Aromatic region of the <sup>1</sup> H NMR spectrum for II.3. ....	39
Figure II.5 Thermal ellipsoid plot for II.2 (left) and II.3 (right) depicted at the 50% probability level. Interstitial solvent molecules, counterions, and hydrogen atoms have been omitted for the sake of clarity. ....	41
Figure II.6 Electronic absorption spectra of compounds II.1 (pink), II.2 (orange), and II.3 (red) in acetonitrile. ....	44
Figure II.7 Gas-phase optimized structures of II.1–3. ....	47

Figure II.8 Electron density maps of the HOMOs and LUMOs of II.1–3 drawn with an isovalue = 0.04. ....	47
Figure II.9 Calculated MO diagrams for II.1–3. ....	48
Figure II.10 Electron density maps of the $Rh_2(\sigma^*)$ of complexes II.1–3 drawn with an isovalue = 0.04. ....	48
Figure II.11 TD-DFT calculated electronic absorption spectra for II.1 (pink), II.2 (orange), and II.3 (red) in acetonitrile. ....	49
Figure II.12 Photoaquation experiment for II.2 in water with a $\lambda_{irr} = 447.5$ nm LED. ....	53
Figure II.13 Photoaquation experiment for II.3 in water with a $\lambda_{irr} = 447.5$ nm LED. The solid blue line corresponds to the compound in the dark and the black dotted line after 4 hours of irradiation with the LED. ....	53
Figure II.14 Ethidium bromide stained agarose gel of 15 mg/ $\mu$ L linearized pUC18 plasmid (10 mM phosphate, pH = 7.5) in the presence of various concentrations of II.1 (a) II.2 (b) and II.3 (c). Lane 1: DNA molecular weight standard (1kb, Sigma); lane 2: plasmid alone; lanes 3 – 6: [complex] = 1, 10, 100, and 1000 $\mu$ M incubated in the dark at 37 °C for 24 hours; lanes 7 – 10: [complex] = 1, 10, 100, and 1000 $\mu$ M incubated in the dark at 37 °C for 24 hours after 20 minutes of irradiation with a 300 W xenon arc lamp ( $\lambda > 515$ nm).....	54
Figure II.15 Ethidium bromide stained agarose gel of 15 mg/ $\mu$ L linearized pUC18 plasmid (10 mM phosphate, pH = 7.5) in the presence of various concentrations of II.1. Lane 1: DNA molecular weight standard (1kb, Sigma); lane 2: plasmid alone; lanes 3 – 6: [II.1] = 1, 10, 100, and 1000 $\mu$ M incubated in the dark at 37 °C for 24 hours; lanes 7 – 10: [II.1] = 1, 10, 100, and 1000 $\mu$ M incubated in the dark at 37 °C for 24 hours after 3.5 hours of irradiation with a 300 W xenon arc lamp ( $\lambda > 515$ nm). ....	55
Figure II.16 Ethidium bromide stained agarose gel of 15 mg/ $\mu$ L linearized pUC18 plasmid (10 mM phosphate, pH = 7.5) in the presence of various concentrations of II.2. Lane 1: DNA molecular weight standard (1kb, Sigma); lane 2: plasmid alone; lanes 3 – 6: [II.2] = 1, 10, 100, and 1000 $\mu$ M incubated in the dark at 37 °C for 24 hours; lanes 7 – 10: [II.2] = 1, 10, 100, and 1000 $\mu$ M incubated in the dark at 37 °C for 24 hours after 3.5 hours of irradiation with a 300 W xenon arc lamp ( $\lambda > 515$ nm). ....	55
Figure III.1 Solar flux as a function of wavelength from the UV to the near-IR and integrated photon flux (dotted line) (adapted from ref. 100).....	58

Figure III.2 Schematic representation of the molecular structures of III.1–4. Reprinted from ref. 74. ....	63
Figure III.3 Synthetic scheme for the synthesis of complexes III.1–4.....	72
Figure III.4 Aromatic region of the <sup>1</sup> H NMR spectrum for III.1. ....	72
Figure III.5 Aromatic region of the <sup>1</sup> H NMR spectrum for III.2. ....	73
Figure III.6 Aromatic region of the <sup>1</sup> H NMR spectrum for III.3. ....	73
Figure III.7 Aromatic region of the <sup>1</sup> H NMR spectrum for III.4. ....	74
Figure III.8 Thermal ellipsoid plots for III.1–4, shown at the 50% probability level; interstitial solvent molecules, counterions, and hydrogen atoms have been omitted for the sake of clarity. Reprinted from ref. 74.....	76
Figure III.9 (a) Parallel and (b) perpendicular intramolecular aromatic donor- acceptor interactions in compound III.4. Reprinted from ref. 74. ....	79
Figure III.10 UV-vis spectra of free np, pynp, qnnp, and qxnp ligands in dichloromethane. Reprinted from ref. 74. ....	80
Figure III.11 Electronic absorption spectra of III.1–4 in CH <sub>3</sub> CN. Inset: Expanded spectra in the visible range. Reprinted from ref. 74. ....	82
Figure III.12 Gas-phase optimized structures of III.1–4. Taken from reference 74. ....	85
Figure III.13. Calculated MO diagrams for complexes III.1–4. Reprinted from ref. 74. ....	87
Figure III.14 fsTA of complex III.1 in CH <sub>3</sub> CN ( $\lambda_{\text{ex}} = 600 \text{ nm}$ ; $2.5 \mu\text{J}$ ). Reprinted from ref. 74. ....	90
Figure III.15. (a) fsTA of III.2 at 0.3, 2, 4, 20, 80, 900, and 2400 ps after laser pulse ( $\lambda_{\text{ex}} = 720 \text{ nm}$ , $2.5 \mu\text{J}$ ) in CH <sub>3</sub> CN and (b) difference spectra of electrochemically reduced ( $E_{\text{app}} = -800 \text{ mV vs Ag/AgCl}$ ) and oxidized ( $+1150 \text{ mV vs Ag/AgCl}$ ) complexes in 0.1 M Bu <sub>4</sub> PF <sub>6</sub> CH <sub>3</sub> CN. Reprinted from ref. 74. ....	92
Figure III.16 nsTA of complex III.2 in CH <sub>3</sub> CN (a) 15 ns (10 ns integration time) after laser pulse ( $\lambda_{\text{ex}} = 610 \text{ nm}$ ; $5 \text{ mJ}$ ; $\text{irf} = 5.5 \text{ ns}$ ) where scatter is seen at 610 nm and (b) kinetic trace taken at 550 nm. Reprinted from ref. 74. ....	94
Figure III.17 (a) fsTA of III.4 at 0.3, 0.7, 4, 10, 40, 70, and 2000 ps after laser pulse ( $\lambda_{\text{ex}} = 720 \text{ nm}$ , $2.5 \mu\text{J}$ ) in CH <sub>3</sub> CN and (b) difference spectra of	



electrochemically reduced ( $E_{app} = -550$ mV vs Ag/AgCl) and oxidized (+1300 mV vs Ag/AgCl) complexes in 0.1 M Bu <sub>4</sub> NPF <sub>6</sub> CH <sub>3</sub> CN. Reprinted from ref. 74. ....	95
Figure III.18 fsTA of complex III.3 in CH <sub>3</sub> CN ( $\lambda_{ex} = 720$ nm; 2.5 $\mu$ J). Reprinted from ref. 74. ....	96
Figure 2. III.19 Spectroelectrochemistry of complex III.3 in 0.1 Bu <sub>4</sub> NPF <sub>6</sub> CH <sub>3</sub> CN when oxidized at 1200 mV and reduced at -700 mV. Reprinted from ref. 74. ....	96
Figure III.20 Example graph of Stern-Volmer quenching of anthracene monitored at 420 nm upon addition of III.2 in CH <sub>3</sub> CN of anthracene ( $\lambda_{ex} = 355$ nm). Reprinted from ref. 74. ....	98
Figure III.21 Complex III.2 in CH <sub>3</sub> CN (85 $\mu$ M) in the presence (red) and absence (black) of 10 mM <i>p</i> -phenylenediamine femtosecond transient absorption after excitation with 700 nm light (2.5 $\mu$ J), trace taken at 465 nm. Reprinted from ref. 74. ....	99
Figure III.22 Complex III.3 in CH <sub>3</sub> CN (25 $\mu$ M) in the presence of 10 mM <i>p</i> -phenylenediamine 1 and 10 $\mu$ s (100 ns gate) after laser pulse ( $\lambda_{ex} = 620$ nm; 5 mJ). Reprinted from ref. 74. ....	99
Figure III.23 Complex III.4 in CH <sub>3</sub> CN (25 $\mu$ M) in the presence of 15 mM <i>p</i> -phenylenediamine at various times after the laser pulse ( $\lambda_{ex} = 620$ nm; 5 mJ). Reprinted from ref. 74. ....	100
Figure III.24 Transient absorption spectrum of III.2 in CH <sub>3</sub> CN (23 $\mu$ M) in the presence of <i>p</i> -phenylenediamine (1:100) collected 100 ns after a 600 nm pulse (5 mJ) and (b) electrochemically reduced 2 in 0.1 M Bu <sub>4</sub> NPF <sub>6</sub> CH <sub>3</sub> CN (solid line) and <i>p</i> -phenylenediamine radical cation generated in a 0.1 M NaN <sub>3</sub> aqueous solution (dashed line). Reprinted from ref. 74. ....	101
Figure III.25 Complex III.2 in 1:1 CH <sub>3</sub> CN:H <sub>2</sub> O (23 $\mu$ M) in the presence of 10 mM MV <sup>2+</sup> ( $\lambda_{ex} = 620$ nm; 5 mJ). Reprinted from ref. 74. ....	102
Figure IV.1 Syntheses of complexes IV.1–5: a) 1,8-naphthyridine in refluxing acetonitrile for 24 h, b) qxnp (2-(1,8-naphthyridin-2-yl)quinoxaline) in refluxing acetonitrile for 30 minutes or stirring in acetonitrile at 40 °C for 24 h, c) refluxing acetonitrile for 24 h, d) qxnp in refluxing acetonitrile for 24 h, and e) qxnp in refluxing chlorobenzene for 24 h. ....	118

Figure IV.2 Aromatic region of the $^1\text{H}$ NMR spectra of $\text{cis-}[\text{Rh}_2(\mu\text{-DTolF})_2(\text{MeCN})_6][\text{BF}_4]_2$ before (a) and after (b) refluxing for 24 h in acetonitrile. ....	119
Figure IV.3 Aromatic region of the $^1\text{H}$ NMR spectra of the crude product of the reaction of $\text{cis-}[\text{Rh}_2(\mu\text{-DTolF})_2(\text{MeCN})_6][\text{BF}_4]_2$ and one equivalent of qxnp. The dirhodium starting material was refluxed for 24 h prior to the addition of the ligand. The ligand was reacted with the metal complex for (a) 24 h at 40 °C or (b) 30 minutes at refluxing temperature in acetonitrile. ....	119
Figure IV.4 Reactions (a) of np and $\text{cis-}[\text{Rh}_2(\text{DTolF})_2(\text{CH}_3\text{CN})_6][\text{BF}_4]_2$ in refluxing acetonitrile for 24 h to yield IV.1, (b) of equimolar amounts of qxnp and $\text{cis-}[\text{Rh}_2(\text{DTolF})_2(\text{CH}_3\text{CN})_6][\text{BF}_4]_2$ in acetonitrile at 40 °C or at reflux for 30 min to yield IV.2 or by refluxing for 24 h in $\text{CH}_3\text{CN}$ to yield IV.3, and (c) of complex IV.3 with 1 eq qxnp in chlorobenzene at reflux for 24 h to yield IV.4. ....	120
Figure IV.5 Thermal ellipsoid plots for IV.1–3, drawn at the 50% probability level. Counterions, interstitial solvent molecules, and hydrogen atoms were omitted for the sake of clarity. ....	125
Figure IV.6 Thermal ellipsoid plots for IV.4, drawn at the 50% probability level: view looking down the rhodium-rhodium bond axis (a) and top view(b). Counterions, interstitial solvent molecules, and hydrogen atoms were omitted for the sake of clarity. ....	126
Figure IV.7 Electronic absorption spectra of IV.4 (red) and IV.5 (black). ....	128
Figure IV.8 Example of the intramolecular $\pi\text{-}\pi$ stacking interactions of IV.3. a) top and b) side views. ....	131
Figure IV.9 Gas-phase optimized structures of IV.1–4 and of the computationally modeled $\text{trans-}[\text{Rh}_2(\text{DTolF})_2(\text{np})(\text{CH}_3\text{CN})_4][\text{BF}_4]_2$ . ....	131
Figure IV.10 Calculated MO diagrams for the <i>cis</i> (IV.5) and <i>trans</i> (IV.4) compounds. ....	132
Figure IV.11 Gas-phase optimized postulated intermediates for the migration of the DTolF bridging ligands through the axial position going from <i>cis</i> to <i>trans</i> monosubstituted $\text{Rh}_2(\text{II,II})$ compounds. ....	141
Figure IV.12 Energies for the gas-phase optimized structures of the products from sequential addition of two equivalents of the qxnp ligand for the <i>cis</i> and <i>trans</i> isomers. ....	142

Figure IV.13 Energies of the <i>cis</i> -[Rh <sub>2</sub> (DTolF) <sub>2</sub> (np)(MeCN) <sub>4</sub> ][BF <sub>4</sub> ] <sub>2</sub> and <i>cis</i> -[Rh <sub>2</sub> (DTolF) <sub>2</sub> (qxnp)(MeCN) <sub>3</sub> ][BF <sub>4</sub> ] <sub>2</sub> starting materials relative to the corresponding <i>trans</i> products, along with those of the proposed intermediates of DTolF migration, where L = MeCN and X is a solvent molecule (black line) or a quinoxalinylyl axially-blocking moiety (red line). .....	143
Figure IV.14 Example of the determination of the bond strength for the <i>trans</i> -equatorial(2) acetonitrile molecule in the <i>trans</i> isomer intermediates. ....	145
Figure IV.15 Example of the 9.84-9.58 ppm portion of the <sup>1</sup> H NMR spectrum for the isomerization reaction of IV.2 → IV.3 in acetonitrile at 80 °C after 8 hours. ....	145
Figure IV.16 (a) Selected <sup>1</sup> H NMR spectroscopic traces following the isomerization reaction from IV.2 to IV.3 and (b) monoexponential decay of the normalized integration for the conversion of IV.2 (blue) to IV.3 (red) at 68 °C in acetonitrile. ....	146
Figure IV.17 Transient absorption spectra of (a) the <i>cis</i> isomer IV.5 (λ <sub>ex</sub> = 720 nm, 2.5 μJ) and (b) the <i>trans</i> isomer IV.4 (λ <sub>ex</sub> = 600 nm, 2.5 μJ). ....	148
Figure IV.18 Kinetic trace (λ <sub>ex</sub> = 600 nm, 2.5 μJ/pulse) of IV.4 in CH <sub>3</sub> CN at 420 nm (at longer time); insert (at shorter time).....	149
Figure IV.19 Arrhenius plot for the calculation of the activation energy of the isomerization reaction for conversion of IV.2 into IV.3 in acetonitrile. ....	149
Figure IV.20 Transient absorption spectrum of the <i>trans</i> isomer IV.4 in acetonitrile (130 μM) in the presence of <i>p</i> -phenylenediamine (1:150) collected at 1 μs after the 600 nm excitation pulse (IRF = 6 ns, 5 mJ). ....	150
Figure V.1 Schematic representation of the molecular structures of complexes V.1 and V.2.....	155
Figure V.2 Synthetic scheme for the synthesis of V.1 and V.2. ....	164
Figure V.3 Aromatic region of the <sup>1</sup> H NMR for V.1 in acetonitrile-d <sub>3</sub> . ....	165
Figure V.4 Aromatic region of the <sup>1</sup> H NMR for V.2 in acetonitrile-d <sub>3</sub> . ....	165
Figure V.5 Low resolution X-ray data refined isotropically for <i>cis</i> -[Rh <sub>2</sub> (DTolF) <sub>2</sub> (qxnp)(np)][BF <sub>4</sub> ] <sub>2</sub> in the presence of HCl. ....	166

Figure V.6 Low resolution X-ray crystal data of V.1 after a two-week exposure to HBF <sub>4</sub> at room temperature.....	166
Figure V.7 Cyclic voltammograms of and V.1 (green) and V.2 (blue). .....	168
Figure V.8 Electronic absorption spectra for V.1 (green) and V.2 (blue).....	169
Figure V.9 Protonation of V.1 and V.2 in the presence of TsOH. ....	170
Figure V.10 Electronic absorption spectra of V.1 as a function of TsOH equivalents. ....	171
Figure V.11 Acid titration of V.2 with a solution of TsOH in acetonitrile followed by UV-vis spectroscopy at 581 nm.....	171
Figure V.12 Aromatic region of the <sup>1</sup> H NMR for V.1 in acetonitrily- <i>d</i> <sub>3</sub> after protonation with DCl in D <sub>2</sub> O.....	173
Figure V.13 Aromatic region of the <sup>1</sup> H NMR for V.2 in acetonitrily- <i>d</i> <sub>3</sub> after protonation with DCl in D <sub>2</sub> O.....	173
Figure V.14 Cyclic voltammograms of V.1 in the presence of AcOH .....	176
Figure V.15 Cyclic voltammograms of V.2 in the presence of AcOH. ....	176
Figure V.16 Gas-phase optimized structures for V.1 (a) and V.2 (b). ....	177
Figure V.17 A comparison of the calculated MO diagrams for V.1 and V.2 with the bis substituted <i>cis</i> -[Rh <sub>2</sub> (DTolF) <sub>2</sub> (np) <sub>2</sub> (MeCN) <sub>2</sub> ][BF <sub>4</sub> ] <sub>2</sub> and <i>cis</i> -[Rh <sub>2</sub> (DtolF) <sub>2</sub> (qxnp) <sub>2</sub> ][BF <sub>4</sub> ] <sub>2</sub> complexes. ....	178
Figure V.18 TD-DFT calculated oscillator frequencies for V.1 (green) and V.2 (blue).....	179
Figure V.19 Calculated oscillator strengths for V.2 (blue), for the complex protonated at the qnp ligand (purple), and the protonated cyclometalated qnp ligand on the dirhodium unit (red).....	184
Figure V.20 Calculated oscillator strengths for V.1 (green) and the protonated analogues with acetonitrile (purple) or a chloride ion (red) in the axial positions respectively.....	184
Figure V.21 fsTA of V.1 in CH <sub>3</sub> CN ( $\lambda_{ex}$ = 720 nm, 2.5 $\mu$ J). ....	186
Figure V.22 fsTA of V.2 in CH <sub>3</sub> CN ( $\lambda_{ex}$ = 720 nm, 2.5 $\mu$ J). ....	187

Figure V.23 Nanosecond transient absorption spectrum of V.1 in CH <sub>3</sub> CN after excitation with 650 nm light (5 μJ) with the trace measured at 460 nm. ....	187
Figure V.24 Nanosecond transient absorption spectrum of V.2 in CH <sub>3</sub> CN after excitation with 650 nm light (5 μJ) with the trace taken at 470 nm. ....	188
Figure VI.1 Electronic absorption spectra for <i>trans</i> -[Rh <sub>2</sub> (DTolF) <sub>2</sub> (qxnp)(MeCN) <sub>3</sub> ][BF <sub>4</sub> ] <sub>2</sub> (3.X) in water in the dark (a) and upon irradiation (b). ....	194
Figure VI.2 Synthetic route to generate the proposed complex <i>cis</i> -[Rh <sub>2</sub> (mhp) <sub>2</sub> (qxnp)(MeCN) <sub>3</sub> ][BF <sub>4</sub> ] <sub>2</sub> . ....	195
Figure VI.3 Synthetic scheme for the π-accepting and axially blocking ligands with anchoring groups (a) and the formamidine electron donating bridging ligand with protected anchoring groups (b). ....	197
Figure VI.4 Aromatic region of the <sup>1</sup> H NMR for the Form-COOEt ligand. ....	197
Figure VI.5 Proposed synthetic scheme for the synthesis of a series of potential p-type dirhodium sensitizers of the type <i>cis</i> -[Rh <sub>2</sub> (Form-COO) <sub>2</sub> (L) <sub>2</sub> ] <sup>2-</sup> where L = pynp, qnnp, and qxnp. ....	198
Figure VI.6 Thermal ellipsoid plots for the compounds <i>cis</i> -[Rh <sub>2</sub> (DTolF) <sub>2</sub> (2COOEt-pynp) <sub>2</sub> ][BF <sub>4</sub> ] <sub>2</sub> (a) and <i>cis</i> -[Rh <sub>2</sub> (DTolF) <sub>2</sub> (4COOEt-pynp) <sub>2</sub> ][BF <sub>4</sub> ] <sub>2</sub> (b) at the 50% probability level. Counterions, hydrogen atoms, and solvent molecules were omitted for the sake of clarity. ....	199
Figure VI.7 Schematic representations of <i>cis</i> -[Rh <sub>2</sub> (DTolF) <sub>2</sub> (4COO-pynp) <sub>2</sub> ][BF <sub>4</sub> ] <sub>2</sub> (a) and <i>cis</i> -[Rh <sub>2</sub> (COO-Form) <sub>2</sub> (pynp) <sub>2</sub> ][BF <sub>4</sub> ] <sub>2</sub> (b) bound to TiO <sub>2</sub> for n-type sensitization and NiO for p-type sensitization respectively. ....	199
Figure VI.8 Schematic representation of <i>cis</i> and <i>trans</i> dirhodium complexes as building blocks for supramolecular architectures. ....	201
Figure VI.9 Synthetic scheme to generate <i>trans</i> -[Rh <sub>2</sub> (DTolF) <sub>2</sub> (MeCN) <sub>6</sub> ][BF <sub>4</sub> ] <sub>2</sub> as a building block for hexagonal supramolecular architectures and ladder-type structures in the presence of appropriate linkers. ....	202
Figure VI.10 Schematic representation of the target complexes <i>cis</i> -[Rh <sub>2</sub> (DTolF) <sub>2</sub> (qxnp)(bncn)][BF <sub>4</sub> ] <sub>2</sub> and <i>cis</i> -[Rh <sub>2</sub> (DTolF) <sub>2</sub> (qnnp)(bncn)][BF <sub>4</sub> ] <sub>2</sub> for photocatalytic H <sub>2</sub> production with low-energy light. ....	205

Figure VI.11 Synthetic route proposed for the syntheses of *cis*-  
[Rh<sub>2</sub>(DTolF)<sub>2</sub>(qxnp)(bncn)][BF<sub>4</sub>]<sub>2</sub> and *cis*-  
[Rh<sub>2</sub>(DTolF)<sub>2</sub>(qnp)(bncn)][BF<sub>4</sub>]<sub>2</sub>.....206

## LIST OF TABLES

	Page
Table II-1 X-ray data parameters and refinement details for II.1–3. ....	42
Table II-2 Electronic Absorption Maxima with Molar Absorptivities in Acetonitrile and Reduction Potentials for II.1–3. ....	44
Table II-3 Comparison of gas phase optimized structures and X-ray crystal structures for II.1–3. ....	46
Table II-4 First eight vertical energies of the singlet excited states, oscillator strengths, $f$ , and major orbital contributions <sup>a</sup> calculated for II.1–3 in acetonitrile (H = HOMO; L = LUMO). <sup>b</sup> .....	50
Table II-5 Orbital contributions <sup>a</sup> for II.1–3 as predicted by TD-DFT calculations in acetonitrile (HOMO–5 through LUMO+6). <sup>b</sup> .....	51
Table III-1 The refinement details for III.1 and III.2. Taken from reference 74. ....	77
Table III-2 The refinement details for III.3 and III.4. Taken from reference 74. ....	78
Table III-3 Electronic Absorption Maxima with Molar Absorptivities in CH <sub>3</sub> CN, Reduction Potentials, Singlet and Triplet Lifetimes for III.1–4. Taken from reference 74. ....	82
Table III-4 Orbital contributions for III.1–4 as predicted by TD-DFT calculations in acetonitrile (HOMO-5 through LUMO+6). Taken from reference 74. ....	84
Table III-5 Calculated orbital contributions for the optimized lowest triplet state in the alpha manifold of acetonitrile of complexes III.1, III.2 and III.4 (LUMO through SOMO-1). Taken from reference 74.....	85
Table III-6 Calculated energy differences in the LUMOs for complexes III.1–4 with their corresponding measured differences in reduction potentials. Taken from reference 74.....	87
Table III-7 Comparison of gas phase optimized structures and X-ray crystal structures for III.1–4. Taken from reference 74. ....	89
Table III-8 Quenching rates of organic quenchers via Stern-Volmer quenching by complex III.2. Taken from reference 74.....	98

Table IV-1 The refinement details for IV.1 and IV.2. ....	123
Table IV-2 Refining parameters for IV.3 and IV.4. ....	124
Table IV-3 Electronic Absorption Maxima ( $\lambda_{\text{abs}}$ ), Molar Absorptivities ( $\epsilon$ ), Reduction Potentials ( $E_{1/2}$ ), Singlet ( $\tau_{\text{S}}$ ) and Triplet ( $\tau_{\text{T}}$ ) Lifetimes for IV.4 and IV.5 in Acetonitrile. ....	128
Table IV-4 Comparison of gas phase optimized structures and X-ray crystal structures for IV.1–4. ....	129
Table IV-5 Electron density maps for IV.4 from its HOMO-1 to its LUMO+2 with an isovalue = 0.04. ....	133
Table IV-6. Vertical energies of the singlet excited states, oscillator strengths, $f$ , and major orbital contributions <sup>a</sup> calculated for IV.4 and IV.5 in acetonitrile (H = HOMO; L = LUMO). <sup>b</sup> ....	134
Table IV-7 Orbital contributions for IV.1–5 as predicted by TD-DFT calculations in acetonitrile (HOMO-5 through LUMO+6). <sup>a</sup> From <i>J. Am. Chem. Soc.</i> 2018, <i>140</i> (15), 5161. ....	136
Table IV-8 Summary of the bond energies in kcal/mol for the equatorial and axial acetonitrile solvent molecules. ....	145
Table V-1 Electronic Absorption Maxima with Molar Absorptivities in Acetonitrile, Reduction Potentials, Singlet ( $\tau_{\text{S}}$ ) and Triplet ( $\tau_{\text{T}}$ ) Lifetimes for V.1 and V.2. ....	169
Table V-2 Calculated bond distances and dihedral angles for V.1 and V.2. ....	178
Table V-3 Orbital contributions for V.1 and V.2 as predicted by TD-DFT calculations in acetonitrile (HOMO-5 through LUMO+6). <sup>a</sup> ....	179
Table V-4 Electron density maps for V.1 and V.2 from its HOMO–1 to its LUMO+3 with an isovalue = 0.04. ....	180
Table V-5 Vertical energies of the singlet excited states, oscillator strengths, $f$ , and major orbital contributions <sup>a</sup> calculated for V.1 and V.2 in acetonitrile (H = HOMO; L = LUMO). <sup>b</sup> ....	182
Table V-6 Photocatalytic H <sub>2</sub> production of V.1 and V.2. ....	189



# CHAPTER I

## INTRODUCTION

### General Introduction

Dirhodium compounds are important in many diverse fields owing, in large measure, to their highly tunable ligand platform and excited state properties. Dirhodium molecules have been used as building blocks for supramolecular architectures,<sup>1, 2</sup> as anticancer<sup>3-7</sup> and photodynamic therapeutic agents (PDT)<sup>8</sup> as well as photoactivated chemotherapeutic drugs (PCT),<sup>9-11</sup> as photocatalysts for water splitting, and as panchromatic absorbers for n-type or p-type sensitization, among others. In this dissertation research, dirhodium complexes were explored as PCT drugs, photosensitizers, and photocatalysts. In order to better understand the nature of the photophysical and electronic properties of these complexes and the effect of the ligand field around the dinuclear core, an understanding of the basic bonding pattern of M-M bonds is essential.<sup>12</sup> Dinuclear metal-metal bonded complexes can be viewed as two face-to-face  $ML_4$  squares (L= equatorial ligands), as well as two additional axial donors in many cases. If one considers only *d*-orbitals, there are only five possible non-zero orbital overlaps between the metal ions due to symmetry considerations. A sigma bonding orbital is obtained from the positive overlap between the  $d_{z^2}^{(1)} + d_{z^2}^{(2)}$ . By the same logic, the antisymmetric combination of these orbitals leads to the formation of an antibonding sigma orbital. The same considerations can be extrapolated to the other four overlapping orbitals, bearing in mind that there are two orbitals of  $\pi$ -symmetry which are orthogonal to each other leading to two degenerate overlapping molecular orbitals (MOs). A qualitative MO energy

ordering can be devised by making use of Huckel's concept that the energy of the MOs is proportional to their overlap, namely that  $\sigma$  has the strongest overlap,  $\pi$  is intermediate and  $\delta$  is the weakest. Given these considerations, the qualitative MO diagram in Figure I.1 can be constructed. Dirhodium(II,II) complexes have a total of 14  $e^-$  leading to an electronic structure of  $\sigma^2\pi^4\delta^2\delta^*\pi^4\sigma^0$  which results in a bond order of 1. This electronic structure, however, is not a valid representation of most carboxylate and formamidinate bridged complexes since the  $\pi$  and  $\pi^*$  orbitals of these ligands possess the appropriate symmetry to interact with the  $\delta$  and  $\delta^*$  MOs of these dinuclear cores which leads to the MO diagram presented in Figure I.2.<sup>13</sup>

Dirhodium complexes exhibit rich photochemistry with some of these properties being highlighted in the Jablonski diagram presented in Figure I.3. Upon irradiation, the complexes can access a singlet excited state that, through intersystem crossing (ISC) facilitated by the spin-orbit (SO) coupling of the heavy metal atoms, can relax to a triplet excited state which can transfer energy to a substrate such as  $^3O_2$  to form the highly reactive  $^1O_2$  species making them potential PDT agents. The excited molecules can also donate electrons to biological substrates and water to generate reactive oxygen species (ROS) for PDT applications or donate holes or electrons to p- or n-type semiconductors for p- or n-type dye-sensitized solar cells (DSSCs) respectively. Lastly, excited state dirhodium compounds can photocatalyze reactions, such as  $H_2$  reduction, upon irradiation.

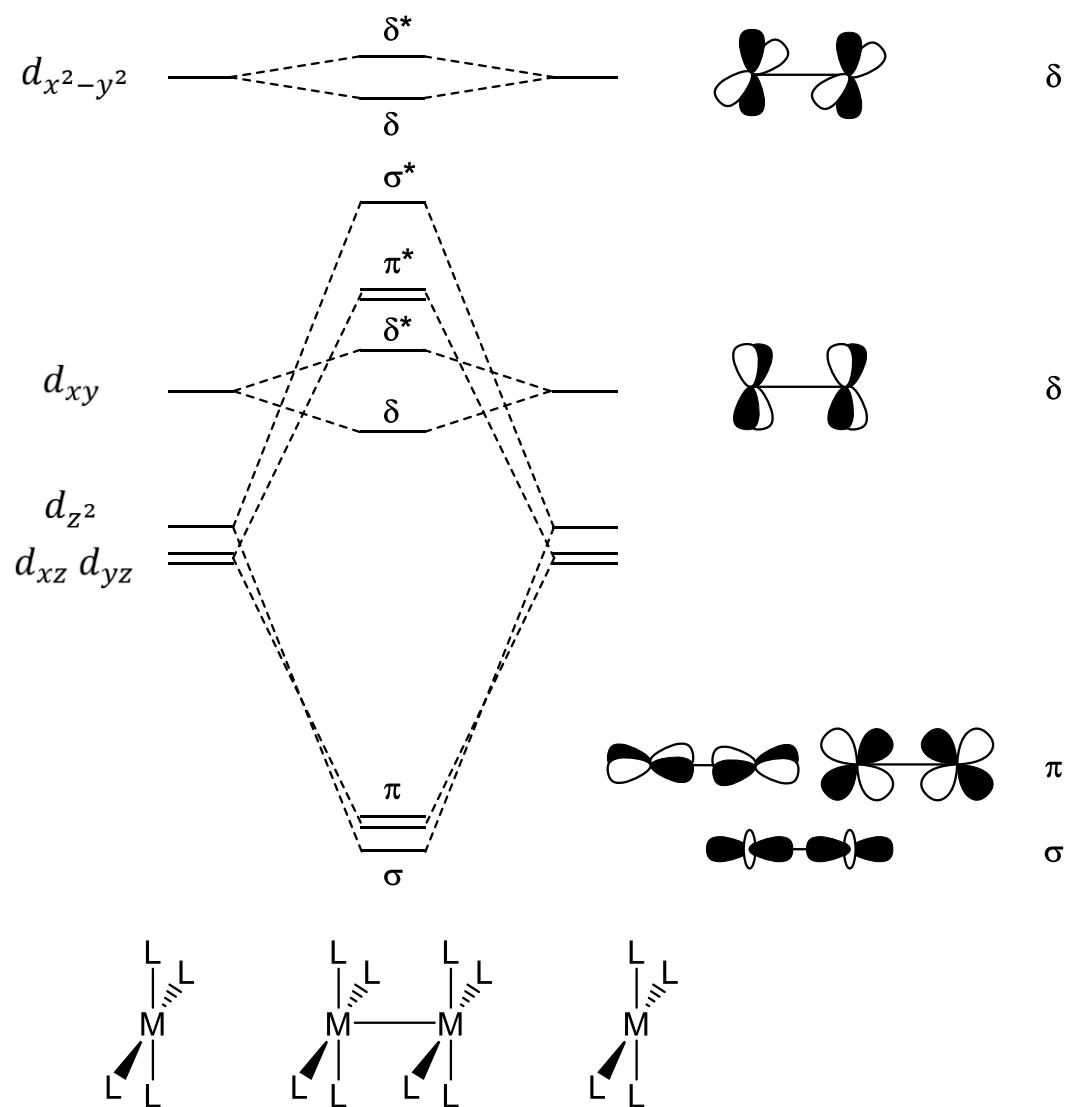


**Figure I.1** Schematic representation of the MO diagram for dinuclear complexes with monodentate ligands.

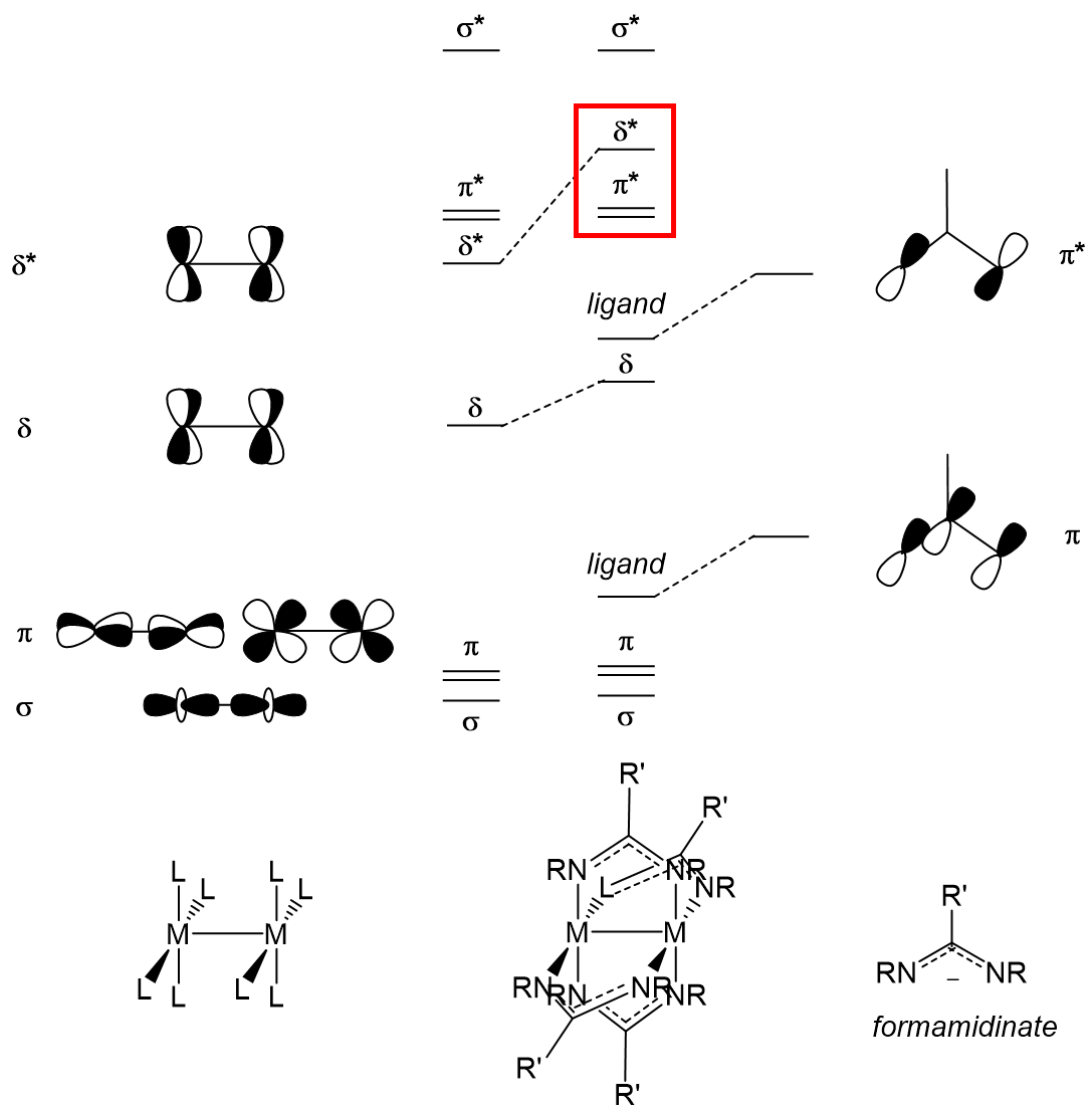


**Figure I.2** Schematic representation of the MO diagram for dinuclear complexes supporting four equivalent formamidinate bridging ligands.

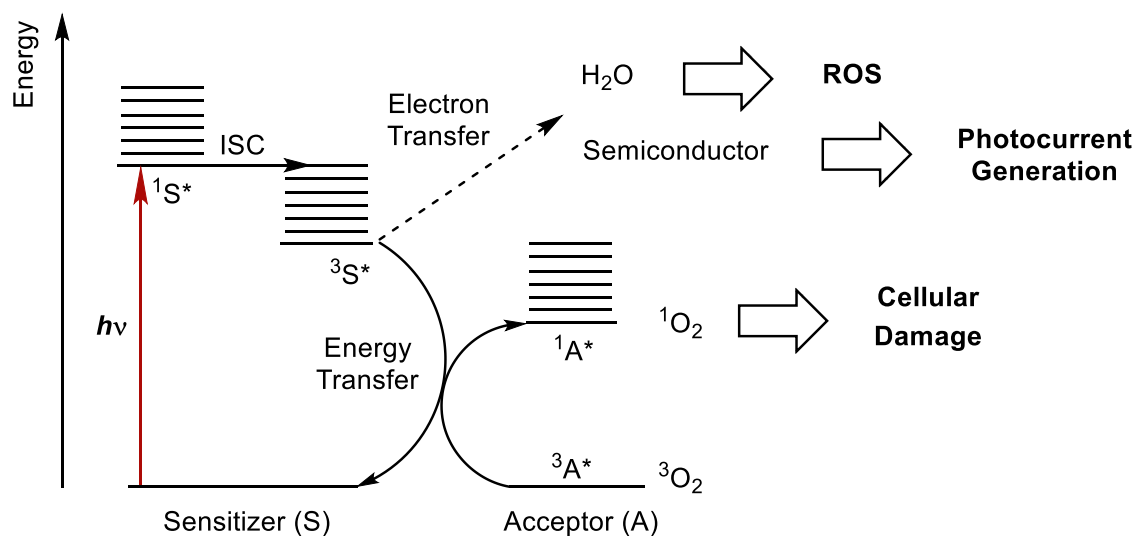


**Figure I.3** General Jablonski diagram for the excitation of a sensitizer for photodynamic therapeutic (PDT) and dye-sensitized solar cell (DSSC) applications.

The molecules can also convert to a ligand field (LF) excited state from the triplet metal-to-ligand charge transfer (MLCT) state. Upon population, this LF excited state can promote ligand dissociation (Figure I.4) leading to two products that can be used in the context of PCT. The dissociated ligand can be a biologically relevant drug molecule for the treatment of cancer such as 5-cyanouracyl and the coordinatively unsaturated metal complex can interact with biological targets such as DNA to promote cell death.<sup>14</sup>

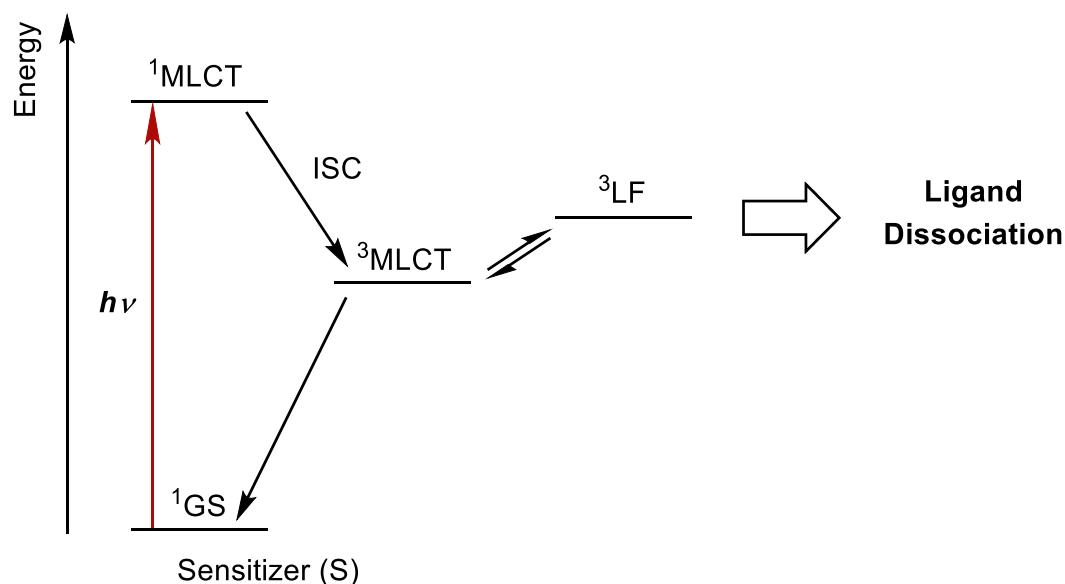


**Figure I.4** Generalized Jablonski diagram for photoactivated chemotherapeutic (PCT) drugs.

### Dirhodium Complexes as PCT and PDT drugs

Cancer is a pervasive disease and is the second leading cause of death worldwide according to the World Health Organization (WHO).<sup>15</sup> It is estimated that in the USA, approximately 1.7 million new cases of cancer will be reported in this year alone of which 600,000 will lead to death.<sup>16</sup> Although the number of deaths over the amount of new cases is proportionally decreasing due to the advent of new and improved techniques, there is still an urgent need for therapies with high efficiencies and fewer side effects.

The anticancer properties of the drug cisplatin,  $cis-[Pt(NH_3)Cl_2]$ , were serendipitously discovered by Rosenberg in 1965 and came to be the leading chemotherapeutic treatment available for a number of cancers. Upon entering the cytoplasm of a cell,  $cis-[Pt(NH_3)Cl_2]$  undergoes aquation to yield  $cis-[Pt(NH_3)(H_2O)_2]^{2+}$

due to the difference in the chloride concentration in the extracellular space versus the cytoplasm (Figure I.5). The aquation product can then bind to DNA crosslinking its structure, preventing the cell from undergoing replication, and leading to an apoptotic mechanism of cell death. The DNA target site was investigated in 1995 by Lippard and coworkers who obtained a crystal structure of a fragment of double-stranded DNA with cisplatin. This drug, although paradigm changing at the time it was approved for use, is inherently flawed in that it is unable to distinguish between healthy and cancer cells. This lack of selectivity leads to numerous deleterious side effects such as nephrotoxicity, ototoxicity, nausea, and vomiting among others.

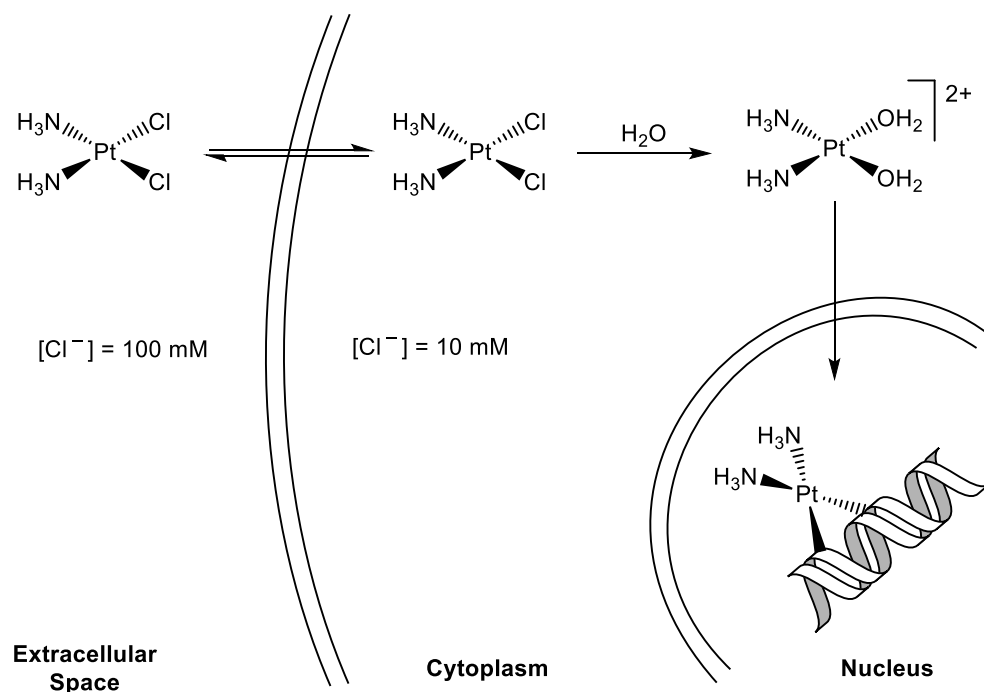


**Figure I.5** Mechanism of action of cis-platin as an anticancer drug.

The discovery of cisplatin, the first metal-based anticancer drug, led to the development of a series of Pt-based drugs that share a common mechanism of action but which produce fewer side effects (Figure I.6). For example, carboplatin, originally described in the 1970s, is a more water-soluble version of the Pt(IV) tetraplatin drug (Pt(cyclohexane-1,2-diamine)Cl<sub>4</sub>)<sup>17</sup> and was found to exhibit sensitivities that are different than those of cisplatin in a 60-cell NCI human tumor panel.<sup>18</sup> Most importantly, carboplatin exhibits more potent anticancer activity against colorectal cancer without the undesired nephrotoxicity caused by its parent drug cisplatin.<sup>19</sup>

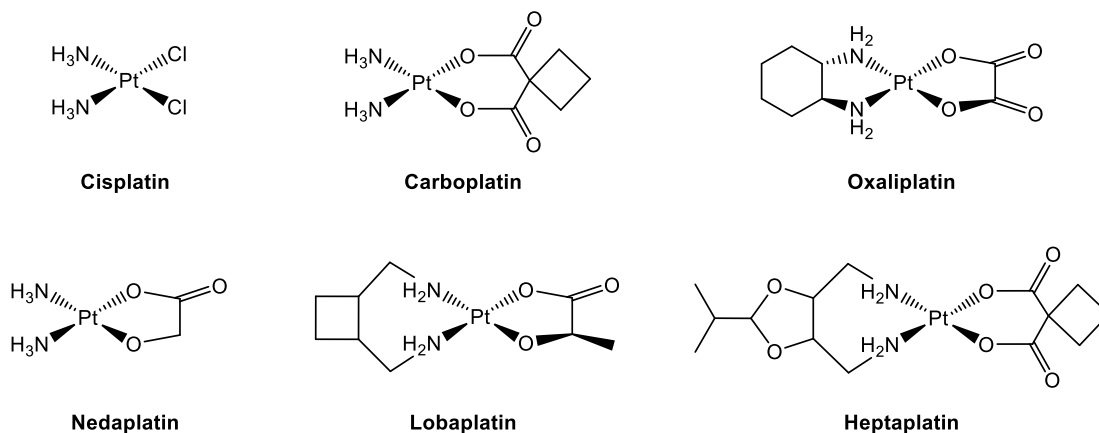


**Figure I.6** Pt based drugs approved for cancer treatment by the FDA (cisplatin, carboplatin, and oxaliplatin) other countries (nedaplatin, lobaplatin, and heptaplatin).

The anticancer activity of Rh<sub>2</sub>(μ-O<sub>2</sub>CR)<sub>4</sub> L<sub>2</sub> (R = Me, Et, Pr, and Bu; L = axial solvent) against Ehrlich ascites and leukemia L1210 tumors was discovered in 1974.<sup>17, 20-</sup>

<sup>25</sup> It was not until much later, however, that the cytotoxicity of these complexes was



attributed to the ability of these complexes to interact with nucleobases through ligand exchange and form adducts with double-strand DNA. Previously unknown bridging interactions of adjacent guanine and adenine nucleobases in short strands of DNA with dirhodium units were established by studies conducted by the Dunbar group and are akin to those of cisplatin but with two metals participating in the interactions instead of only one metal ion.<sup>3-7, 9, 26-35</sup>

It was also found that  $\text{Rh}_2(\text{AcO})_4\text{L}_2$  molecules can be modified to yield complexes with improved cytotoxicity. A series of complexes of formula  $[\text{Rh}_2(\mu\text{-O}_2\text{CCH}_3)_2(\eta^1\text{-O}_2\text{CCH}_3)(\text{L})(\text{CH}_3\text{OH})]^+$  (where L = bpy (2,2'-bipyridine), phen (1,10-phenanthroline), dpq (dipyrido[3,2-*f*:2',3'-*h*]quinoxaline), dppz (dipyrido[3,2-*a*:2',3'-*c*]phenazine), dppn (benzo[*i*]dipyrido[3,2-*a*:2',3'-*c*]phenazine), and dap (4,7-dihydrodibenzo[*de,gh*][1,10]phenanthroline)) were prepared by the Dunbar group and studied with respect to their interactions with nuclear DNA. The complexes with the highly conjugated planar dppn ligand were shown to have the strongest interaction with DNA as well as being capable of causing the most damage to DNA after cellular internalization. The molecule supporting a dppz ligand is, however, the most cytotoxic one of the series due to its optimal lipophilicity for cellular uptake.<sup>36</sup>

A series of axially blocked dirhodium complexes was designed in the Dunbar laboratories; their molecular structures are depicted in Figure I.7.<sup>31</sup> The ligands used in this study – 1,8-naphthyridine and 2-(pyridin-2-yl)-1,8-naphthyridine (pynp), in contrast to dppn or dppz, are not extended pi-systems and therefore cannot intercalate DNA. The only possible interactions with biological substrates must occur through the axial

positions. The ability of these compounds to stabilize DNA and inhibit transcription *in vitro* was studied and it was observed that the compounds with substitutionally labile axial positions exhibit the lowest  $C_{inh}^{50}$  (concentration needed to inhibit 50% of the transcription) whereas the fully blocked complex incapable of inhibiting DNA transcription. This study also demonstrated that the incorporation of highly conjugated  $\pi$ -accepting ligands can change the parentage of the lowest energy transitions which leads to an increase in their molar absorptivity coefficients. Additionally, the role of the equatorial position in transcription inhibition was studied using the partially solvated cation  $cis\text{-}[\text{Rh}_2(\mu\text{-O}_2\text{CCH}_3)_2(\text{NCCH}_3)_6]^{2+}$  and it was found that the  $C_{inh}^{50}$  is similar to that of cisplatin.<sup>29</sup>

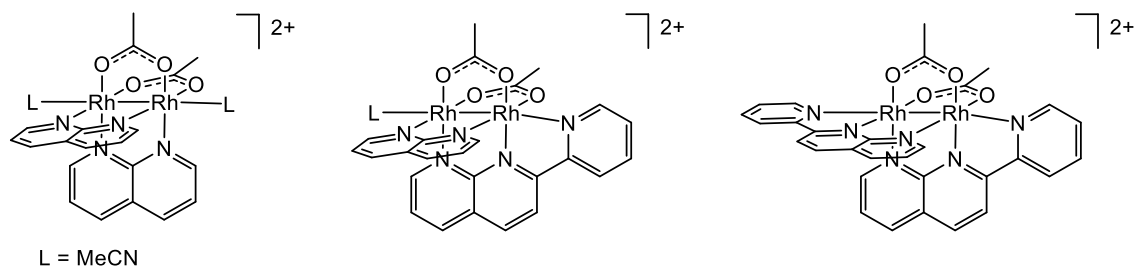


**Figure I.7** Cytotoxic axially-blocked dirhodium complexes as inhibitors of DNA transcription *in vitro* for cancer treatment.

All of the aforementioned Rh and Pt-based cytotoxic compounds suffer from lack of selectivity for targeting healthy versus cancer cells. Photodynamic therapy and photoactivated chemotherapy are attractive alternatives to conventional chemotherapy since they provide spatial and temporal control over the treatment (Figure I.8). The patient

is administered with a drug that accumulates in healthy as well as tumor tissue which is non-toxic until it is irradiated with an appropriate source of light only in the area of the cancer to produce either singlet oxygen (in the case of PDT drugs) or TO release a drug that can damage cellular targets (in the case of PCT agents) as indicated in Figures I.3 and 4. These therapies rely on the ability of light to penetrate tissue which generally limits their use to the treatment of superficial tumors or endoscopically accessible cancers such as lung, bladder, esophageal, prostate, and gastrointestinal among others.<sup>37-39</sup> Optimal tissue penetration occurs with light in the 600 – 900 nm range, widely known as the “PDT window”.<sup>40,41</sup> PDT drugs can sensitize the formation of the highly cytotoxic species single oxygen (Type II) or transfer electrons to generate free radicals (hydroxide radical, superoxide radical, or hydrogen peroxide) thereby promoting cell death.<sup>42, 43</sup> The damage can be to the tumors themselves or the vasculature around them.<sup>37</sup>

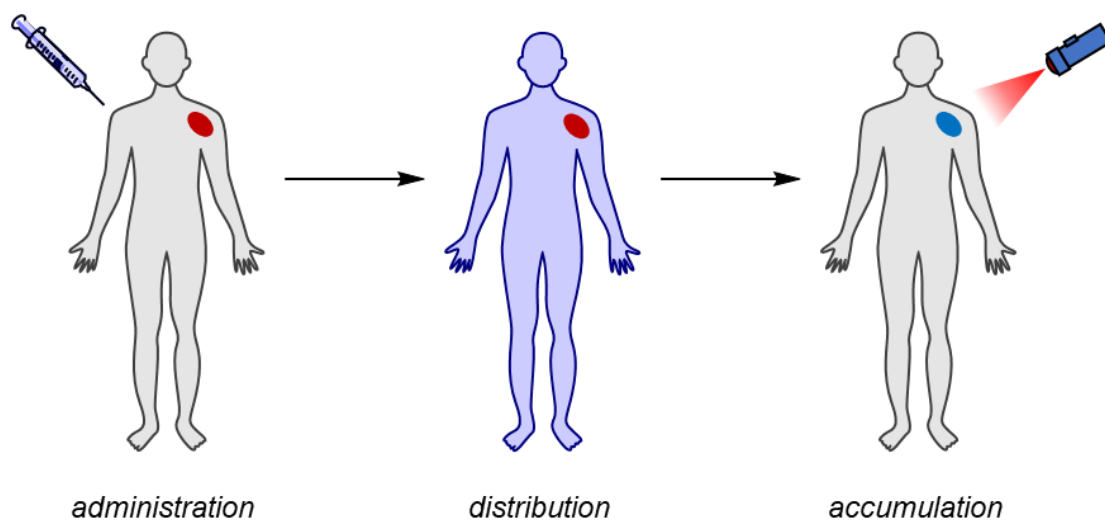


**Figure I.8** Treatment scheme for PDT and PCT drugs.

The “gold standard” PDT anticancer drug is porfimer sodium (Photofrin®) which is an oligomeric mixture of hematoporphyrin (Figure I.9). This drug sensitizes oxygen to produce singlet oxygen upon irradiation with 630 nm light due to sufficiently long excited state lifetimes and it is mostly employed in the treatment of esophageal cancer. The oligomeric mixture has two main deficiencies that lower its efficacy, namely low absorption coefficients ( $3000 \text{ M}^{-1}\text{cm}^{-1}$ ) at the excitation wavelength (630 nm) and low quantum yields for singlet oxygen generation ( $\sim 20\%$ ), both of which lead to the requirement of high therapeutic concentrations. In addition, the low rate of clearance from the organism causes prolonged photosensitivity in the patients which is a highly undesirable side effect. Some of these drawbacks can be circumvented by minor modifications to the structure of this photosensitizer. For example, the use of metal porphyrins can increase the rate of intersystem crossing (ISC) which facilitates the population of the triplet excited states, concomitantly increasing the quantum yield for oxygen sensitization.<sup>42, 43</sup> Another approach is the topical use of the hematoporphyrin precursor  $\delta$ -aminolevulinic acid ( $\delta$ -ALA, Figure I.9) which generates the sensitizer *in situ* to lower the systemic side effects associated with this type of treatment.<sup>44</sup>

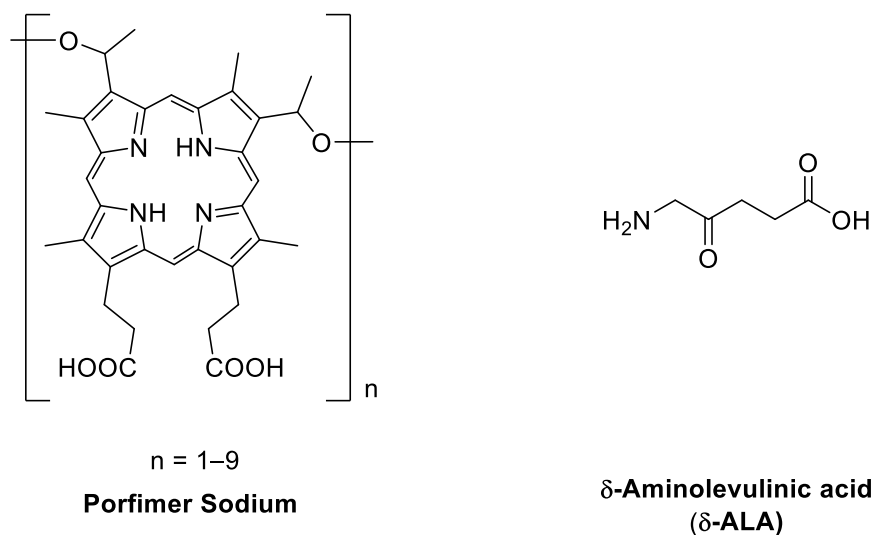


**Figure I.9** Molecular structures of porfimer sodium and  $\delta$ -aminolevulinic acid.

PDT relies on the presence of a high concentration of molecular oxygen for the treatment to be effective. Some tumors, however, have very low oxygen concentrations (hypoxic) which renders this treatment ineffective. An oxygen-independent alternative to PDT that retains the spatial and temporal controls of light activated processes is photoactivated chemotherapy (PCT). Upon irradiation, the pro-drug can populate a  $^3LF$  excited state and promote ligand dissociation to release the active drug. The drug can be the ligand that is released (e.g. 5-cyanouracil) or the metal fragment which is free to react with biologically relevant targets. A few examples of Pt(IV)-based drugs are shown in Figure I.10. These Pt(VI) drugs, in contrast to their Pt(II) analogies, are octahedral and contain OH groups in the axial positions. Upon irradiation, the excited state pro-drug Pt(IV) can be reduced by two electrons supplied by the medium to Pt(II) which releases the axial ligands and yields the active form of the drug (Figure I.11).

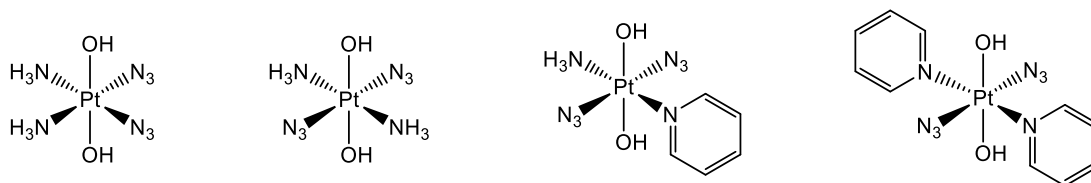


**Figure I.10** Examples of Pt(IV) pro-drugs as PCT agents.

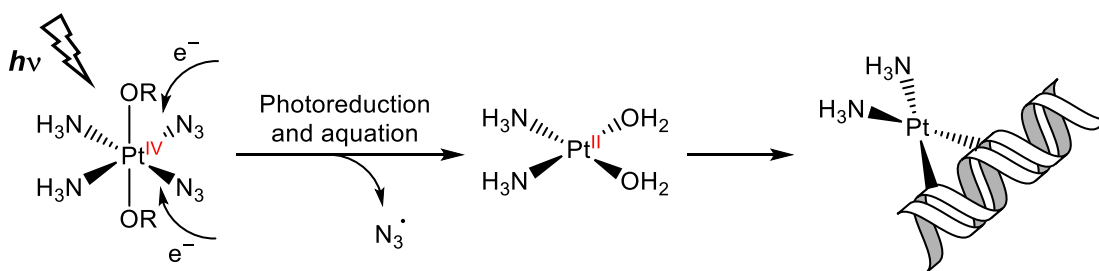


**Figure I.11** Mechanisms of action of the pro-drug Pt(IV) complexes for PCT application.

In 2006, the Turro group studied the photoactivated properties of the partially solvated dirhodium complex  $cis\text{-}[\text{Rh}_2(\text{AcO})_2(\text{MeCN})_6][\text{BF}_4]_2$  which behaves similarly to the aforementioned Pt(IV) drugs.<sup>11</sup> This complex, upon irradiation ( $\lambda_{\text{irr}} \geq 455 \text{ nm}$ ), undergoes photoaquation from population of metal-centered (MC) excited states to yield a bis-aqua dirhodium complex which is capable of DNA binding in a manner akin to that of cisplatin (Figure I.12). The molecule exhibits a 20-fold lower dark cytotoxicity compared to hematoporphyrin and a 7-fold increase in cytotoxicity when irradiated in the presence of human skin cells. Although this “cisplatin photoactivated analogue” shows promise as a proof-of-concept PCT agent, the energy of light required is far higher in

energy that what is required for deep-tissue penetration. The use of more electron donating bridging ligands such as amidates<sup>10</sup> and 2-oxypyridinates<sup>9</sup> (Figure I.13) red-shift the absorption profiles of these complexes into the PDT window making them better candidates for PCT applications.

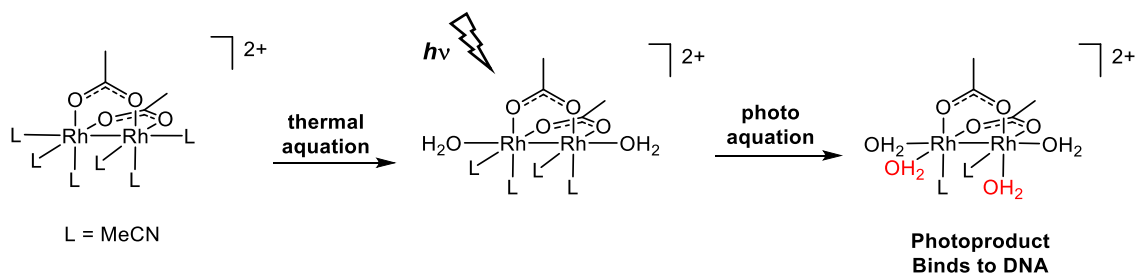


**Figure I.12** Schematic representation of the formation of the aqua dirhodium complex *cis*-[Rh<sub>2</sub>(AcO)<sub>2</sub>(MeCN)<sub>4</sub>(H<sub>2</sub>O)<sub>2</sub>][BF<sub>4</sub>]<sub>2</sub> upon irradiation.

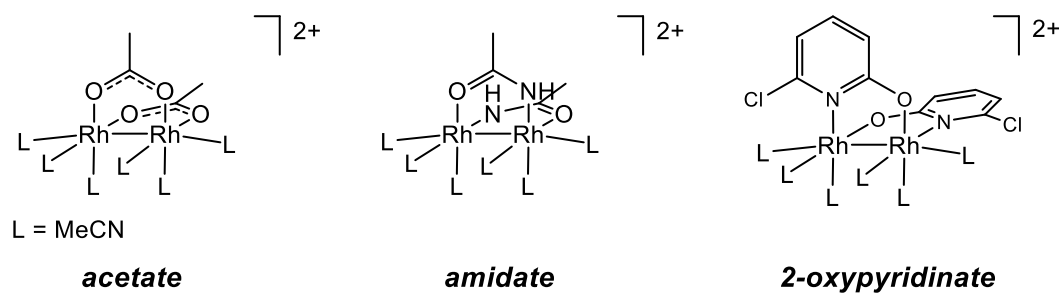


**Figure I.13** Molecular structures of cationic dirhodium complexes for PCT applications.

### Dirhodium Complexes as Photocatalysts and Sensitizers for DSSCs and DSPECs

As energy demands increase worldwide, the need for renewable energy sources that can produce energy or carbon-neutral fuels becomes of paramount importance. Solar

energy conversion, although an attractive alternative to non-renewable sources, is only responsible for 6 % of the energy produced by renewable sources.<sup>45</sup> Commercially available devices are composed of a p-n junctions and operate at an efficiency of ~ 15 %. These devices have several shortcomings, namely, cost, low durability, high dependence of the angle of incidence with efficiency, and low efficiencies under low-light conditions.<sup>46</sup> Dye-sensitized solar cells (DSSCs) can circumvent some of the drawbacks of commercially available devices and have the potential to yield highly-efficient and cost-effective devices.<sup>47</sup>

Standard DSSC devices are composed of a semiconductor,<sup>48-51</sup> a counter electrode,<sup>52</sup> a binary redox couple,<sup>53</sup> and a sensitizer (Figure I.14).<sup>54</sup> When the device is irradiated, the sensitizer absorbs the photons to achieve an excited state, and, if the redox potentials are appropriate, the excited state can either donate to or accept an electron from a semiconductor yielding an n-type or p-type sensitized DSSC respectively. In the case of an n-type DSSC, the injected electron travels through the conduction band of the semiconductor and through the wire to the counter electrode where the electrolyte (typically  $\Gamma/I_3^-$ ) can be reduced and later reoxidized regenerating the sensitizer. The overall efficiency of these devices is represented by the photo-current efficiency (PCE,  $\eta$ ) calculated using the following equation:

$$\eta = \frac{J_{SC}V_{OC}FF}{P_S}$$

where  $J_{SC}$  is the short-circuit current density,  $V_{OC}$  is the open-circuit voltage (difference between Fermi level,  $E_F$ , of  $TiO_2$  and redox potential of the electrolyte<sup>55</sup>),  $P_S$  is the incident-light power efficiency, and  $FF$  is the fill factor.<sup>56</sup> Another important figure-of-



merit for these devices is the incident-photon-to-electron conversion efficiency (IPCE) which is defined as the ratio between incident photons and the generated charge carriers as shown in the equation:

$$IPCE = 1240 \frac{J_{sc}(\lambda)}{\lambda P_s}$$

This parameter is usually plotted as a function of wavelength of irradiation and gives a measure for the performance of the device under standard test conditions, which are AM 1.5 spectrum, T = 25 °C, and PS = 100 mW cm<sup>-2</sup>.

The theoretical efficiency limit of these devices can be calculated and it is 33 % for n-type sensitized DSSCs and 44 % in the case of n- and p-type tandem cells.<sup>57</sup> These efficiencies, however, are far higher than what has been achieved experimentally with a varied array of semiconductors, sensitizers, and electrolytes. One of the limitations of these devices is the lack of panchromatic absorbers capable of participating in electron transfer reactions from their excited states upon irradiation with low-energy light. The efficiency is therefore lowered by the lack of absorption of the full solar spectrum and new sensitizers with absorption that extends into the red/near-IR region are in high demand.

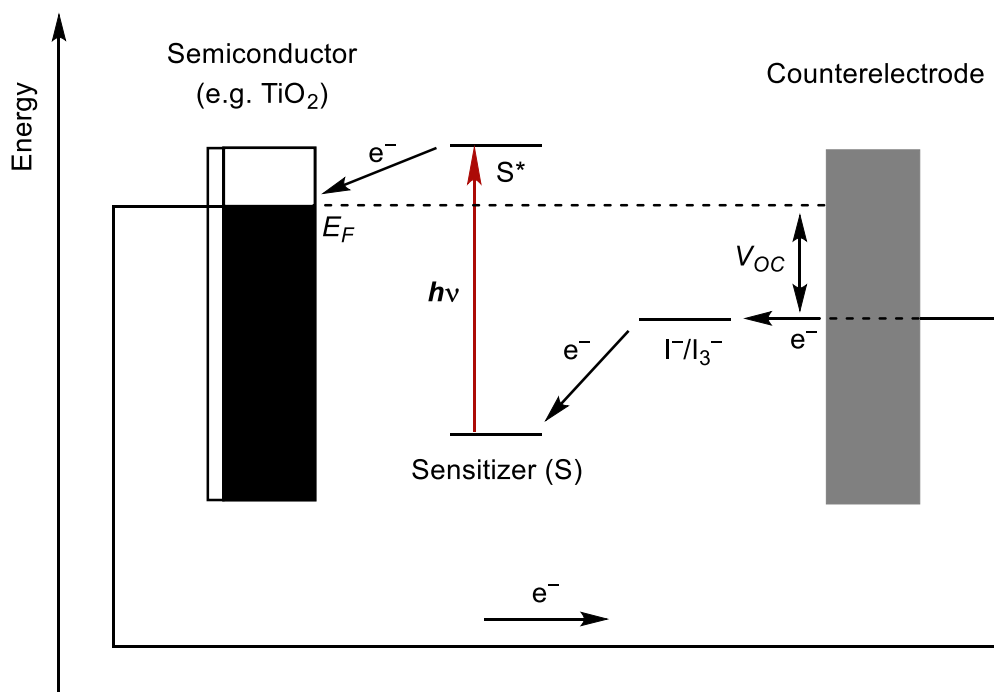


**Figure I.14** Schematic representation of the mechanism of action of an n-type sensitized solar cell, where  $E_F$  is the Fermi level of the semiconductor and  $V_{OC}$  is the open circuit potential of the device.

There are general considerations for the design of efficient sensitizers which include: panchromatic absorption profiles (UV – 900 nm), support of anchoring groups to bind to semiconductors,  $E^{\circ\prime}_{excited\ state} < E^{\circ\prime}_{CB, semiconductor}$ , and efficient excited state injection. The gold standard for n-type sensitization is the Ru(II) N3 dye which contains anchoring carboxylate groups for semiconductor binding and sufficiently reducing excited state potentials for electron injection (Figure I.15).<sup>58</sup> Devices sensitized by this dye, however, do not reach efficiencies beyond 10–12 % which is attributed to the lack of panchromatic absorption since it does not significantly absorb light beyond ~ 600 nm. Figure I.15 shows the structure of other types of recently developed dyes with marginally

higher efficiencies than the archetypal N3 dye.<sup>59</sup> Both dyes, the SM315<sup>60</sup> and ADEKA,<sup>61</sup> have similar structural features, namely, an electron donating moiety, an electron accepting region, and anchoring groups for semiconductor binding. Upon irradiation, the compounds can transfer an electron from one region of the molecule to another leading to a charge separated state which can inject electrons into the semiconductors. The devices sensitized by these dyes have efficiencies of 13.0 and 12.5 for SM315 and ADEKA respectively. As in the case of the Ru N3 dye, these low efficiencies are attributed to poor absorption in the red/near-IR region which remains underutilized by most current dyes. Additionally, other promising dyes such as porphyrins and phthalocyanines suffer from aggregation issues due to the planarity of their structures which ultimately results in lower efficiencies.<sup>62</sup> Therefore, new panchromatic absorbers that can partake in electron injection processes upon irradiation with low-energy light are highly desired.

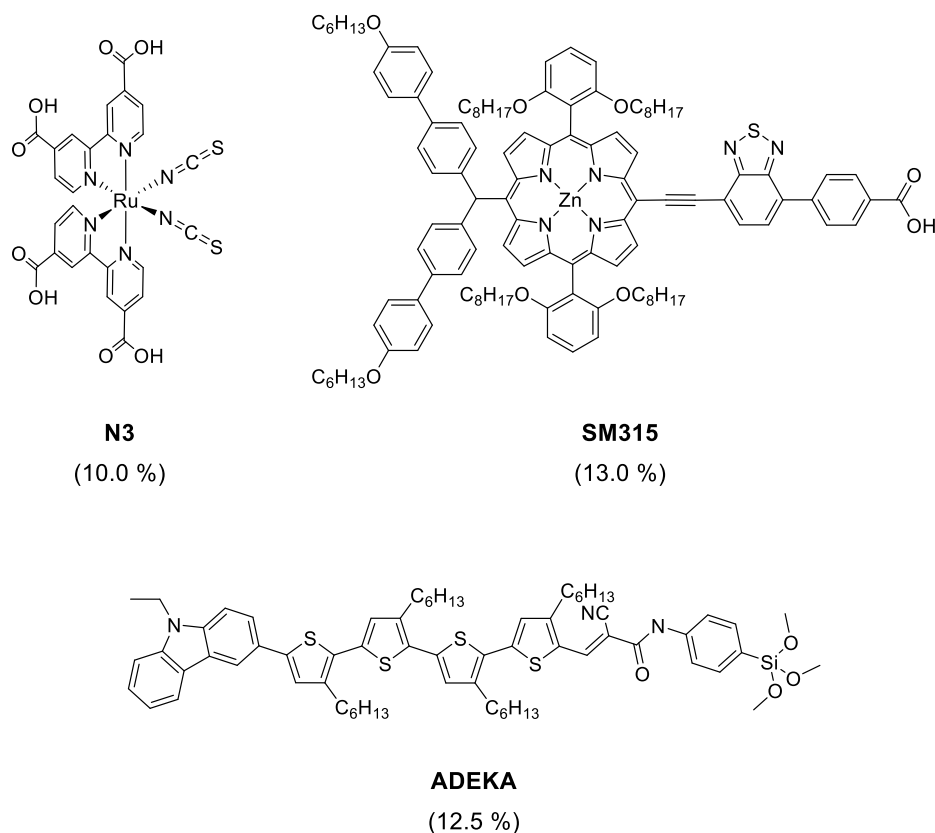


**Figure I.15** Molecular structures of three different types of dyes for n-type semiconductor sensitization: N3 (ruthenium(II) dye), SM315 (Zn(II) phthalocyanine dye), and ADEKA (organic dye) with their respective IPCEs.

Recently, a series of dirhodium complexes capable of n-type sensitization were published by the Turro group (Figure I.16).<sup>63</sup> The compounds display panchromatic absorption profiles and low-lying metal/ligand-to-ligand charge transfer (ML-LCT) excited states. These excited states were characterized by ultrafast and nanosecond transient absorption and time-resolved infrared spectroscopies and assigned to singlet and triplet transitions that are Rh2/form-to-naphthyridine in nature. More importantly, due to the rigidity imparted by the axial-blocking ligands, the molecules display relatively long-

lived excited states with appropriate reduction potentials to reduce the methyl viologen cation upon irradiation with low energy light, in contrast to the axially free analogue *cis*-[Rh<sub>2</sub>(DTolF)<sub>2</sub>(np)<sub>2</sub>][BF<sub>4</sub>]<sub>2</sub>. These excited state properties make them attractive candidates as TiO<sub>2</sub> sensitizers for n-type DSSCs applications.

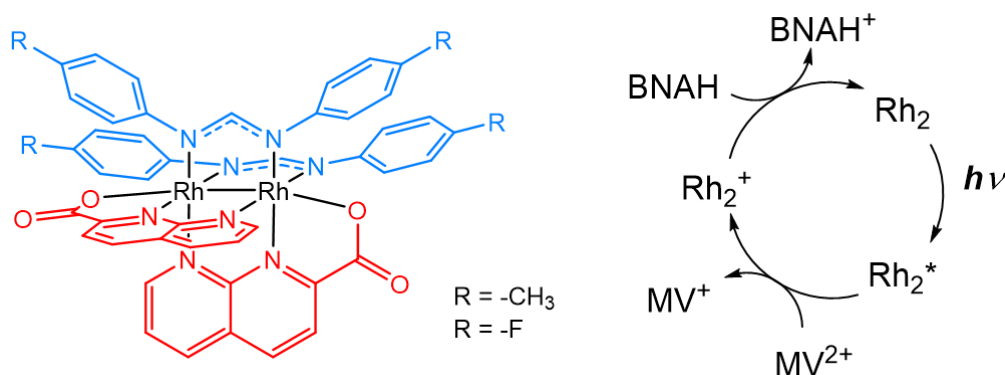


**Figure I.16** Structure of the complexes *cis*-[Rh<sub>2</sub>(μ-form)<sub>2</sub>(μ-npCOO)<sub>2</sub>][BF<sub>4</sub>]<sub>2</sub> (where form = *p*-ditolylformamidinate or *p*-difluorobenzylformamidinate, and npCOO<sup>-</sup> = 1,8-naphthyridine-2-carboxylate) on the left and photo-induced electron transfer cycle on the right where MV<sup>2+</sup> (methyl viologen) is the substrate and BNAH (1-benzyl-1,4-dihydropyridine-3-carboxamide) is the sacrificial donor.

Since the IPCEs of traditional DSSCs are far below the theoretical predicted maximum efficiencies, a more attractive alternative is the production of carbon-neutral fuels in dye-sensitized photoelectrosynthesis cells (DSPECs, Figure I.17). The mechanism of action of these devices is similar to that of DSSCs but the sensitizer is substituted by a chromophore-catalyst assembly and the binary redox couple for a substrate, such as water, that can be oxidized and reduced yielding a desired product (e. g. H<sub>2</sub>) and a current. In these devices, the chromophore transfers electrons from the catalyst to the semiconductor

upon irradiation. The oxidized catalyst can now, itself, oxidize a substrate such as water promoting the reduction of protons to  $H_2$  at the surface of the counter electrode. The design criteria for the chromophore is similar to the sensitizers used in DSSCs with the added requirement of a reduction potential that is appropriate for catalyst oxidation. The catalyst, on the other hand, must have a catalytically active form accessible by chromophore oxidation, it has to be robust, display low overpotentials, and minimize competitive light absorption.<sup>64</sup>

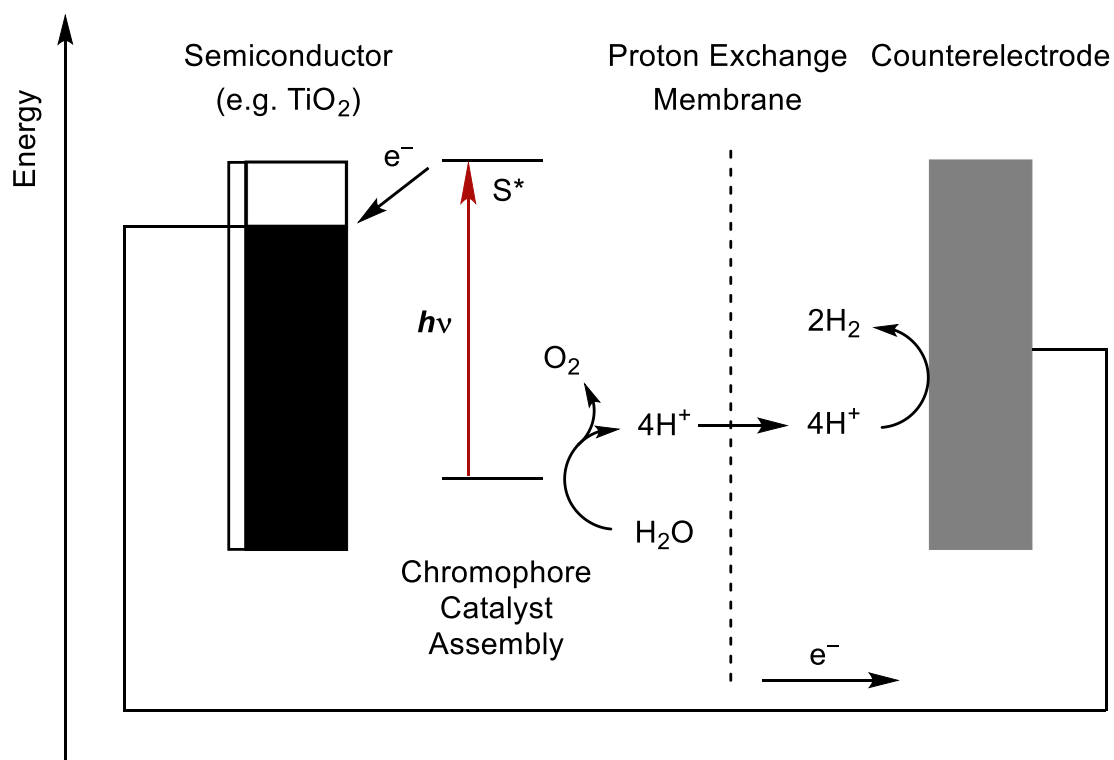


**Figure I.17** Schematic representation of the mechanism of action of an n-type sensitized photoelectrosynthesis cell.

There are many different approaches to the design of chromophore-catalyst assemblies. Figure I.18 displays a molecular Ru-based assembly,  $[(4,4'-\text{PO}_3\text{H}_2)_2\text{bpy})_2\text{Ru}(4\text{-Mebpy-4'-bimpy})\text{Ru}(\text{tpy})(\text{OH}_2)]^{4+}$  (where 4-Mebpy-4'-bimpy = 4-(methylbipyridin-4'-yl)-N-benzimid-N'-pyridine; tpy = 2,2':6',2''-terpyridine), that consists of two main parts.<sup>65</sup> The first moiety in the chromophore supports phosphate-anchoring groups for semiconductor binding and bipyridine ligands for light absorption. This complex is tethered by a linker to a Ru catalyst that has a position occupied by a water molecule. Upon light irradiation ( $\lambda_{\text{irr}} = 445 \text{ nm}$ ), the chromophore can transfer electrons to the semiconductor and oxidizing the catalyst in the process. Upon oxidation by four electrons, the water molecule is oxidized to  $\text{O}_2$  and  $\text{H}^+$  which are reduced to  $\text{H}_2$  at the counterelectrode. The absorbed photocurrent efficiency for the assembly reaches ~20% with a  $\text{H}_2$  production efficiency of less than 1%. This type of covalently linked chromophore-catalyst assembly is a great proof-of-concept for DSPECs, but they require multiple synthetic steps which ultimately lowers the yields of such assemblies. Other types of assemblies for which the catalyst is not covalently bound to the chromophore, but is in the vicinity of it, have been developed and show great promise for these types of applications.<sup>64, 66</sup>

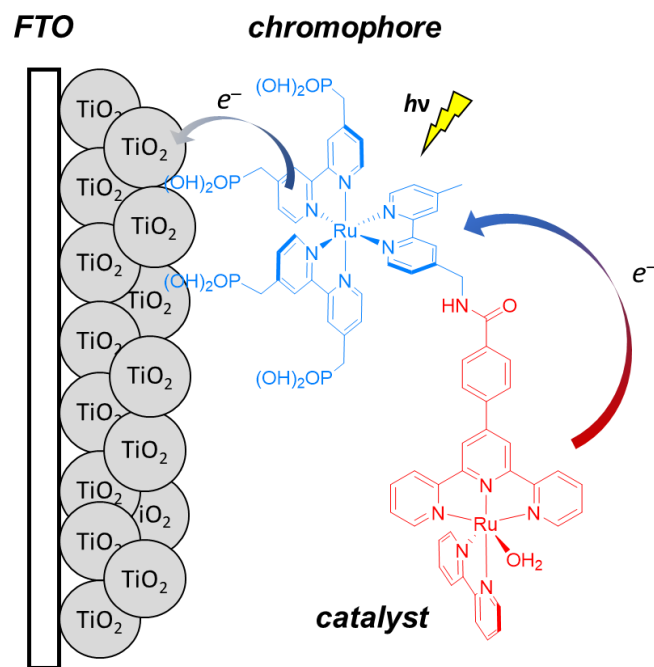
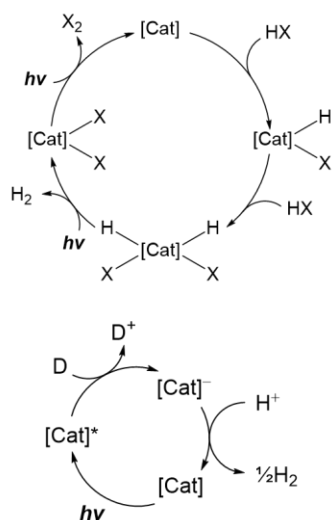


**Figure I.18** Schematic representation of the chromophore-catalyst assembly  $[(4,4'\text{-PO}_3\text{H}_2)_2\text{bpy})_2\text{Ru}(4\text{-Mebpy-4'-bimpy})\text{Ru}(\text{tpy})(\text{OH}_2)]^{4+}$  in a DSPEC device for water splitting.

Although dirhodium complexes are excellent candidates for DSSCs or DSPECs, there are no reported examples of devices using dirhodium complexes as sensitizers or as part of a chromophore-catalyst assembly. Nevertheless, there are a few examples of dirhodium complexes as photocatalyst or as sensitizers in photocatalytic assemblies for H<sub>2</sub> production. There are several types of molecular photocatalysts or photocatalytic systems for H<sub>2</sub> production, depicted in Figure I.19, that can be divided in two groups, namely, single and multi-component systems.<sup>67</sup>



Single component photocatalytic HX splitting



Multi-component photocatalytic  $H_2$  production

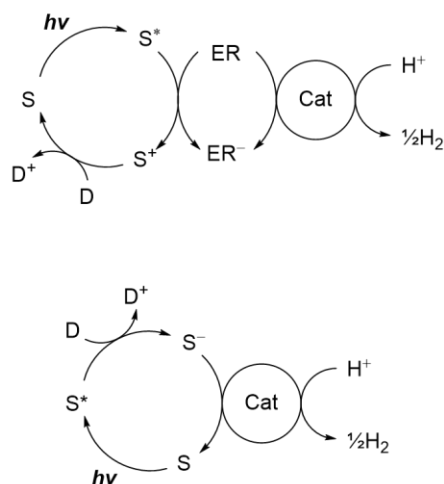


**Figure I.19** Photocatalytic cycle schemes for single and multi-component assemblies for  $H_2$  production.

Nocera and coworkers developed several single component dirhodium photocatalytic systems for HX splitting.<sup>68-70</sup> These compounds have a main advantage over multi-component systems due to the fact that they require one fewer charge-transfer step. For example, the mixed valence single component photocatalyst shown in Figure I.20,  $Rh_2^{0,II}(tfepma)_2(CNAd)_2Cl_2$  (CNAd = 1-adamantylisocyanide), has a TON for hydrogen production of 7 (after 144 h) when irradiated with at  $\lambda_{exc} > 305$  nm. This complex has remarkable durability, but the TON is low and, more importantly, it requires UV light irradiation to produce  $H_2$  gas. The high-energy requirements for this process are due to the energetically demanding reductive elimination process to produce  $X_2$  and regenerate the catalyst. The use of a system with an electron donor to regenerate the catalyst would be beneficial if low-energy light catalysis is to be achieved.

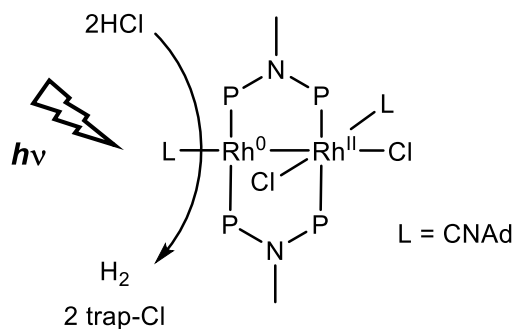


**Figure I.20** Molecular structure representation of the mixed valence dirhodium photocatalyst  $\text{Rh}_2^{0,\text{II}}(\text{tfepma})_2(\text{CNAAd})_2\text{Cl}_2$ .

### Dissertation Objectives and Outline

Dirhodium complexes show great promise in fields where a good sensitizer is needed due to the highly tunable excited state properties of these bimetallic metal-bonded complexes. By a judicious choice of ligands around the bimetallic core, different properties can be imbued in the final complexes such as a panchromatic absorption profile, improved water solubility, long-lived excited states, and highly reducing or oxidizing excited states, to name a few. It is because of this that these complexes show great promise in the fields of photoactivated chemotherapy (PCT), dye-sensitized solar cells (DSSCs), and photocatalytic hydrogen production.

In Chapter II, the synthesis and characterization of a new dirhodium complex that supports an axial blocking ligand while retaining equatorial solvent molecules will be discussed in the context of PCT. This complex has the potential to undergo photo-induced

ligand exchange upon irradiation and the DNA binding properties of this complex will be contrasted with the fully blocked analogue and the fully solvated parent complex.

The complexes synthesized in Chapter II led to the design and synthesis of the complexes presented in Chapter III. These dirhodium complexes support two axial blocking ligands and two electron-rich formamidinate ligands. Their photophysical properties are studied as well as their ability to transfer electrons to an organic substrate evaluated. This new class of compounds represents the first example of light-induced electron acceptors for p-type sensitization in the context of DSSC applications.

A new synthetic methodology for the synthesis of the first example of a *trans*-dirhodium complex is presented in Chapter IV. The methodology is supported by computational calculations, experimental data, and opens a new door for the synthesis of the unexplored *trans* isomers as sensitizers for DSSC applications. This work also provides a synthetic methodology that would allow the synthesis of new dirhodium supramolecular architectures with potentially interesting photophysical properties.

In Chapter V, the synthesis and characterization of a new class of dirhodium photocatalysts for H<sub>2</sub> production with low energy light is discussed. These complexes display an axial open position for catalysis and a blocked position that impart rigidity to the complexes leading to long-lived excited states and panchromatic absorption profiles. The photocatalytic H<sub>2</sub> production capabilities of these complexes upon low-energy light irradiation in the presence of a sacrificial electron donor is assessed in this chapter.

Lastly, overall conclusions and future directions for this work are provided in Chapter VI.

CHAPTER II  
EFFECT OF THE EQUATORIAL POSITION ON THE PHOTOINDUCED  
BIOLOGICAL ACTIVITY OF DIRHODIUM(II,II) COMPLEXES WITH A SINGLE  
AXIAL BLOCKING LIGAND

**Introduction**

Cancer is the second leading cause of death in the United States as well as worldwide.<sup>15, 16</sup> It is estimated that 1.7 million new cases of cancer will be reported in the United States alone this year, and 600,000 of them will lead to death. Although the mortality rates have decreased due to the development and implementation of various new therapies, there remains a critical need for new and improved chemotherapeutic agents with fewer side effects. The serendipitous discovery of the archetypal cisplatin drug in 1965 by Rosenberg et. al represents a paradigm change in cancer chemotherapy. The cis-[Pt(NH<sub>3</sub>)<sub>2</sub>Cl<sub>2</sub>] complex can undergo hydrolysis once inside the cells due to the dramatic decrease of Cl<sup>-</sup> ions in the cytosol in contrast to the extracellular space. The aqua complex cis-[Pt(NH<sub>3</sub>)<sub>2</sub>(H<sub>2</sub>O)<sub>2</sub>]<sup>2+</sup> has the ability to bind to DNA, with the major adduct being the cisplatin-DNA GG intrastrand species characterized by X-ray crystallography.<sup>71</sup> The lesion produced by the Pt binding is unable to be recognized by DNA repair enzymes which prevents cellular replication and ultimately induces apoptotic cell death. This drug, as is the case with many others, however, presents many drawbacks as a chemotherapeutic agent due to the lack selectivity as well as of temporal and spatial control which leads to many undesired side effects due to the unregulated high cytotoxicity of the complex.

Photodynamic therapy (PDT) and photoactivated chemotherapy (PACT) are promising alternatives to common chemotherapy treatments by using a light source to trigger the cytotoxic response of the compounds in a well-defined region of the tissue via sensitization of  $^3\text{O}_2$  to generate  $^1\text{O}_2$ , highly reactive species or by photo-inducing the release of a toxic molecule from a pro-drug.<sup>72</sup> The gold standard for PDT, Photofrin®, is used primarily for cancers that are either superficial or endoscopically accessible owing to the fact that the absorption profile of this oligomeric mixture of porphyrins does not absorb significantly beyond 550 nm, which is below the PDT window for good penetration (600–900 nm). This fact reduces the PDT agent's efficiency to target tumors located deeper in the tissue, as the absorption of the tissue itself prevents the complex from generating  $^1\text{O}_2$  in sufficient quantum yields. In addition, the photocytotoxicity index (PI =  $\text{LC}_{50}/\text{LC}_{50}^*$ , where  $\text{LC}_{50}$  is the lethal concentration 50% in the dark and  $\text{LC}_{50}^*$  is upon irradiation) of this drug is only ~5, which is far from ideal. Lastly, oxygen dependence limits its use to tumors under normoxic conditions, since hypoxic tumors do not have a good supply of oxygen to be sensitized.

There is a variety of d-block metals that are potentially attractive to use for photochemotherapeutic agents due to their highly tunable excited state properties for oxygen sensitization or ligand release that can be used to overcome the challenges presented by the porphyrin-based PDT drugs. For example, Ru(II) complexes such as the photoactivated arene complexes  $[(\eta^6\text{-p-cym})\text{Ru}(\text{bmp})(\text{Cl})]^+$  (where bmp = 2,2'-bipyrimidine and  $\eta^6\text{-p-cym}$  = para-cymene) functionalized with a tripeptide to improve tumor targeting undergo photoaquation to yield  $[(\eta^6\text{-p-cym})\text{Ru}(\text{bmp})(\text{H}_2\text{O})]^{2+}$  upon

irradiation with  $\lambda_{\text{max}} = 420$  nm light, a species that was shown to bind to nucleobases and DNA in a manner akin to that of cisplatin.<sup>73</sup> The compound however, does not absorb significantly beyond 450 nm and therefore is not optimal for PACT applications. Clearly, the development of new drugs with high quantum yields for singlet oxygen production or ligand dissociation with low energy light that exhibit a marked difference in cytotoxicity in the presence and absence of light remains a challenge. To tackle this issue, dirhodium(II,II) complexes that display highly tunable electronic structures and panchromatic absorption profiles that extend throughout the PDT window are being designed. Conveniently, these complexes are air and water stable and have well documented photochemical and anticancer properties.

The antiproliferative properties of dirhodium(II,II) tetracarboxylate complexes of the type  $\text{Rh}_2(\mu\text{-O}_2\text{CR})_4$  (where R = Me, Et, Pr, and Bu) against Ehrlich ascites and leukemia L1210 tumors was first reported in 1974.<sup>17, 20-25</sup> It was later shown that this activity is caused by the ability of the model complex  $\text{Rh}_2(\mu\text{-O}_2\text{CCH}_3)_4$  to interact with nucleobases and nucleosides through the axial positions at room temperature and also to its capability to undergo ligand exchange and bind to ds-DNA.<sup>26-30</sup> These Rh-DNA interactions can be axial, axial-equatorial, or equatorial-equatorial depending on the lability of the ligands in the parent complex. The parital paddlewheel compounds *cis*- $[\text{Rh}_2(\mu\text{-O}_2\text{CCH}_3)_2(\text{pynp})_2](\text{BF}_4)_2$  (pynp = 2-(pyridin-2-yl)-1,8-naphthyridine) with blocked axial sites and equatorial positions that are not labile cannot inhibit DNA transcription which reinforces the hypothesis that accessible equatorial and axial positions are required to promote the formation of a Rh-DNA adduct.<sup>31</sup>

In the vein of pursuing dirhodium compounds with desired reactivity, the partially solvated analogue  $cis\text{-}[\text{Rh}_2(\mu\text{-O}_2\text{CCH}_3)_2(\text{MeCN})_6](\text{BF}_4)_2$  was explored in cancer cells with the aim of using light to activate the release of acetonitrile ligands.<sup>11</sup> Indeed, it was found that there is a drastic increase in cytotoxicity upon irradiation. Upon excitation, metal-centered (MC) states are populated that promote the release of equatorial solvent molecules which allows the complex to bind to cellular targets. The compound has a PI value of 34 against Hs-27 human skin cells when irradiated with visible light (400–700 nm), which is a vast improvement over the performance of the FDA approved drug Photofrin®. This study prompted the development of other partially solvated complexes such as  $cis\text{-}[\text{Rh}_2(\text{chp})_2(\text{MeCN})_6](\text{BF}_4)_2$  (where  $\text{chp}$  = 6-chloro-2-hydroxypyridine) that displays a 16.4-fold increase in cytotoxicity against HeLa cells upon irradiation with visible light.<sup>9</sup> In order to further red-shift the absorption profiles of these complexes into the PDT window, extended  $\pi$ -accepting diimine ligands were installed that lower the energy of the LUMO, which is primarily diimine in character, leading to a decrease in the HOMO-LUMO gap.<sup>74</sup> The photophysical properties of complexes that display available axial and equatorial sites while supporting  $\pi$ -accepting ligands, however, have remained unexplored.

In the present study we have focused on the synthesis and characterization of two new dicationic dirhodium(II,II) complexes, *viz.*,  $cis\text{-}[\text{Rh}_2(\mu\text{-O}_2\text{CCH}_3)_2(\text{qxnp})(\text{MeCN})_2](\text{BF}_4)_2$  (**II.2**) and  $cis\text{-}[\text{Rh}_2(\mu\text{-O}_2\text{CCH}_3)_2(\text{qxnp})_2](\text{BF}_4)_2$  (**II.3**). Their photoactivated DNA binding properties were assessed and compared to the previously reported partially solvated complex  $cis\text{-}[\text{Rh}_2(\mu\text{-O}_2\text{CCH}_3)_2(\text{MeCN})_6](\text{BF}_4)_2$

(II.1) (Figure II.1).<sup>11</sup> The new complexes display MLCT bands in the visible region with enhanced absorption coefficients compared to the lowest energy transition of II.1 which is MC in nature. In addition, II.2 contains two equatorial acetonitrile molecules that are hydrolyzed upon irradiation with visible light which leads to DNA binding and also possesses a  $\pi$ -accepting ligand that lowers the energy of the MLCT band of the complex. This new approach for designing new complexes that display appropriate absorption profiles while retaining key features for DNA binding is aimed at the development of more efficient dirhodium PACT drugs.

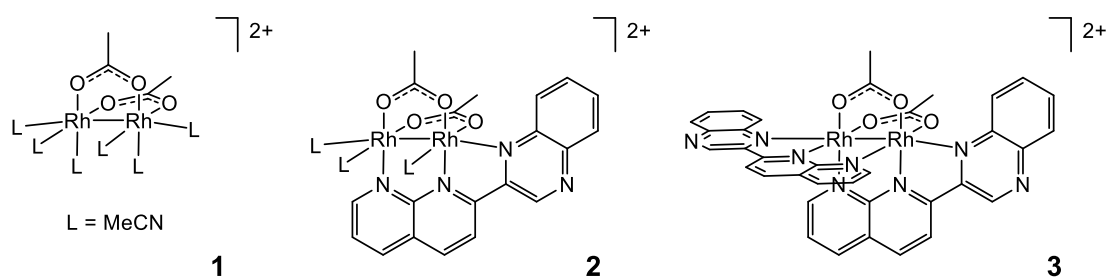


**Figure II.1** Schematic representations of the molecular structures of compounds II.1–3.

## Experimental Section

### Materials

The starting material  $[\text{Rh}_2(\mu\text{-O}_2\text{CCH}_3)_4]$  was purchased from Pressure Chemicals and used without further purification. The ligand 1,8-Diazanaphthalene (np) was purchased from Oakwood Chemical and used as received. Tetrabutylammonium hexafluorophosphate (TBAPF<sub>6</sub>) was purchased from Alfa Aesar and used as received. The



compounds  $\text{cis-}[\text{Rh}_2(\mu\text{-O}_2\text{CCH}_3)_2(\text{MeCN})_6](\text{BF}_4)_2$  (**II.1**) and 2-(1,8-naphthyridin-2-yl)quinoxaline (qxnp) were synthesized following reported procedures. Acetonitrile was dried over 3 Å molecular sieves and distilled under nitrogen prior to use. All reactions, unless otherwise noted, were performed using standard Schlenk-line techniques. Crystallizations, purifications, and further manipulation of the compounds were conducted in air.

$\text{cis-}[\text{Rh}_2(\mu\text{-O}_2\text{CCH}_3)_2(\text{qxnp})(\text{MeCN})_2](\text{BF}_4)_2$  (**II.2**). A 20 mL acetonitrile solution containing  $\text{cis-}[\text{Rh}_2(\mu\text{-O}_2\text{CCH}_3)_2(\text{MeCN})_6](\text{BF}_4)_2$  (164.2 mg, 0.221 mmol) and qxnp (59.9 mg, 0.230 mmol) was refluxed for 24 h in an oil bath at 90 °C. The resulting red solution was cooled to room temperature, concentrated under vacuum to approximately 5 mL, and diethyl ether was added to precipitate the product. The red-orange solid was filtered through a medium frit and dried under vacuum. The product was further purified by slow vapor diffusion of diethyl ether into a concentrated solution of the compound in acetonitrile to afford 82.3 mg of a red crystalline material (42.4% yield) suitable for X-ray crystallography.  $^1\text{H-NMR}$  (500 MHz,  $\text{cd}_3\text{cn}$ )  $\delta$  10.17 (s, 1H), 9.79 (d,  $J = 4.7$  Hz, 1H), 9.47 (dd,  $J = 8.2, 1.7$  Hz, 1H), 9.05 (d,  $J = 8.8$  Hz, 1H), 8.93 (d,  $J = 8.8$  Hz, 1H), 8.81 (dd,  $J = 8.3, 1.7$  Hz, 1H), 8.49 (dd,  $J = 7.1, 2.7$  Hz, 1H), 8.35–8.23 (m, 2H), 8.01 (dd,  $J = 8.3, 5.3$  Hz, 1H), 2.35 (s, 3H), 2.30 (s, 3H), 1.96 (s, 6H), 1.64 (s, 3H). HRMS (ESI-MS)  $m/z$ :  $[\text{M} - \text{MeCN}]^{2+}$  ( $\text{C}_{24}\text{H}_{22}\text{N}_6\text{O}_4\text{Rh}_2$ ) 331.9895 calc.  $[\text{M} - \text{MeCN}]^{2+}$  ( $\text{C}_{24}\text{H}_{22}\text{N}_6\text{O}_4\text{Rh}_2$ ) 331.9901.

$\text{cis-}[\text{Rh}_2(\mu\text{-O}_2\text{CCH}_3)_2(\text{qxnp})_2](\text{BF}_4)_2$  (**II.3**). Quantities of  $\text{cis-}[\text{Rh}_2(\mu\text{-O}_2\text{CCH}_3)_2(\text{MeCN})_6](\text{BF}_4)_2$  (150.1 mg, 0.202 mmol) and the qxnp ligand (109.5 mg, 0.424 mmol%) were refluxed in a 1:1 mixture of chlorobenzene and acetonitrile for 2 days. After

48 h of reflux, the reaction was cooled to room temperature, the solvent was evaporated to near dryness, and diethyl ether was added to precipitate the product. After filtration, the red powder was re-dissolved in acetonitrile and a crystalline product was obtained after crystallization by slow vapor diffusion of diethyl ether (yield 131.1 mg, 65.5 %).  $^1\text{H}$  NMR (500 MHz,  $\text{cd}_3\text{cn}$ )  $\delta$  10.36 (s, 2H), 9.70 (d,  $J = 5.3$  Hz, 2H), 9.12 (d,  $J = 8.2$  Hz, 2H), 8.75 (s, 2H), 8.66 (dd,  $J = 5.2, 4.6$  Hz, 2H), 8.54 (d,  $J = 27.2$  Hz, 4H), 8.38 (dd,  $J = 8.7, 5.8$  Hz, 4H), 7.42 (dd,  $J = 7.5, 5.7$  Hz, 2H), 1.91 (s, 6H). HRMS (ESI-MS)  $m/z$ :  $[\text{M}]^{2+}$  ( $\text{C}_{36}\text{H}_{26}\text{N}_8\text{O}_4\text{Rh}_2$ ) 420.0077 calc.  $[\text{M}]^{2+}$  ( $\text{C}_{36}\text{H}_{26}\text{N}_8\text{O}_4\text{Rh}_2$ ) 420.0088 and  $[\text{M} + \text{BF}_4]^+$  ( $\text{C}_{36}\text{H}_{26}\text{N}_8\text{O}_4\text{Rh}_2\text{BF}_4$ ) 927.0196 calc.  $[\text{M} + \text{BF}_4]^+$  ( $\text{C}_{36}\text{H}_{26}\text{N}_8\text{O}_4\text{Rh}_2\text{BF}_4$ ) 927.0216.

#### *Instrumentation and methods*

$^1\text{H}$  NMR spectra were obtained on an Inova 500 MHz spectrometer; chemical shifts were referenced to the residual peak of the residual  $\text{CD}_3\text{CN}-d_3$  deuterated solvent signal at 1.96 ppm.<sup>75</sup> Electronic spectroscopy was performed on a Shimadzu UV-1601PC spectrophotometer in  $1 \times 1$  cm quartz cuvettes. Extinction coefficients in acetonitrile were determined in triplicate.

Electrochemical measurements for **II.2** and **II.3** ( $1 \times 10^{-3}$  M) were recorded under an inert atmosphere using dry acetonitrile and 0.1 M  $[\text{n-Bu}_4\text{N}][\text{PF}_6]$  as the supporting electrolyte with a CH Instruments electrochemical analyzer model CH1620A. A three-electrode cell was used with a Ag/AgCl reference electrode standardized to ferrocene ( $E_{1/2} = +0.55$  V vs Ag/AgCl), a Pt wire as the counter electrode, and a glassy carbon disk as the working electrode. High-resolution Electrospray Ionization mass spectrometry (ESI-MS) data were obtained in the Laboratory for Biological Mass Spectrometry at Texas

A&M University using a using a Thermo Scientific Q Exactive Focus. The sample was directly infused at a flow rate of 10  $\mu\text{L}/\text{min}$ . The Q Exactive Focus HESI source was operated in full MS in positive mode. The mass resolution was tuned to 17500 FWHM at  $m/z$  200, the spray voltage was set to 3.75 kV, and the sheath gas and auxiliary gas flow rates were set to 7 and 0 arbitrary units, respectively. The transfer capillary temperature was held at 250  $^{\circ}\text{C}$  and the S-Lens RF level was set at 50 v. Exactive Series 2.8 SP1/Xcalibur 4.0 software was used for data acquisition and processing.

Density Functional Theory (DFT) calculations using the Gaussian09 program package were performed to elucidate the molecular and electronic structures of the complexes. The mPW1PW91<sup>76</sup> correlation and exchange functionals were used with the Stuttgart RSC 1997 Electron Core Potential (ECP) basis set for the Rh atoms and the 6-31G $\dagger$  basis set for the C, N, and H atoms. The geometric parameters of the crystal structures of **II.1–3** without the counter ions and interstitial solvent molecules were used as the starting point for these calculations. The structures were optimized in the gas-phase followed by optimization with the polarized continuum model (PCM) with  $\text{CH}_3\text{CN}$  as the solvent. These optimizations were followed by Time-Dependent Density Functional Theory (TD-DFT)<sup>59</sup> calculations using the same solvent model and, from the ground state of these optimized structures, the first sixty lowest singlet-to-singlet excitations were calculated. The molecular orbitals were plotted with the graphic software ‘Agui’61 with an isovalue = 0.04 and Natural Transition Orbital (NTO) analyses were performed with the Chemissian program.<sup>77</sup>

Single crystals of the compounds were collected from mineral oil under ambient conditions using a MiTeGen microloop or a nylon loop. Crystals were placed in a cold N<sub>2</sub> stream at 110 K on a Bruker D8-QUEST diffractometer equipped with a I $\mu$ S Mo microsource ( $\lambda = 0.71073 \text{ \AA}$ ). Initial unit cell determinations were made using SAINT from a set of three  $\omega$ -scans consisting of 0.5° frames and a sweep width of 15°. An appropriate data collection strategy was determined using these unit cells in order to collect all independent reflections to a resolution of at least 0.83  $\text{\AA}$ . Details of the collection parameters can be found in Table II-1. For both structures, SADABS was used to correct the data for absorption and XPREP was used to determine the space group from analysis of systematic absences. The intrinsic phasing routine in SHELXT was used to solve the structures. The non-hydrogen atoms were located from the Fourier difference map by least-squares refinement of the structure using SHELXL-2014.<sup>52</sup> All non-hydrogen atoms were refined anisotropically and hydrogen atoms were placed in calculated positions and refined with thermal parameters constrained to their parent atom. Specific details of the refinements are presented in Table II-1.

Photoaquation experiments with **II.2** and **II.3** were performed to study the stability of the complexes in water in the dark and upon irradiation, and to assess their ability to undergo hydrolysis upon irradiation. Two sets of solutions of the compounds in water were prepared and followed over time by steady state spectroscopy. One set of solutions was kept in the dark while the other set of solutions was irradiated with a  $\lambda_{\text{irr}} = 447.5 \text{ nm}$  LED and monitored over the course of 4 hours.

In order to study the ds-DNA binding capability of the complexes upon irradiation and in the dark, a series of mobility assays in agarose gels were performed. The compounds were dissolved in Milli-Q® water and a series of dilutions were made to yield final working concentrations of 1, 10, 100, and 1000  $\mu\text{M}$ . The solutions of the complexes were stored in the dark to avoid premature dissociation of the equatorial solvent molecules. A stock solution of 15 mg/ $\mu\text{L}$  linearized pUC18 plasmid (10 mM phosphate, pH = 7.5) was prepared and incubated with the complexes and divided into two groups: light and irradiated. The group that was left in the dark was incubated for 24 hours at 37 °C. The other group was irradiated with a 300 W xenon arc lamp ( $\lambda > 515 \text{ nm}$ ) for either 20 minutes or 3 hours after which time they were incubated for 24 hours in the dark. The DNA binding ability of the complexes was visualized by performing shift mobility assays in ethidium bromide stained agarose gels.

## **Results and Discussion**

### *Synthesis and Characterization*

Compounds **II.2** and **II.3** were synthesized following the reaction scheme presented in Figure II.2. The isolation of **II.2** was achieved from a 24-hour reflux of a mixture of **II.1** and the qxn<sub>p</sub> ligand suspended in dry acetonitrile. The salt, **II.3**, on the other hand, required a mixture of solvents to promote the incorporation of the second qxn<sub>p</sub> ligand into the product. For this purpose, a 1:1 mixture of acetonitrile/chlorobenzene was used to reach a higher refluxing temperature and drive the reaction to completion. Both products were obtained as dicationic  $[\text{BF}_4]^-$  salts and characterized by HRMS and  $^1\text{H}$ -NMR spectroscopy (Figures II.3 and 4).

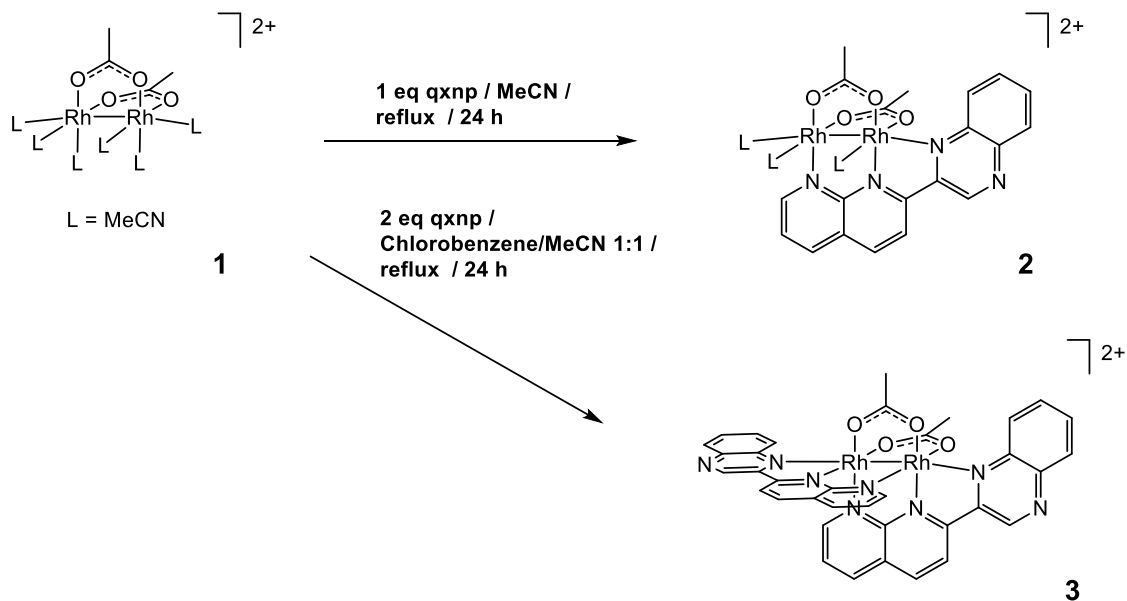


**Figure II.2** Synthetic scheme for the syntheses of **II.2** and **II.3** from the starting material.

The mass spectra for **II.3** contain the molecular ion,  $[\text{M}]^{2+}$ , as the major peak while the highest intensity peak for **II.2** is  $[\text{M} - \text{MeCN}]^{2+}$  which is not surprising because the axial acetonitrile solvent molecule is labile and is therefore fragmented during the ionization process. The  $^1\text{H}$  NMR spectrum of **II.2** contains ten unique signals in the aromatic region (Figure II.3) that correspond to the ten non-equivalent protons of the qxnp ligand. Compound **II.3** also displays ten unique signals in the aromatic region that integrate to 20 with respect to the methyl groups from the acetate bridging ligands due to the presence of two qxnp axial-blocking ligands.

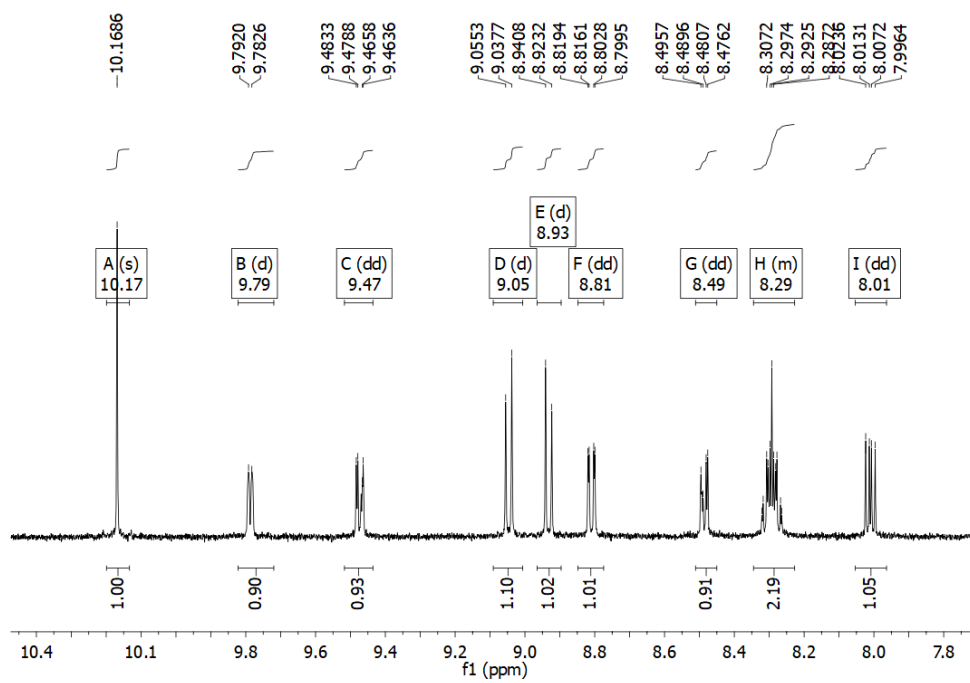


**Figure II.3** Aromatic region of the  $^1\text{H}$  NMR spectrum for **II.2**.

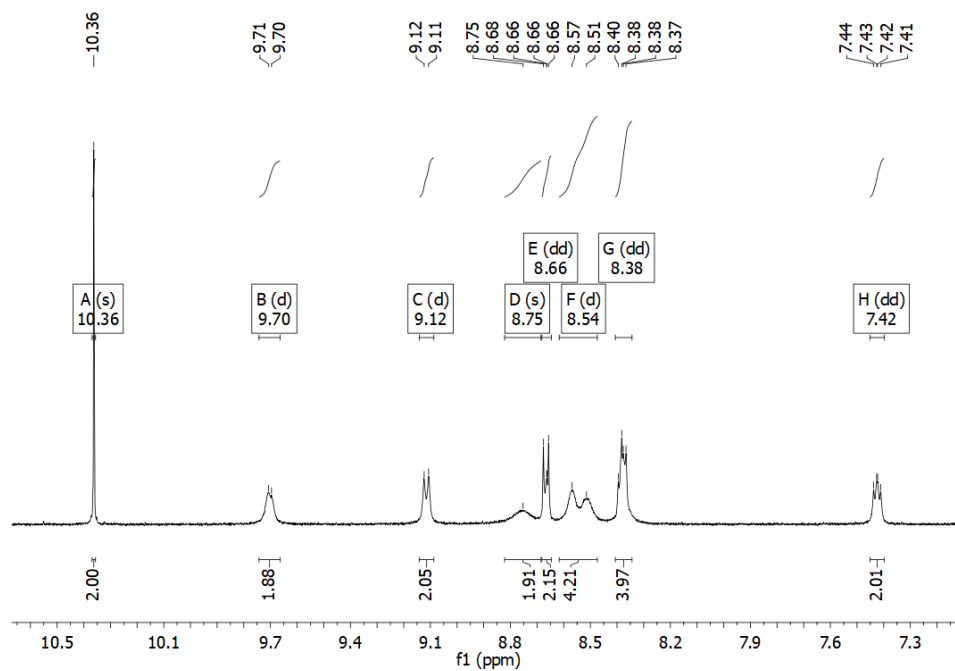


**Figure II.4** Aromatic region of the  $^1\text{H}$  NMR spectrum for **II.3**.

### *X-ray crystal structures*

The molecular structures of complexes **II.2** and **II.3** (Figures II.5 and 6) were determined from single crystal X-ray diffraction experiments. These salts contain dicationic dirhodium(II,II) complexes bridged by two acetate ligands with two tetrafluoroborate anions. In addition, **II.2** supports a single qxnp ligand (2-(1,8-naphthyridin-2-yl)quinoxaline) that binds to the dirhodium(II,II) core in a tridentate fashion, blocking one of the axial positions while leaving the second position accessible to a solvent molecule or a substrate. The remaining two equatorial positions of this complex are occupied by acetonitrile molecules. Compound **II.3** contains two qxnp ligands that block both axial positions as well as four of the eight equatorial positions. The Rh-Rh bond distances for **II.2** and **II.3** are 2.4573(2) Å and 2.41237(16) Å respectively, which are well within the expected range for Rh-Rh single bonds. These distances are shorter than that in the previously reported compound **II.1** with a bond length of 2.536(3) Å. The marked shortening of the Rh-Rh bond distances is a result of the increase in the number of bridging ligands supported by the dirhodium core going from two to three and to four in compounds **II.1**, **II.2**, and **II.3** respectively. In addition, these bond distances are comparable to that of the axially blocked *cis*-[Rh<sub>2</sub>(μ-O<sub>2</sub>CCH<sub>3</sub>)<sub>2</sub>(pynp)<sub>2</sub>][BF<sub>4</sub>]<sub>2</sub> which has a Rh–Rh bond distance of 2.408(2) Å. They are, however, significantly shorter than other acetate bridged dirhodium complexes with κ-chelating π-accepting ligands such as those of the type [Rh<sub>2</sub>(O<sub>2</sub>CCH<sub>3</sub>)<sub>2</sub>(L)<sub>2</sub>]<sup>2+</sup> (L = bpy, phen, 4,7-dimethyl-phen, 3,4,7,8-tetramethyl-phen, and dppz) which exhibit Rh-Rh bond distances of 2.548(4), 2.5557(4), 2.565(1), 2.564(1), and 2.5519(6) Å respectively.<sup>31, 78-81</sup> Compound **3** displays similar Rh-



$N_{ax}$  bond distances of 2.22909(14) Å and 2.23762(14) Å while the asymmetric complex **II.2** displays a much longer bond distance for the Rh- $N_{ax}$  bond to the acetonitrile solvent molecule of 2.255(2) Å with respect to the qxnp moiety of 2.1984(18) Å. This lengthening of the Rh-NCMe<sub>ax</sub> bond can be attributed to the strong *trans* influence exerted by the quinoxalinylyl moiety of the sigma donor qxnp ligand across the Rh-Rh( $\sigma$ ) bond. Lastly, due to the bite angle of the qxnp ligand, there is a significant distortion from linearity for the Rh-Rh- $N_{ax}$  angle of 169.2629(9)° and 168.8305(9)° for complex **II.3**. This distortion is consistent with other axially-blocked dirhodium complexes previously reported of general formula [Rh<sub>2</sub>(DTolF)<sub>2</sub>(L)<sub>2</sub>]<sup>2+</sup> (L = pynp, qnnp, and qxnp) which exhibit angles 164.31(12)°, 164.368(13)°, and 161.73(4)° respectively. Compound **II.2** exhibits angles of 167.56(5)° for Rh-Rh-qxnp<sub>ax</sub> and 172.98(5)° Rh-Rh-NCMe<sub>ax</sub> which can be explained by the fact that acetonitrile is a monodentate ligand and therefore does not have the binding constraints of the tridentate ligand qxnp allowing it to adopt a more linear conformation.

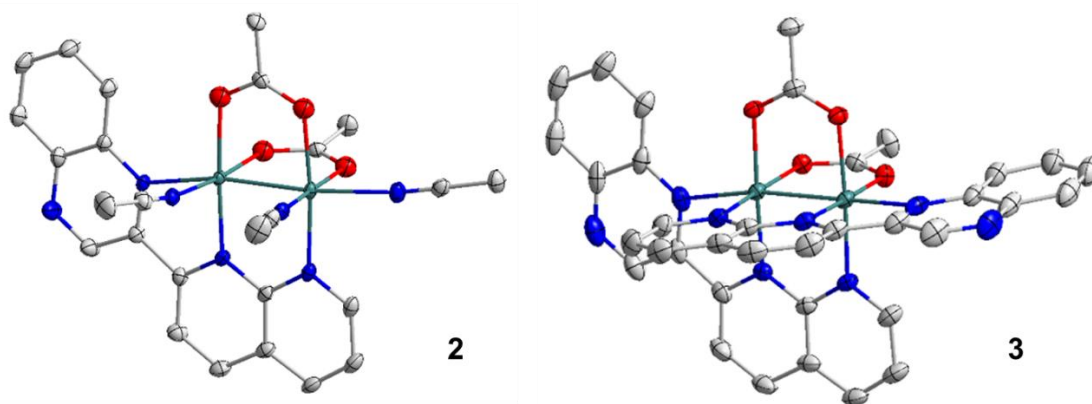


**Figure II.5** Thermal ellipsoid plot for **II.2** (left) and **II.3** (right) depicted at the 50% probability level. Interstitial solvent molecules, counterions, and hydrogen atoms have been omitted for the sake of clarity.

**Table II-1** X-ray data parameters and refinement details for **II.1–3**.

Compound	II.2	II.3
Empirical Formula	C <sub>34.02</sub> H <sub>35.51</sub> B <sub>2</sub> F <sub>8</sub> N <sub>7.51</sub> O <sub>4.49</sub> Rh <sub>2</sub>	C <sub>44.03</sub> H <sub>38.05</sub> B <sub>2</sub> F <sub>8</sub> N <sub>12.02</sub> O <sub>4</sub> Rh <sub>2</sub>
Formula weight	1000.81	175.75
Temperature/K	100.0	273.15
Crystal system	triclinic	monoclinic
Space group	P-1	P2 <sub>1</sub> /c
a/Å	12.4055(6)	10.1796(6)
b/Å	12.7053(6)	21.5783(14)
c/Å	13.4129(6)	21.2717(14)
α/°	81.824(2)	90
β/°	67.322(2)	96.397(3)
γ/°	89.236(2)	90
Volume/Å <sup>3</sup>	1928.81(16)	4643.4(5)
Z	2	4
ρ <sub>calc</sub> /cm <sup>3</sup>	1.723	2.703
μ/mm <sup>-1</sup>	0.945	3.808
F(000)	1000.0	3483.0
Crystal size/mm <sup>3</sup>	1.038 × 0.117 × 0.112	0.4 × 0.3 × 0.2
Radiation	MoKα (λ = 0.71073)	MoKα (λ = 0.71073)
2θ range for data collection/°	4.98 to 55.092	2.696 to 61.476
Index ranges	-16 ≤ h ≤ 16 -16 ≤ k ≤ 16 -17 ≤ l ≤ 17	-14 ≤ h ≤ 14 -30 ≤ k ≤ 30 -30 ≤ l ≤ 30
Reflections collected	68805 8891	259068 14338
Independent reflections	R <sub>int</sub> = 0.0513 R <sub>sigma</sub> = 0.0262	R <sub>int</sub> = 0.0420 R <sub>sigma</sub> = 0.0172
Data/restraints/parameters	8891/170/626	14338/774/890
Goodness-of-fit on F <sup>2</sup>	1.022	1.132
Final R indexes [I ≥ 2σ (I)]	R <sub>1</sub> = 0.0274, wR <sub>2</sub> = 0.0602	R <sub>1</sub> = 0.0345, wR <sub>2</sub> = 0.0894
Final R indexes [all data]	R <sub>1</sub> = 0.0379, wR <sub>2</sub> = 0.0641	R <sub>1</sub> = 0.0469, wR <sub>2</sub> = 0.1038
Largest diff. peak/hole / e Å <sup>-3</sup>	0.75/-0.81	1.21/-0.97

<sup>a</sup>R<sub>1</sub> = Σ(|F<sub>o</sub>| - |F<sub>c</sub>|)/Σ|F<sub>o</sub>|. <sup>b</sup>wR<sub>2</sub> = [Σ[w(F<sub>o</sub><sup>2</sup> - F<sub>c</sub><sup>2</sup>)<sup>2</sup>]/Σ[w(F<sub>o</sub><sup>2</sup>)]<sup>1/2</sup>, w = 1/[σ<sup>2</sup>(F<sub>o</sub><sup>2</sup>) + (ap)<sup>2</sup> + bp], where p = [max(F<sub>o</sub><sup>2</sup>, 0) + 2F<sub>c</sub><sup>2</sup>]/3.

### *Electronic Absorption Spectroscopy*

The steady state absorption spectra of **II.1–3** are shown in Figure II.7 and their maxima and absorption coefficients are listed in Table II-2. The previously reported compound **1** displays two maxima at 363 nm ( $\epsilon = 420 \text{ M}^{-1} \text{ cm}^{-1}$ ) and 525 nm ( $\epsilon = 218 \text{ M}^{-1} \text{ cm}^{-1}$ ) in acetonitrile.<sup>11</sup> The lowest energy transition was assigned as metal-centered (MC) in character with  $\text{Rh}_2(\pi^*) \rightarrow \text{Rh}_2(\sigma^*)$  parentage. The lowest energy transition for **II.2** and **II.3** have absorption coefficients that are 10 to 20-fold times greater than that of complex **II.1** which is consistent with a change in parentage of the transitions from MC to MLCT in character. Compounds such as  $[\text{Rh}_2(\text{O}_2\text{CCH}_3)_2(\text{L})_2]^{2+}$  (where L = np and pynp) possess similar features in their absorption profiles but are blue-shifted with respect to **II.2** and **II.3** due to the highly conjugated nature of the qxnp ligand.<sup>31</sup> Compounds **II.2** and **II.3** also display absorption peaks at 258 nm and the absorption coefficient for **II.3** is almost twice that of **II.2**. This transition is consistent with a  $\pi\pi^*$  transition of the qxnp ligand since the intensity ratio of the absorption coefficient scales with the number of qxnp ligands. In addition, the energy of this transition is similar to that of *cis*- $[\text{Rh}_2(\text{DTolF})_2(\text{qxnp})_2][\text{BF}_4]_2$  of 259 nm which is in accord with the  $\pi\pi^*$  transition of the qxnp free ligand.

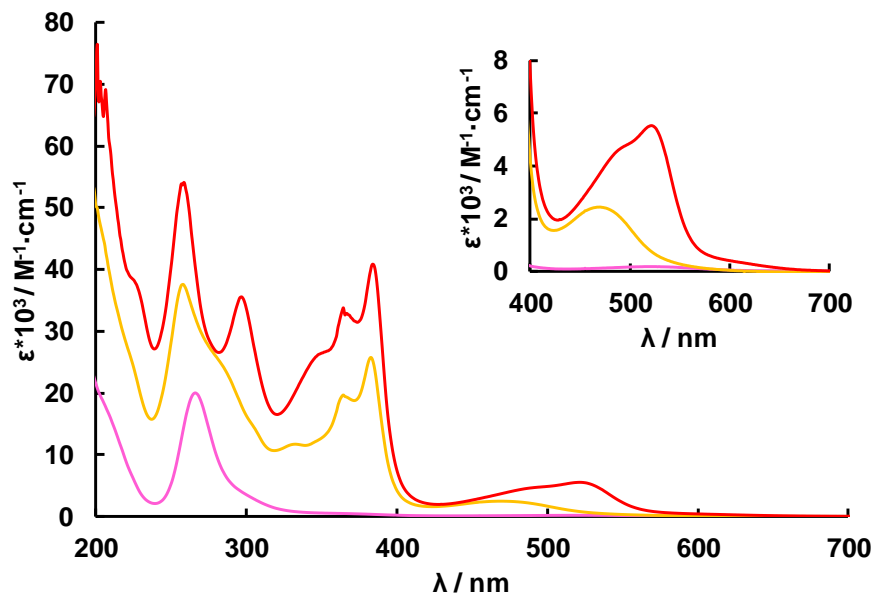


**Figure II.6** Electronic absorption spectra of compounds **II.1** (pink), **II.2** (orange), and **II.3** (red) in acetonitrile.

**Table II-2** Electronic Absorption Maxima with Molar Absorptivities in Acetonitrile and Reduction Potentials for **II.1–3**.

Complex	$\lambda_{\text{abs}} / \text{nm}$ ( $\epsilon / \times 10^3 \text{ M}^{-1} \text{ cm}^{-1}$ )
<b>II.1</b> <sup>11</sup>	363 (420), 525 (218)
<b>II.2</b>	258 (37.6), 364 (19.7), 383 (25.7), 470 (2.45)
<b>II.3</b>	258 (54.1) 297 (35.5) 364 (33.8), 384 (40.8), 521 (5.54)

<sup>a</sup><sub>vs</sub> Ag/AgCl in 0.1 M Bu<sub>4</sub>NPF<sub>6</sub>/CH<sub>3</sub>CN.

### *Electronic Structure Calculations*

To better understand the origins of the electronic transitions of these complexes, computational calculations were performed. Geometrical parameters were taken from the crystal structures as a starting point for the gas-phase optimization, omitting counterions and interstitial solvent molecules (Figure II.10 and Table II-3). The results show that the HOMOs of **II.1–3** are predominantly Rh( $\pi^*$ ) in character with contributions that range from 83% to 68% respectively (Figure II.11, Tables II-4 and 5). There is also a small contribution of the qxnp ligand to the HOMOs of **II.2** and **II.3**, which increases the energy of these orbitals with respect to **1**. The LUMOs, however, are of different nature for **II.1** versus **II.2** and **II.3**. The LUMO for **II.1** is 75% Rh( $\sigma^*$ ) in character while the LUMO for complexes **II.2** and **II.3** are 93% and 96% qxnp in character, respectively. The MO diagram reveals a systematic increase in the energy of the Rh( $\sigma^*$ ) orbital when going from **II.1** to **II.3** (Figures II.12 and 13). The sequential substitution of the acetonitrile solvent molecules for the quinoxaliny axial-blocking moiety of the qxnp ligands results in better sigma donation in the axial positions that causes an increase in the energy to the antisymmetric Rh( $\sigma^*$ ) orbital.

The lowest energy bands for these complexes appear in the visible region and TD-DFT calculations were performed to assign these transitions (Figure II.12). The lowest energy band of complex **II.1** was previously assigned to a MC transition with Rh<sub>2</sub>( $\pi^*$ )  $\rightarrow$  Rh<sub>2</sub>( $\sigma^*$ ) character.<sup>11</sup> The lowest energy bands for **II.2** and **II.3**, however, are assigned as MLCT transitions with Rh<sub>2</sub>( $\pi^*$ )  $\rightarrow$  qxnp character (Figure II.13). The change in parentage has a profound effect on the absorption coefficients. This 10 to 20-fold increase in the

complexes with qxnp ligands are consistent with the oscillator frequencies obtained for the lowest energy transitions. The calculated energies of the transitions for all complexes are slightly blue-shifted with respect to the experimental data as the energies of highly conjugated  $\pi$ -ligands can be overestimated in DFT calculations.

**Table II-3** Comparison of gas phase optimized structures and X-ray crystal structures for **II.1–3**.

<b>II.1<sup>82</sup></b>	Crystal Structure	Calculated Structure
Rh1-Rh1 <sup>1</sup>	2.536(3)	2.54305
Rh1-O1	2.018(3)	2.03731
Rh1-O3	2.013(3)	2.03686
Rh1-N1	1.979(4)	1.99384
Rh1-N3	1.984(4)	1.99358
Rh1-N5	2.232(4)	2.21008
O1-Rh1-Rh2-O2	-1.51(13)	9.08061
N3-Rh1-Rh2-N4	-1.87(16)	10.25157
<b>II.2</b>	Crystal Structure	Calculated Structure
Rh1-Rh2	2.4573(2)	2.47278
Rh1-O1	2.0409(16)	2.05736
Rh1-O3	2.0180(16)	2.03789
Rh1-N1	2.0540(19)	2.06697
Rh1-N3	1.979(2)	1.98918
Rh1-N5	2.255(2)	2.24526
Rh2-O2	2.0414(16)	2.06936
Rh2-O4	2.0267(16)	2.03903
Rh2-N2	2.0008(18)	2.01249
Rh2-N4	1.983(2)	1.98986
Rh2-N6	2.1984(18)	2.21200
O1-Rh1-Rh2-O2	-0.13(7)	3.11638
N3-Rh1-Rh2-N4	0.13(8)	3.26508
<b>II.3</b>	Crystal Structure	Calculated Structure
Rh1-Rh2	2.41237(16)	2.41837
Rh1-O1	2.04436(9)	2.05302
Rh1-O3	2.04680(9)	2.06761
Rh1-N1	2.05066(9)	2.07193
Rh1-N3	1.99122(9)	2.00854
Rh1-N5	2.22909(14)	2.24254
Rh2-O2	2.04454(9)	2.06761
Rh2-O4	2.05049(9)	2.05302
Rh2-N2	1.99022(9)	2.00854
Rh2-N4	2.04974(9)	2.07193
Rh2-N6	2.23762(14)	2.24254
O1-Rh1-Rh2-O2	2.164460(10)	5.56008
N3-Rh1-Rh2-N4	2.475097(15)	5.55502

<sup>1</sup>The molecule resides in a special position and only half of it is unique.

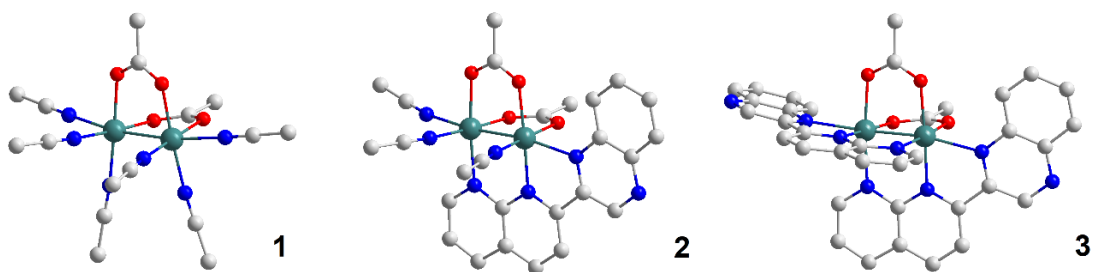


**Figure II.7** Gas-phase optimized structures of **II.1–3**.

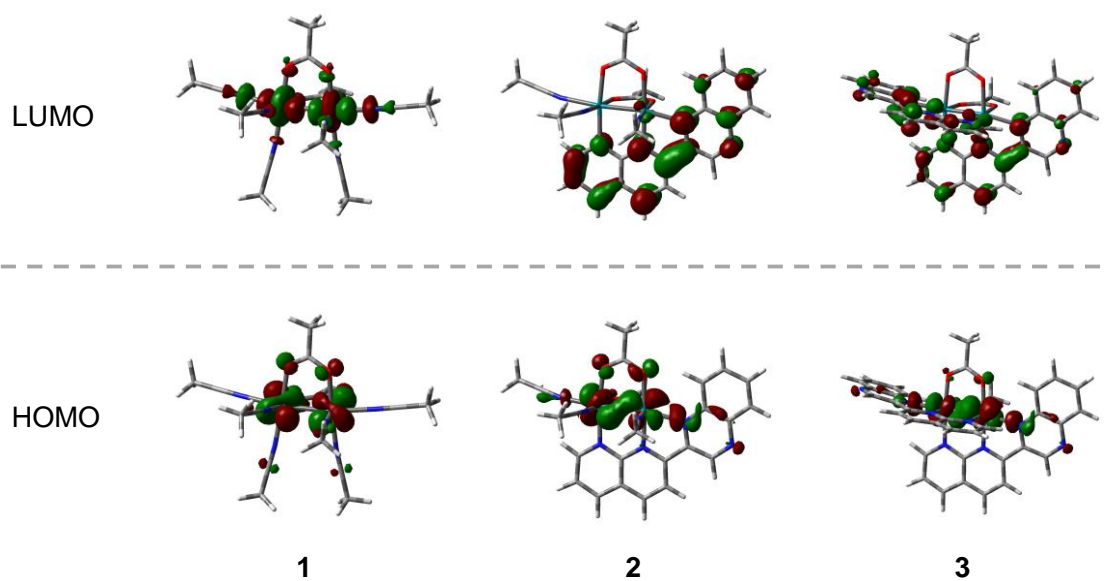


**Figure II.8** Electron density maps of the HOMOs and LUMOs of **II.1–3** drawn with an isovalue = 0.04.

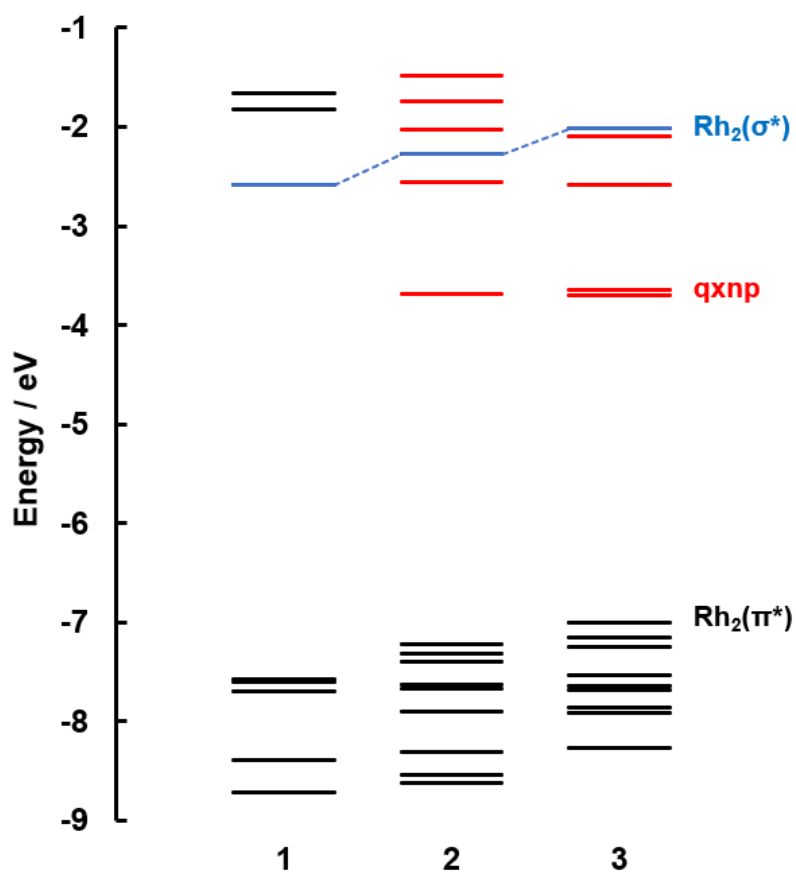


**Figure II.9** Calculated MO diagrams for **II.1-3**.

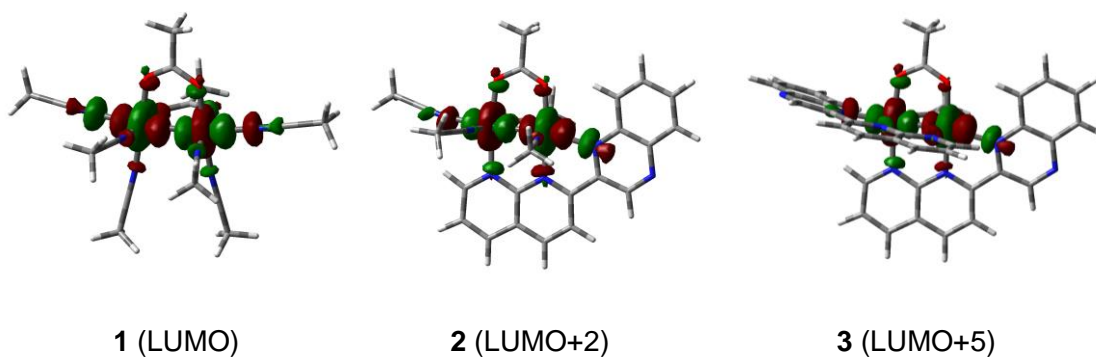


**Figure II.10** Electron density maps of the  $Rh_2(\sigma^*)$  of complexes **II.1-3** drawn with an isovalue = 0.04.



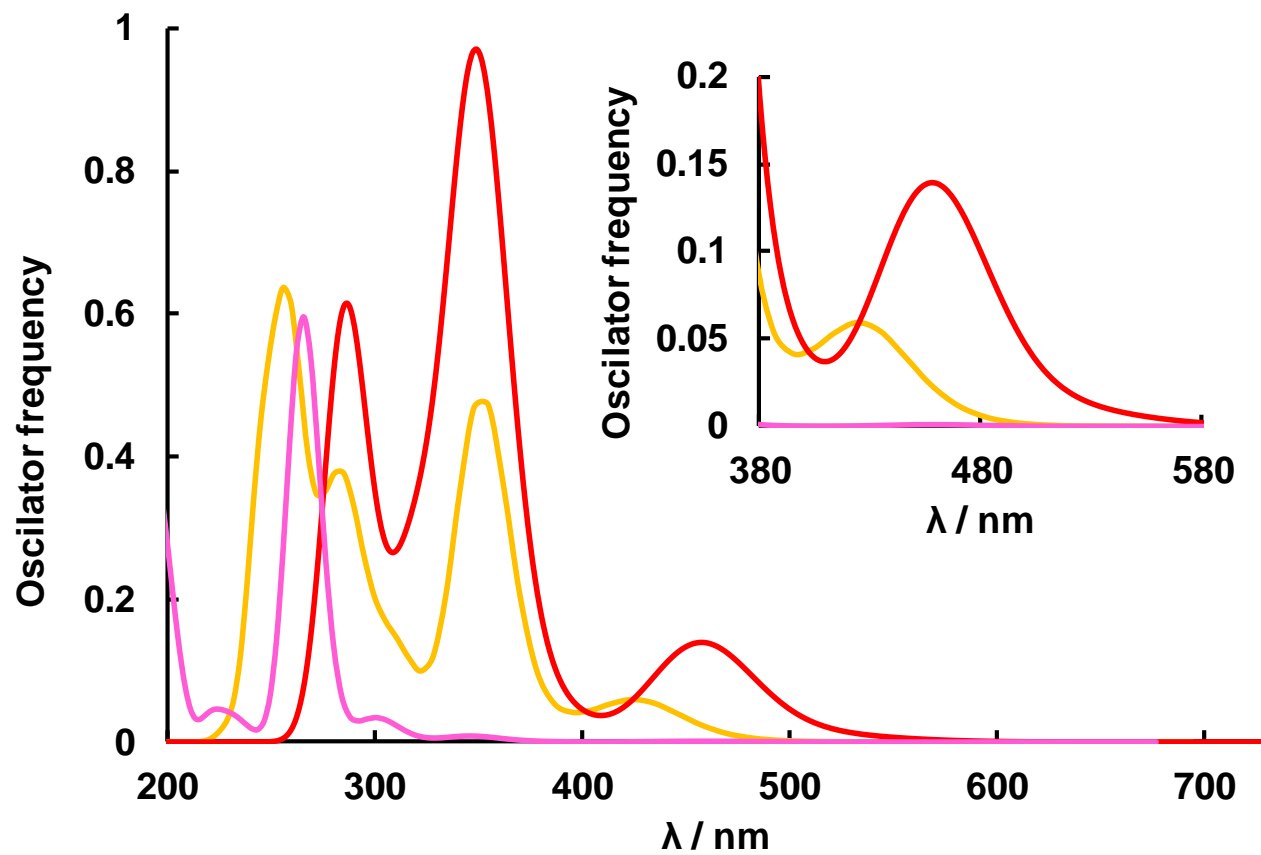


**Figure II.11** TD-DFT calculated electronic absorption spectra for **II.1** (pink), **II.2** (orange), and **II.3** (red) in acetonitrile.

**Table II-4** First eight vertical energies of the singlet excited states, oscillator strengths,  $f$ , and major orbital contributions<sup>a</sup> calculated for **II.1–3** in acetonitrile (H = HOMO; L = LUMO).<sup>b</sup>

Excited State	II.1	II.2	II.3
1	21,739 cm <sup>-1</sup> (460 nm), $f = 0.001$ , H → L (%)	20,534 cm <sup>-1</sup> (487 nm), $f = 0.001$ , H → L (90.3%)	18,975 cm <sup>-1</sup> (527 nm), $f = 0.006$ , H → L+1 (96.0%)
2	21,882 cm <sup>-1</sup> (457 nm), $f = 0.001$ , H-1 → L (%)	20,692 cm <sup>-1</sup> (461 nm), $f = 0.002$ , H-1 → L (86.5%)	19,084 cm <sup>-1</sup> (524 nm), $f = 0.002$ , H → L (96.0%)
3	26,525 cm <sup>-1</sup> (377 nm), $f = 0.000$ , H-3 → L (%)	22,321 cm <sup>-1</sup> (448 nm), $f = 0.007$ , H → L+2 (51.8%)	20,619 cm <sup>-1</sup> (485 nm), $f = 0.004$ , H-1 → L (75.7%) H-2 → L (22.1%)
4	26,810 cm <sup>-1</sup> (373 nm), $f = 0.000$ , H-3 → L+1 (%) H-4 → L+2 (%)	22,472 cm <sup>-1</sup> (445 nm), $f = 0.001$ , H-1 → L+2 (64.0%)	20,661 cm <sup>-1</sup> (484 nm), $f = 0.000$ , H-1 → L+1 (62.4%) H-2 → L+1 (33.6%)
5	27,322 cm <sup>-1</sup> (366 nm), $f = 0.000$ , H-3 → L+2 (%) H-4 → L+1 (%)	23,419 cm <sup>-1</sup> (427 nm), $f = 0.047$ , H-2 → L (88.4%)	21,739 cm <sup>-1</sup> (460 nm), $f = 0.120$ , H-2 → L (74.0%) H-1 → L (23.0%)
6	28,901 cm <sup>-1</sup> (346 nm), $f = 0.008$ , H-1 → L+2 (%)	24,331 cm <sup>-1</sup> (411 nm), $f = 0.008$ , H-4 → L (59.3%) H-3 → L (31.4%)	22,676 cm <sup>-1</sup> (441 nm), $f = 0.008$ , H-2 → L+1 (53.3%) H-1 → L+1 (31.4%)
7	28,986 cm <sup>-1</sup> (345 nm), $f = 0.000$ , H → L+2 (%) H-5 → L (%)	25,840 cm <sup>-1</sup> (387 nm), $f = 0.000$ , H-2 → L+4 (42.3%)	22,727 cm <sup>-1</sup> (440 nm), $f = 0.011$ , H → L+5 (54.8%)
8	29,674 cm <sup>-1</sup> (337 nm), $f = 0.000$ , H-3 → L+1 (%)	25,907 cm <sup>-1</sup> (386 nm), $f = 0.025$ , H-3 → L (60.8%) H-4 → L (31.4%)	22,988 cm <sup>-1</sup> (435 nm), $f = 0.005$ , H-2 → L+5 (49.0%)

<sup>a</sup>Only contributions of  $\geq 20\%$  are listed. <sup>b</sup>Blue = MLCT (Rh → qxn<sub>p</sub>), green = MC (Rh<sub>2</sub>( $\delta^*$ ) → Rh<sub>2</sub>( $\sigma^*$ )), red = MC (Rh<sub>2</sub>( $\delta^*$ ) → Rh<sub>2</sub>( $\pi^*$ )), and orange = MC (Rh<sub>2</sub>( $\pi^*$ ) → Rh<sub>2</sub>( $\pi^*$ )).

**Table II-5** Orbital contributions<sup>a</sup> for **II.1–3** as predicted by TD-DFT calculations in acetonitrile (HOMO–5 through LUMO+6).<sup>b</sup>

Orbital	II.1	II.2	II.3
LUMO+6	40% Rh, 22% AcO, 38% MeCN	10% Rh, 85% qxnp	97% qxnp
LUMO+5	14% Rh, 30% AcO, 57% MeCN	52% Rh, 22% AcO, 16% qxnp, 10% MeCN	74% Rh, 5% AcO, 21% qxnp
LUMO+4	84% Rh, 13% MeCN	54% Rh, 18% AcO, 16% qxnp	96% qxnp
LUMO+3	26% Rh, 71% MeCN	97% qxnp	96% qxnp
LUMO+2	54% Rh, 23% AcO, 23% MeCN	75% Rh, 5% AcO, 13% qxnp	9% Rh, 91% qxnp
LUMO+1	56% Rh, 20% AcO, 24% MeCN	98% qxnp	11% Rh, 88% qxnp
LUMO	75% Rh, 6% AcO, 19% MeCN	93% qxnp	96% qxnp
HOMO	83% Rh, 9% AcO, 8% MeCN	73% Rh, 8% AcO, 15% qxnp	68% Rh, 27% qxnp
HOMO–1	84% Rh, 6% AcO, 20% MeCN	77% Rh, 9% AcO, 12% qxnp	70% Rh, 13% AcO, 17% qxnp
HOMO–2	72% Rh, 24% MeCN	69% Rh, 14% AcO, 12% qxnp	82% Rh, 7% AcO, 11% qxnp
HOMO–3	72% Rh, 20% AcO, 8% MeCN	38% Rh, 55% qxnp	37% Rh, 61% qxnp
HOMO–4	79% Rh, 7% AcO, 14% MeCN	59% Rh, 31% qxnp	23% Rh, 75% qxnp
HOMO–5	74% Rh, 11% AcO, 14% MeCN	93% qxnp	46% Rh, 50% qxnp

<sup>a</sup>Only contributions of  $\geq 20\%$  are listed. <sup>b</sup>Blue Rh( $\sigma^*$ ) and red Rh( $\pi^*$ ) orbitals.

### Photoaquation Experiments

In order to study the release of the equatorial acetonitrile molecules upon irradiation, photoaquation experiments were performed for **II.2** and **II.3** in water (Figures II.15 and 16). Aqueous solutions of the compounds were irradiated with 447.5 nm LEDs and their absorption profiles were recorded over time. Compound **II.3** does not undergo any changes even after 4 hours upon irradiation which indicates that these complexes are not only water stable, but also that the qxnp ligand dissociation cannot be promoted with light. On the other hand, **II.2** undergoes complete ligand exchange over the course of 3.5

hours. The isosbestic point suggests that the integrity of the molecule remains intact and an exchange of equatorial acetonitrile molecules for water can be promoted with the use of visible light.

#### *DNA binding experiments*

A series of mobility assays in ethidium bromide stained agarose gels of 15 mg/ $\mu$ L linearized pUC18 plasmid in the presence of **II.1–3** were performed (Figures II.17, 18, and 19). An array of aqueous solutions of the compounds with concentrations ranging from 1 to 1000  $\mu$ M were incubated in the presence of the plasmid in the dark and after 20 minutes or 3 hours of irradiation with a 300 W xenon arc lamp ( $\lambda_{\text{irr}} > 515$  nm). Compound **3** does bind DNA significantly even after 3 hours of irradiation at a 1000  $\mu$ M working concentration. This fact can be attributed to the inavailability of axial positions which is crucial for the formation of Rh-DNA adducts, as previously demonstrated by the inability to inhibit DNA transcription of other complexes with axially-impaired positions such as *cis*-[Rh<sub>2</sub>( $\mu$ -O<sub>2</sub>CCH<sub>3</sub>)<sub>2</sub>(pynp)<sub>2</sub>](BF<sub>4</sub>)<sub>2</sub>.<sup>31</sup>

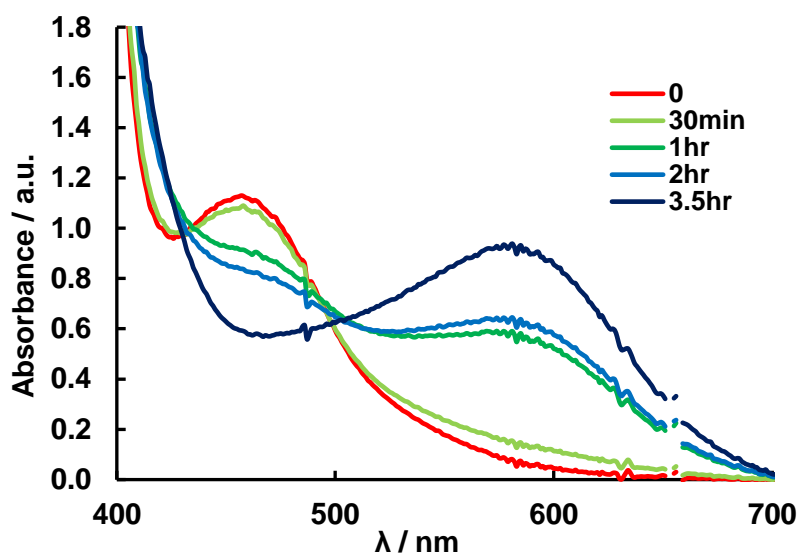


**Figure II.12** Photoaquation experiment for **II.2** in water with a  $\lambda_{\text{irr}} = 447.5$  nm LED.

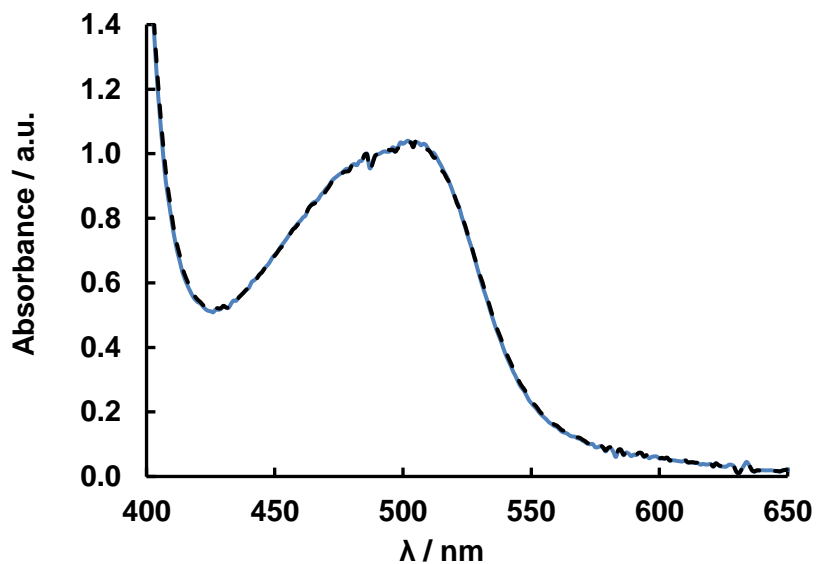


**Figure II.13** Photoaquation experiment for **II.3** in water with a  $\lambda_{\text{irr}} = 447.5$  nm LED. The solid blue line corresponds to the compound in the dark and the black dotted line after 4 hours of irradiation with the LED.

On the other hand, **II.1** was found to bind to DNA upon irradiation, although at high concentrations it can bind to DNA even when kept in the dark. The absence of a ds-DNA band at 100 and 1000  $\mu\text{M}$  concentrations when irradiated for 3 hours indicates that **II.2** can bind to the pUC18 plasmid and, in contrast to **II.1**, it requires longer irradiation times to exchange its equatorial ligands for water in order to form an intermediate that can bind to DNA. An increase in binding activity after 3 hours of irradiation was observed as compared to 20 minutes. These results are not surprising given that the partially solvated compound **II.1** contains four equatorial acetonitrile molecules, two of which can be replaced by water which enhances the binding capabilities of this complex with respect to **II.2** which has only two equatorial acetonitrile molecules. In addition, **II.2** contains only one open axial position for DNA binding which could also affect its binding efficiency as was observed for the asymmetric complex *cis*-[Rh<sub>2</sub>( $\mu$ -O<sub>2</sub>CCH<sub>3</sub>)<sub>2</sub>(np)(pynp)](BF<sub>4</sub>)<sub>2</sub> which exhibits decreased activity for inhibiting DNA transcription.<sup>31</sup>

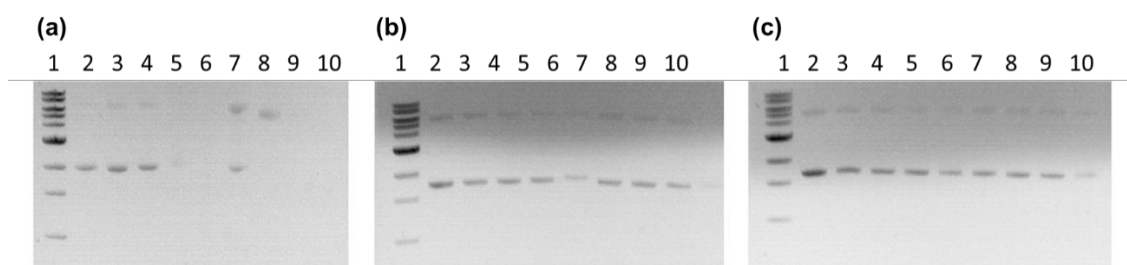


**Figure II.14** Ethidium bromide stained agarose gel of 15 mg/ $\mu\text{L}$  linearized pUC18 plasmid (10 mM phosphate, pH = 7.5) in the presence of various concentrations of **II.1** (a) **II.2** (b) and **II.3** (c). Lane 1: DNA molecular weight standard (1kb, Sigma); lane 2: plasmid alone; lanes 3 – 6: [complex] = 1, 10, 100, and 1000  $\mu\text{M}$  incubated in the dark at 37  $^{\circ}\text{C}$  for 24 hours; lanes 7 – 10: [complex] = 1, 10, 100, and 1000  $\mu\text{M}$  incubated in the dark at 37  $^{\circ}\text{C}$  for 24 hours after 20 minutes of irradiation with a 300 W xenon arc lamp ( $\lambda > 515 \text{ nm}$ ).

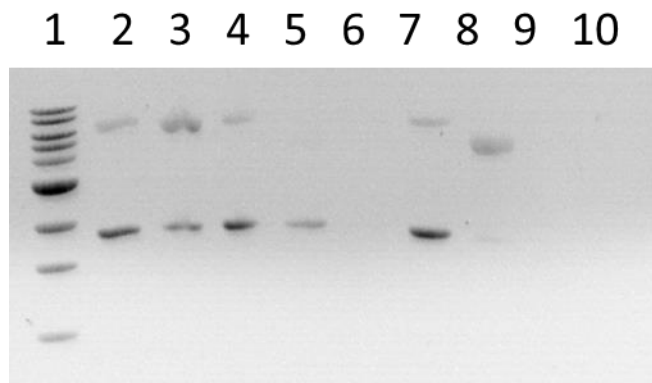


**Figure II.15** Ethidium bromide stained agarose gel of 15 mg/ $\mu$ L linearized pUC18 plasmid (10 mM phosphate, pH = 7.5) in the presence of various concentrations of **II.1**. Lane 1: DNA molecular weight standard (1kb, Sigma); lane 2: plasmid alone; lanes 3 – 6: [**II.1**] = 1, 10, 100, and 1000  $\mu$ M incubated in the dark at 37  $^{\circ}$ C for 24 hours; lanes 7 – 10: [**II.1**] = 1, 10, 100, and 1000  $\mu$ M incubated in the dark at 37  $^{\circ}$ C for 24 hours after 3.5 hours of irradiation with a 300 W xenon arc lamp ( $\lambda > 515$  nm).

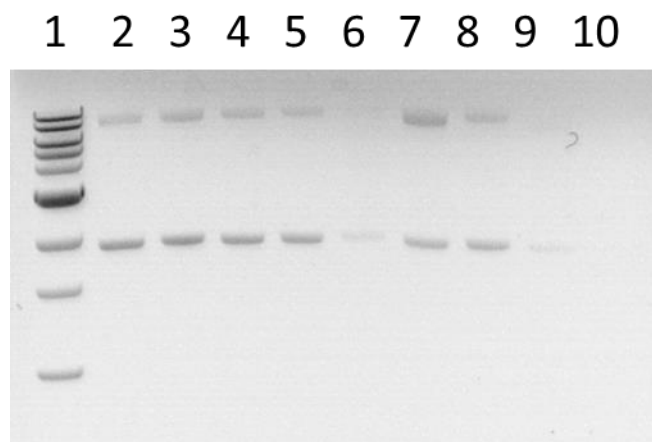


**Figure II.16** Ethidium bromide stained agarose gel of 15 mg/ $\mu$ L linearized pUC18 plasmid (10 mM phosphate, pH = 7.5) in the presence of various concentrations of **II.2**. Lane 1: DNA molecular weight standard (1kb, Sigma); lane 2: plasmid alone; lanes 3 – 6: [**II.2**] = 1, 10, 100, and 1000  $\mu$ M incubated in the dark at 37  $^{\circ}$ C for 24 hours; lanes 7 – 10: [**II.2**] = 1, 10, 100, and 1000  $\mu$ M incubated in the dark at 37  $^{\circ}$ C for 24 hours after 3.5 hours of irradiation with a 300 W xenon arc lamp ( $\lambda > 515$  nm).

## Conclusions

Two new dirhodium complexes are reported and their ability to bind to DNA was assessed. Compounds **II.2** and **II.3** exhibit strong absorption bands in the visible regions due to the incorporation of the highly conjugated qxnp  $\pi$ -accepting ligand. Computational calculations indicate that the lowest energy transitions for these complexes are MLCT transitions with  $\text{Rh}_2(\pi^*) \rightarrow \text{qxnp}$  character in contrast to complex **II.1** for which the lowest energy transition is a MC transition with  $\text{Rh}_2(\pi^*) \rightarrow \text{Rh}_2(\sigma^*)$  character. The major change in parentage of these transitions leads to **II.2** and **II.3** exhibiting low-energy absorption bands that have 10 to 20-fold higher absorptivity coefficients. The compounds were subjected to irradiation in aqueous solutions which produces the hydrolyzed form of complex **II.2**. Importantly, **II.2** does not undergo thermal aquation (in the dark) which makes it a good candidate for PACT applications. In addition, the aqua form of this complex can bind to DNA as evidenced by the disappearance of the pUC-18 plasmid band in the agarose gel electrophoresis experiments when **II.2** is incubated under irradiation conditions. Compound **3**, however, does not undergo photoaquation but is stable in the dark and upon irradiation. The lack of a photoaquation event for **II.3** renders it unable to bind to DNA even after 3 hours of irradiation with visible light ( $\lambda > 515$  nm). The results in this study demonstrate that with a judicious choice of a ligand environment around the dirhodium core one can tune the photophysical properties of these dirhodium species. Efforts are underway to replace the acetate ligands with more electron donating bridging ligands, such as 2-hydroxypyridines, to further red-shift the absorption profiles of these complexes while retaining some solvent equatorial ligands for biological applications.



CHAPTER III  
TUNABLE RHODIUM(II,II) LIGHT ABSORBERS AS EXCITED STATE  
ELECTRON DONORS AND ACCEPTORS ACCESSIBLE WITH RED/NEAR-IR  
IRRADIATION\*

**Introduction**

The worldwide increase in energy demand and the continued use of coal and hydrocarbons to meet these needs requires the development of more efficient sources of green and renewable energy. The use of solar energy to inject holes and electrons into semiconductors and to drive homogeneous and heterogeneous catalysis represents a promising approach for the production of electricity and clean fuels from abundant sources, such as H<sub>2</sub> gas from H<sub>2</sub>O.<sup>83-91</sup> One challenge in this field includes the development of new sensitizers that can help increase efficiency of dye-sensitized solar cells (DSSCs)<sup>57, 92-95</sup> and dye-sensitized photoelectrosynthesis cells (DSPEC).<sup>85, 87, 96-98</sup>

One limit of the efficiency of traditional dyes is their poor absorption of low energy visible and near-infrared light, such that the extension of their absorption profiles to include these spectral regions is important to improve the output of these devices. The spectral distribution of the solar flux is depicted in Figure III.1, where the area shaded in red represents the wavelengths absorbed by traditional Ru(II)-based dyes, from the UV to

---

\*Adapted with permission from Whittemore, T. J.; Millet, A.; Sayre, H. J.; Xue, C.; Dolinar, B. S.; White, E. G.; Dunbar, K. R.;Turro, C., Tunable Rh<sub>2</sub>(II,II) Light Absorbers as Excited-State Electron Donors and Acceptors Accessible with Red/Near-Infrared Irradiation. *J. Am. Chem. Soc.* **2018**, *140* (15), 5161-5170. Copyright 2018 American Chemical Society.

~650 nm, where poor light absorption results in low incident photo-to-current efficiencies (IPCE).<sup>99, 100</sup> The area shaded in grey in Figure III.1 shows the result of the extension of the absorption from 650 nm to 900 nm, integrating this represents a twofold increase in both the number of photons available and thus the theoretical IPCE.<sup>101, 102</sup> Therefore, harvesting these low energy photons by designing new dyes that strongly absorb and convert red and near-IR photons into chemical or electrical energy provides a means to improve the utilization of the solar output.

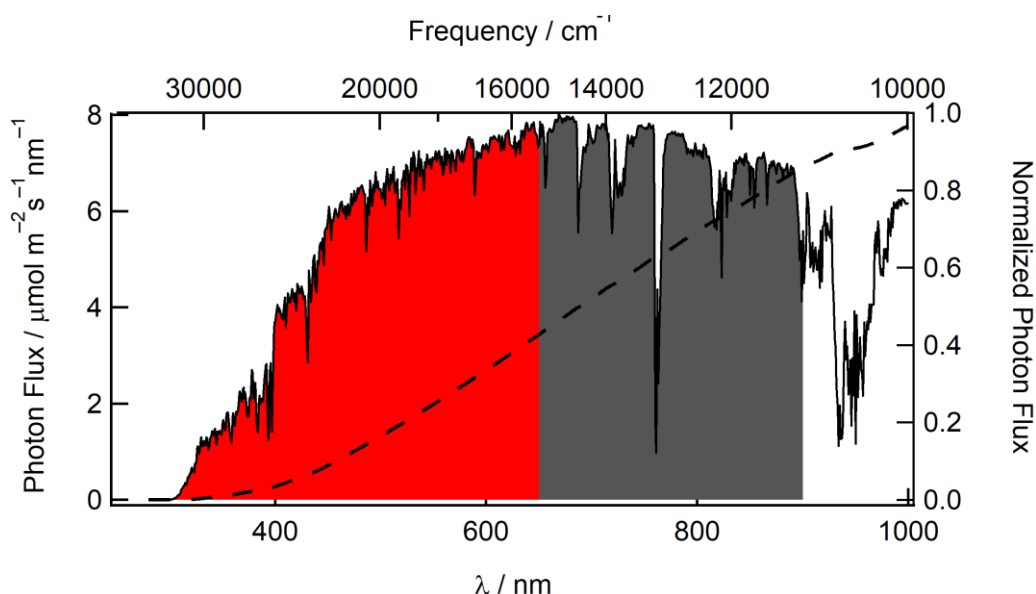


**Figure III.1** Solar flux as a function of wavelength from the UV to the near-IR and integrated photon flux (dotted line) (adapted from ref. 100).

Following photon absorption by the sensitizer in a DSSC, it transfers an electron or a hole from its excited state to a n- or p-type semiconductor, respectively.<sup>103</sup> This event can be used to generate current or to perform a chemical transformation on a substrate to

generate fuels or useful chemicals. The archetypal N3 dye, *cis*-bis(thiocyanato)bis(2,2'-bipyridyl-4,4'-dicarboxylic acid)ruthenium(II), and related Ru(II) complexes have been investigated extensively as sensitizers for nanocrystalline TiO<sub>2</sub> for n-type dye-sensitized applications.<sup>59, 104</sup> The lowest energy absorption maximum of the N3 dye is observed at 534 nm in ethanol ( $\epsilon = 1.42 \times 10^4 \text{ M}^{-1}\text{cm}^{-1}$ ),<sup>59</sup> tailing to ~ 650 nm, and this complex does not generate photocurrent on p-type NiO because its excited state is not sufficiently oxidizing.<sup>105</sup> Other d<sup>6</sup> metal complexes have been explored for DSSC and DSPEC applications, including cyclometallated iridium complexes as sensitizers for both n- and p-type semiconductors.<sup>106-108</sup> These complexes, however, display limited absorption in the visible region resulting in low efficiency cells.<sup>109, 110</sup> Porphyrin-sensitized n-type and p-type solar cells have garnered attention in the past decade due to their ease in tunability and large absorption cross-sections that can be extended into the near-IR, but, due to the planar structures,  $\pi$ -stacked aggregates are common which are known to reduce their performance.<sup>111, 112</sup> Therefore, in order to utilize both high and low energy photons from sunlight, charge transfer reactions must be achieved following absorption over the complete range of the solar spectrum. Consequently, the development of new complexes with high molar extinction coefficients, lower energy absorption maxima, and appropriate excited state lifetimes and redox potentials for reactivity is highly desirable.

The sensitization of p-type semiconductors, such as NiO, used together with that of traditional n-type DSSCs in tandem cells is theoretically predicted to increase the efficiency from 33% to 43%,<sup>57, 109, 113-116</sup> but dyes for hole injection are not as well developed as those for electron injection. This difference is partially due to the limitations

of p-type NiO, where short hole diffusion distances, Ni(III) surface trap states, and charge recombination reactions result in low photovoltaic performance.<sup>114, 117, 118</sup> The most efficient p-type dyes to date are based on  $\alpha$ -pyranylidene donors but are limited by poor light absorption beyond 500 nm despite performing with a device efficiency of 2.51%.<sup>119</sup> Boron-dipyrromethene (BODIPY) dyes are among the most promising light absorbers and have the highest photon-to-current efficiencies, although they suffer from narrow absorption profiles.<sup>120, 121</sup> Porphyrin and phthalocyanine-based dyes are amongst the most widely investigated for p-type sensitization, featuring efficiencies  $\sim$  0.01% on p-type NiO.<sup>122-124</sup> The most efficient dyes are asymmetrically substituted using electron acceptor units, such as nitro groups or fullerene acceptors, to ensure that the HOMO and LUMO have poor spatial overlap to help prevent charge recombination.

Dirhodium(II,II) paddlewheel complexes have the potential to overcome the obstacles posed by the current class of light absorbers for both p-type and n-type applications. Dirhodium(II,II) complexes with formamidinate electron donating bridging ligands and naphthyridine-based electron accepting ligands are air and water stable, highly soluble in aqueous media and organic solvents, are easily synthesized, and feature relatively long-lived triplet metal/ligand-to-ligand charge transfer (ML-LCT) excited states capable of performing electron transfer to methyl viologen ( $MV^{2+}$ ).<sup>63</sup> Upon excitation, the <sup>3</sup>ML-LCT excited state of these Rh<sub>2</sub>(II,II) complexes is populated, which features localized electron density on the naphthyridine  $\pi$ -accepting ligand and the hole localized on the formamidinate bridge, making the electron density in the excited state well-suited to both p- and n-type semiconductor applications. Furthermore, these

complexes exhibit <sup>1</sup>ML-LCT maxima at ~ 640 nm ( $\epsilon \sim 3,500 \text{ M}^{-1}\text{cm}^{-1}$ ) that tails to ~800 nm and broad absorption profiles that extend from the UV into the red and near-IR, unlike traditional organic and inorganic dyes.<sup>63</sup> An important issue that typically limits the use of red and near-IR light to sensitize DSSCs is the low driving force for charge transfer reactions arising from the dye's low-lying excited states. In addition, the Energy Gap Law predicts the faster nonradiative deactivation into high-energy ground-state vibrational modes in the low energy excited states that are accessible with red and near-IR photons, resulting in short lifetimes.<sup>125</sup> The rigid paddlewheel architecture of the Rh<sub>2</sub>(II,II) complexes helps to overcome these issues, further aided by the incorporation of axial blocking ligands, a feature that was previously shown to increase the lifetime of the charge transfer excited states of these complexes by ~2 orders of magnitude. It is also important to note that the substitution of the bridging ligands in these complexes is facile, lending to wide tunability of the reducing and oxidizing excited states that arise from Rh<sub>2</sub>/formamidinate-to-naphthyridine charge transfer electronic transitions.<sup>63, 126, 127</sup>

The present study focuses on the development of three new cationic dirhodium(II,II) complexes with improved absorption, redox, and excited state properties to access both hole transfer into p-type semiconductors and electron injection into n-type semiconductors, featuring panchromatic absorption reaching the near-IR and reactive low energy excited states. These complexes are derived from the known complex *cis*-[Rh<sub>2</sub>( $\mu$ -DTolF)<sub>2</sub>( $\mu$ -np)<sub>2</sub>][BF<sub>4</sub>]<sub>2</sub> (DTolF = N,N'-di(p-tolyl)-formamidinate, np = 1,8-naphthyridine), **III.1**, depicted in Figure III.2.<sup>47</sup> The new complexes of general formula *cis*-[Rh<sub>2</sub>( $\mu$ -DTolF)<sub>2</sub>( $\mu$ -L)<sub>2</sub>][BF<sub>4</sub>]<sub>2</sub>, where L = 2-(pyridin-2-yl)-1,8-naphthyridine (pynp,

**III.2**), 2-(quinolin-2-yl)-1,8-naphthyridine (**qnp**, **III.3**), and 2-(1,8-naphthyridin-2-yl)quinoxaline (**qxp**, **III.4**) were synthesized and characterized (Figure III.2), and their properties compared to those of **III.1** and related Rh<sub>2</sub>(II,II) complexes. In **III.2–4**, the bridging ligand is appended with a moiety that coordinates to one of the axial sites on the bimetallic core, thus blocking access from solvent, providing a more rigid paddlewheel structure, and preventing Rh-Rh bond elongation in the excited state, all of which are believed to result in slower rates of nonradiative deactivation of the excited state. Importantly, irradiation of **III.2–4** with red/near-IR light results in hole transfer, the oxidation of an electron donor, showing their potential in applications that require p-type semiconductor sensitization. Additionally, complex **III.2** is also able to effect electron transfer to MV<sup>2+</sup> upon irradiation. To our knowledge, these complexes represent the first bimetallic architecture to achieve excited state hole transfer with low energy light.

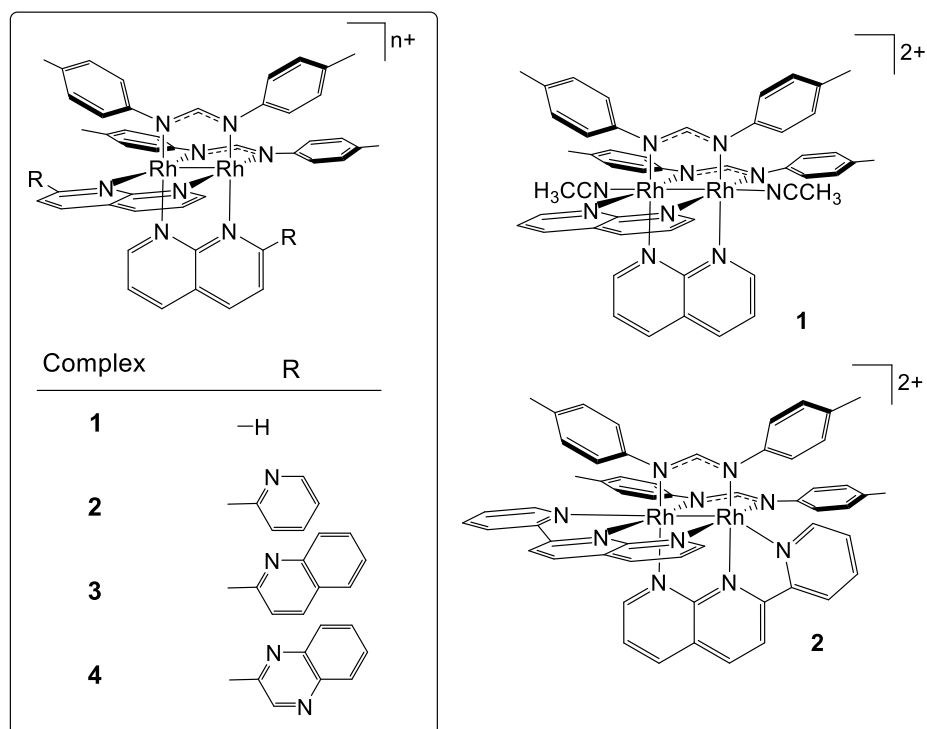


**Figure III.2** Schematic representation of the molecular structures of **III.1–4**. Reprinted from ref. 74.

## Experimental Section

### Materials

The starting material  $cis\text{-}[\text{Rh}_2(\text{DTolF})_2(\text{CH}_3\text{CN})_6](\text{BF}_4)_2$  was synthesized from  $[\text{RhCl}(\text{COD})]_2$  following reported procedures.<sup>34</sup> The latter compound was purchased from Pressure Chemicals and used without further purification. The reagent 1,8-naphthyridine (np) was purchased from Oakwood Chemicals and 2-acetylpyridine, 2-acetylquinoxaline, and 2-amino-3-formylpyridine were purchased from AK Scientific; all were used without further purification. The *p*-toluidine was purchased from Alfa Aesar, triethyl orthoformate was purchased from TCI, and 1-(quinoline-2-yl)ethenone was obtained from Enamine Chemicals. The ligands *N,N'*-di(*p*-tolyl) formamidine (DTolF), 2-(2-pyridinyl)-1,8-

naphthyridine (pynp), and 2-(1,8-naphthyridine-2-yl)quinoxaline (qxnq) were synthesized from reported procedures.<sup>64</sup> Acetonitrile was dried over 3 Å molecular sieves and distilled under a nitrogen atmosphere. Reactions were conducted with Schlenk-line techniques unless otherwise stated. Filtrations and further manipulation of the products were conducted in air.

2-(quinoline-2-yl)-1,8-naphthyridine (qnp). Quantities of 2-amino-3-formylpyridine (229.6 mg, 1.88 mmol) and 1-(quinolin-2-yl)ethanone (315.3 mg, 1.84 mmol) were dissolved in 5 mL of methanol to yield an orange solution. Upon addition of an aqueous solution of potassium hydroxide (268.3 mg in 5 mL of water) an orange precipitate rapidly appeared. After stirring overnight at 60 °C for 12 h, the reaction was quenched by the addition of 20 mL of water and placed in an ice bath prior to vacuum filtration. The solid was washed with ice cold water and dried under vacuum to yield 436 mg of an off-white powder (92% yield).  $\delta_{\text{H}}$  (300 MHz;  $\text{CDCl}_3$ -*d*): 9.14 (1H, *dd*,  $J = 4.4$  Hz,  $J = 1.9$  Hz), 9.04 (H, *d*,  $J = 8.6$  Hz), 8.98 (H, *d*,  $J = 8.6$  Hz), 8.33 (2H, *dd*,  $J = 8.3$  Hz,  $J = 6.9$  Hz), 8.25 (2H, *m*), 7.85 (1H, *dd*,  $J = 8.2$  Hz,  $J = 1.0$  Hz), 7.69 (1H, *ddd*,  $J = 8.4$  Hz,  $J = 6.9$  Hz,  $J = 1.4$  Hz), 7.53 (2H, *m*).

*cis*-[Rh<sub>2</sub>(DTolF)<sub>2</sub>(np)<sub>2</sub>](BF<sub>4</sub>)<sub>2</sub> (**III.1**). Synthesis of **1** was carried out with minor modifications of a reported procedure.<sup>47</sup> Samples of *cis*-[Rh<sub>2</sub>(DTolF)<sub>2</sub>(CH<sub>3</sub>CN)<sub>6</sub>](BF<sub>4</sub>)<sub>2</sub> (121.7 mg, 0.113 mmol) and np (29.8 mg, 0.229 mmol) were suspended in 20 mL of dry CH<sub>3</sub>CN and refluxed for 24 h under N<sub>2</sub> in an oil bath at 110 °C to give a dark purple solution after 1 h. After 24 h, the reaction was cooled to room temperature and the solution was concentrated under reduced pressure to ~5 mL. Diethyl ether was added to induce



precipitation of the product which was subsequently filtered through a medium frit under vacuum. The dark-purple crystalline solid was washed with Et<sub>2</sub>O and dried under vacuum to yield 113 mg of product (92% yield). X-ray quality crystals were obtained by layering toluene onto a concentrated solution of the compound in CH<sub>3</sub>CN. Anal. Calcd. for C<sub>49.75</sub>H<sub>47</sub>B<sub>2</sub>F<sub>8</sub>N<sub>9</sub>Rh<sub>2</sub> (**III.1**·0.25(toluene)): C, 51.94; H, 4.12; N, 10.96. Found: C, 51.71; H, 4.03; N, 11.05. δ<sub>H</sub> (300 MHz; CD<sub>3</sub>CN-*d*<sub>3</sub>): 9.53 (4H, *d*, *J* = 3.1 Hz, np), 8.60 (4H, *dd*, *J* = 5.0 Hz, *J* = 0.9 Hz, np), 7.77 (4H, *dd*, *J* = 5.0 Hz, *J* = 3.2 Hz, np), 7.57 (2H, *t*, *J* = 2.0 Hz, DTolF), 7.00 (8H, *d*, *J* = 5.0 Hz, DTolF), 6.58 (8H, *d*, *J* = 5.0 Hz, DTolF), 2.28 (12H, *s*, DTolF). ESI-MS: *m/z*: 456.22 for [Rh<sub>2</sub>(DTolF)<sub>2</sub>(np)<sub>2</sub>]<sup>2+</sup>.

*cis*-[Rh<sub>2</sub>(DTolF)<sub>2</sub>(pynp)<sub>2</sub>](BF<sub>4</sub>)<sub>2</sub> (**III.2**). Samples of *cis*-[Rh<sub>2</sub>(DTolF)<sub>2</sub>(CH<sub>3</sub>CN)<sub>6</sub>](BF<sub>4</sub>)<sub>2</sub> (151.8 mg, 0.142 mmol) and pynp (59.0 mg, 0.285 mmol) were suspended in 20 mL of dry CH<sub>3</sub>CN and refluxed for 24 h under N<sub>2</sub> at 110 °C to give a green solution after 5 min of reflux. The dark green solution was cooled to room temperature and concentrated under reduced pressure to ~5 mL. Diethyl ether was added and the resulting green precipitate was filtered through a medium frit under vacuum. The green solid was washed with Et<sub>2</sub>O and dried under vacuum to yield 164 mg of a green powder (93% yield). X-ray quality crystals were obtained by slow diffusion of Et<sub>2</sub>O into a concentrated solution of the compound in dichloromethane. Anal. Calcd. for C<sub>60</sub>H<sub>55</sub>B<sub>2</sub>Cl<sub>4</sub>F<sub>8</sub>N<sub>11</sub>Rh<sub>2</sub> (2·(CH<sub>2</sub>Cl<sub>2</sub>)<sub>2</sub>(CH<sub>3</sub>CN)): C, 49.65; H, 3.82; N, 10.62. Found: C, 49.95; H, 4.11; N, 10.93. δ<sub>H</sub> (300 MHz; CD<sub>3</sub>CN-*d*<sub>3</sub>): 8.67 (2H, *d*, *J* = 5.1 Hz, pynp), 8.53 (6H, *m*, pynp), 8.40 (2H, *d*, *J* = 8.3 Hz, pynp), 8.10 (2H, *td*, *J* = 7.8 Hz, *J* = 1.9 Hz, DTolF), 7.50 (4H, *m*, pynp), 7.39 (4H, *m*, pynp), 7.24 (4H, *d*, *J* = 8.0 Hz, DTolF), 6.87 (4H, *d*, *J* =

8.3 Hz, DTolF), 6.52 (4H, *d*, *J* = 7.2 Hz, DTolF), 6.17 (4H, *d*, *J* = 8.0 Hz, DTolF), 2.42 (6H, *s*, DTolF), 2.07 (6H, *s*, DTolF). ESI-MS: *m/z*: 1153.35 for  $[\text{Rh}_2(\text{DTolF})_2(\text{pynp})_2](\text{BF}_4)^+$  and 533.10 for  $[\text{Rh}_2(\text{DTolF})_2(\text{pynp})_2]^{2+}$ .

*cis*- $[\text{Rh}_2(\text{DTolF})_2(\text{qnp})_2](\text{BF}_4)_2$  (**III.3**). Quantities of *cis*- $[\text{Rh}_2(\text{DTolF})_2(\text{CH}_3\text{CN})_6](\text{BF}_4)_2$  (200.9 mg, 0.187 mmol) and qnp (99.6 mg, 0.387 mmol) were suspended in 20 mL of dry  $\text{CH}_3\text{CN}$  and refluxed for 24 h under  $\text{N}_2$  at 110 °C. The resulting dark colored reaction solution was cooled to room temperature and was concentrated under reduced pressure to ~5 mL. The addition of  $\text{Et}_2\text{O}$  led to precipitation of a dark-blue solid which was filtered through a medium frit under vacuum, washed with diethyl ether and dried under vacuum to yield 232 mg of a dark-blue powder (93% yield). X-ray quality crystals were obtained by slow diffusion of  $\text{Et}_2\text{O}$  into a concentrated solution of the compound in  $\text{CH}_3\text{OH}$ . Anal. Calcd. for  $\text{C}_{64}\text{H}_{52}\text{B}_2\text{F}_8\text{N}_{10}\text{Rh}_2$  (**III.3**): C, 57.34; H, 3.91; N, 10.45. Found: C, 57.36; H, 4.14; N, 10.64.  $\delta_{\text{H}}$  (300 MHz;  $\text{CD}_3\text{CN}-d_3$ ): 9.12 (2H, *dd*, *J* = 3.2 Hz, *J* = 0.9 Hz, qnp), 8.34 (2H, *d*, *J* = 5.3 Hz, qnp), 8.74 (2H, *d*, *J* = 5.3 Hz, qnp), 8.71 (2H, *dd*, *J* = 5.0 Hz, *J* = 0.9 Hz, qnp), 8.55 (2H, *d*, *J* = 5.2 Hz, qnp), 8.48 (2H, *d*, *J* = 5.2 Hz, qnp), 7.88 (2H, *dd*, *J* = 4.9 Hz, *J* = 0.4 Hz, qnp), 7.59 (6H, *m*, qnp), 7.27 (2H, *d*, *J* = 5.2 Hz, qnp), 7.10 (4H, *d*, *J* = 4.9 Hz, DTolF), 6.98 (2H, *ddd*, *J* = 5.0 Hz, *J* = 4.1 Hz, *J* = 0.8 Hz, DTolF), 6.28 (4H, *d*, *J* = 5.0 Hz, DTolF), 6.15 (4H, *d*, *J* = 4.8 Hz, DTolF), 6.02 (4H, *d*, *J* = 4.6 Hz, DTolF), 2.41 (6H, *s*, DTolF), 1.89 (6H, *s*, DTolF). ESI-MS: 1253.36 *m/z*: for  $[\text{Rh}_2(\text{DTolF})_2(\text{qnp})_2](\text{BF}_4)^+$ .

*cis*- $[\text{Rh}_2(\text{DTolF})_2(\text{qxp})_2](\text{BF}_4)_2$  (**III.4**). Samples of *cis*- $[\text{Rh}_2(\text{DTolF})_2(\text{CH}_3\text{CN})_6](\text{BF}_4)_2$  (151.7 mg, 0.141 mmol) and qxp (75.3 mg, 0.292 mmol)

were suspended in 20 mL of dry CH<sub>3</sub>CN and refluxed for 24 h under N<sub>2</sub> at 110 °C. After 40 min, the solution had turned black and most of the ligand had dissolved. After 24 h, the reaction was cooled to room temperature and the dark solution was concentrated under reduced pressure to ~5 mL. Diethyl ether was added to precipitate a dark green product which was collected by filtration on a medium frit, washed with Et<sub>2</sub>O, and dried under vacuum to yield 176 mg of a dark-blue powder (92 % yield). X-ray quality crystals were obtained by slow diffusion of Et<sub>2</sub>O into a concentrated solution of the compound in CH<sub>3</sub>CN. Anal. Calcd. for C<sub>62</sub>H<sub>50</sub>B<sub>2</sub>F<sub>8</sub>N<sub>12</sub>Rh<sub>2</sub> (**III.4**): C, 55.47; H, 3.75; N, 12.52. Found: C, 54.87; H, 4.04; N, 12.33.  $\delta_{\text{H}}$  (300 MHz; CD<sub>3</sub>CN-*d*<sub>3</sub>): 9.88 (2H, *s*, qxnp), 8.95 (3H, *t*, *J* = 5.4 Hz, qxnp), 8.91 (3H, *t*, *J* = 5.3 Hz, qxnp), 8.73 (2H, *d*, *J* = 4.9 Hz, qxnp), 8.02 (2H, *d*, *J* = 5.1 Hz, qxnp), 7.82 (2H, *t*, *J* = 5.0 Hz, DTolF), 7.61 (2H, *t*, *J* = 2.1 Hz, qxnp), 7.59 (2H, *dd*, *J* = 4.9 Hz, *J* = 3.2 Hz, qxnp), 7.11 (4H, *d*, *J* = 5.0 Hz, DTolF), 7.06 (2H, *ddd*, *J* = 5.1 Hz, *J* = 4.3 Hz, *J* = 0.8 Hz, qxnp), 6.95 (2H, *d*, *J* = 5.2 Hz, qxnp), 6.37 (4H, *d*, *J* = 4.9 Hz, DTolF), 6.16 (4H, *d*, *J* = 5.0 Hz, DTolF), 6.06 (4H, *d*, *J* = 4.7 Hz, DTolF), 2.40 (6H, *s*, DTolF), 1.85 (6H, *s*, DTolF). ESI-MS: *m/z*: 584.34 for [Rh<sub>2</sub>(DTolF)<sub>2</sub>(qxnp)<sub>2</sub>]<sup>2+</sup>.

#### *Instrumentation and Methods*

<sup>1</sup>H NMR spectra were obtained on a Varian 300 MHz spectrometer and the chemical shifts were referenced to the residual peak of the residual CD<sub>3</sub>CN-*d*<sub>3</sub> deuterated solvent signal at 1.96 ppm.<sup>75</sup> Electronic spectroscopy was performed on a Hewlett-Packard 8453 diode array spectrometer or on a Shimadzu UV-1601PC spectrophotometer. Elemental analyses were performed by Atlantic Microlab, Inc. Electrospray mass spectral

data were obtained in the Laboratory for Biological Mass Spectrometry at Texas A&M University using a PE Sciex (Concord, Ontario, Canada) API Qstar Pulsar with an Ionwerks time-to-digital converter, TDCx4, for data recording. Single crystals of **III.1–4** were selected from oil under ambient conditions using a MiTeGen microloop or nylon loop. For each complex, a crystal was placed in a cold N<sub>2</sub> stream at 110 K on a Bruker D8-QUEST diffractometer equipped with a I $\mu$ S Mo microsource ( $\lambda = 0.71073 \text{ \AA}$ ). An initial unit cell was determined using SAINT from a set of three  $\omega$ -scans consisting of 0.5° frames and a sweep width of 15°. Using this unit cell, a data collection strategy was implemented to collect all independent reflections to a resolution of at least 0.83 Å. Full details of the data collection and parameters are presented in Tables III-1 and 2. For each structure, the data were corrected for absorption using SADABS,<sup>128</sup> and the space group was determined from analysis of the systematic absences using XPREP. The structures were solved using the intrinsic phasing routine in SHELXT or by direct methods implemented in SHELXS. The non-hydrogen atoms were located from the Fourier difference map by least-squares refinement of the structure using SHELXL-2014.<sup>129</sup> All non-hydrogen atoms were refined anisotropically and hydrogen atoms were placed in calculated positions and refined with thermal parameters constrained to their parent atom. Specific details of the refinements are presented in Tables III-1 and 2.

Femtosecond transient absorption spectroscopy was performed using a modified instrument whose details were previously reported.<sup>130</sup> Briefly, the fundamental 800 nm from a Ti:Sapph Astrella laser system (Coherent) was 8 mJ. Part of this output (3 mJ) was used to pump an OPA (OPerA Solo) which was used to generate all excitation

wavelengths. White light continuum was generated using CaF<sub>2</sub> on a rotating mount. The samples were excited at 2.0 to 2.5 μJ at the sample. The instrument response function was determined to be 85 fs via the optical Kerr effect in cyclohexane. All samples were flowed in a 1 mm path-length flow cell (Harrick Scientific) equipped with 1 mm CaF<sub>2</sub> plates. The polarization angle between the pump and probe pulses was set to the magic angle to account for the effects of rotational diffusion. Multiple retroreflector cycles were taken and all samples were measured via steady-state UV-Vis before and after to ensure no sample decomposition occurred.

Nanosecond transient absorption data were collected on an Edinburgh LP980 Spectrometer equipped with single wavelength and broadband capabilities. The excitation pulse was generated from a Basiscan OPO (Spectraphysics) pumped with 100 mJ of the third harmonic of a Nd:YAG laser at 10 Hz (Spectraphysics, INDI-40). All samples were pumped with 5 to 7 mJ of power and deoxygenated prior to photolysis and were subjected to steady state UV-Vis studies before and after data collection to ensure that no degradation had occurred. Solutions of *p*-paraphenylene diamine radical cation were generated in 0.1 M aqueous solutions of sodium azide by a previously reported method.<sup>54</sup>

The quenching experiments of the long-lived triplet excited state organic sensitizers were performed to estimate  $E_{00}^T$ , the triplet excited state energy, of **2** using nanosecond transient absorption. Stern-Volmer plot,  $\tau_0/\tau$  vs [III.2], varied from 12 μM to 200 μM, were constructed to obtain the quenching constant. In these experiments, anthracene ( $E^T = 1.83$  eV,  $\lambda_{ex} = 355$  nm), tetracene ( $E^T = 1.27$  eV,  $\lambda_{ex} = 470$  nm), rubrene ( $E^T = 1.15$  eV,  $\lambda_{ex} = 525$  nm) and β-carotene ( $E^T = 0.78$  eV,  $\lambda_{ex} = 490$  nm) were used as

energy donors, with **2** as the quencher in deaerated acetonitrile in a method similar to one previously reported.<sup>63</sup> Oxidative and reductive quenching mechanisms were ruled out due to an unfavorable thermodynamic driving force for all donors.

Cyclic voltammograms were recorded under an inert atmosphere with a BASi CV-50W potentiostat (Bioanalytical Systems, Inc.; West Lafayette, IN, USA) using a three-electrode cell consisting of a glassy carbon disc working electrode, Pt wire counter electrode and a Ag/AgCl reference electrode standardized to ferrocene ( $E_{1/2} = +0.55$  V vs Ag/AgCl). A 1.0 mM solution of complex was dissolved in DMF with 0.1 M Bu<sub>4</sub>NPF<sub>6</sub> supporting electrolyte. The applied scan rate was 200 mV/s. Spectroelectrochemical measurements were carried out under an inert atmosphere in a two-compartment cell. Electronic absorption spectra were obtained with an Agilent 8453 diode array spectrophotometer (Agilent Technologies; Santa Clara, CA, USA) during bulk electrolysis with a BASi CV-50W potentiostat. A glassy carbon rod working electrode and a Ag/AgCl (3 M NaCl) reference electrode were contained in the 1.0 cm glass spectrometer cell working compartment and a carbon mesh counter electrode was contained in the auxiliary compartment. Complexes were dissolved in CH<sub>3</sub>CN with 0.1 M Bu<sub>4</sub>NPF<sub>6</sub> electrolyte. Applied potentials were held at 200 mV more positive than the first oxidation and 100 mV more negative than the first reduction, prior to the onset of the second reduction current.

Molecular and electronic structure calculations were performed using Density Functional Theory (DFT) methods in the Gaussian09 (G09) program package.<sup>131</sup> The B3LYP<sup>132, 133</sup> correlation and exchange functionals were used with the Stuttgart RSC 1997 Electron Core Potential (ECP) basis set for the Rh atoms and the 6-31G† basis set for the

C, N, and H atoms.<sup>134</sup> As a starting point, geometric parameters were taken from the crystal structures without the counter ions or the interstitial solvent molecules. These structures were optimized in the gas phase followed by Time-Dependent Density Functional Theory (TD-DFT)<sup>135</sup> calculations using the polarized continuum model (PCM) with CH<sub>3</sub>CN as the solvent,<sup>136</sup> and the first sixty lowest singlet-to-singlet excitations were calculated from the optimized singlet ground state. In addition, the first triplet excited state structures for complexes **III.1**, **III.2** and **III.4** were optimized in the gas phase and the orbital contributions were calculated using a PCM model with acetonitrile. The molecular orbitals were plotted with the graphic software 'Agui'<sup>137</sup> with an isovalue = 0.04. Natural transition orbital (NTO) analyses were performed with the Chemissian program (<http://www.chemissian.com>).<sup>77</sup>

## Results and Discussion

### *Synthesis and Characterization*

Complexes **III.1–4** were synthesized following the reaction scheme presented in Figure III.3. The general synthesis consisted of refluxing the starting material *cis*-[Rh<sub>2</sub>(DTolF)<sub>2</sub>(CH<sub>3</sub>CN)<sub>6</sub>](BF<sub>4</sub>)<sub>2</sub> in the presence of 2 equivalents of the  $\pi$ -accepting ligand (NNN) for 24 hours. The aromatic region of the <sup>1</sup>H NMR spectra for all four complexes shows that all H atoms in the NNN ligands are non-equivalent (Figures III.4–7). The integration for all complexes is consistent with the presence of 2 NNN ligands (Figure III.8). Positive ESI-MS for the complexes display the molecular ion [M]<sup>2+</sup> as the main product of ionization. The bulk purities of complexes **III.1–4** was evaluated through elemental analyses experiments with a 0.5% tolerance.

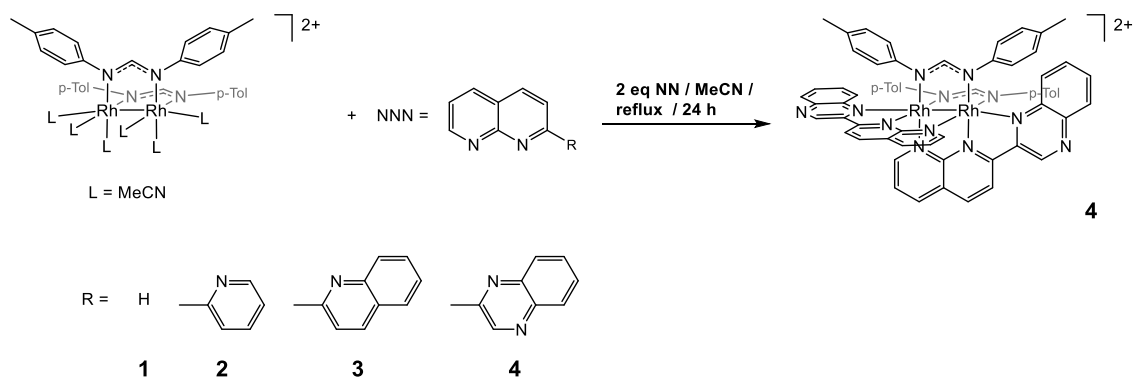


**Figure III.3** Synthetic scheme for the synthesis of complexes **III.1–4**.

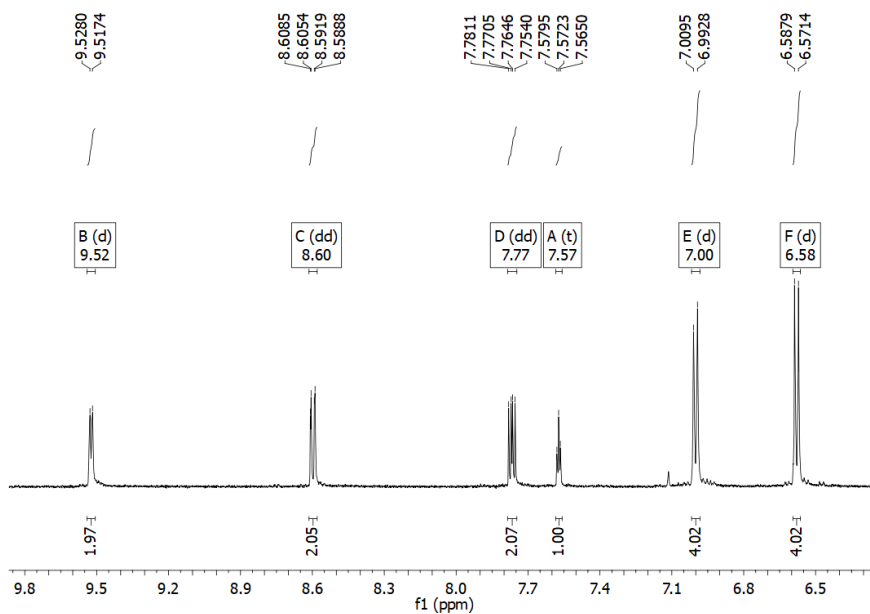


**Figure III.4** Aromatic region of the  $^1\text{H}$  NMR spectrum for **III.1**.



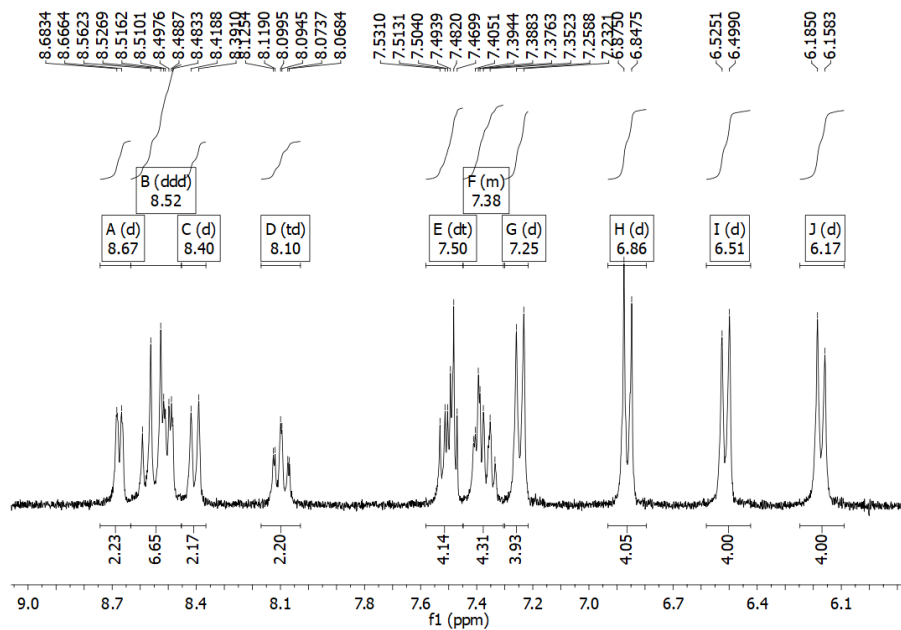


Figure III.5 Aromatic region of the  $^1\text{H}$  NMR spectrum for **III.2**.

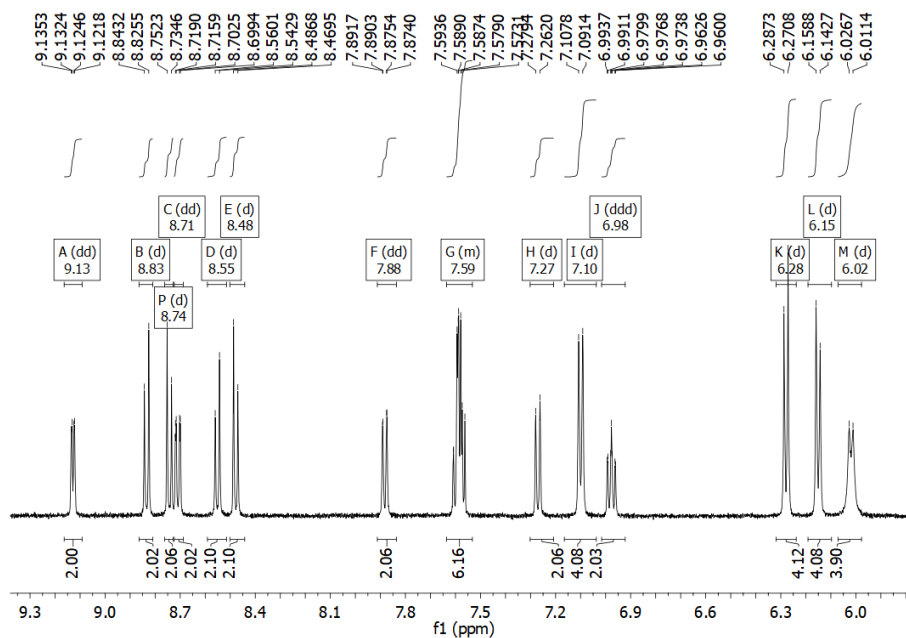
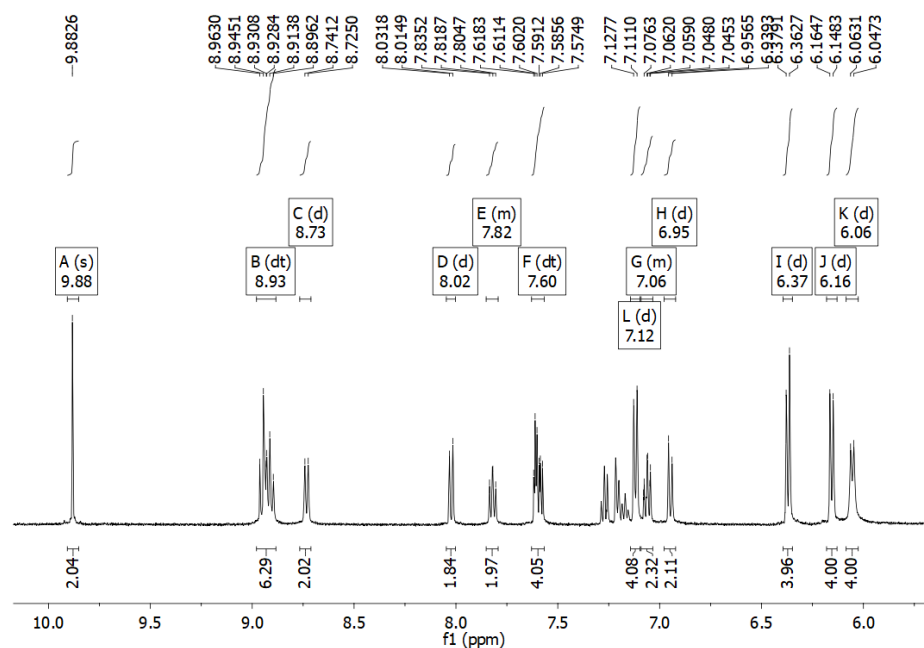


Figure III.6 Aromatic region of the  $^1\text{H}$  NMR spectrum for **III.3**.



**Figure III.7** Aromatic region of the  $^1\text{H}$  NMR spectrum for **III.4**.

### *X-ray Crystal Structures*

The molecular structures of **III.1–4** were determined by X-ray crystallography and are shown in Figure III.8. The compounds consist of a cationic dirhodium unit bridged by two [DTolF] $^-$  ligands and two outer-sphere [BF $_4$ ] $^-$  anions. Complex **III.1** contains a 1,8-naphthyridine ligand, and the increasingly bulky and more highly conjugated axial blocking moieties are incorporated into compounds **III.2** through **III.4**. The Rh–Rh distances of **III.1–4** are 2.4466(7) Å, 2.4771(5) Å, 2.4288(15) Å, and 2.4498(2) Å, respectively, which are slightly shorter than those reported for other dirhodium formamidinate complexes that contain two  $\mu$ -type bridging ligands in a *cis* disposition.<sup>126</sup> The presence of naphthyridine-type moieties in **III.1–4** that bind to the dirhodium core in

a bridging fashion holds the two metals at a closer distance than when two  $\kappa_2$ -chelating diimine ligands form a partial paddlewheel structure, such as *cis*-[Rh<sub>2</sub>(DTolF)<sub>2</sub>(dppn)<sub>2</sub>Cl][BF<sub>4</sub>] and *cis*-[Rh<sub>2</sub>(F-Form)<sub>2</sub>(dppz)<sub>2</sub>][BF<sub>4</sub>]<sub>2</sub>, both of which display longer Rh-Rh bond distances.<sup>126</sup> In addition, *cis*-[Rh<sub>2</sub>( $\mu$ -O<sub>2</sub>CCH<sub>3</sub>)<sub>2</sub>(pynp)<sub>2</sub>][BF<sub>4</sub>]<sub>2</sub> has a Rh–Rh bond distance of 2.408(2) Å, shorter than the DTolF analogue, **III.2**, which is attributed to shorter C–O as compared to C–N bond distances, 1.266 Å and 1.318(8) Å, respectively.<sup>138</sup> Due to the bite angle of these axial blocking ligands, there is a substantial deviation from linearity in the Rh-Rh-N<sub>ax</sub> angle, 164.31(12)°, 164.368(13)°, and 161.73(4)° for complexes **III.2–4**, respectively, which is maintained across the series.

Complexes **III.2–4** also contain *p*-tolyl moieties of the formamidinate bridging ligands that in the crystal structure arrange themselves perpendicularly to the naphthyridine moiety and parallel to the 2-pyridine, 2-quinoline, or 2-quinoxaline moieties of the axial blocking ligands, respectively (Figure III.9).

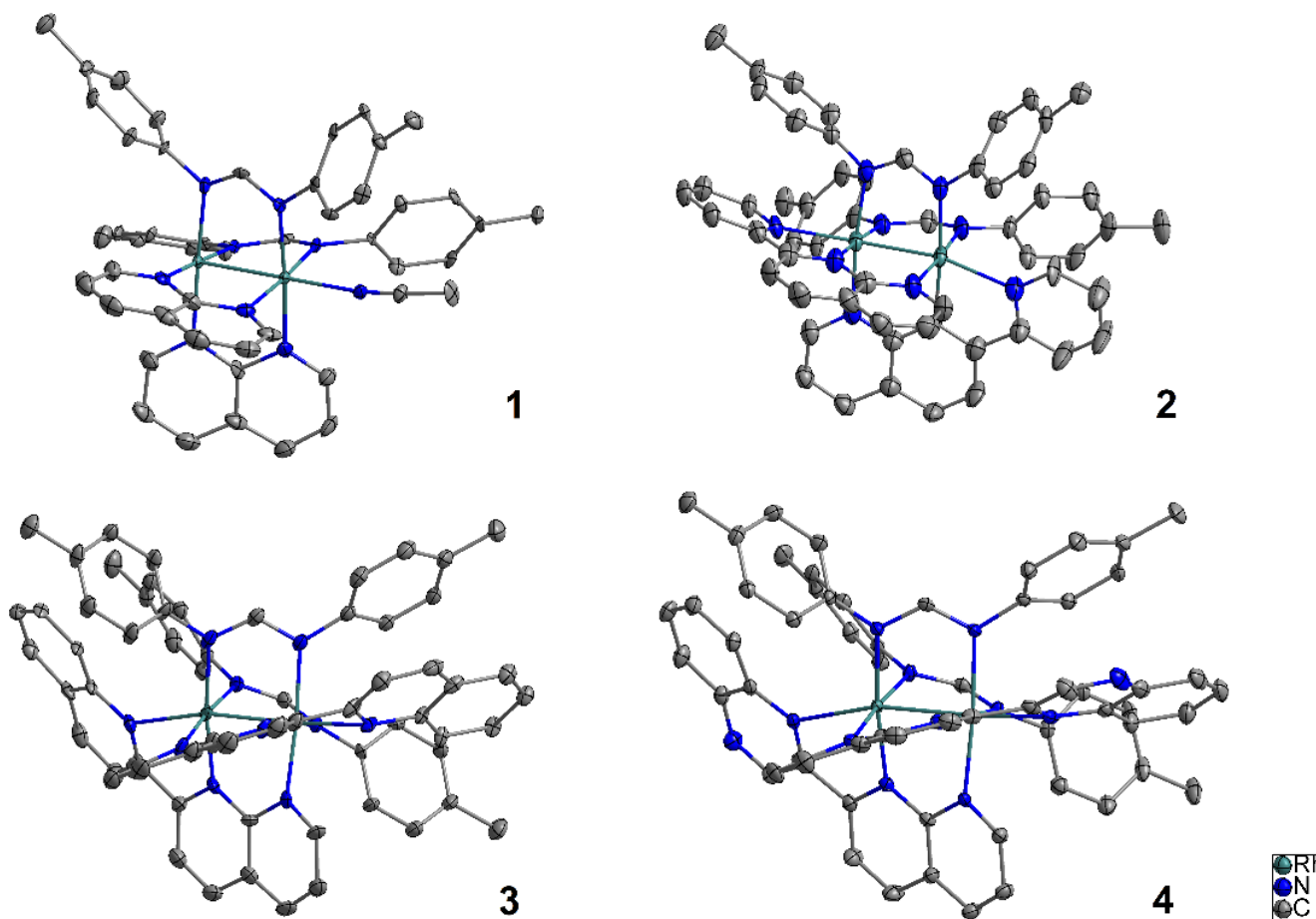


**Figure III.8** Thermal ellipsoid plots for **III.1–4**, shown at the 50% probability level; interstitial solvent molecules, counterions, and hydrogen atoms have been omitted for the sake of clarity. Reprinted from ref. 74.

**Table III-1** The refinement details for **III.1** and **III.2**. Reprinted from ref. 74.

Compound	III.1	III.2
Empirical Formula	C <sub>55</sub> H <sub>53</sub> B <sub>2</sub> F <sub>8</sub> N <sub>9</sub> Rh <sub>2</sub>	C <sub>59.3</sub> H <sub>55.3</sub> B <sub>2</sub> Cl <sub>4.4</sub> F <sub>8</sub> N <sub>10</sub> O <sub>0.3</sub> Rh <sub>2</sub>
Formula weight	1219.50	1449.66
Temperature/K	100(1)	100(1)
Crystal system	monoclinic	triclinic
Space group	<i>P</i> 2 <sub>1</sub> / <i>n</i>	<i>P</i> $\bar{1}$
<i>a</i> /Å	12.2957(4)	13.4157(9)
<i>b</i> /Å	31.6914(11)	14.5243(10)
<i>c</i> /Å	13.9199(5)	15.9753(11)
$\alpha$ /°	90	99.377(2)
$\beta$ /°	105.9550(10)	105.721(2)
$\gamma$ /°	90	94.593(2)
Volume/Å <sup>3</sup>	5215.2(3)	2931.0(3)
<i>Z</i>	4	2
$\rho_{\text{calc}}$ /cm <sup>3</sup>	1.553	1.643
$\mu$ /mm <sup>-1</sup>	0.709	0.842
<i>F</i> (000)	2472.0	1462.0
Crystal size/mm <sup>3</sup>	0.27 × 0.04 × 0.031	0.721 × 0.135 × 0.062
Radiation	MoK $\alpha$ ( $\lambda$ = 0.71073)	MoK $\alpha$ ( $\lambda$ = 0.71073)
2 $\Theta$ range for data collection/°	4.912 to 51.5	4.61 to 52.902
Index ranges	-15 ≤ <i>h</i> ≤ 12 -38 ≤ <i>k</i> ≤ 38 -16 ≤ <i>l</i> ≤ 16	-13 ≤ <i>h</i> ≤ 16 -18 ≤ <i>k</i> ≤ 18 -19 ≤ <i>l</i> ≤ 19
Reflections collected	51141 9917	125877 12058
Independent reflections	<i>R</i> <sub>int</sub> = 0.1277 <i>R</i> <sub>sigma</sub> = 0.0860	<i>R</i> <sub>int</sub> = 0.0915 <i>R</i> <sub>sigma</sub> = 0.0383
Data/restraints/parameters	9917/6/691	12058/338/915
Goodness-of-fit on <i>F</i> <sup>2</sup>	1.111	1.061
Final <i>R</i> indexes [ <i>I</i> ≥ 2 $\sigma$ ( <i>I</i> )]	<i>R</i> <sub>1</sub> = 0.0710 <sup>a</sup> <i>wR</i> <sub>2</sub> = 0.1156 <sup>b</sup>	<i>R</i> <sub>1</sub> = 0.0518 <sup>a</sup> <i>wR</i> <sub>2</sub> = 0.1174 <sup>b</sup>
Final <i>R</i> indexes [all data]	<i>R</i> <sub>1</sub> = 0.1177 <sup>a</sup> <i>wR</i> <sub>2</sub> = 0.1288 <sup>b</sup>	<i>R</i> <sub>1</sub> = 0.0715 <sup>a</sup> <i>wR</i> <sub>2</sub> = 0.1269 <sup>b</sup>
Largest diff. peak/hole / e Å <sup>-3</sup>	1.04/-1.74	1.22/-1.77

**Table III-2** The refinement details for **III.3** and **III.4**. Reprinted from ref. 74.

Compound	<b>III.3</b>	<b>III.4</b>
Empirical Formula	$C_{64.5}H_{55.5}B_2F_8N_{10}O_{1.2}Rh_2$	$C_{65}H_{54.2}B_2F_8N_{13.5}Rh_2$
Formula weight	1369.83	1404.09
Temperature/K	110(1)	100(1)
Crystal system	monoclinic	triclinic
Space group	$C2/c$	$P\bar{1}$
$a/\text{\AA}$	24.378(18)	12.7992(8)
$b/\text{\AA}$	19.183(14)	14.1913(9)
$c/\text{\AA}$	12.511(9)	18.0156(11)
$\alpha/^\circ$	90	110.593(2)
$\beta/^\circ$	100.314(9)	96.603(3)
$\gamma/^\circ$	90	99.188(3)
Volume/ $\text{\AA}^3$	5756(7)	2971.6(3)
Z	4	2
$\rho_{\text{calc}}/\text{g/cm}^3$	1.581	1.569
$\mu/\text{mm}^{-1}$	0.654	0.636
F(000)	2777.0	1422.0
Crystal size/ $\text{mm}^3$	$0.332 \times 0.319 \times 0.256$	$1.596 \times 1.095 \times 0.437$
Radiation	MoK $\alpha$ ( $\lambda = 0.71073$ )	MoK $\alpha$ ( $\lambda = 0.71073$ )
2 $\Theta$ range for data collection/ $^\circ$	2.718 to 56.71	4.73 to 55.296
Index ranges	-32 $\leq$ h $\leq$ 31 -25 $\leq$ k $\leq$ 25 -16 $\leq$ l $\leq$ 16	-16 $\leq$ h $\leq$ 16 -18 $\leq$ k $\leq$ 18 -23 $\leq$ l $\leq$ 23
Reflections collected	48449 6812	104916 13777
Independent reflections	$R_{\text{int}} = 0.0403$ $R_{\text{sigma}} = 0.0292$	$R_{\text{int}} = 0.0494$ $R_{\text{sigma}} = 0.0256$
Data/restraints/parameters	6812/1213/763	13777/208/938
Goodness-of-fit on $F^2$	1.057	1.044
Final R indexes [ $I \geq 2\sigma(I)$ ]	$R_1 = 0.0288^a$ $wR_2 = 0.0632^b$	$R_1 = 0.0262^a$ $wR_2 = 0.0645^b$
Final R indexes [all data]	$R_1 = 0.0422^a$ $wR_2 = 0.0694^b$	$R_1 = 0.0303^a$ $wR_2 = 0.0668^b$
Largest diff. peak/hole / $e \text{\AA}^{-3}$	0.44/-0.68	0.68/-1.25

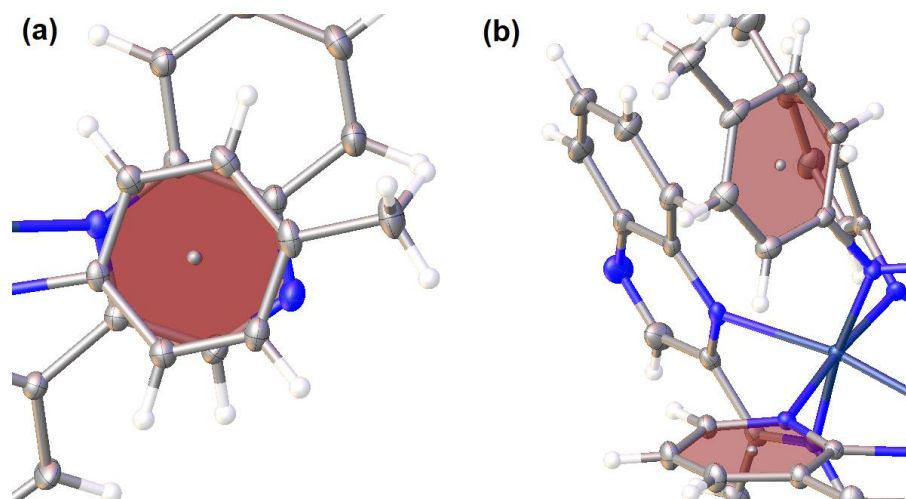


**Figure III.9** (a) Parallel and (b) perpendicular intramolecular aromatic donor-acceptor interactions in compound **III.4**. Reprinted from ref. 74.

#### *Electrochemistry and Electronic Absorption Spectroscopy*

The electrochemical analyses presented in Table III-3 indicate that each complex **III.1–4** exhibits a reversible one-electron oxidation that vary slightly in 0.1 M Bu<sub>4</sub>NPF<sub>6</sub> CH<sub>3</sub>CN, with  $E_{1/2}$  values of +0.87, +0.92, +0.99, and +1.08 V vs Ag/AgCl, respectively. These oxidation couples are assigned as having mixed formamidinate-Rh<sub>2</sub> character based on previous studies on **III.1** and related complexes.<sup>63, 127</sup> Upon scanning cathodically, **III.1–4** display a one-electron reduction of the naphthyridine-based ligand. The electron withdrawing nature of the pyridyl axial moiety in **2** and the extended  $\pi$ -system of pynp as compared to np makes the ligand-based reduction more favorable than in **III.1**, which lacks this moiety,  $-0.70$  and  $-0.94$  V vs Ag/AgCl, respectively. The reduction of the naphthyridine-based ligands is more facile in **III.3** and **III.4** with  $E_{1/2}$  values of  $-0.62$ , and

–0.43 V vs Ag/AgCl, respectively, and is attributed to the further extended  $\pi$ -system and greater electron withdrawing character of the quinolinyl and quinoxalinyll moieties.

The steady state absorption spectra of **III.1–4** are shown in Figure III.11 and their maxima and molar extinction coefficients are listed in Table III-3. Complex **III.1** exhibits ligand-centered  $\pi\pi^*$  transitions in the ultraviolet (UV) region with maxima at 235 and 300 nm, as well as visible absorption bands at 436 and 566 nm that were previously assigned as  $\text{Rh}_2/\text{DTolF} \rightarrow np$  charge transfer in character.<sup>127</sup> Complex **III.2** exhibits similar features in the UV region to those of the related  $[\text{Rh}_2(\text{CH}_3\text{CO}_2)_2(\text{pynp})]^{2+}$  complex and the free pynp ligand in  $\text{CH}_2\text{Cl}_2$  (Figure III.10), and features intense charge transfer bands spanning the visible region with maxima at 442 and 690 nm.<sup>31</sup> The low energy absorption is not observed in  $[\text{Rh}_2(\text{CH}_3\text{CO}_2)_2(\text{pynp})]^{2+}$ , a difference that can be attributed to the change in energy of the HOMO upon introduction of an electron-donating formamidinate ligand as compared to acetate.<sup>127</sup>

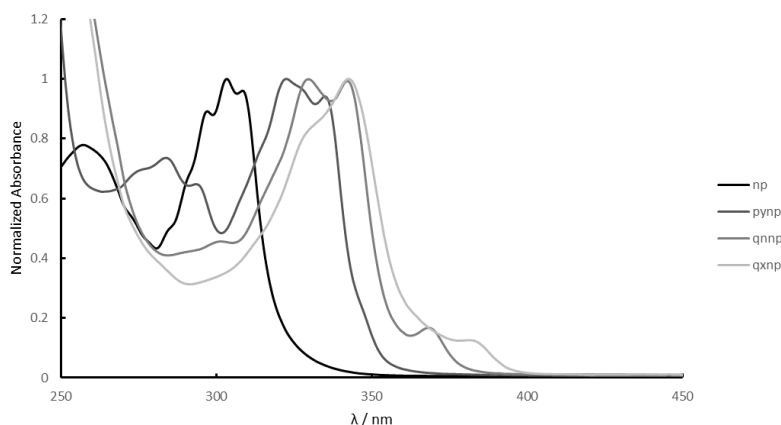


**Figure III.10** UV-vis spectra of free np, pynp, qnnp, and qxnp ligands in dichloromethane. Reprinted from ref. 74.



It should be noted that the formamidinate ligands also impact the metal orbitals that make up the HOMO.<sup>13, 139-142</sup> While archetypal  $d^7d^7$  metal paddlewheels, considering only d orbitals, have a  $(\sigma)^2(\pi)^4(\delta)^2(\delta^*)^2(\pi^*)^4(\sigma^*)^0$  electronic configuration,<sup>12, 143</sup> formamidinate ligands  $L(\pi^*)$  orbitals have the correct symmetry to interact with  $Rh_2(\delta^*)$  MO, thus raising its energy above the  $Rh_2(\pi^*)$  orbitals in some cases. This switch is observed in tetraformamidinate complexes of rhodium,<sup>13</sup> as well those of other metals,<sup>139-141</sup> where the formamidinate  $\pi^*$  orbitals of  $b_{1u}$  symmetry interact with the  $\delta^*$  orbitals of the same symmetry to impart mixed  $DTolF(\pi^*)/Rh_2(\delta^*)$  HOMO character.

Similarly, **III.3** and **III.4** exhibit maxima at 256 nm and 259 nm, respectively, consistent with the electronic absorption of the free ligands in  $CH_2Cl_2$  (Figure III.10). The charge transfer bands of **III.3** and **III.4** are bathochromically shifted relative to those of **III.1** and **III.2**, and dominate the visible to near-IR region with maxima at 583 and 704 nm for **III.3**, and 554 and 758 nm for **III.4**. This bathochromic shift is consistent with the greater electron accepting character of the naphthyridine-based ligands in **III.1–4** as demonstrated in the electrochemical reduction of these complexes, where the reduction of the naphthyridine-based ligands in **III.2–4** shift to increasingly positive potentials.

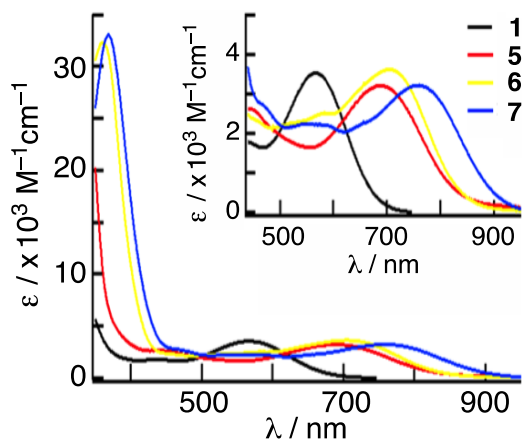


**Figure III.11** Electronic absorption spectra of **III.1–4** in  $\text{CH}_3\text{CN}$ . Inset: Expanded spectra in the visible range. Reprinted from ref. 74.

**Table III-3** Electronic Absorption Maxima with Molar Absorptivities in  $\text{CH}_3\text{CN}$ , Reduction Potentials, Singlet and Triplet Lifetimes for **III.1–4**. Reprinted from ref. 74.

Complex	$\lambda_{\text{abs}} / \text{nm}$ ( $\epsilon / \times 10^3 \text{ M}^{-1} \text{ cm}^{-1}$ )	$E_{1/2} / \text{V}^a$	$\tau_{\text{S}} / \text{ps}^b$	$\tau_{\text{T}} (\text{err}) / \text{ns}^b$
<b>III.1</b>	235 (55), 300 (25), 436 (1.8), 566(3.6)	+0.87, -0.94	14	0.64 (0.08)
<b>III.2</b>	251 (67), 347 (22), 442 (2.6), 692 (3.2)	+0.92, -0.70	13	12 (0.24)
<b>III.3</b>	256 (90.4), 366 (32), 583 (2.5), 704(3.4)	+0.99, -0.62	8	7.0 (0.26)
<b>III.4</b>	259 (83), 369 (32), 554 (2.2), 758(3.2)	+1.08, -0.43	8	7.2 (0.25)

<sup>a</sup>vs  $\text{Ag}/\text{AgCl}$  in 0.1 M  $\text{Bu}_4\text{NPF}_6/\text{CH}_3\text{CN}$ . <sup>b</sup>From transient absorption experiments in  $\text{CH}_3\text{CN}$ .

### *Electronic Structure Calculations*

In order to gain a deeper understanding of the orbital contributions and the origins of the electronic transitions, computational studies were performed on **III.1–4**. Geometrical parameters were taken from the crystal structures as starting points for the gas-phase optimizations (Figure III.12), omitting the counterions and the interstitial solvent molecules. For **III.1**, a second acetonitrile molecule was added to the unoccupied axial position due to the molecular symmetry observed in the solution  $^1\text{H}$  NMR spectrum of this complex. The results indicate that the HOMOs of **III.1–4** possess 31–37% orbital contribution from the  $\text{Rh}_2(\delta^*)$  orbital of the bimetallic core and a 63–70% from the formamidinate bridging ligand (Table III-4). The LUMOs of **III.1–4**, on the other hand, are mostly localized on the  $\pi$ -accepting ligand, with np-ligand contributions that range from 84% to 96%. In addition, even though the electron density is delocalized across the entirety of the  $\pi$ -accepting ligands, there is a higher contribution of the naphthyridine moiety to the LUMOs in complexes **III.2–4**, 77%, 61%, and 58%, respectively. Optimizations of the lowest triplet states for complexes **III.1**, **III.2**, and **III.4** (Table III-5) show a marked difference in electron density. The SOMO–1 for all complexes are calculated to contain very similar amounts of metal contributions, however, complexes **III.1** and **2** display a SOMOs with a 4–6% rhodium contribution while a 23% contribution is calculated for **III.4**. The higher electron density contribution of the Rh-based orbitals to the SOMO of **III.4** when compared to **III.2** may indicate greater mixing of the  $\text{Rh}_2(\sigma^*)$  in the triplet state of the former.

**Table III-4** Orbital contributions for **III.1–4** as predicted by TD-DFT calculations in acetonitrile (HOMO-5 through LUMO+6). Reprinted from ref. 74.

Orbital	III.1	III.2	III.3	III.4
HOMO-5	70% Rh, 26% DTolF	65% Rh, 32% DTolF	70% Rh, 21% DTolF, 10% qnp	81% Rh, 13% DTolF
HOMO-4	88% Rh, 8% DTolF	77% DTolF, 16% Rh, 8% pynp	77% DTolF, 13% qnp, 10% Rh	59% Rh, 25% DTolF, 16% qxnp
HOMO-3	68% DTolF, 28% Rh	79% Rh, 17% DTolF	49% Rh, 44% DTolF, 7% qnp	56% DTolF, 38% Rh
HOMO-2	47% Rh, 50% DTolF	76% Rh, 20% pynp	75% Rh, 16% qnp, 9% DTolF	53% DTolF, 40% Rh
HOMO-1	90% DTolF	92% DTolF	90% DTolF	90% DTolF
HOMO	59% DTolF, 37% Rh	57% DTolF, 37% Rh	63% DTolF, 31% Rh	63% DTolF, 31% Rh
LUMO	93% np	96% pynp	94% qnp	84% qxnp, 13% Rh
LUMO+1	85% np, 12% Rh	86% pynp, 12% Rh	84% qnp, 12% Rh	94% qxnp
LUMO+2	66% Rh, 15% MeCN, 10% DTolF	87% pynp, 10% Rh	60% Rh, 32% qnp	48% Rh, 46% qxnp
LUMO+3	76% np, 16% Rh, 8% DTolF	72% pynp, 24% Rh	92% qnp	95% qxnp
LUMO+4	70% np, 21% Rh	47% pynp, 46% Rh	76% qnp, 20% Rh	59% qxnp, 35% Rh
LUMO+5	43% np, 37% Rh, 20% DTolF	81% pynp, 13% Rh	87% qnp, 11% Rh	85% qxnp, 13% Rh
LUMO+6	45% Rh, 28% DTolF, 25% np	68% pynp, 26% Rh	91% qnp, 8% Rh	95% qxnp

**Table III-5** Calculated orbital contributions for the optimized lowest triplet state in the alpha manifold of acetonitrile of complexes **III.1**, **III.2** and **III.4** (LUMO through SOMO-1). Reprinted from ref. 74.

	<b>III.1</b>	<b>III.2</b>	<b>III.4</b>
LUMO	13% Rh, 82.5% np, 4.5% DTolF	12.5% Rh, 85% pynp, 2.5% DTolF	4% Rh, 94.5% qxnp, 1.5% DTolF
SOMO	6% Rh, 92 % np, 2% DTolF	4% Rh, 94% pynp, 1 % DTolF	23% Rh, 74% qxnp, 3% DTolF
SOMO-1	28% Rh, 4% np, 68% DTolF	29% Rh, 5% pynp, 66% DTolF	26% Rh, 5% qxnp, 69% DTolF

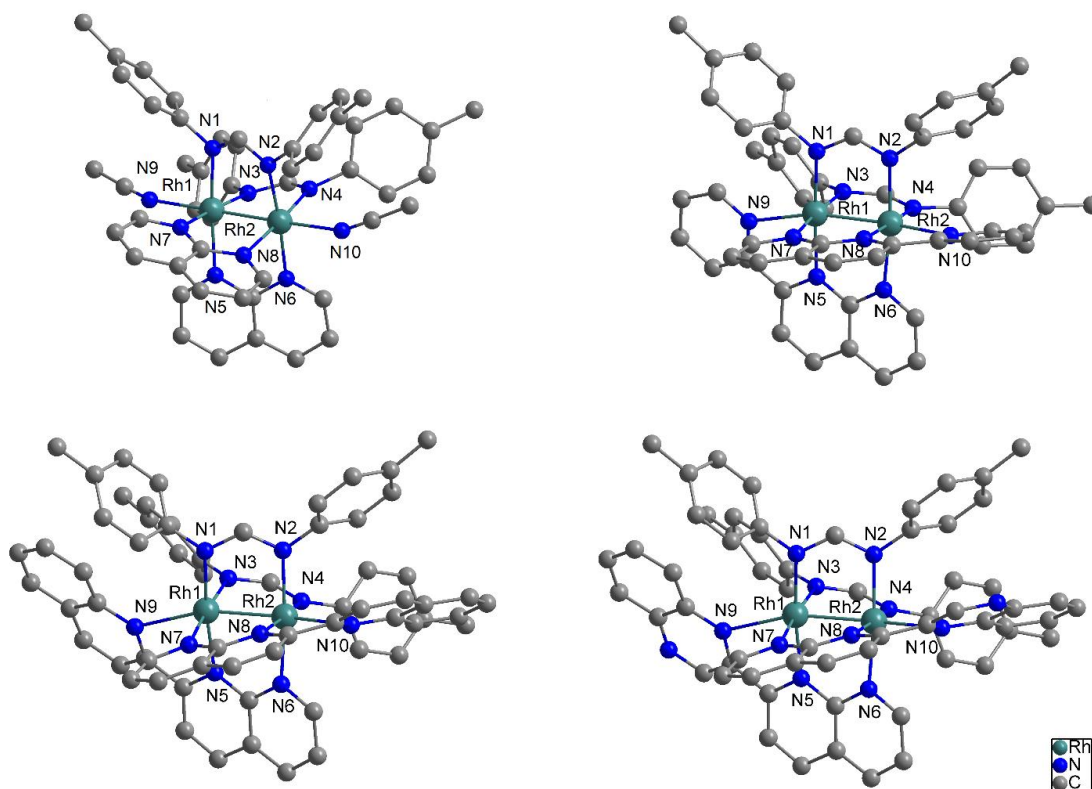


**Figure III.12** Gas-phase optimized structures of **III.1–4**. Taken from reference 74.

The lowest energy bands of **III.1–4** appear in the visible and near-IR regions (Figure III.11), and TD-DFT calculations confirm the <sup>1</sup>ML-LCT nature of these states resulting mainly from HOMO–LUMO transitions. Figure III.13 shows that as the conjugation of the ligand increases, there is a decrease in the energy of the LUMO. This observation is consistent with the decrease of the reduction potentials from **III.1** to **III.4** (Tables III-1 and 2). In addition, the shifts in the electrochemical reduction potentials among the complexes closely track with the differences in the calculated energies of the LUMOs (Table III-4). The oxidation potentials of **III.2–4** also follow a trend consistent with the electrochemical data in Tables III-1 and 2. However, the computed energies of the HOMOs reveal that **III.1** should be more difficult to oxidize than **III.2** and **III.3** by ~55 meV and ~21 meV, respectively, but this is not observed experimentally. This discrepancy is attributed to an overestimation of the calculated electron withdrawing character of the more conjugated ligands in **III.2–4**, since an overall overestimation of the energies of the HOMOs have been reported for other conjugated  $\pi$ -systems.<sup>144</sup>

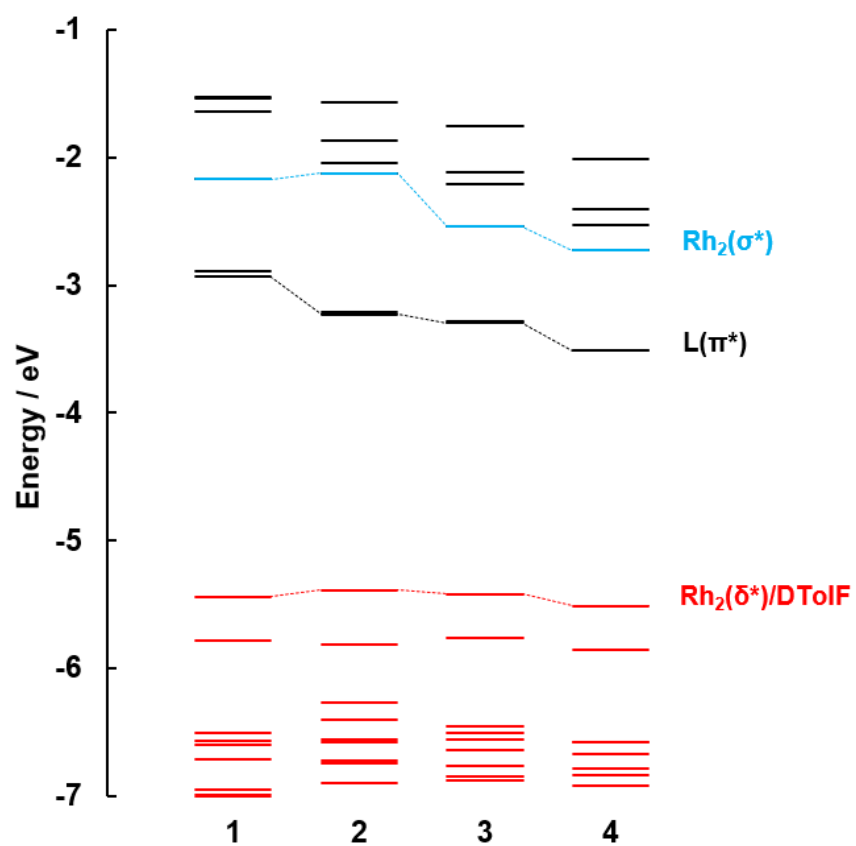


**Figure III.13.** Calculated MO diagrams for complexes **III.1–4**. Reprinted from ref. 74.

**Table III-6** Calculated energy differences in the LUMOs for complexes **III.1–4** with their corresponding measured differences in reduction potentials. Reprinted from ref. 74.

	$\Delta\text{LUMO} / \text{eV}$	$\Delta E / \text{V}$
<b>III.1 - 2</b>	-0.295784	-0.24
<b>III.2 - 3</b>	-0.070476	-0.08
<b>III.3 - 4</b>	-0.216872	-0.19

The  $Rh_2(\sigma^*)$  antibonding orbital lies at a higher energy in **III.2** as compared to **III.1**, which is attributed to the greater  $\sigma$ -donating character of the pyridyl moiety in **III.2** relative to the axial solvent  $CH_3CN$  ligands in **III.1**. In **III.2**, the antisymmetric linear combination of the axial pyridine lone pairs interacts with  $Rh_2(\sigma^*)$ , raising its energy. The  $Rh_2(\sigma^*)$  orbitals of **III.3** and **III.4** are lower in energy as compared to those of **III.2**; this is attributed to the greater  $\sigma$ -donation of pyridyl versus quinolinyl and quinoxalinyll groups. In addition, the steric strain in the axial coordination modes of **III.3** and **III.4** imposed by the larger ring system weakens the axial bonds, as apparent by the longer  $Rh-N_{ax}$  bond lengths (Table III-7).



**Table III-7** Comparison of gas phase optimized structures and X-ray crystal structures for **III.1–4**. Reprinted from ref. 74.

Compound <b>III.1</b>	Crystal Structure	Calculated Structure
Rh1-Rh2	2.44660(8)	2.47056
Rh1-N1	2.03106(6)	2.04445
Rh1-N3	2.01555(6)	2.03813
Rh1-N5	2.02764(6)	2.11483
Rh1-N7	2.02645(6)	2.10876
Rh2-N2	2.05106(5)	2.09023
Rh2-N4	2.04491(6)	2.08646
Rh2-N6	2.07419(5)	2.15247
Rh2-N8	2.08097(6)	2.16217
Rh2-N9	2.09941(7)	2.18870
N1-Rh1-Rh2-N2	11.2833(3)	12.42181
N7-Rh1-Rh2-N8	15.0955(3)	13.96806
Compound <b>III.2</b>	Crystal Structure	Calculated Structure
Rh1-Rh2	2.47714(14)	2.50901
Rh1-N1	2.07491(12)	2.07762
Rh1-N3	2.02233(11)	2.07375
Rh1-N5	2.03991(11)	2.09015
Rh1-N7	2.07180(12)	2.15424
Rh1-N9	2.25037(11)	2.30958
Rh2-N2	2.03415(11)	2.07373
Rh2-N4	2.07009(10)	2.07761
Rh2-N6	2.06664(11)	2.15427
Rh2-N8	2.04907(10)	2.09013
Rh2-N10	2.24774(10)	2.30979
N1-Rh1-Rh2-N2	-11.8927(7)	-6.33193
N7-Rh1-Rh2-N8	-12.1834(7)	-6.25325
Compound <b>III.3</b>	Crystal Structure	Calculated Structure
Rh1-Rh1	2.4288(15)	2.49597
Rh1-N1	2.0475(11)	2.10245
Rh1-N3	1.9183(10)	2.11392
Rh1-N5	2.2307(16)	2.51638
Rh11-N2	2.0922(10)	2.06650
Rh11-N4	1.9701(11)	2.11321
N1-Rh1-Rh1A-N2	-23.5925(6)	-15.78397
N3-Rh1-Rh1A-N4	-21.165(3)	-14.53889
Compound <b>III.4</b>	Crystal Structure	Calculated Structure
Rh1-Rh2	2.44985(11)	2.49457
Rh1-N1	2.08752(10)	2.09595
Rh1-N3	2.04178(12)	2.06534
Rh1-N5	2.0311(1)	2.11674
Rh1-N7	2.04022(12)	2.11802
Rh1-N9	2.34816(11)	2.51497
Rh2-N2	2.0380(1)	2.06531
Rh2-N4	2.07904(12)	2.09588
Rh2-N6	2.03386(10)	2.11800
Rh2-N8	2.03276(12)	2.11680
Rh2-N10	2.37833(11)	2.51557
N1-Rh1-Rh2-N2	-19.9041(13)	-15.05694
N7-Rh1-Rh2-N8	-18.6183(12)	-13.82327

### Time-Resolved Spectroscopy

Femtosecond transient absorption (fsTA) spectroscopy was performed on **III.1-4** to help elucidate the identity and dynamics of the singlet and triplet excited states. It was previously reported by us that excitation into the lowest energy absorption band of **III.1** results in the population of the Rh<sub>2</sub>/DTolF→np <sup>1</sup>ML-LCT excited state which decays with  $\tau_S = 13$  ps to the corresponding <sup>3</sup>ML-LCT triplet state, and the latter regenerates the ground state with  $\tau_T = 450$  ps in DMSO ( $\lambda_{ex} = 600$  nm).<sup>63</sup> In the present work, we repeated the fsTA spectroscopy of **1** in CH<sub>3</sub>CN and observed similar spectral features and lifetimes,  $\tau_S = 14$  ps and  $\tau_T = 640$  ps (Figure III.14). The shorter lifetime of the <sup>3</sup>ML-LCT state of **1** in DMSO as compared to CH<sub>3</sub>CN is consistent with the bathochromic shift of **1** in the more polar DMSO solvent as compared to CH<sub>3</sub>CN ( $\Delta E = 337$  cm<sup>-1</sup>) as predicted by the Energy Gap Law.<sup>125</sup> Both states were previously assigned as Rh<sub>2</sub>/DTolF→np charge transfer in character.

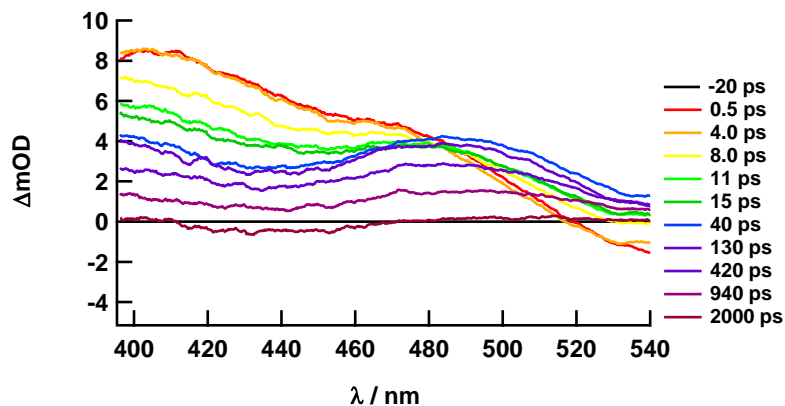


**Figure III.14** fsTA of complex **III.1** in CH<sub>3</sub>CN ( $\lambda_{ex} = 600$  nm; 2.5  $\mu$ J). Reprinted from ref. 74.

The fsTA spectra of **III.2** collected following 720 nm excitation (irf = 85 fs) are shown in Figure III.15a and exhibit a broad excited state absorption that extends from 420 to 620 nm with a pronounced shoulder at 470 nm, similar to the <sup>1</sup>ML-LCT and <sup>3</sup>ML-LCT absorption spectra reported for **III.1**.<sup>63</sup> The decay of the peak at 470 nm can be fitted to a monoexponential function with  $\tau_s = 13$  ps and is assigned to the singlet state of the complex. The spectral features of this state are consistent with the absorption spectrum recorded for electrochemically oxidized **III.2** which exhibits a peak at 467 nm, superimposed with the strong absorption of reduced **III.2**, with absorption at  $\lambda \leq 450$  nm (Figure III.15b). The 13 ps <sup>1</sup>ML-LCT excited state lifetime of **III.2** is consistent with singlet excited states of other Rh<sub>2</sub>(II,II) half lantern complexes and related Rh<sub>2</sub>(II,II) naphthyridine complexes with intersystem crossing rates in the 8 to 100 ps range.<sup>63, 126</sup> Similar results were also reported for other paddlewheel complexes, including those of dirhodium(I,I) isocyanide, diplatinum(II,II) pyrophosphito, ditungsten(II,II), and dimolybdenum(II,II).<sup>145-148</sup>

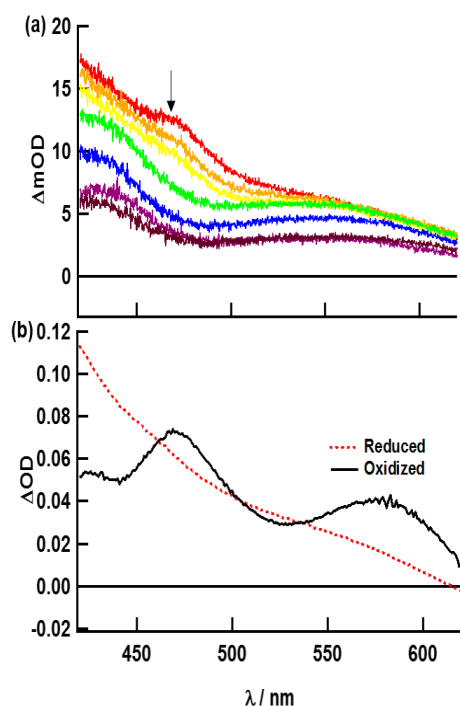


**Figure III.15.** (a) fsTA of **III.2** at 0.3, 2, 4, 20, 80, 900, and 2400 ps after laser pulse ( $\lambda_{\text{ex}} = 720 \text{ nm}$ ,  $2.5 \mu\text{J}$ ) in  $\text{CH}_3\text{CN}$  and (b) difference spectra of electrochemically reduced ( $E_{\text{app}} = -800 \text{ mV}$  vs  $\text{Ag}/\text{AgCl}$ ) and oxidized ( $+1150 \text{ mV}$  vs  $\text{Ag}/\text{AgCl}$ ) complexes in  $0.1 \text{ M}$   $\text{Bu}_4\text{PF}_6 \text{ CH}_3\text{CN}$ . Reprinted from ref. 74.

Nanosecond transient absorption experiments were undertaken and revealed the lifetime of the  $^3\text{ML-LCT}$  excited state of **III.2** to be  $\tau_T = 12 \text{ ns}$  ( $\lambda_{\text{ex}} = 610 \text{ nm}$ ,  $\text{irf} = 5.5 \text{ ns}$ , Figure III.15). The longer  $^3\text{ML-LCT}$  lifetime of **III.2** relative to that of **III.1** is consistent with previous work that shows that blocking the axial sites with the carboxylate substituents in  $[\text{Rh}_2\text{DTolF}_2(\text{npCOO})]$  ( $\text{npCOO}^- = 1,8\text{-naphthyridine-2-carboxylate}$ ) extends the  $^3\text{ML-LCT}$  lifetime.<sup>63</sup> It is important to note that at delay times longer than 20 ps, the 470 nm shoulder of **III.2** disappears (Figure III.15a), resulting in broad peaks at 430 and 570 nm that persist beyond the 2 ns duration of the experiment and are observed

in the  $^3\text{ML-LCT}$  nanosecond TA spectra (Figure III.16). The loss of the  $^1\text{ML-LCT}$  shoulder at 470 nm in **III.2** upon intersystem crossing may indicate a change in the portion of the complex that is oxidized in the singlet and triplet states. It was previously shown that there is greater metal character in the  $^3\text{ML-LCT}$  excited state of  $[\text{Rh}_2(\text{DTolF})_2(\text{npCOO})]$  than in the corresponding singlet state. In the latter the hole is more localized on the bridging DTolF ligand, whereas the positive charge appears more localized on the metals in the corresponding triplet state.<sup>63</sup> Based on a comparison to these prior results, the spectral changes observed in the fsTA spectra of **III.2** at long delay times may be attributed to changes in the localization of the hole from a  $\text{Rh}_2/\text{DTolF}$  molecular orbital to one with more metal-centered  $\text{Rh}_2^{\text{II/III}}$  mixed-valence character in the triplet state as compared to the singlet state.

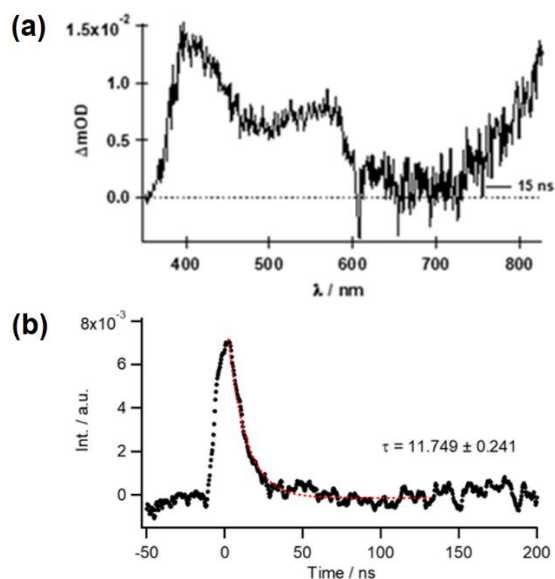


**Figure III.16** nsTA of complex **III.2** in CH<sub>3</sub>CN (a) 15 ns (10 ns integration time) after laser pulse ( $\lambda_{\text{ex}} = 610$  nm; 5 mJ; irf = 5.5 ns) where scatter is seen at 610 nm and (b) kinetic trace taken at 550 nm. Reprinted from ref. 74.

The fsTA spectra of **III.4** are shown in Figure III.17a and exhibit a positive absorption at 435 nm attributed to the <sup>1</sup>ML-LCT excited state that decays monoexponentially with  $\tau_s = 8$  ps ( $\lambda_{\text{ex}} = 720$  nm, irf = 85 fs). The positive absorption features compare well to those observed following the electrochemical one-electron reduction of the complex (Figure III.17b). There is little contribution from the one-electron oxidized complex in the fsTA because of the relatively broad, featureless absorption profile of this species in the spectral window of interest (Figure III.17). This result, together with the similarities of the fsTA of **III.4** with those of **III.1** and **III.2**, is consistent with a charge transfer from the mixed Rh<sub>2</sub>/DTolF HOMO to the qxnp( $\pi^*$ ) LUMO in the <sup>1</sup>ML-LCT state. Intersystem crossing leads to a longer-lived <sup>3</sup>ML-LCT state with very similar spectral features and  $\tau_T \sim 7.2$  ns as determined from nanosecond transient

absorption spectroscopy ( $\text{irf} = 5.5 \text{ ns}$ ). The shorter lifetimes of the  $^1\text{ML-LCT}$  and  $^3\text{ML-LCT}$  states of **III.4** as compared to the corresponding states in **III.2** are attributed to both the greater accessibility of deactivating  $^3\text{MC}$  (metal-centered) states. This is best illustrated in the triplet calculations where the SOMO of **III.4** has significantly more metal character than **III.2**, indicating greater mixing in the excited state (Table III-5). Furthermore, this is also attributable to the lower energy transitions of **III.4** as in the former as expected from the Energy Gap Law.<sup>125</sup> Due to their structural similarities, the fsTA spectra and spectroelectrochemistry of **III.3** parallel those of **III.4**, with  $^1\text{ML-LCT}$  and  $^3\text{ML-LCT}$  states with lifetimes of 8 ps and  $\sim 7.0 \text{ ns}$ , respectively (Figures III.18 and 19).

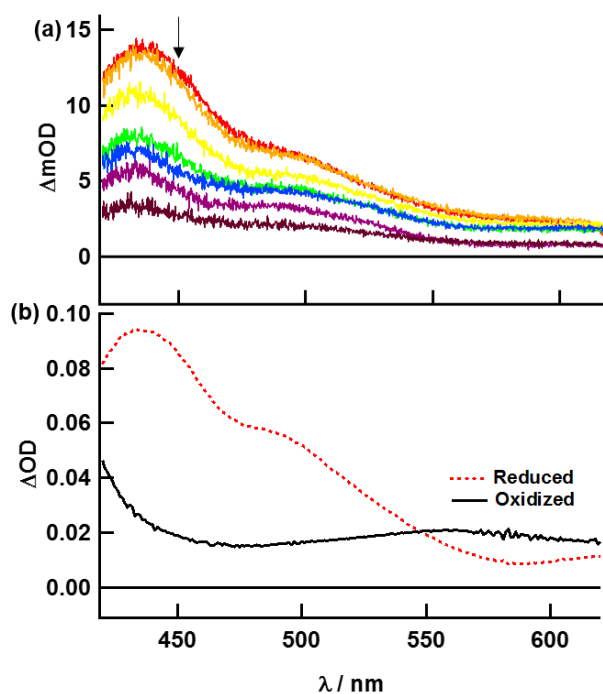


**Figure III.17** (a) fsTA of **III.4** at 0.3, 0.7, 4, 10, 40, 70, and 2000 ps after laser pulse ( $\lambda_{\text{ex}} = 720 \text{ nm}$ ,  $2.5 \mu\text{J}$ ) in  $\text{CH}_3\text{CN}$  and (b) difference spectra of electrochemically reduced ( $E_{\text{app}} = -550 \text{ mV vs Ag/AgCl}$ ) and oxidized ( $+1300 \text{ mV vs Ag/AgCl}$ ) complexes in  $0.1 \text{ M Bu}_4\text{NPF}_6 \text{ CH}_3\text{CN}$ . Reprinted from ref. 74.

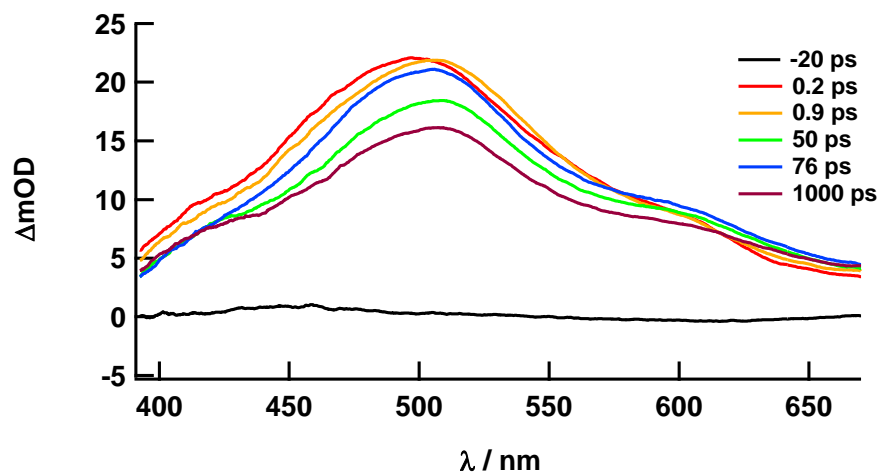


**Figure III.18** fsTA of complex **III.3** in  $\text{CH}_3\text{CN}$  ( $\lambda_{\text{ex}} = 720 \text{ nm}$ ;  $2.5 \mu\text{J}$ ). Reprinted from ref. 74.

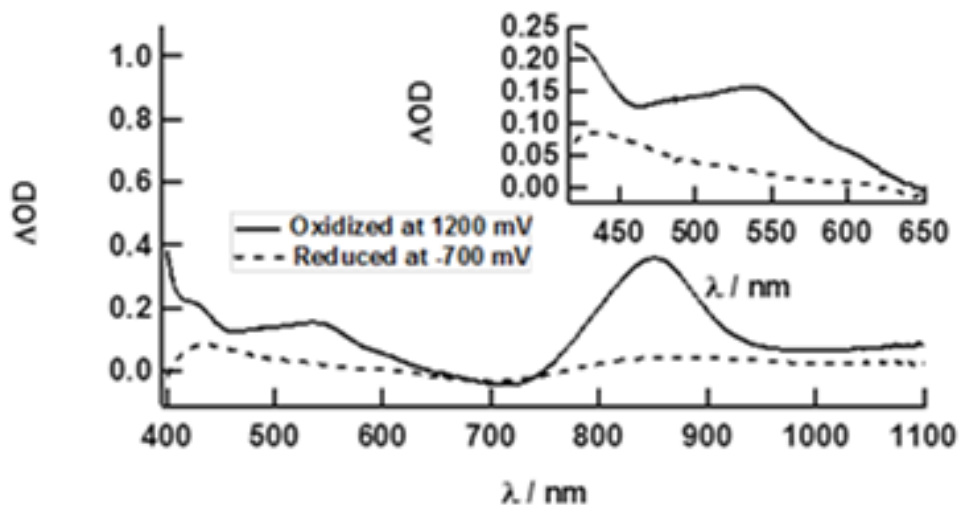


**Figure 2. III.19** Spectroelectrochemistry of complex **III.3** in  $0.1 \text{ Bu}_4\text{NPF}_6 \text{ CH}_3\text{CN}$  when oxidized at  $1200 \text{ mV}$  and reduced at  $-700 \text{ mV}$ . Reprinted from ref. 74.



### *Excited State Charge Transfer*

In order to evaluate the usefulness of the relatively long-lived  $^3\text{ML-LCT}$  states of **III.2–4** as potential light absorbers in solar energy applications, their photoinduced charge transfer reactivity was measured using the reversible electron donor *p*-phenylene diamine ( $E_{1/2} = +0.28$  V vs Ag/AgCl). Upon excitation with low energy light, complexes **III.2–4** display absorption difference spectra consistent with the formation of the *p*-phenylene diamine radical cation, with an absorption maximum at 460 nm (Figures III. 22–24),<sup>149</sup> superimposed upon the spectra of the corresponding reduced complex, observed within the 5.5 ns instrument response ( $k_{\text{ET}} < 2 \times 10^{-8}$ ). The charge separation persists on the order of ~40–60  $\mu\text{s}$  for **III.2–4** ( $k_{\text{BET}} \sim 2 \times 10^{-4}$ ); this behavior is presented for **III.2** in Figure III.24 ( $\lambda_{\text{ex}} = 600$  nm, irf = 5.5 ns). Quenching studies help ascertain that the  $E_{00}$  of these molecules is at the onset of triplet quenching at approximately 1.3 eV, using this and the electrochemical data, the excited state reduction potential is estimated to be +0.5 V vs Ag/AgCl (Table III-8 and Figure III.20), giving ~200 mV of driving force for oxidation of *p*-type NiO. In order to determine that this excited state process is in fact occurring from the lowest triplet state, femtosecond transient absorption was performed in the presence of the *p*-phenylenediamine, where no quenching of the singlet state lifetime or appearance of oxidized compound was observed at early times (Figure III.21). This finding builds on previous studies on  $\text{Rh}_2(\text{DTolF})_2(\text{npCOO})$ ,<sup>63</sup> which lacks the driving force for excited state oxidation of *p*-phenylenediamine.

**Table III-8** Quenching rates of organic quenchers via Stern-Volmer quenching by complex **III.2**. Reprinted from ref. 74.

anthracene	1.83	$7.2 \times 10^9$
tetracene	1.27	$8.7 \times 10^8$
rubrene	1.15	$2.9 \times 10^8$
$\beta$ -carotene	0.78	<i>a</i>

<sup>a</sup>no quenching observed

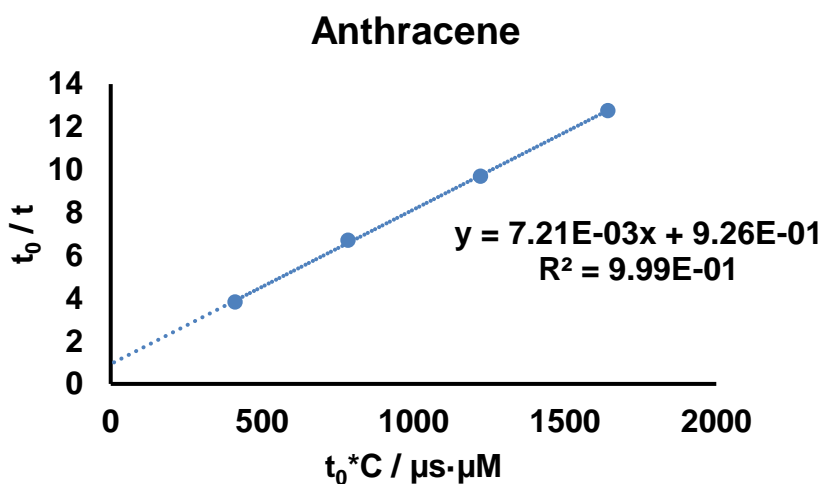


**Figure III.20** Example graph of Stern-Volmer quenching of anthracene monitored at 420 nm upon addition of **III.2** in  $\text{CH}_3\text{CN}$  of anthracene ( $\lambda_{\text{ex}} = 355 \text{ nm}$ ). Reprinted from ref. 74.

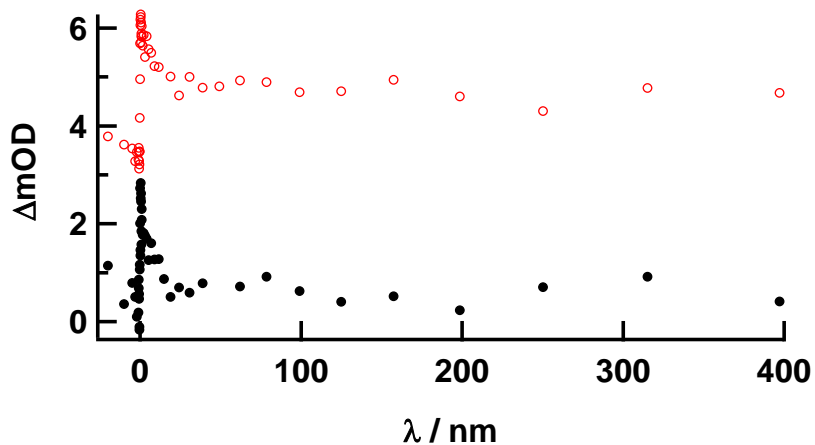


**Figure III.21** Complex **III.2** in  $\text{CH}_3\text{CN}$  ( $85 \mu\text{M}$ ) in the presence (red) and absence (black) of  $10 \text{ mM}$  *p*-phenylenediamine femtosecond transient absorption after excitation with  $700 \text{ nm}$  light ( $2.5 \mu\text{J}$ ), trace taken at  $465 \text{ nm}$ . Reprinted from ref. 74.

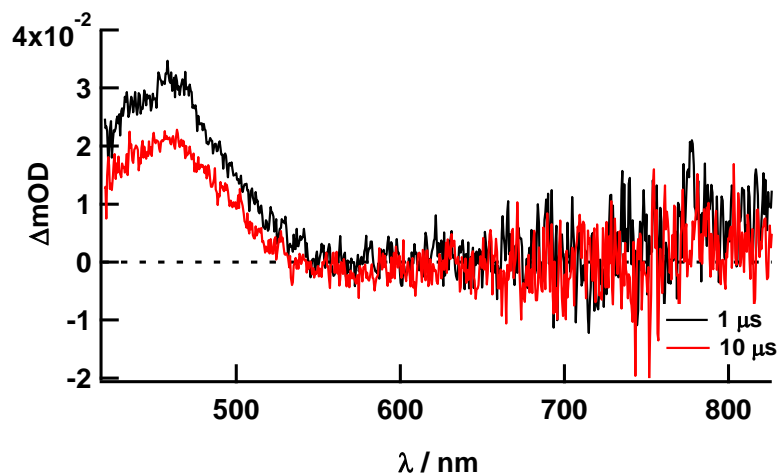


**Figure III.22** Complex **III.3** in  $\text{CH}_3\text{CN}$  ( $25 \mu\text{M}$ ) in the presence of  $10 \text{ mM}$  *p*-phenylenediamine  $1$  and  $10 \mu\text{s}$  ( $100 \text{ ns}$  gate) after laser pulse ( $\lambda_{\text{ex}} = 620 \text{ nm}$ ;  $5 \text{ mJ}$ ). Reprinted from ref. 74.

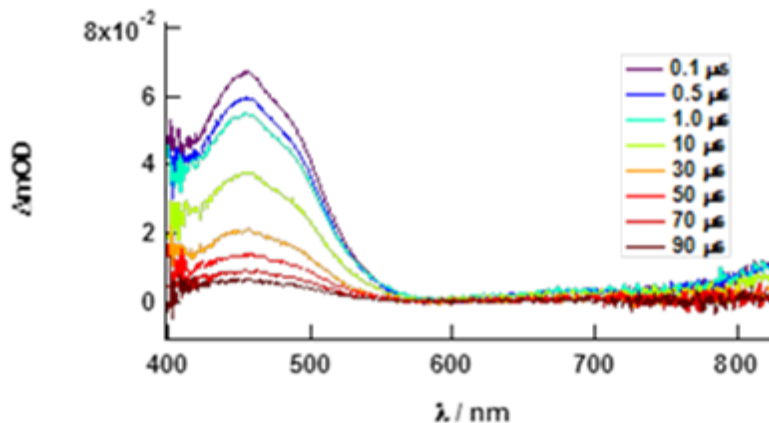


**Figure III.23** Complex **III.4** in  $\text{CH}_3\text{CN}$  ( $25 \mu\text{M}$ ) in the presence of  $15 \text{ mM}$  p-phenylenediamine at various times after the laser pulse ( $\lambda_{\text{ex}} = 620 \text{ nm}$ ;  $5 \text{ mJ}$ ). Reprinted from ref. 74.

The difference in reactivity of **III.2–4** as compared to  $\text{Rh}_2(\text{DTolF})_2(\text{npCOO})_2$  towards oxidation of substrates can be attributed to the more easily reduced pynp, qxnp, and qnnp bridging ligands relative to the anionic axial donor in the ligand  $\text{npCOO}^-$  ( $E_{1/2} = -1.07 \text{ V vs Ag/AgCl}$ ). This finding demonstrates how minor synthetic modifications can have a profound effect on the excited state reactivities of this class of molecules. Furthermore, given the valence band edge of NiO ( $E_{\text{VB}} = +0.2\text{--}+0.3 \text{ V vs Ag/AgCl}$ ),<sup>150</sup> **III.2–4** possess sufficient driving force for hole injection into this p-type semiconductor from both the  $^1\text{ML-LCT}$  and  $^3\text{ML-LCT}$  states. The potential hole injection from the latter is important because it lies at a lower energy than the singlet states typically involved in hole injection in NiO films.<sup>48</sup> Currently, synthetic modifications to anchor these molecules onto a p-type semiconductor surface are underway.

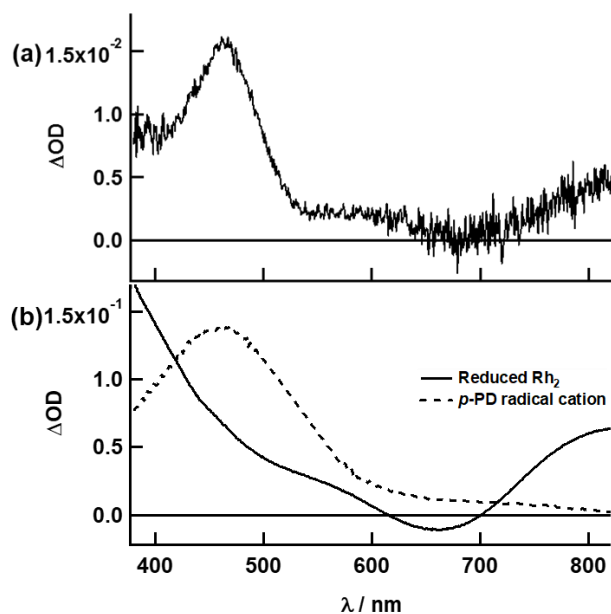


**Figure III.24** Transient absorption spectrum of **III.2** in  $\text{CH}_3\text{CN}$  ( $23 \mu\text{M}$ ) in the presence of *p*-phenylenediamine (1:100) collected 100 ns after a 600 nm pulse (5 mJ) and (b) electrochemically reduced **2** in 0.1 M  $\text{Bu}_4\text{NPF}_6$   $\text{CH}_3\text{CN}$  (solid line) and *p*-phenylenediamine radical cation generated in a 0.1 M  $\text{NaN}_3$  aqueous solution (dashed line). Reprinted from ref. 74.

In addition to the ability of the  $^3\text{ML-LCT}$  states of **III.2–4** to serve as oxidizing agents in the excited state, complex **III.2** also shows potential to reduce methyl viologen in the excited state, where the transient absorption spectra of  $23 \mu\text{M}$  **III.2** in  $\text{CH}_3\text{CN}:\text{H}_2\text{O}$  (1:1 v:v) in the presence of 10 mM  $\text{MV}^{2+}$ , with  $E_{1/2}(\text{MV}^{2+/+}) \sim -0.4 \text{ V vs Ag/AgCl}$  in  $\text{CH}_3\text{CN}$ ,<sup>151</sup> recorded 10  $\mu\text{s}$  after the 620 nm excitation (irf = 5 ns), are consistent with the formation of  $\text{MV}^+$ , with its characteristic absorption features at 395 nm and 605 nm (Figure III.25). This is very close to the estimated excited state oxidation potential of **III.2**, which is estimated to be approximately  $-0.4 \text{ V vs Ag/AgCl}$  (0.1 M  $\text{TBAPF}_6$ ). In contrast,

excited state electron transfer to  $MV^{2+}$  was not observed upon excitation of **III.3** and **III.4**, attributed to the more positive oxidation potentials and shorter  $^3ML-LCT$  lifetimes of these complexes relative to **III.2** (Tables III-1 and 2). Moreover, the absorption profiles of **III.3** and **III.4** are bathochromically shifted as compared to **III.2**, thereby lowering the energy of the  $^3ML-LCT$  state, which taken together with the more positive oxidation potentials, result in less reducing excited states in **III.3** and **III.4**. Extension of this finding to semiconductor applications with complex **III.2** is expected to lead to injection of electrons into the n-type semiconductor  $TiO_2$  given the similarity of the reduction potential of  $MV^{2+}$  and the conduction band of  $TiO_2$  ( $E_{CB} = -0.4$  V vs Ag/AgCl).<sup>152</sup>

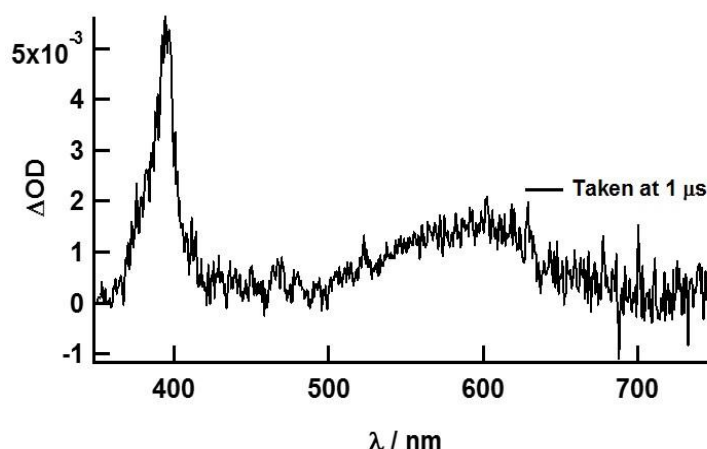


**Figure III.25** Complex **III.2** in 1:1  $CH_3CN:H_2O$  ( $23 \mu M$ ) in the presence of  $10$  mM  $MV^{2+}$  ( $\lambda_{ex} = 620$  nm;  $5$  mJ). Reprinted from ref. 74.

## Conclusions

A series of four dirhodium formamidinate paddlewheel complexes with electron accepting naphthyridine-based ligands were synthesized and their structural, electronic, and

photophysical properties investigated. Complexes **III.2–4** absorb strongly from the ultraviolet and visible spectral regions into the near-IR and were designed to feature axial blocking ligands with increasingly more conjugated  $\pi$ -systems composed of pyridyl, quinoliny, and quinoxaliny moieties, respectively. Complexes **III.2–4** feature relatively long-lived  $^1\text{ML-LCT}$  and  $^3\text{ML-LCT}$  states accessible with low energy light. Transient absorption spectroscopy studies show that the lifetimes of the  $^3\text{ML-LCT}$  states are drastically increased by incorporation of axial blocking ligands with respect to the 1,8-naphthyridine containing complex **III.1**, which has a short lifetime attributed to solvent assisted deactivation pathways. It was also found that the low-lying  $^3\text{ML-LCT}$  state of **III.2** is capable of transferring an electron to  $\text{MV}^{2+}$  and to also oxidize *p*-phenylenediamine when irradiated with low energy light, in contrast to the previously reported  $\text{npCOO}^-$  dirhodium complexes which did not possess sufficient excited state energy to oxidize substrates. Complexes **III.3** and **III.4** can also perform electron transfer reactions to oxidize *p*-phenylene diamine, but lack the driving force to partake in electron-transfer to  $\text{MV}^{2+}$  upon irradiation. The photophysical and excited state redox properties of the new complexes presented herein illustrate the advantages of this rigid bimetallic architecture for tuning their ability to undergo photoinduced electron and hole transfer. Given a judicious choice of ligands, these complexes provide a new platform for solar energy conversion applications that require charge injection into n- and p-type semiconductors accessible with photons from the UV to the near-IR.

CHAPTER IV

SYNTHETIC STRATEGIES FOR TRAPPING THE ELUSIVE *TRANS*-  
DIRHODIUM(II,II) FORMAMIDINATE ISOMER AND THE EFFECTS  
OF ISOMERISM ON THE PHOTOPHYSICAL PROPERTIES

**Introduction**

The increasing demand for energy requires more efficient carbon-free renewable energy sources.<sup>45</sup> Solar energy conversion has proven to be an environmentally friendly method for producing electricity and clean fuels, such as hydrogen.<sup>153-157</sup> The use of dye-sensitized solar cells (DSSCs) is attractive due to the relatively low cost of fabrication, high tunability, flexibility, and durability.<sup>58, 95, 158-160</sup> While DSSCs have theoretical efficiencies of 35% and 43% in the case of n-type and tandem (n-type and p-type) sensitized solar cells,<sup>103, 114</sup> respectively, the highest efficiency measured thus far in commercial devices is ~11.9%.<sup>161, 162</sup> Ideally, DSSC photosensitizers should exhibit a panchromatic absorption profile in order to efficiently harvest the full solar spectrum, as well as excited state properties that support hole injection even with low energy light excitation.

There are numerous limitations to the design of efficient sensitizers. The current record is held by the SM315 porphyrin coupled to a Co(II/III) redox shuttle.<sup>60</sup> This system exhibits a 13% photocurrent efficiency (PCE) and displays panchromatic absorption, but the lowest energy electronic transition has a maximum at 668 nm and does not absorb beyond 800 nm. Other types of phthalocyanines and porphyrins have very large absorption



coefficients in the near-IR region but aggregate on the surface of the semiconductor which decreases their overall efficiency.<sup>112</sup> The gold standard for n-type sensitized DSSCs, the N3 Ru(II) dye, has an efficiency of 10-12%, in part due to its inability to absorb light beyond 600 nm.<sup>59, 163</sup> Other promising dyes are BODIPY derivatives,<sup>120, 121, 164</sup> but their very narrow absorption profiles preclude absorption of the full solar spectrum. Given these shortcomings, the design of new panchromatic photosensitizers with good solubility and chemical stability that utilize both high and low energy light to undergo charge transfer reactions is critical for the development of improved DSSCs.

Recently, our groups reported a series of dirhodium(II,II) complexes that feature electron donating formamidinate bridging ligands and  $\pi$ -accepting bridging ligands with substituents designed to block the axial coordination sites.<sup>63, 74</sup> These complexes are capable of participating in electron transfer reactions upon irradiation with low-energy light, including the oxidation of p-phenylenediamine and reduction of electron acceptors, rendering them suitable for both n-type and p-type semiconductor applications. As the coordination sphere is chemically modified, the excited state redox potential of these partial paddlewheel Rh<sub>2</sub>(II,II) complexes can be tuned such that they are capable of undergoing electron transfer to acceptors and n-type semiconductors.<sup>63, 74</sup> In this vein, it was discovered that axially-blocked complexes exhibit significantly longer <sup>3</sup>ML-LCT lifetimes (7 – 25 ns) compared to those with solvent accessible axial sites, such as cis-[Rh<sub>2</sub>( $\mu$ -DTolF)<sub>2</sub>( $\mu$ -np)<sub>2</sub>][BF<sub>4</sub>]<sub>2</sub> (DTolF = N,N'-di(p-tolyl)formamidinate; np = 1,8-naphthyridine), with a <sup>3</sup>ML-LCT lifetime of ~ 0.5 ns.<sup>63, 74</sup> The longer lifetimes are necessary for bimolecular electron transfer reactions, but are not required for charge

injection into semiconductors, which has been shown to occur within fs to ps.<sup>92</sup> In addition, this class of Rh<sub>2</sub>(II,II) complexes was shown to photosensitize the production of H<sub>2</sub> with  $\lambda_{\text{irr}} = 655 \text{ nm}$ ,<sup>165</sup> as well as to inject electrons into TiO<sub>2</sub> from its <sup>1</sup>ML-LCT state with 600 nm light,<sup>166</sup> both of which represent improvements over the N3 dye.

Bis-substituted *cis*- and *trans*-dirhodium(II,II) complexes have been used extensively as catalysts for organic transformations,<sup>167</sup> but the excited state properties and photochemistry of these complexes were not investigated. Our groups have studied the excited states and reactivity,<sup>63, 126, 168</sup> photochemistry,<sup>169</sup> and photoinduced biological activity of *cis*-dirhodium(II,II) complexes,<sup>32, 33, 35, 78, 170, 171</sup> but the photochemistry of the *trans* isomers remains unexplored. The possibility of obtaining the *trans* isomers opens up new opportunities for the exploration of novel supramolecular assemblies with potentially interesting photophysical properties. In this vein, we note that *cis* isomers of dirhodium(II,II) complexes with amidines or triphenylphosphine bridging ligands are interesting but of limited use. These complexes have been used as corner motifs to prepare square and triangular-shaped supramolecular assemblies since the angle between bridging ligands is  $\sim 90^\circ$ .<sup>172, 173</sup> Given that the *trans* isomers display a  $\sim 180^\circ$  between bridging ligands, they are much more versatile as building blocks for a wide variety of shapes including ladder structures and numerous polygonal assemblies, including triangles, rectangles, and hexagons, among others.<sup>174, 175</sup>

The synthesis of heteroleptic dirhodium(II,II) complexes is governed by the kinetic *trans* effect which explains why the vast majority of partial paddlewheel complexes in the literature are bis-substituted with a *cis* configuration.<sup>12</sup> The substitution chemistry of

dirhodium complexes follows the same criteria as the archetypal square planar complexes *cis*-Pt(NH<sub>3</sub>)Cl<sub>2</sub> and *trans*-Pt(NH<sub>3</sub>)Cl<sub>2</sub>. The basicity of a ligand is proportional to the *trans* effect exerted on the ligand opposite to it, which determines the geometric arrangement of the final product. For example, given that CH<sub>3</sub>CO<sub>2</sub><sup>-</sup> is more basic than CF<sub>3</sub>CO<sub>2</sub><sup>-</sup>, the complex *cis*-Rh<sub>2</sub>(CH<sub>3</sub>CO<sub>2</sub>)<sub>2</sub>(CF<sub>3</sub>CO<sub>2</sub>)<sub>2</sub> can be obtained from Rh<sub>2</sub>(CH<sub>3</sub>CO<sub>2</sub>)<sub>4</sub> in the presence of two equivalents of CF<sub>3</sub>CO<sub>2</sub>H, while the *trans* analogue can be obtained from the reaction of Rh<sub>2</sub>(CF<sub>3</sub>CO<sub>2</sub>)<sub>4</sub> and CH<sub>3</sub>CO<sub>2</sub>H.<sup>176</sup> Of particular relevance to the current study is the fact that formamidinate ligands have a very strong *trans* effect due to their markedly strong basicity with respect to other bridging ligands such as amidinates and acetates. As a consequence, there are no examples of *trans* formamidinate-containing dirhodium complexes reported in the literature to this date. Other examples of note are the rare *cis/trans* isomeric pairs of [Rh<sub>2</sub>(CH<sub>3</sub>CO<sub>2</sub>)<sub>2</sub>(PhTCB)<sub>2</sub>] (where PhTCB = phenylthiocarbamoyl benzoate) which were isolated as isomeric mixtures and tested as catalysts for cyclopropanation of alkene substrates.<sup>177</sup> This chemistry, however, did not lead to pure compounds, which prevents correlation between geometry and properties.

Herein we report a new synthetic methodology for the preparation of *trans*-Rh<sub>2</sub>(II,II) isomers containing two DTolF formamidinate ligands, namely, *cis*-[Rh<sub>2</sub>(μ-DTolF)<sub>2</sub>(μ-np)(MeCN)<sub>4</sub>][BF<sub>4</sub>]<sub>2</sub> (**IV.1**, where np = 1,8-naphthyridine), *cis/trans*-[Rh<sub>2</sub>(μ-DTolF)<sub>2</sub>(μ-qxnp)(MeCN)<sub>3</sub>][BF<sub>4</sub>]<sub>2</sub> (**IV.2/3** respectively, where qxnp = 2-(1,8-naphthyridin-2-yl)quinoxaline), and *trans*-[Rh<sub>2</sub>(μ-DTolF)<sub>2</sub>(μ-qxnp)<sub>2</sub>][BF<sub>4</sub>]<sub>2</sub> (**IV.4**) (Scheme 1). The photophysical and electronic properties were measured and compared to those of the previously reported complex **IV.5**, *cis*-[Rh<sub>2</sub>(μ-DTolF)<sub>2</sub>(μ-qxnp)<sub>2</sub>][BF<sub>4</sub>]<sub>2</sub>.

The new compounds display panchromatic absorption spectra from the UV to the near-IR region. The synthetic approach used in these studies represents a new strategy for the preparation of rare dirhodium trans derivatives that constitute a new family of bimetallic architectures. These complexes have potentially useful photochemical properties for applications in solar energy conversion and photochemotherapy, as well as for the design and synthesis of new supramolecular assemblies with interesting photophysical properties.

## Experimental Section

### *Materials*

The starting material  $[\text{RhCl}(\text{COD})]_2$  (COD = 1,5-cyclooctadiene) was purchased from Pressure Chemicals and used without further purification to prepare the partially solvated compound  $\text{cis-}[\text{Rh}_2(\mu\text{-DTolF})_2(\text{CH}_3\text{CN})_6][\text{BF}_4]_2$  following a reported procedure.<sup>34</sup> The 1,8-naphthyridine (np) ligand was purchased from Oakwood Chemicals and used as received. The ligand 2-(1,8-naphthyridin-2-yl)quinoxaline (qxnp) and the protonated form of DTolF, N,N'-di(*p*-tolyl)formamidinium (HDTolF) were synthesized following reported procedures,<sup>178</sup> using *p*-toluidine purchased from Alfa Aesar and triethyl orthoformate obtained from TCI which were used without further purification. Chlorobenzene was used as received and acetonitrile was dried over 3 Å molecular sieves and distilled under a N<sub>2</sub> atmosphere. The salt  $\text{cis-}[\text{Rh}_2(\mu\text{-DTolF})_2(\text{qxnp})_2][\text{BF}_4]_2$  (**IV.5**) was prepared by a reported method.<sup>74</sup> All compounds were synthesized under inert atmosphere conditions using Schlenk-line techniques with subsequent manipulation and purification of the complexes being performed in air.

*cis*-[Rh<sub>2</sub>(μ-DTolF)<sub>2</sub>(μ-np)(CH<sub>3</sub>CN)<sub>4</sub>][BF<sub>4</sub>]<sub>2</sub> (**IV.1**). Quantities of *cis*-[Rh<sub>2</sub>(μ-DTolF)<sub>2</sub>(CH<sub>3</sub>CN)<sub>6</sub>][BF<sub>4</sub>]<sub>2</sub> (100.1 mg, 0.093 mmol) and 11.9 mg of np (0.091 mmol) were added to a Schlenk flask and refluxed for 24 h in 20 mL of dry acetonitrile. The dark purple solution was evaporated under vacuum to near dryness and the product was precipitated with diethyl ether. The solution was filtered through a fine frit, and the dark pink solid was washed with diethyl ether. The product was purified by slow diffusion of diethyl ether into a concentrated acetonitrile solution to yield 89.1 mg of compound (85 %). Dark pink X-ray quality crystals were obtained by slow diffusion of diethyl ether into a concentrated solution of the compound in acetonitrile. <sup>1</sup>NMR (500 MHz, CD<sub>3</sub>CN) δ 9.65 (dd, J = 5.2, 1.6 Hz, 2H), 8.59 (dd, J = 8.2, 1.6 Hz, 2H), 7.75 (dd, J = 8.2, 5.2 Hz, 2H), 7.68 (t, J = 3.5 Hz, 1H), 7.26 (t, J = 3.9 Hz, 1H), 7.03 (q, J = 8.3 Hz, 8H), 6.90 (d, J = 7.9 Hz, 4H), 6.63 – 6.55 (m, 4H), 2.29 (s, 6H), 2.21 (s, 6H). HRMS (ESI-MS) m/z: [M - 2MeCN]<sup>2+</sup> (C<sub>42</sub>H<sub>42</sub>N<sub>8</sub>Rh<sub>2</sub>) 432.0812 calc. [M - 3MeCN]<sup>2+</sup> (C<sub>42</sub>H<sub>42</sub>N<sub>8</sub>Rh<sub>2</sub>) 432.0816.

*cis*-[Rh<sub>2</sub>(μ-DTolF)<sub>2</sub>(μ-qxnp)(CH<sub>3</sub>CN)<sub>3</sub>][BF<sub>4</sub>]<sub>2</sub> (**IV.2**). Quantities of *cis*-[Rh<sub>2</sub>(μ-DTolF)<sub>2</sub>(CH<sub>3</sub>CN)<sub>6</sub>][BF<sub>4</sub>]<sub>2</sub> (50.7 mg, 0.047 mmol) and qxnp (12.2 mg, 0.047 mmol) were added to a Schlenk flask with 20 mL of dry acetonitrile and refluxed in an oil bath at 110 °C for 30 minutes. The resulting dark orange solution was evaporated under vacuum to near dryness and diethyl ether was added to precipitate the product which was filtered under vacuum through a fine frit and washed with diethyl ether to yield 43.5 mg of a dark brown powder (76 %). Orange needle-like crystals suitable for X-ray diffraction were obtained by slow diffusion of diethyl ether into a concentrated solution of the compound in acetonitrile. <sup>1</sup>H NMR (500 MHz, CD<sub>3</sub>CN) δ 9.75 – 9.71 (m, 2H), 8.95 – 8.88 (m, 1H),

8.83 (dd,  $J = 8.4, 2.0$  Hz, 2H), 8.68 (d,  $J = 8.8$  Hz, 1H), 8.06 (d,  $J = 8.1$  Hz, 1H), 8.00 (dd,  $J = 8.2, 5.2$  Hz, 1H), 7.87 – 7.82 (m, 2H), 7.53 (d,  $J = 8.3$  Hz, 2H), 7.35 (d,  $J = 8.1$  Hz, 2H), 7.22 – 7.19 (m, 3H), 7.12 – 7.02 (m, 4H), 7.00 (d,  $J = 8.4$  Hz, 1H), 6.98 – 6.94 (m, 2H), 6.87 (d,  $J = 8.0$  Hz, 2H), 6.31 – 6.27 (m, 2H), 2.48 (s, 3H), 2.28 (s, 3H), 2.19 (s, 3H), 1.83 (s, 3H). HRMS (ESI-MS)  $m/z$ :  $[M - 3MeCN]^{2+}$  ( $C_{46}H_{40}N_8Rh_2$ ) 910.1454 calc.  $[M - 3MeCN]^{2+}$  ( $C_{46}H_{40}N_8Rh_2$ ) 910.1486.

*trans*- $[Rh_2(\mu-DTolF)_2(\mu-qxnp)(CH_3CN)_3][BF_4]_2$  (**IV.3**). The partially solvated precursor *cis*- $[Rh_2(DTolF)_2(MeCN)_6][BF_4]_2$  (99.9 mg, 0.093 mmol) and an equimolar amount of qxnp (24.1 mg, 0.093 mmol) were suspended in 20 mL of acetonitrile. The mixture was refluxed for 24 h in an oil bath at 110 °C which led to the formation of a dark orange solution over the period of ~ 2 h. The reaction was cooled to room temperature and the solvent was evaporated to near dryness. Diethyl ether was added to precipitate the product which was collected by filtration under vacuum through a fine frit and washed with diethyl ether. The resulting dark orange-green powder was purified by flash column chromatography packed with silica gel using 5% MeOH in dichloromethane as the eluent to yield 27.2 mg of a dark orange powder (24 %). X-ray quality crystals were obtained by layering a concentrated solution of the product in acetonitrile with toluene.  $^1H$  NMR (500 MHz,  $CD_3CN$ )  $\delta$  9.65 (s, 1H), 9.40 (d,  $J = 5.3$  Hz, 1H), 9.01 (d,  $J = 8.7$  Hz, 1H), 8.91 (dd,  $J = 8.2, 1.6$  Hz, 1H), 8.86 (d,  $J = 8.8$  Hz, 1H), 8.21 (d,  $J = 8.2$  Hz, 1H), 8.00 – 7.91 (m, 3H), 7.87 (ddd,  $J = 8.4, 6.4, 2.0$  Hz, 1H), 7.22 (t,  $J = 2.8$  Hz, 2H), 7.01 (d,  $J = 8.2$  Hz, 4H), 6.59 (d,  $J = 8.2$  Hz, 4H), 6.26 (d,  $J = 8.1$  Hz, 4H), 6.08 (d,  $J = 8.2$  Hz, 4H), 2.25 (s, 6H),

2.15 (s, 12H), 1.82 (s, 6H). HRMS (ESI-MS) m/z:  $[M - 3MeCN]^{2+}$  ( $C_{46}H_{40}N_8Rh_2$ ) 910.1440 calc.  $[M - 3MeCN]^{2+}$  ( $C_{46}H_{40}N_8Rh_2$ ) 910.1486.

*trans*- $[Rh_2(\mu-DTolF)_2(\mu-qxnp)_2][BF_4]_2$  (**IV.4**). Equimolar quantities of **3** (98.9 mg, 0.082 mmol) and qxnp (21.2 mg, 0.082 mmol) were suspended in 20 mL of chlorobenzene/acetonitrile (1:1) and refluxed in an oil bath for 24 h at 130 °C. The cooled reaction solution was concentrated by evaporation under reduced pressure and diethyl ether was added. The resulting brown product was filtered through a fine frit under vacuum and washed with copious amounts of diethyl ether. To separate the final product from **5**, a short silica gel column using  $CH_2Cl_2/MeOH$  90:10 as the eluent was used. The solvent was evaporated under reduced pressure and diethyl ether was added to precipitate the product. The resulting orange-brown powder was recrystallized by slow diffusion of diethyl ether into a solution of acetonitrile to yield 28.5 mg (26 %) of dark orange X-ray quality crystals.  $^1H$  NMR (500 MHz,  $CD_3CN$ )  $\delta$  10.32 (d,  $J = 5.6$  Hz, 2H), 9.64 (s, 2H), 9.10 (d,  $J = 8.0$  Hz, 2H), 9.04 (d,  $J = 8.8$  Hz, 2H), 8.80 (d,  $J = 8.7$  Hz, 2H), 8.32 (dd,  $J = 8.0, 4.7$  Hz, 2H), 8.10 (d,  $J = 9.0$  Hz, 2H), 7.98 (t,  $J = 8.2$  Hz, 2H), 7.86 (t,  $J = 7.6$  Hz, 2H), 7.69 (d,  $J = 9.0$  Hz, 2H), 7.10 (t,  $J = 2.6$  Hz, 2H), 6.30 (d,  $J = 7.9$  Hz, 8H), 5.72 (d,  $J = 8.2$  Hz, 8H), 1.89 (s, 12H). HRMS (ESI-MS) m/z:  $[M + BF_4]^+$  ( $C_{62}H_{50}N_{12}BF_4Rh_2$ ) 1255.240102 and  $[M]^{2+}$  ( $C_{62}H_{50}N_{12}Rh_2$ ) 584.118165 calc.  $[M + BF_4]^+$  ( $C_{62}H_{50}N_{12}BF_4Rh_2$ ) 1255.242061 and  $[M]^{2+}$  ( $C_{62}H_{50}N_{12}Rh_2$ ) 584.119572.

#### *Instrumentation and methods*

$^1H$  NMR spectra were obtained on an Inova 500 MHz spectrometer; the chemical shifts were referenced to the residual peak of the residual  $CD_3CN-d_3$  deuterated solvent signal

at 1.96 ppm.<sup>75</sup> The activation energy of the isomerization reaction from the *cis* to the *trans* isomer was determined by preparing *cis*-[Rh<sub>2</sub>(μ-DTolF)<sub>2</sub>(μ-qxnp)(CH<sub>3</sub>CN)<sub>3</sub>][BF<sub>4</sub>]<sub>2</sub> solutions in CD<sub>3</sub>CN-*d*<sub>3</sub> which were placed in an oil bath at temperatures ranging from 64 – 80 °C (with 4 °C increments) and monitored by <sup>1</sup>H NMR spectroscopy. The resonance at 9.74 ppm corresponds to two H atoms of the *cis* isomer and was set to an integration of 2. The peak at 9.64 ppm for the *trans* isomer, corresponding to one H atom of the complex was integrated and referenced to the former feature (Figure IV. 2). The relative integrations with respect to the total integration for the *cis* and *trans* isomers were used to calculate a percentage of converted *cis* isomer. The conversion was plotted over time, and the rate of the reaction was obtained from a mono-exponential decay fitting for each temperature. The activation energy for the isomerization was determined through an Arrhenius plot of ln(k) vs 1/T. The qxnp addition reaction was monitored over time by <sup>1</sup>H NMR methods. Electronic spectroscopy was performed on a Hewlett-Packard 8453 diode array spectrometer or on a Shimadzu UV-1601PC spectrophotometer in 1 × 1 cm quartz cuvettes. Extinction coefficients were determined in triplicate.

Single crystals of **IV.1–4** were selected from @Paratone oil under ambient conditions using a MiTeGen microloop. The crystals were placed in a cold N<sub>2</sub> stream (**IV.1**, **IV.3**, and **IV.4** at 110 K and **IV.2** at 140 K) on a Bruker D8-QUEST diffractometer equipped with an IμS Mo microsource (λ = 0.71073 Å). Initial unit cells determined using SAINT from a set of three ω-scans consisting of 0.5° frames and a sweep width of 15° were used for the data collection strategies to collect all independent reflections to a resolution of at least 0.83 Å. Full details of the data collection and refinement parameters are presented in Table IV-1.



The data were corrected for absorption using SADABS,<sup>128</sup> and the space group was determined from analysis of the systematic absences using XPREP. The structures were solved using the intrinsic phasing routine in SHELXT or by direct methods implemented in SHELXS. The non-hydrogen atoms were located from Fourier difference maps by least-squares refinement of the structure using SHELXL-2014.<sup>129</sup> All non-hydrogen atoms were refined anisotropically and hydrogen atoms were placed in calculated positions and refined with thermal parameters constrained to their parent atom. Specific details of the refinements are presented in Table IV-1.

Electrochemical measurements for **IV.4** ( $1 \times 10^{-3}$  M) were recorded under nitrogen in dry acetonitrile with 0.1 M [n-Bu<sub>4</sub>N][PF<sub>6</sub>] as the supporting electrolyte using a CH Instruments electrochemical analyzer model CH1620A. A three-electrode cell was used with a glassy carbon disc working electrode, a Pt wire counter electrode, and a Ag/AgCl reference electrode standardized to ferrocene ( $E_{1/2} = +0.55$  V vs Ag/AgCl). Electrospray ionization mass spectrometry (ESI-MS) data were obtained in the Laboratory for Biological Mass Spectrometry at Texas A&M University using a Thermo Scientific Q Exactive Focus. The sample was directly infused at a flow rate of 10  $\mu$ L/min. The Q Exactive Focus HESI source was operated in full MS in positive mode. The mass resolution was tuned to 17500 FWHM at  $m/z$  200, the spray voltage was set to 3.75 kV, and the sheath gas and auxiliary gas flow rates were set to 7 and 0 arbitrary units, respectively. The transfer capillary temperature was held at 250 °C and the S-Lens RF level was set at 50 v. Exactive Series 2.8 SP1/Xcalibur 4.0 software was used for data acquisition and processing.

Ultrafast transient absorption experiments were performed on a previously described system.<sup>179</sup> Briefly, the output of a Ti:sapphire regenerative amplifier (Astrella 1K-USP, Coherent) was split to generate the white light probe through a rotating CaF<sub>2</sub> crystal and to a pump an OPA (OPerA Solo, Coherent/Positive Light) to generate the pump pulse at 600 nm. A thermally cooled CCD camera with home-built software written in LabVIEW 2015 was used to collect and manipulate the data. The sample solution was prepared with ~ 0.5 OD at the excitation wavelength and ~ 5 mL solution containing the sample was flowed through a 1 mm path-length Harrick Scientific flow cell (1 mm thick CaF<sub>2</sub> windows) and excited with ~ 2.5  $\mu$ J at the pump wavelength. An instrument response of fwhm ~ 85 fs was measured using the Kerr effect in cyclohexane. The polarization angle between the pump and probe was set to 54.7° to avoid rotational diffusion effects. Nanosecond transient absorption spectroscopy was performed on a previously reported instrument.<sup>180</sup> For these experiments, the 600 nm excitation pulse was generated from an OPO (basiScan, Spectra-Physics) pumped by the third harmonic (355 nm) of a Nd:YAG laser (Quanta-Ray INDI, Spectra-Physics) and the output of a continuous 150 W xenon arc lamp gated using a Uniblitz shutter was used as the probe. The excitation and probe pulses were overlapped at a 90° geometry at the sample. The spectral measurements were collected on a spectrometer (LP 980, Edinburgh Instruments) equipped with an ICCD camera. Sample concentrations were adjusted such that they absorbed ~ 0.5 at the excitation wavelength in a 1  $\times$  1 quartz cuvette.

Density Functional Theory (DFT) calculations were performed to calculate the molecular and electronic structures of complexes **IV.1–4** using the Gaussian (09) program

package.<sup>131</sup> The Stuttgart RSC 1997 Electron Core Potential (ECP)<sup>181</sup> basis set was used for the Rh atoms, the 6-31G† basis set for the C, N, and H atoms,<sup>134</sup> and B3LYP<sup>132, 133</sup> correlation and exchange functionals were used. As a starting point for the gas-phase optimizations, geometric parameters were taken from the crystal structures for the complexes; interstitial solvent molecules and counterions were omitted. For the theoretical molecule, *trans*-[Rh<sub>2</sub>(DTolF)<sub>2</sub>(np)(MeCN)<sub>4</sub>][BF<sub>4</sub>]<sub>2</sub>, the geometrical parameters of complex **IV.1** were used as a starting point and modified in ‘Agui’ to build the corresponding *trans* isomer. A similar procedure was employed for building the postulated intermediates *cis/trans*-[Rh<sub>2</sub>(μ-DTolF)(κ-DTolF)(qxnp)(MeCN)<sub>3</sub>]<sup>2+</sup> and *cis/trans*-[Rh<sub>2</sub>(μ-DTolF)(κ-DTolF)(np)(MeCN)<sub>4</sub>]<sup>2+</sup>. Following gas-phase optimization, Time-Dependent Density Functional Theory (TD-DFT)<sup>135</sup> calculations were performed using the polarized continuum model (PCM)<sup>136</sup> with acetonitrile as the solvent. The first sixty lowest singlet-to-singlet excited states were calculated from the optimized singlet ground state. Single point energy calculations at different bond lengths ranging from 2 to 50 Å were used to estimate the Rh-N bond dissociation energies for the equatorial and axial acetonitrile molecules of *cis/trans*-[Rh<sub>2</sub>(μ-DTolF)<sub>2</sub>(qxnp)(MeCN)<sub>3</sub>]<sup>2+</sup> (Figure IV.14). A relaxed potential energy scan calculation with 10 steps of 0.5 Å was carried out to estimate the Rh-N<sub>DTolF</sub> bond dissociation energy for the *cis*-[Rh<sub>2</sub>(μ-DTolF)<sub>2</sub>(qxnp)(MeCN)<sub>3</sub>]<sup>2+</sup> complex. The graphic software ‘Agui’<sup>137</sup> with an isovalue = 0.04 was used to plot molecular orbitals (Table IV-5). In order to estimate the bond dissociation energies for the axial and equatorial acetonitrile molecules in **IV.2** and **IV.3**, single point energy calculations at different Rh-NCCH<sub>3</sub> distances were performed using the gas-phase

optimized structures as a starting point. The Chemissian program<sup>77</sup> was used to perform Natural Transition Orbital (NTO) analyses.

## Results and Discussion

### *Synthesis*

Compounds **IV.1–4** were synthesized by a methodology that was optimized to control the geometric isomerism of the products (Scheme 1). The syntheses and isolation of the mono-substituted complexes **IV.1–3** are influenced by stoichiometry, temperature, and reaction time.

Compound **IV.1** was synthesized in refluxing acetonitrile from a 1:1 ratio of the np ligand and *cis*-[Rh<sub>2</sub>(DTolF)<sub>2</sub>(CH<sub>3</sub>CN)<sub>6</sub>][BF<sub>4</sub>]<sub>2</sub> as depicted in Scheme 2a. Complexes **IV.2** and **IV.3** were also prepared in acetonitrile from a 1:1 ratio of the qxn timer ligand and the same dirhodium partial-paddlewheel starting material as depicted in Scheme 2b but under different conditions. In the case of **IV.2**, the 1:1 mixture was refluxed in acetonitrile for 30 minutes, or was heated for 24 h at 40 °C. Both reactions yielded **IV.2** along with a small amount of **IV.5** (12% as determined by <sup>1</sup>H NMR spectroscopy of the crude product which were separated by slow diffusion of diethyl ether into a concentrated solution of the mixture in acetonitrile to yield pure crystals of **IV.2**. The thermodynamic product, compound **IV.3**, was obtained by refluxing the initial equimolar mixture of starting materials for 24 h, as the isomerization from the *cis* isomer **IV.2** to the *trans* analog **IV.3** is a slow kinetic process that requires the migration of a DTolF ligand. The direct conversion of *cis*-[Rh<sub>2</sub>(μ-DTolF)<sub>2</sub>(MeCN)<sub>6</sub>][BF<sub>4</sub>]<sub>2</sub> to **3** upon addition of one equivalent of ligand does not occur as evidenced by <sup>1</sup>H NMR spectra obtained before and after refluxing

the dirhodium starting material in acetonitrile (Figure IV.2). A 24 h reflux of the *cis*- $[\text{Rh}_2(\mu\text{-DTolF})_2(\text{MeCN})_6][\text{BF}_4]_2$  compound alone does not yield *trans*- $[\text{Rh}_2(\mu\text{-DTolF})_2(\text{MeCN})_6][\text{BF}_4]_2$  and, furthermore, does not alter the ratios of **IV.2** and **IV.3** obtained after addition of the ligand (Figure IV.3). The product was purified by layering a concentrated solution of the compound in acetonitrile with toluene. As demonstrated by  $^1\text{H}$  NMR spectral experiments, compound **IV.3** is also obtained in quantitative yields by refluxing **IV.2** for 24 h in acetonitrile and heating to temperatures near the boiling point of the solvent.

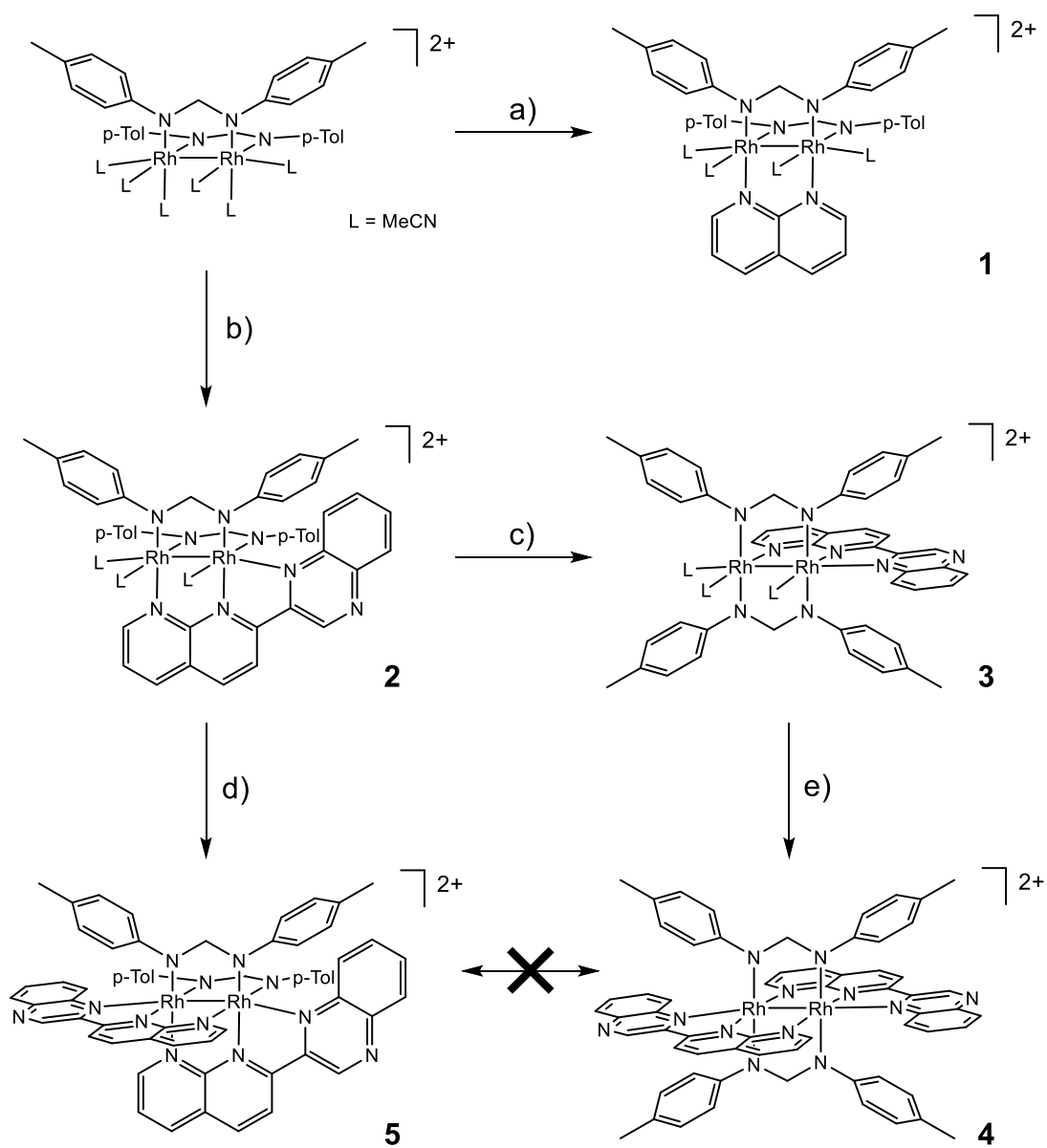


**Figure IV.1** Syntheses of complexes **IV.1–5**: a) 1,8-naphthyridine in refluxing acetonitrile for 24 h, b) qxnp (2-(1,8-naphthyridin-2-yl)quinoxaline) in refluxing acetonitrile for 30 minutes or stirring in acetonitrile at 40 °C for 24 h, c) refluxing acetonitrile for 24 h, d) qxnp in refluxing acetonitrile for 24 h, and e) qxnp in refluxing chlorobenzene for 24 h.

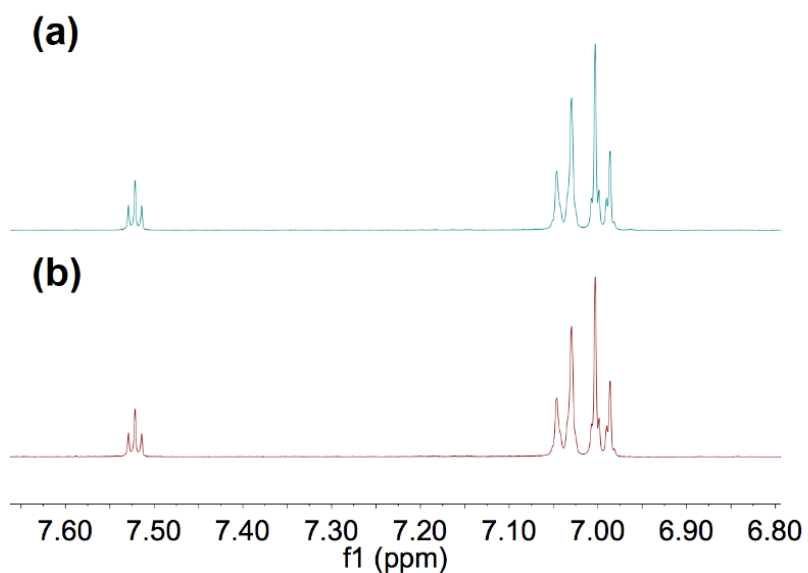


**Figure IV.2** Aromatic region of the  $^1\text{H}$  NMR spectra of  $\text{cis-}[\text{Rh}_2(\mu\text{-DTolF})_2(\text{MeCN})_6][\text{BF}_4]_2$  before (a) and after (b) refluxing for 24 h in acetonitrile.

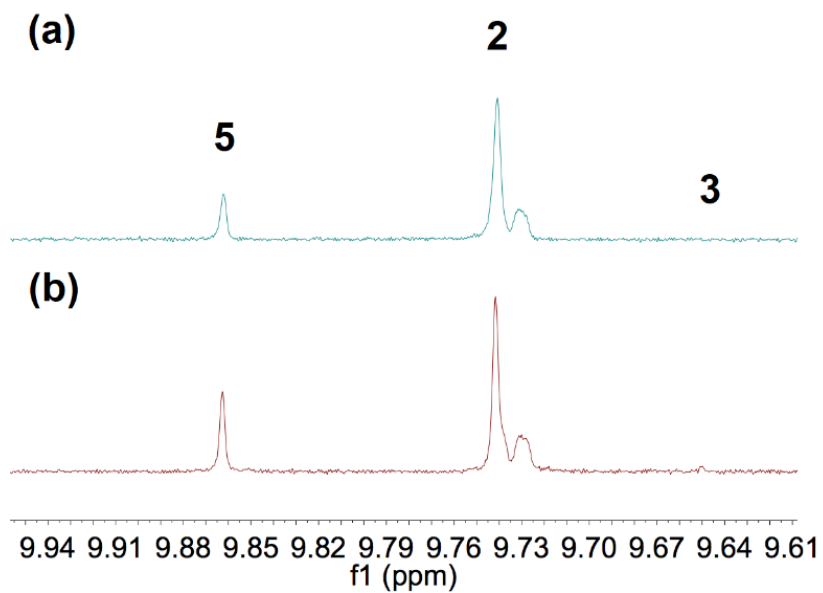


**Figure IV.3** Aromatic region of the  $^1\text{H}$  NMR spectra of the crude product of the reaction of  $\text{cis-}[\text{Rh}_2(\mu\text{-DTolF})_2(\text{MeCN})_6][\text{BF}_4]_2$  and one equivalent of qxnp. The dirhodium starting material was refluxed for 24 h prior to the addition of the ligand. The ligand was reacted with the metal complex for (a) 24 h at 40 °C or (b) 30 minutes at refluxing temperature in acetonitrile.

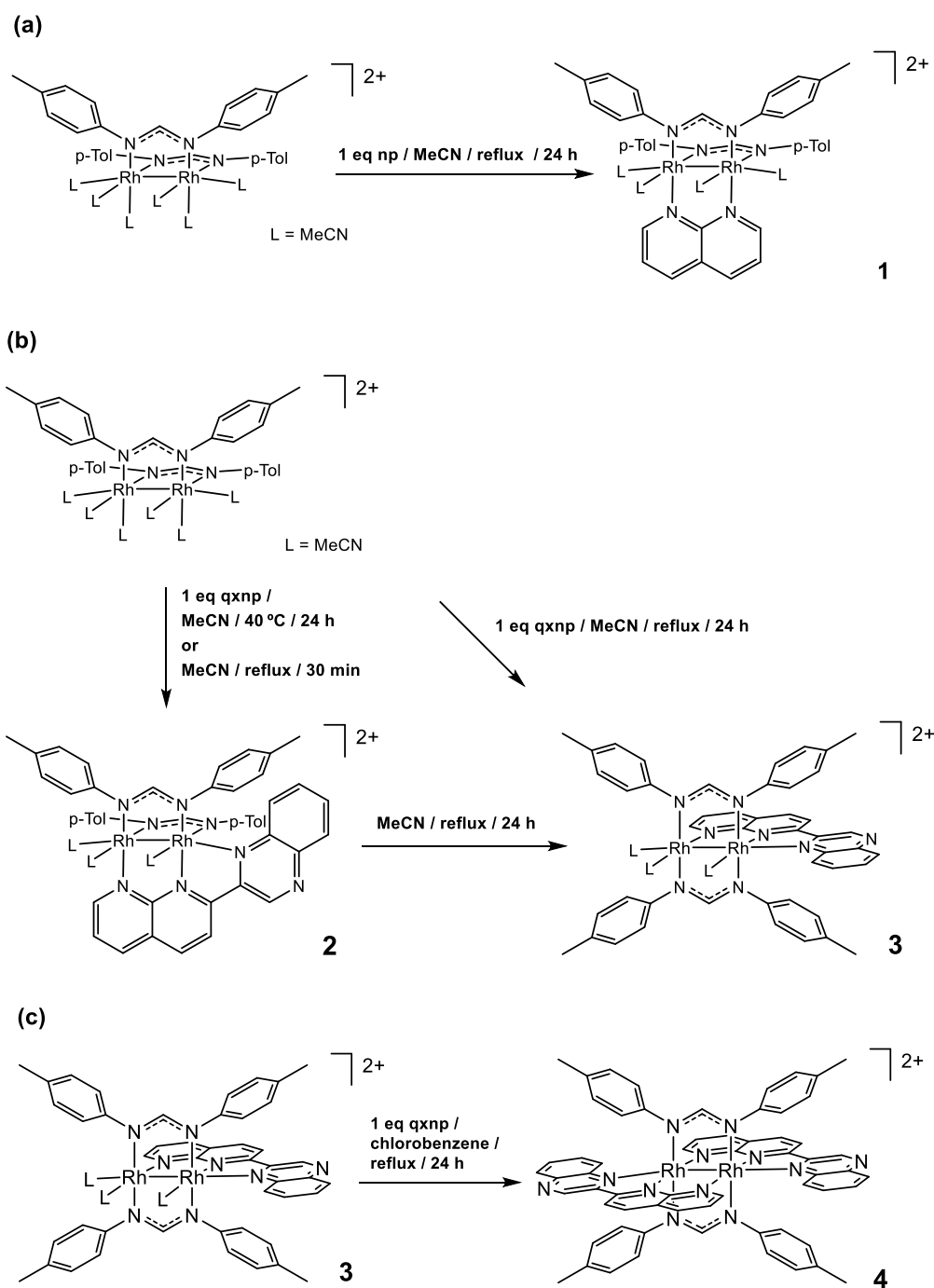


**Figure IV.4** Reactions (a) of np and *cis*-[Rh<sub>2</sub>(DTolF)<sub>2</sub>(CH<sub>3</sub>CN)<sub>6</sub>][BF<sub>4</sub>]<sub>2</sub> in refluxing acetonitrile for 24 h to yield **IV.1**, (b) of equimolar amounts of qxnp and *cis*-[Rh<sub>2</sub>(DTolF)<sub>2</sub>(CH<sub>3</sub>CN)<sub>6</sub>][BF<sub>4</sub>]<sub>2</sub> in acetonitrile at 40 °C or at reflux for 30 min to yield **IV.2**



or by refluxing for 24 h in CH<sub>3</sub>CN to yield **IV.3**, and (c) of complex **IV.3** with 1 eq qxnp in chlorobenzene at reflux for 24 h to yield **IV.4**.

The synthesis of **IV.4** is substantially different from those used to isolate the other complexes, as no reaction occurs when qxnp is refluxed in the presence of **IV.3** in acetonitrile. In order to obtain the *trans* bis-substituted complex **IV.4**, it was necessary to reflux **IV.3** in a non-coordinating solvent with a high boiling point. A 24-hour reflux of a 1:1 mixture of qxnp and the *trans* intermediate **IV.3** in chlorobenzene yielded **IV.4** as the final product (Scheme 2c).

#### *X-ray Crystal Structures*

The molecular structures of complexes **IV.1–4** (Figures IV.1 and 4) were determined by single crystal X-ray diffraction experiments. The dicationic compounds consist of a dirhodium core bridged by two anionic N,N'-(*p*-tolyl)formamidinate ligands with two [BF<sub>4</sub>]<sup>-</sup> anions. Compound **IV.1** is a 1,8-naphthyridine monosubstituted complex with two equatorial and two axial acetonitrile molecules. Complexes **IV.2** and **IV.3** contain a quinoxaline derivatized naphthyridine ligand (qxnp) that binds to one of the axial positions, leaving only one acetonitrile molecule to occupy the second axial site, whereas **IV.4**, with two qxnp ligands, is fully axially-blocked. The Rh-Rh bond distances are 2.5049(7) Å, 2.49896(11) Å, 2.50067(14) Å, and 2.4942(8) Å for compounds **IV.1–4**, respectively, longer than the Rh-Rh bond distance of 2.4498 Å for compound **5** (Table IV-4).<sup>74</sup> Compounds **IV.1–3** and **IV.5** exhibit N<sub>eq</sub>-Rh-Rh-N<sub>eq</sub> torsion angles that range between 17-23°, attributed to the steric strain from the equatorial acetonitrile molecules in **IV.1–3** and  $\pi$ - $\pi$  stacking interactions as well as steric strain between the DTolF ligands in

**IV.5.** In contrast, the torsion angle of **IV.4** is only  $-1.3337(4)^\circ$ , which results in a near-perfect alignment with the N-C-N moiety of the bridging formamidinate ligand (Figure IV.4b). The longer Rh-Rh bond distances for **IV.1–3** as compared to that of **IV.5** is not surprising given that **IV.5** has four bridging ligands as opposed to three bridges in **IV.1–3**. In addition, all of the Rh-Rh bond distances are consistently shorter than those for complexes with  $\kappa$ -chelating ligands, *e.g.*,  $2.5818(3) \text{ \AA}$  for *cis*- $[\text{Rh}_2(\text{DTolF})_2(\text{dppn})_2][\text{BF}_4]_2$ ,<sup>126</sup> due to the presence of a third (**IV.1–3**) or fourth (**IV.4** and **IV.5**) bridging np or qxnp moiety. The bite angle of the  $\pi$ -accepting qxnp ligand results in considerable deviation from linearity of the Rh-Rh-N<sub>ax</sub> bond angles in **IV.2–5**,  $159.6559(12)^\circ$ ,  $162.5328(14)^\circ$ ,  $165.539(4)^\circ$ , and  $161.73(4)^\circ$ , respectively which results in longer Rh-N<sub>ax</sub>(qxnp) bond distances for **IV.2** and **IV.3** of  $2.16872(9) \text{ \AA}$  and  $2.14851(12) \text{ \AA}$ , respectively and concomitant shortening of the Rh-NCCH<sub>3</sub> axial bond on the other rhodium metal center.

**Table IV-1** The refinement details for **IV.1** and **IV.2**.

Compound	IV.1	IV.2
Empirical Formula	C <sub>46</sub> H <sub>48</sub> B <sub>2</sub> F <sub>8</sub> N <sub>10</sub> Rh <sub>2</sub>	C <sub>110</sub> H <sub>111</sub> B <sub>4</sub> F <sub>16</sub> N <sub>23</sub> O <sub>1.4</sub> Rh <sub>4</sub>
Formula weight	1120.38	2536.49
Temperature/K	100.01	140.04
Crystal system	orthorhombic	triclinic
Space group	Pbca	P-1
a/Å	14.544(3)	12.2642(6)
b/Å	21.470(4)	17.0096(8)
c/Å	31.369(7)	28.0520(13)
$\alpha$ /°	90	98.203(2)
$\beta$ /°	90	90.465(2)
$\gamma$ /°	90	103.580(2)
Volume/Å <sup>3</sup>	9795(3)	5624.8(5)
Z	8	2
$\rho_{\text{calc}}$ /cm <sup>3</sup>	1.519	1.498
$\mu$ /mm <sup>-1</sup>	0.748	0.663
F(000)	4528.0	2574.0
Crystal size/mm <sup>3</sup>	2 x 0.2 x 0.2	0.2 x 0.1 x 0.1
Radiation	MoK $\alpha$ ( $\lambda$ = 0.71073)	MoK $\alpha$ ( $\lambda$ = 0.71073)
2 $\Theta$ range for data collection/°	4.598 to 53	4.406 to 52.83
Index ranges	-18 ≤ h ≤ 18 -26 ≤ k ≤ 24 -37 ≤ l ≤ 39	-14 ≤ h ≤ 15 -21 ≤ k ≤ 21 -35 ≤ l ≤ 35
Reflections collected	85946	246797
Independent reflections	10106 R <sub>int</sub> = 0.0627 R <sub>sigma</sub> = 0.0399	23052 R <sub>int</sub> = 0.1086 R <sub>sigma</sub> = 0.0469
Data/restraints/parameters	10106/1335/1049	23052/866/1756
Goodness-of-fit on F <sup>2</sup>	1.202	1.133
Final R indexes [ $I \geq 2\sigma(I)$ ]	R <sub>1</sub> = 0.0680 wR <sub>2</sub> = 0.1249	R <sub>1</sub> = 0.0616 wR <sub>2</sub> = 0.1233
Final R indexes [all data]	R <sub>1</sub> = 0.0942 wR <sub>2</sub> = 0.1339	R <sub>1</sub> = 0.0770 wR <sub>2</sub> = 0.1294
Largest diff. peak/hole / e Å <sup>-3</sup>	0.64/-1.00	0.91/-1.24

**Table IV-2** Refining parameters for **IV.3** and **IV.4**.

Compound	<b>IV.3</b>	<b>IV.4</b>
Empirical Formula	C <sub>54.16</sub> H <sub>52.56</sub> B <sub>2</sub> F <sub>8</sub> N <sub>11.92</sub> O <sub>0.08</sub> Rh <sub>2</sub>	C <sub>37</sub> H <sub>33.78</sub> B <sub>0.99</sub> F <sub>3.94</sub> N <sub>8.45</sub> Rh
Formula weight	1251.16	785.18
Temperature/K	100.0	110.0
Crystal system	monoclinic	triclinic
Space group	P2 <sub>1</sub> /n	P-1
a/Å	13.5743(11)	7.906(3)
b/Å	22.1018(16)	14.141(5)
c/Å	18.4253(14)	16.225(6)
α/°	90	114.844(10)
β/°	96.661(2)	97.300(10)
γ/°	90	93.081(12)
Volume/Å <sup>3</sup>	5490.6(7)	1621.0(11)
Z	4	2
ρ <sub>calc</sub> /cm <sup>3</sup>	1.514	1.609
μ/mm <sup>-1</sup>	0.677	4.873
F(000)	2534.0	801.0
Crystal size/mm <sup>3</sup>	0.3 × 0.2 × 0.1	0.3 x 0.1 x 0.1
Radiation	MoKα (λ = 0.71073)	MoKα (λ = 0.71073)
2θ range for data collection/°	4.452 to 52.91	12.024 to 151.276
Index ranges	-16 ≤ h ≤ 16 -27 ≤ k ≤ 23 -23 ≤ l ≤ 23	-9 ≤ h ≤ 9 -17 ≤ k ≤ 17 -20 ≤ l ≤ 20
Reflections collected	88020 11196	9468 5870
Independent reflections	R <sub>int</sub> = 0.0417 R <sub>sigma</sub> = 0.0276	R <sub>int</sub> = 0.0239 R <sub>sigma</sub> = 0.0385
Data/restraints/parameters	11196/898/1058	5870/0/526
Goodness-of-fit on F <sup>2</sup>	1.136	1.166
Final R indexes [I ≥ 2σ (I)]	R <sub>1</sub> = 0.0418 wR <sub>2</sub> = 0.0853	R <sub>1</sub> = 0.0364 wR <sub>2</sub> = 0.0912
Final R indexes [all data]	R <sub>1</sub> = 0.0569 wR <sub>2</sub> = 0.0951	R <sub>1</sub> = 0.0442 wR <sub>2</sub> = 0.1017
Largest diff. peak/hole / e Å <sup>-3</sup>	0.97/-1.22	0.48/-0.89

Compounds **IV.2–5** engage in intramolecular  $\pi$ - $\pi$  stacking interactions between the *p*-tolyl substituents of the formamidinate bridging ligands and the quinoxalinyll moieties of the axially blocking qxnp ligands (Figure IV.8). Given that the *cis* and *trans* complexes have distinct molecular geometries, the distances between the rings range from 3.348 Å to 3.654 Å in the series. Changes in symmetry and intramolecular interactions are consistent with the chemical shifts observed in the  $^1\text{H}$  NMR spectra of these complexes, particularly in the quinoxalinyll moiety. These shifts provide a useful spectroscopic tool for differentiating between the complexes and to study the kinetics of the incorporation of qxnp ligands and the isomerization reactions.

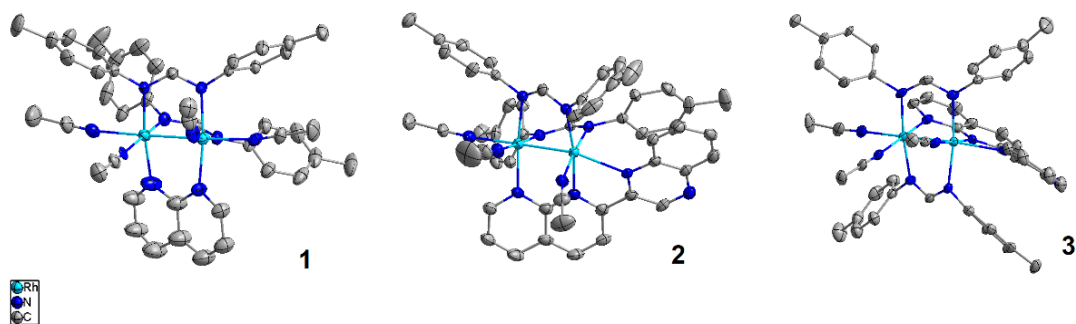


**Figure IV.5** Thermal ellipsoid plots for **IV.1–3**, drawn at the 50% probability level. Counterions, interstitial solvent molecules, and hydrogen atoms were omitted for the sake of clarity.

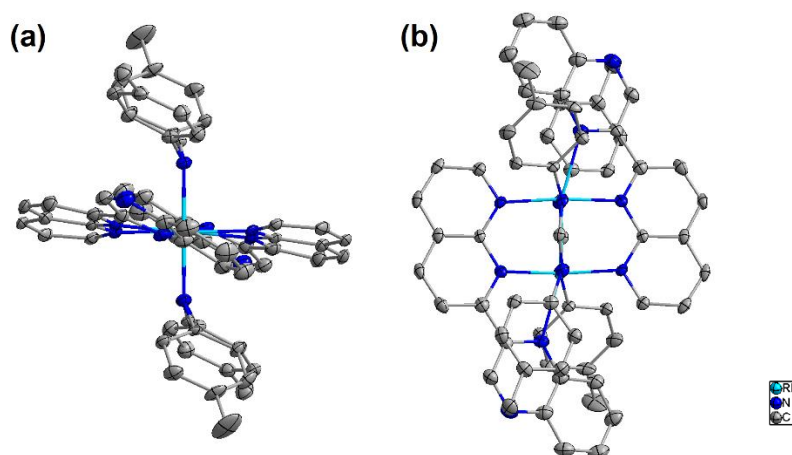


**Figure IV.6** Thermal ellipsoid plots for **IV.4**, drawn at the 50% probability level: view looking down the rhodium-rhodium bond axis (a) and top view (b). Counterions, interstitial solvent molecules, and hydrogen atoms were omitted for the sake of clarity.

#### *Electrochemistry and Electronic Absorption Spectroscopy*

The electrochemical data for **IV.4** are presented in Table IV-3 along with the previously reported data for **IV.5**. Compound **IV.4** displays a one-electron reversible couple at  $E_{1/2} = +1.00$  V *vs* Ag/AgCl in acetonitrile (0.1 M Bu<sub>4</sub>NPF<sub>6</sub>) which is an oxidation of the metal-formamidinate HOMO, as assigned for **IV.5** and related formamidinate-bridged dirhodium(II,II) complexes,<sup>63, 127</sup> and a one-electron reduction of one of the qxnp  $\pi$ -accepting ligands at  $E_{1/2} = -0.34$  V *vs* Ag/AgCl. This reduction potential is more positive than that observed for **IV.5** and other axially blocked complexes such as *cis*-[Rh<sub>2</sub>(DTolF)<sub>2</sub>(L)<sub>2</sub>][BF<sub>4</sub>]<sub>2</sub>, where L = 2-(pyridin-2-yl)-1,8-naphthyridine or 2-(quinolin-2-yl)-1,8-naphthyridine) of  $E_{1/2} = -0.70$  V *vs* Ag/AgCl and  $E_{1/2} = -0.62$  V *vs* Ag/AgCl respectively, indicating that **IV.4** is easier to reduce, a point that will be discussed in the DFT calculations section.

A comparison of the steady state absorption spectra of **IV.4** and **IV.5** is presented in Figure IV.7, and the maxima,  $\lambda_{\text{abs}}$ , with their corresponding molar extinction coefficients,  $\epsilon$ , are listed in Table IV-3. Compound **IV.4** exhibits intense absorption maxima in the ultraviolet region at 258 nm and 367 nm, similar to those reported for **IV.5** at 259 nm and 369 nm (Table IV-3). These absorption peaks of **IV.4** and **IV.5** are similar to those observed for the free qxnp ligand in  $\text{CH}_2\text{Cl}_2$ , 254 nm ( $\epsilon = 99(13) \times 10^3 \text{ M}^{-1}\text{cm}^{-1}$ ) and 342 nm ( $\epsilon = 70(8) \times 10^3 \text{ M}^{-1}\text{cm}^{-1}$ ), and are assigned as ligand-centered  $^1\pi\pi^*$  transitions. There is minimal shift in the peak at 560 nm in **IV.4** to 554 nm in **IV.5**. In contrast, the lowest energy transition of **IV.4** at 832 nm ( $12,020 \text{ cm}^{-1}$ ) is shifted bathochromically from the 758 nm ( $13,190 \text{ cm}^{-1}$ ) maximum recorded for **5** and is assigned as  $^1\text{ML-LCT}$  with  $\text{Rh}_2/\text{DTolF} \rightarrow \text{qxnp}(\pi^*)$  character. The 74 nm ( $1,170 \text{ cm}^{-1}$ ) red shift of this transition is consistent with the more easily reduced qxnp ligand by 0.09 V in **IV.4** as compared to that in **IV.5**, together with a more easily oxidized  $\text{Rh}_2/\text{DTolF}$  HOMO in **IV.4** relative to **IV.5** (Table IV-3).

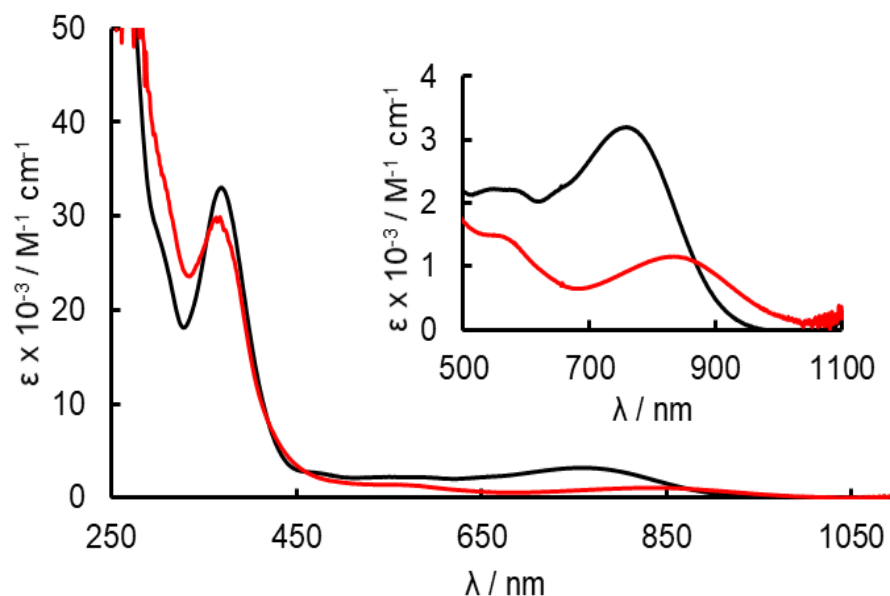


**Figure IV.7** Electronic absorption spectra of **IV.4** (red) and **IV.5** (black).

**Table IV-3** Electronic Absorption Maxima ( $\lambda_{\text{abs}}$ ), Molar Absorptivities ( $\epsilon$ ), Reduction Potentials ( $E_{1/2}$ ), Singlet ( $\tau_{\text{S}}$ ) and Triplet ( $\tau_{\text{T}}$ ) Lifetimes for **IV.4** and **IV.5** in Acetonitrile.

Complex	$\lambda_{\text{abs}} / \text{nm}$ ( $\epsilon / \times 10^3 \text{ M}^{-1} \text{ cm}^{-1}$ )	$E_{1/2} / \text{V}^b$	$\tau_{\text{S}} / \text{ps}^c$	$\tau_{\text{T}} / \text{ns}^c$
<b>IV.4</b>	258 (124), 367 (47), 560 (2.3), 832(1.9)	+1.00, -0.34	3	0.40
<b>IV.5<sup>a</sup></b>	259 (83), 369 (32), 554 (2.2), 758(3.2)	+1.08, -0.43	8	7.2

<sup>a</sup>From reference 23. <sup>b</sup>vs Ag/AgCl in 0.1 M Bu<sub>4</sub>NPF<sub>6</sub>/CH<sub>3</sub>CN. <sup>c</sup>From transient absorption experiments at 298 K ( $\lambda_{\text{exc}} = 600 \text{ nm}$ , fwhm = 85 fs).



### Electronic Structure Calculations

DFT calculations were performed to assess the contributions of atomic orbitals to the molecular orbitals (MOs) in these dirhodium cations and to better understand the synthetic methodology designed to obtain the *trans*-substituted dirhodium complexes in this study. The geometrical parameters of the crystal structures of complexes **IV.1–4** were used as starting points. The energies of the metal-metal bonding MOs are  $(\sigma)^2(\pi)^4(\delta)^2(\pi^*)^4(\delta^*)^2(\sigma^*)^0$  in **IV.1–5** due to the presence of strong  $\pi$ -donor formamidinate ligands with the correct symmetry to interact with the  $\text{Rh}_2(\delta^*)$  MO. This interaction raises the energy of the  $\text{Rh}_2(\delta^*)$  MO such that it lies above the  $\text{Rh}_2(\pi^*)$  orbital. This electronic configuration is a departure from archetypal  $d^7-d^7$  dinuclear complexes with weaker  $\pi$ -donor bridging ligands for which the molecular orbital levels are  $(\sigma)^2(\pi)^4(\delta)^2(\delta^*)^2(\pi^*)^4(\sigma^*)^0$ , but is consistent with other formamidinate containing complexes.<sup>28, 182</sup>

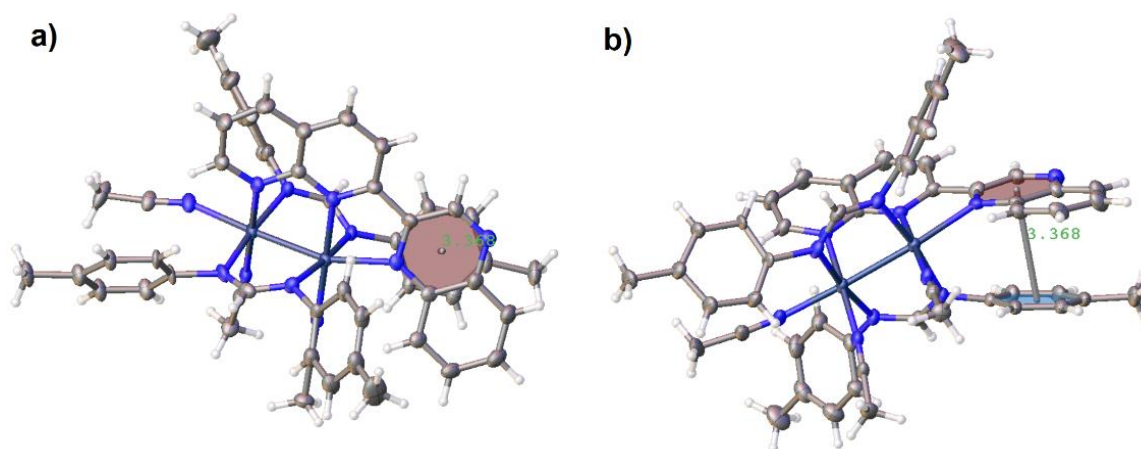
**Table IV-4** Comparison of gas phase optimized structures and X-ray crystal structures for **IV.1–4**.

<b>IV.1</b>	Crystal Structure	Calculated Structure
Rh1-Rh2	2.5049(7)	2.53988
Rh1-N1	2.030(5)	2.07224
Rh1-N3	2.017(5)	2.05870
Rh1-N5	2.062(13)	2.14095
Rh1-N7	2.007(11)	2.06956
Rh1-N9	2.218(6)	2.28381
Rh2-N2	2.037(5)	2.08168
Rh2-N4	2.035(5)	2.06234
Rh2-N6	2.064(12)	2.13578
Rh2-N8	2.0107(5)	2.07448
Rh2-N10	2.253(5)	2.27658
N1-Rh1-Rh2-N2	-17.7(2)	15.54491
N7-Rh1-Rh2-N8	-23.3(4)	23.06920

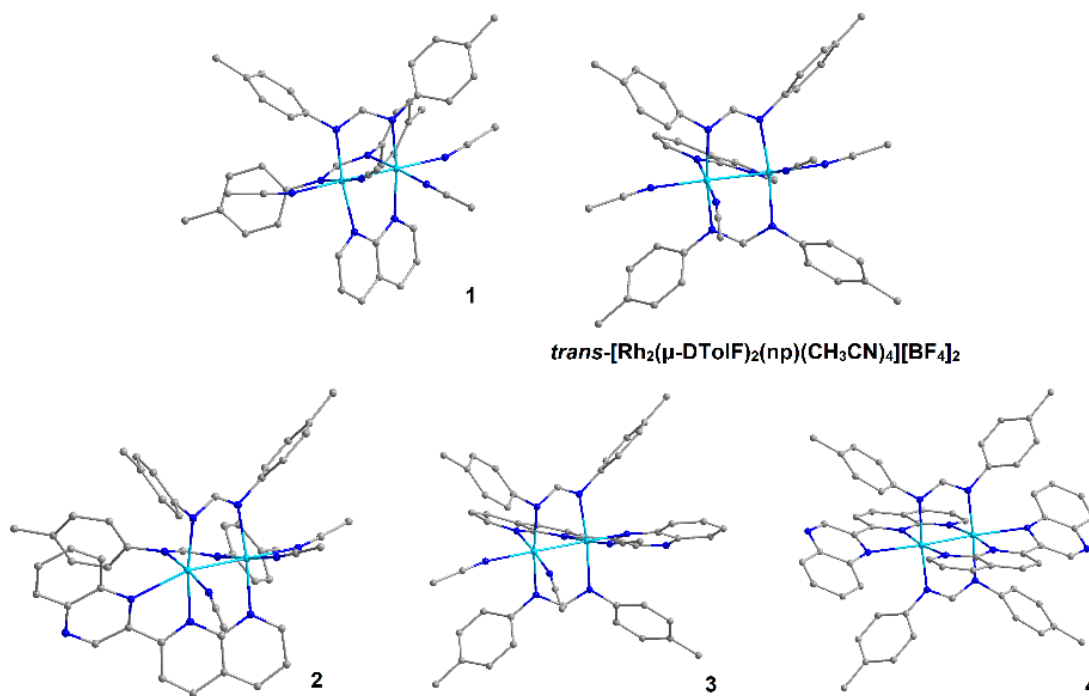
**Table IV-4 Continued.**

<b>IV.2</b>	<b>Crystal Structure</b>	<b>Calculated Structure</b>
Rh1-Rh2	2.49896(11)	2.54752
Rh1-N1	2.08012(8)	2.10206
Rh1-N3	2.01919(7)	2.05757
Rh1-N5	2.05126(7)	2.11759
Rh1-N7	2.02666(7)	2.07134
Rh1-N9	2.36268(10)	2.48898
Rh2-N2	2.03019(7)	2.06982
Rh2-N4	2.04267(8)	2.06712
Rh2-N6	2.06483(8)	2.13117
Rh2-N8	2.02504(9)	2.06785
Rh2-N10	2.16872(9)	2.25120
N1-Rh1-Rh2-N2	18.9516(7)	-16.71713
N7-Rh1-Rh2-N8	21.8281(8)	-23.10073
<b>IV.3</b>	<b>Crystal Structure</b>	<b>Calculated Structure</b>
Rh1-Rh2	2.50067(14)	2.54390
Rh1-N1	2.06510(11)	2.11350
Rh1-N3	2.01532(11)	2.04261
Rh1-N5	2.06183(11)	2.10568
Rh1-N7	2.00758(12)	2.02760
Rh1-N9	2.27573(14)	2.30749
Rh2-N2	2.06949(10)	2.11147
Rh2-N4	2.02915(12)	2.07729
Rh2-N6	2.05291(10)	2.09704
Rh2-N8	2.01714(12)	2.02834
Rh2-N10	2.14851(12)	2.29084
N1-Rh1-Rh2-N2	-19.1122(7)	-16.45061
N7-Rh1-Rh2-N8	-23.2238(9)	-23.29449
<b>IV.4<sup>1</sup></b>	<b>Crystal Structure</b>	<b>Calculated Structure</b>
Rh1-Rh1'	2.4942(8)	2.50614
Rh1-N1	2.0649(6)	2.11586
Rh1-N3	2.0083(5)	2.05869
Rh1-N2	2.0696(6)	2.10333
Rh1-N4	2.0635(6)	2.10679
Rh1-N5	2.3648(7)	2.50525
Rh1'-N2	2.0696(6)	2.10698
Rh1'-N4	2.0635(6)	2.11571
Rh1'-N1'	2.0649(6)	2.11146
Rh1'-N3'	2.0083(5)	2.04967
Rh1'-N5'	2.3648(7)	2.37627
N1-Rh1-Rh1'-N2	-1.3337(4)	-8.45476
N4-Rh1-Rh1'-N3'	6.922(2)	-3.54168

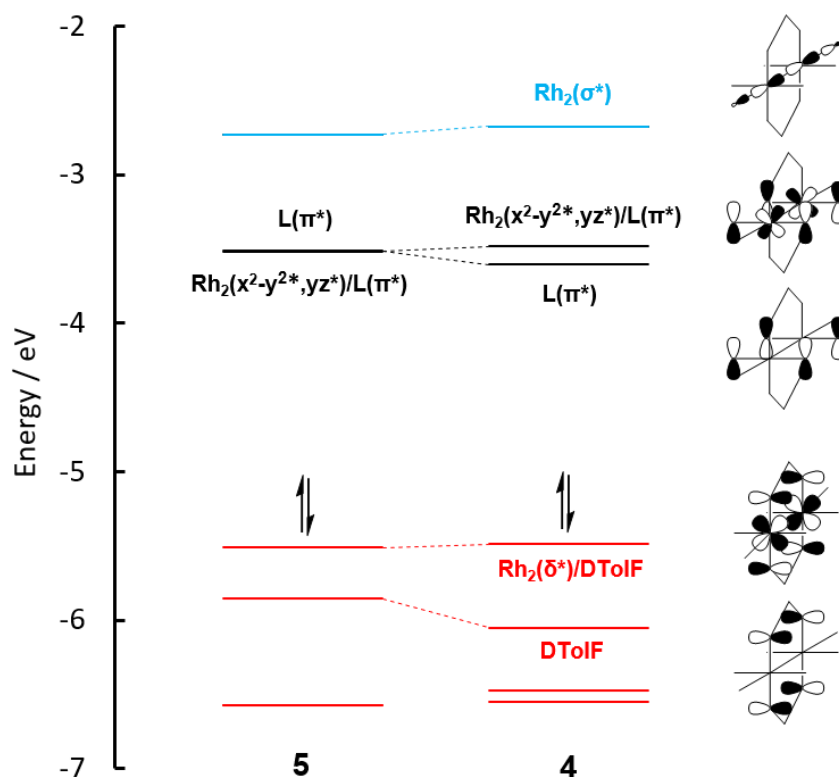
<sup>1</sup>The molecule resides on a special position that contains an inversion center, therefore the asymmetric unit only displays half of the molecule. The atoms marked with an apostrophe correspond to atoms generated by symmetry.



**Figure IV.8** Example of the intramolecular  $\pi$ - $\pi$  stacking interactions of **IV.3**. a) top and b) side views.



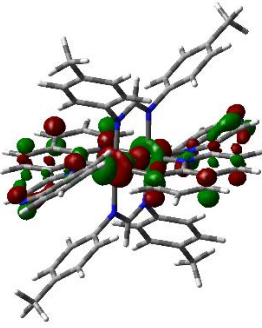
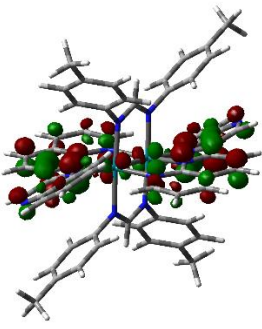
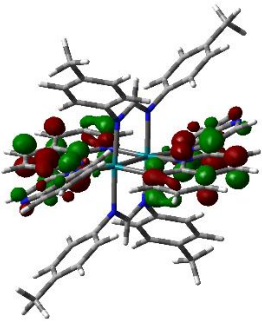
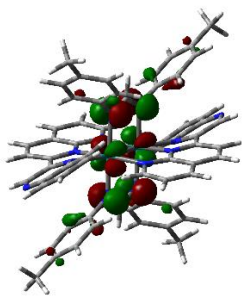
**Figure IV.9** Gas-phase optimized structures of **IV.1–4** and of the computationally modeled *trans*-[Rh<sub>2</sub>(DTolF)<sub>2</sub>(np)(CH<sub>3</sub>CN)<sub>4</sub>][BF<sub>4</sub>]<sub>2</sub>.



**Figure IV.10** Calculated MO diagrams for the *cis* (IV.5) and *trans* (IV.4) compounds.

The calculations reveal that the HOMOs in IV.1–4 possess 25–34%  $\text{Rh}_2(\delta^*)$  and 63–72% formamidate contributions (Table IV-7). These results are in accord with related dirhodium formamidate complexes including the previously reported compound IV.5 which has a 31% contribution from the  $\text{Rh}_2(\delta^*)$  MO and 63% from the formamidate ligand.<sup>63, 74</sup> The LUMOs of IV.1–4 are primarily localized on the  $\pi$ -accepting ligand, np or qxnp, as expected from prior work.<sup>74, 63</sup> Compound IV.1 has an orbital contribution to the LUMO of only 66% from the np ligand, whereas the LUMOs of IV.2–4 possess qxnp contributions that range from 89% to 94%.

**Table IV-5** Electron density maps for **IV.4** from its HOMO-1 to its LUMO+2 with an isovalue = 0.04

LUMO+2	 A 3D ball-and-stick model of a molecule with red and green electron density lobes. The LUMO+2 orbital shows a complex distribution of lobes, with a prominent positive lobe (red) on the right side and a negative lobe (green) on the left side, extending across the central part of the molecule.
LUMO+1	 A 3D ball-and-stick model of a molecule with red and green electron density lobes. The LUMO+1 orbital shows a similar distribution to LUMO+2, with a positive lobe (red) on the right and a negative lobe (green) on the left, but with slightly different lobe shapes and positions.
LUMO	 A 3D ball-and-stick model of a molecule with red and green electron density lobes. The LUMO orbital shows a positive lobe (red) on the right and a negative lobe (green) on the left, with a more concentrated distribution compared to the higher energy orbitals.
HOMO	 A 3D ball-and-stick model of a molecule with red and green electron density lobes. The HOMO orbital shows a positive lobe (red) on the right and a negative lobe (green) on the left, with a more localized distribution compared to the LUMO orbitals.

**Table IV-5** Continued.

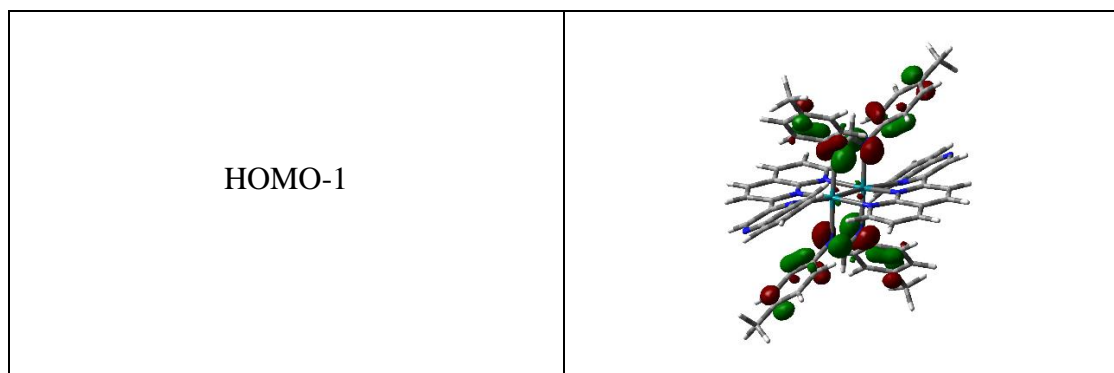


**Table IV-6.** Vertical energies of the singlet excited states, oscillator strengths,  $f$ , and major orbital contributions<sup>a</sup> calculated for **IV.4** and **IV.5** in acetonitrile (H = HOMO; L = LUMO).<sup>b</sup>

Excited State	<b>IV.4</b>	<b>IV.5</b>
1	10,661 cm <sup>-1</sup> (938 nm), $f = 0.018$ , H → L (100%)	11,390 cm <sup>-1</sup> (878 nm), $f = 0.020$ , H → L (92.2%)
2	10,858 cm <sup>-1</sup> (921 nm), $f = 0.000$ , H → L+1 (96.0%)	11,614 cm <sup>-1</sup> (861 nm), $f = 0.024$ , H → L+1 (96.0%)
3	14,881 cm <sup>-1</sup> (672 nm), $f = 0.000$ , H-1 → L (98.0%)	14,620 cm <sup>-1</sup> (684 nm), $f = 0.028$ , H-1 → L (96.0%)
4	15,129 cm <sup>-1</sup> (661 nm), $f = 0.004$ , H-1 → L+1 (96%)	14,641 cm <sup>-1</sup> (683 nm), $f = 0.001$ , H-1 → L+1 (68.9%) H → L+2 (24.0%)

**Table IV-6** Continued.

5	15,576 cm <sup>-1</sup> (642 nm), <i>f</i> = 0.000, H → L+2 (72.2%) H → L+4 (20.3%)	15,198 cm <sup>-1</sup> (658 nm), <i>f</i> = 0.008, H → L+2 (49.0%) H-1 → L+1 (29.2%)
6	17,606 cm <sup>-1</sup> (568 nm), <i>f</i> = 0.002, H-3 → L+1 (56.2%)	17,007 cm <sup>-1</sup> (588 nm), <i>f</i> = 0.009, H-4 → L (27.0%) H-2 → L (21.2%)
7	18,116 cm <sup>-1</sup> (552 nm), <i>f</i> = 0.000, H-3 → L (98.0%)	17,857 cm <sup>-1</sup> (560 nm), <i>f</i> = 0.001, H-5 → L+2 (28.1%) H-5 → L (22.1%)
8	18,248 cm <sup>-1</sup> (548 nm), <i>f</i> = 0.002, H-5 → L+1 (30.2%)	19,305 cm <sup>-1</sup> (518 nm), <i>f</i> = 0.012, H-1 → L+2 (75.7%)

<sup>a</sup>Only contributions of ≥ 20% are listed. <sup>b</sup>Yellow = ML-LCT (Rh/DTolF → qxnp), blue = LLCT (DTolF → qxnp), green = <sup>1</sup>MC (Rh<sub>2</sub>(π\*) → Rh<sub>2</sub>(σ\*)), orange = MLCT (Rh → qxnp), and purple = LMCT (DTolF → Rh<sub>2</sub>(σ\*)).

**Table IV-7** Orbital contributions for **IV.1–5** as predicted by TD-DFT calculations in acetonitrile (HOMO-5 through LUMO+6). <sup>a</sup>From *J. Am. Chem. Soc.* 2018, *140* (15), 5161.

Orbital	IV.1	IV.2	IV.3
HOMO-5	71% Rh, 25% DTolF	76% Rh, 14% DTolF, 8% qxnp	75% Rh, 15% DTolF, 8% qxnp
HOMO-4	86% Rh, 8% DTolF, 7% MeCN	75% Rh, 12 % DTolF, 11% qxnp	75% Rh, 13% qxnp, 7% MeCN
HOMO-3	25% Rh, 72% DTolF	17% Rh, 80% DTolF	35% Rh, 63% DTolF
HOMO-2	20% Rh, 78% DTolF	31% Rh, 64% DTolF	19% Rh, 79% DTolF
HOMO-1	8% Rh, 89% DTolF	7% Rh, 90% DTolF	93% DTolF
HOMO	32% Rh, 66% DTolF	29% Rh, 66% DTolF	25% Rh, 72% DTolF
LUMO	7% Rh, 27% DTolF, 66% np	9% Rh, 89% qxnp	7% Rh, 90% qxnp
LUMO+1	67% Rh, 13% DTolF, 17% MeCN	44% Rh, 47% qxnp	17% Rh, 78% qxnp
LUMO+2	30% Rh, 17% DTolF, 48% np, 5% MeCN	37% Rh, 55% qxnp	58% Rh, 27% qxnp, 8% MeCN
LUMO+3	36% Rh, 27% DTolF, 29% np, 7% MeCN	10% Rh, 88% qxnp	10% Rh, 86% qxnp
LUMO+4	46% Rh, 39% DTolF, 12% MeCN	44% Rh, 27% DTolF, 26% qxnp	55% Rh, 19% DTolF, 19% qxnp
LUMO+5	34% Rh, 25% DTolF, 40 % np	47% Rh, 31% DTolF, 17% qxnp	52% Rh, 27% DTolF, 12% qxmp
LUMO+6	37% Rh, 54% DTolF, 7% MeCN	28% Rh, 7% DTolF, 64% qxnp	18% Rh, 12% DTolF, 67% qxnp



**Table IV-7** Continued.

Orbital	IV.4	IV.5 <sup>a</sup>
HOMO-5	58% Rh, 34% DTolF, 7% qxnp	81% Rh, 13% DTolF
HOMO-4	53% Rh, 39% DTolF, 8% qxnp	59% Rh, 25% DTolF, 16% qxnp
HOMO-3	79% Rh, 17% DTolF	38% Rh, 56% DTolF
HOMO-2	6% Rh, 92% DTolF	40% Rh, 53% DTolF
HOMO-1	7% Rh, 90% DTolF	90% DTolF
HOMO	34% Rh, 63% DTolF	31% Rh, 63% DTolF
LUMO	94% qxnp	13% Rh, 84% qxnp
LUMO+1	15% Rh, 82% qxnp	94% qxnp
LUMO+2	35% Rh, 60% qxnp	48% Rh, 46% qxnp
LUMO+3	96% qxnp	95% qxnp
LUMO+4	42% Rh, 53% qxnp	35% Rh, 59% qxnp
LUMO+5	93% qxnp	13% Rh, 85% qxnp
LUMO+6	58% Rh, 16% DTolF, 26% qxnp	95% qxnp

The *trans* bis-substituted compound **IV.4** displays a nearly perfectly eclipsed configuration when viewed down the Rh-Rh bond (Figure IV.4a) while the other complexes exhibit more distorted structures due to the steric strain caused by the *p*-tolyl moieties of the formamidinate bridging ligands as well as the presence of intramolecular  $\pi$ -stacking interactions between the quinoxalinylligands and the *p*-tolyl groups (Figure IV.8). The eclipsed conformation of **IV.4** increases the electron donation from the electron-rich bridging ligands to the Rh<sub>2</sub>( $\delta^*$ ) MO which raises the energy of the HOMO

leading to a weaker  $\sigma$ -bond. As a consequence, this results in a longer Rh-Rh bond of 2.4942(8) Å when compared to **IV.5**, Rh-Rh = 2.4498(2) Å.<sup>74</sup> This result is in agreement with experimental observations, namely, that **IV.4** is more easily oxidized than **IV.5** by 0.08 V (Table IV-3). In addition, the elongation of the Rh-Rh bond and concomitant shortening of the Rh-N<sub>ax</sub> distance is a reflection of an increase in the axial  $\sigma$ -donation of the quinoxalinylyl moiety which raises the energy of the Rh<sub>2</sub>( $\sigma^*$ ) molecular orbital. The LUMO of **IV.4** is primarily qxnp in character and is calculated to lie at -0.0898 eV lower in energy than the qxnp-based LUMO of **IV.5**. This finding is consistent with the more positive first reduction potential of **IV.4** by +0.09 V compared to that of **IV.5** (Table IV-3). This difference is attributed to the variation in orbital overlap between **IV.4** and **IV.5**; the Rh<sub>2</sub>( $\delta^*$ ) is interacting with two formamidinate bridging ligands in **IV.4**, whereas, in **IV.5**, two lobes of this orbital are shared by the formamidinate ligands (Table IV-5). This difference in participation of the dirhodium core in bonding to the formamidinate ligands translates to increased electron density on the qxnp ligands positioned *trans* to DTolF in the *cis* isomer **IV.5**, rendering the compound more difficult to reduce.

The lowest energy transition observed in the steady state absorption spectrum of **IV.4** appears in the near-IR region, extending beyond 950 nm with a maximum at 832 nm, which is red-shifted by 1,170 cm<sup>-1</sup> as compared to **IV.5**. The TD-DFT calculations predict this transition at 938 nm and 878 nm for **IV.4** and **IV.5**, respectively, and reveal that it is primarily HOMO-LUMO in nature and <sup>1</sup>ML-LCT in character. The difference in energies between the calculated and experimentally determined <sup>1</sup>MLCT bands are consistently red-shifted in both compounds which can be attributed to the limitations of DFT

calculations.<sup>144</sup> Therefore, the smaller calculated and experimentally measured HOMO-LUMO gap in **IV.4** can be associated directly with the red shift of the lowest energy transition relative to that of **IV.5**. The second lowest energy transition is predicted to occur at 661 nm for **IV.4** and 684 nm for **IV.5** and is HOMO-1 → LUMO+1 in character (Table IV-6).

In order to elucidate the mechanism of DTolF migration, gas-phase single-point energy calculations were undertaken for **IV.2** and **IV.3** and for two possible intermediates (Figures IV.11 and 12). The calculated species, *cis/trans*-[Rh<sub>2</sub>(μ-DTolF)(κ-DTolF)(qxnP)(MeCN)<sub>3</sub>]<sup>2+</sup> and *cis/trans*-[Rh<sub>2</sub>(μ-DTolF)(κ-DTolF)(np)(MeCN)<sub>3</sub>]<sup>2+</sup>, are proposed as intermediates in a pathway for migration of the formamidinate bridging ligand. The logical first step of the migration is Rh<sub>1</sub>-N<sub>1</sub> bond scission, rotation along the remaining Rh<sub>2</sub>-N<sub>2</sub> bond, and binding of the N<sub>1</sub> to Rh<sub>2</sub> in the axial position by displacement of the axial MeCN molecule. The second step is postulated to involve binding of N<sub>2</sub> to the Rh<sub>2</sub>, but in a *trans* configuration, to produce the mono-substituted *trans* isomer **IV.3** (Figure IV.14). The calculated energies for these intermediates and the *cis/trans*-[Rh<sub>2</sub>(μ-DTolF)<sub>2</sub>(qxnP)(MeCN)<sub>3</sub>]<sup>2+</sup> and *cis/trans*-[Rh<sub>2</sub>(DTolF)<sub>2</sub>(np)(MeCN)<sub>2</sub>]<sup>2+</sup> complexes indicate that axial chelation of the qxnP ligand has a profound effect on the energies of these axially-bound intermediates due to the *trans* influence across the Rh<sub>2</sub>(σ) bond from the quinoxalinylyl moiety. The energies of the intermediates are, on average, 3.5 kcal/mol lower in energy for the qxnP-bearing complex. Most importantly, there is a significant difference between the energies of the *cis* and *trans* complexes when qxnP is the π-accepting ligand (about 5 kcal/mol higher than the np complex), which supports the notion

that the axial blocking nature of the qxnp ligand is required for the migration of the formamidinate bridging ligands to take place. These calculations are consistent with experimentally observed phenomena reported in axially blocked Mo-Mo complexes in which axial chelation allowed for the synthesis of the *trans* isomers.<sup>183, 184</sup>

The energies of complexes **IV.4** and **IV.5** were also calculated and compared with those of **IV.2** and **IV.3** as a function of a stepwise qxnp addition reaction (Figure IV.12). The computations indicate that there is no significant energy difference between the *cis* and *trans* bis-substituted compounds **IV. 4** and **IV.5**, which indicates that both isomers should be synthetically accessible. There is, however, a large difference in energy between **IV.2** and **IV.3** which allows for the isolation of these compounds and the formation of **IV.5** and **IV.4**, respectively upon addition of a second equivalent of qxnp ligand. The calculated energies are in agreement with experimental observations regarding the isolation of **IV.2** and **IV.3**, for which a significant amount of complex **IV.5** is obtained due to the energetically downhill nature of the reaction.

The synthesis of the final *trans* complex **IV.4** does not occur by treating **IV.3** with one equivalent of qxnp ligand in refluxing acetonitrile. In order to gain understanding into the synthetic requirements for this reaction, energy calculations were performed for **IV.2** and **IV.3** as functions of the Rh-MeCN<sub>ax</sub> and Rh-MeCN<sub>eq</sub> bonds (Table IV-8), the results of which indicate a significant difference in the equatorial acetonitrile binding energies for the two isomers. Compound **IV.3** has weaker calculated axial interaction energies and stronger equatorial Rh-N interactions for the acetonitrile ligands than those of complex **IV.2**. This behavior is consistent with the geometric arrangement of the formamidinate

bridging ligands. In **IV.2**, the formamidinate ligand, known to exert a strong *trans* effect, facilitates Rh-MeCN<sub>eq</sub> ligand exchange with the  $\pi$ -accepting ligands.<sup>12</sup> Compound **IV.3** has a marginally stronger Rh-MeCN<sub>eq</sub> bond based the bond distances and the results of DFT calculations and requires higher energies to promote ligand exchange, consistent with experimental observations. In this case it was necessary to use a non-coordinating solvent with a higher boiling point to obtain the desired bis-substituted *trans* complex **IV.4**.

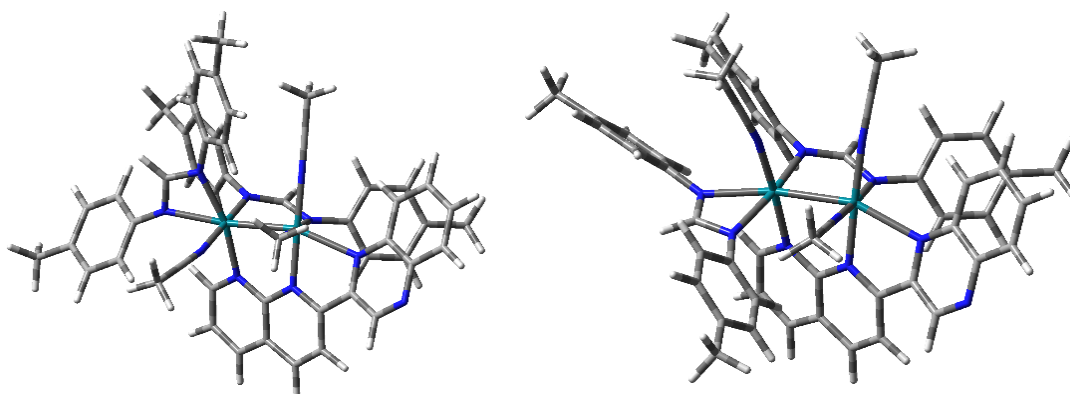


**Figure IV.11** Gas-phase optimized postulated intermediates for the migration of the DTolF bridging ligands through the axial position going from *cis* to *trans* monosubstituted Rh<sub>2</sub>(II,II) compounds.

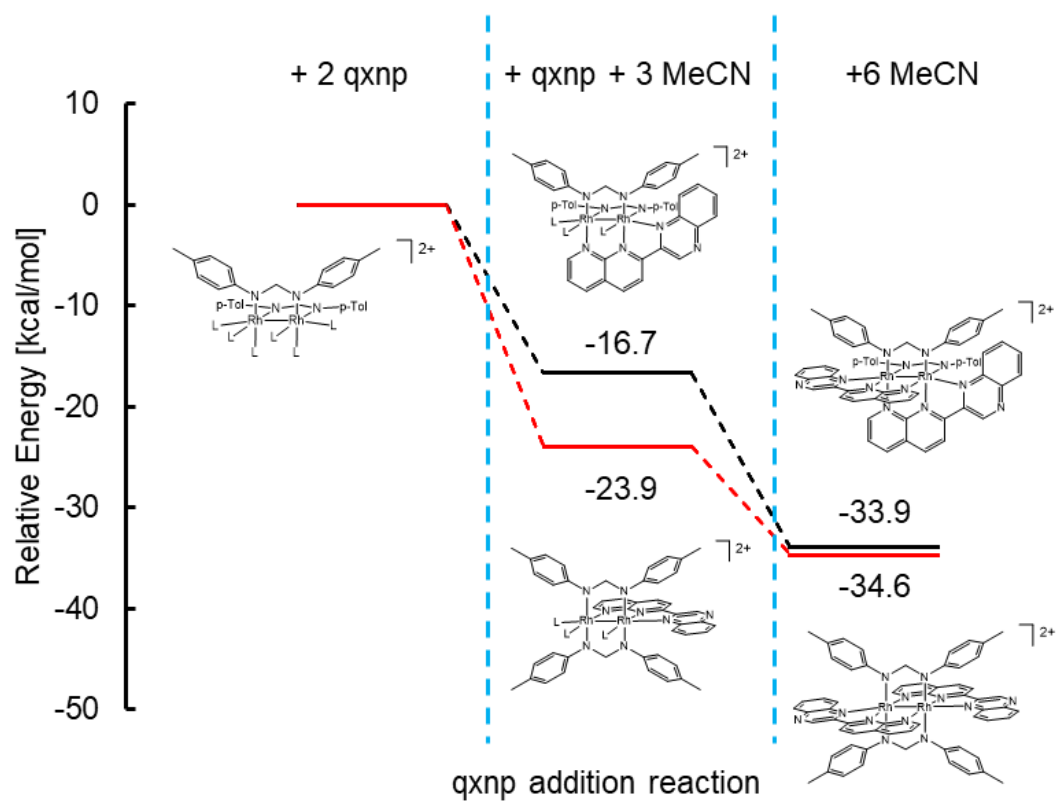


**Figure IV.12** Energies for the gas-phase optimized structures of the products from sequential addition of two equivalents of the qxnp ligand for the *cis* and *trans* isomers.

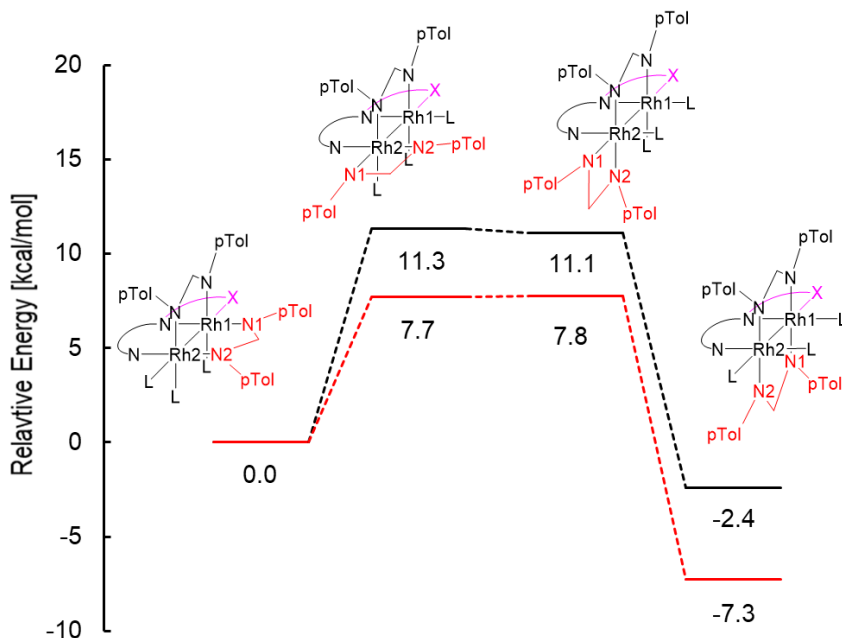


**Figure IV.13** Energies of the *cis*-[Rh<sub>2</sub>(DTolF)<sub>2</sub>(np)(MeCN)<sub>4</sub>][BF<sub>4</sub>]<sub>2</sub> and *cis*-[Rh<sub>2</sub>(DTolF)<sub>2</sub>(qxnp)(MeCN)<sub>3</sub>][BF<sub>4</sub>]<sub>2</sub> starting materials relative to the corresponding *trans* products, along with those of the proposed intermediates of DTolF migration, where L = MeCN and X is a solvent molecule (black line) or a quinoxalinylyl axially-blocking moiety (red line).

### Kinetic Studies

In order to determine the activation energy of the isomerization reaction from **IV.2** to **IV.3**, solutions of *cis*-[Rh<sub>2</sub>(μ-DTolF)<sub>2</sub>(μ-qxnp)(CH<sub>3</sub>CN)<sub>3</sub>][BF<sub>4</sub>]<sub>2</sub> in CD<sub>3</sub>CN-*d*<sub>3</sub> were placed in an oil bath at temperatures ranging from 64 – 80 °C (with 4 °C increments) and monitored by <sup>1</sup>H NMR spectroscopy. Owing to differences in the symmetry of the complexes and the resulting changes in the intramolecular π-π stacking interactions (Figure IV.8), the quinoxalinylyl moiety of the axial blocking ligand displays markedly

different chemical shifts for **2** and **3** that allow for the reaction to be followed by  $^1\text{H}$  NMR spectroscopy (Figure IV.16). For **2**, the area of the peak that corresponds to two hydrogen atoms of the quinoxalinylyl moiety at 9.74 ppm was set to a value of 2. The transformation of **IV.2** to **IV.3** was then referenced to the total area of the latter species, which exhibits a resonance at 9.64 ppm for the hydrogen atom in the quinoxalinylyl moiety. The percent transformation of **IV.2** was calculated and plotted over time and the rate of reaction for each temperature was obtained from a mono-exponential decay fitting (Figure IV.16b), which is consistent with the appearance of **IV.3**. The conversion takes place over 24 h in refluxing acetonitrile which allows for the isolation of complex **IV.3** at relatively short reactions times. The reaction is significantly slower at 60 °C, however, and requires four days to achieve full conversion of **IV.2** to **IV.3**. The reaction performed at 40 °C did not yield the *trans* isomer over a 24 h period and was used to isolate **IV.2**. An activation energy of 38 kcal/mol was determined from a linear fit of an Arrhenius plot of the logarithm of the observed rates of reaction versus reciprocal temperature (Figure IV.19). This activation energy is consistent with a rate-limiting step involving Rh-N<sub>DTolF</sub> bond dissociation which is proposed as the first step for the DTolF migration, in agreement with the computationally calculated bond energy of 54 kcal/mol for the Rh-N<sub>DTolF</sub> bond as well as previously reported Rh-N<sub>eq</sub> energies of 33 kcal/mol.<sup>185, 186</sup>



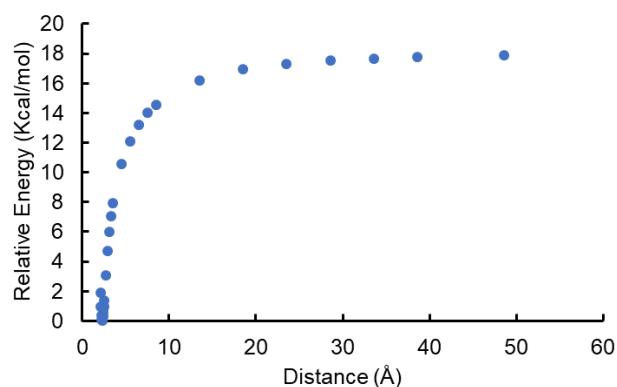


**Figure IV.14** Example of the determination of the bond strength for the trans-equatorial(2) acetonitrile molecule in the *trans* isomer intermediates.

**Table IV-8** Summary of the bond energies in kcal/mol for the equatorial and axial acetonitrile solvent molecules.

	IV.4	IV.5	IV.5 - 4
ax	-17.8043	-19.9398	-2.13554
eq1	-34.3491	-31.5854	2.763615
eq2	-34.0196	-29.4018	4.617718

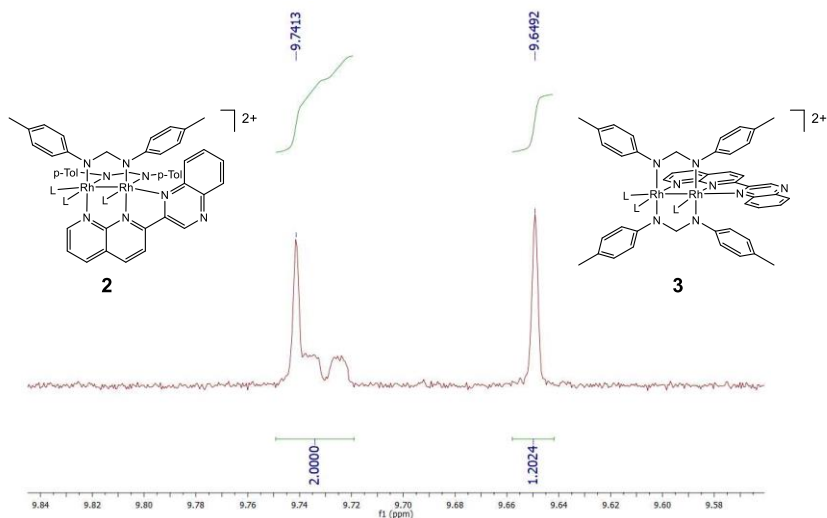


**Figure IV.15** Example of the 9.84-9.58 ppm portion of the  $^1\text{H}$  NMR spectrum for the isomerization reaction of **IV.2**  $\rightarrow$  **IV.3** in acetonitrile at 80 °C after 8 hours.

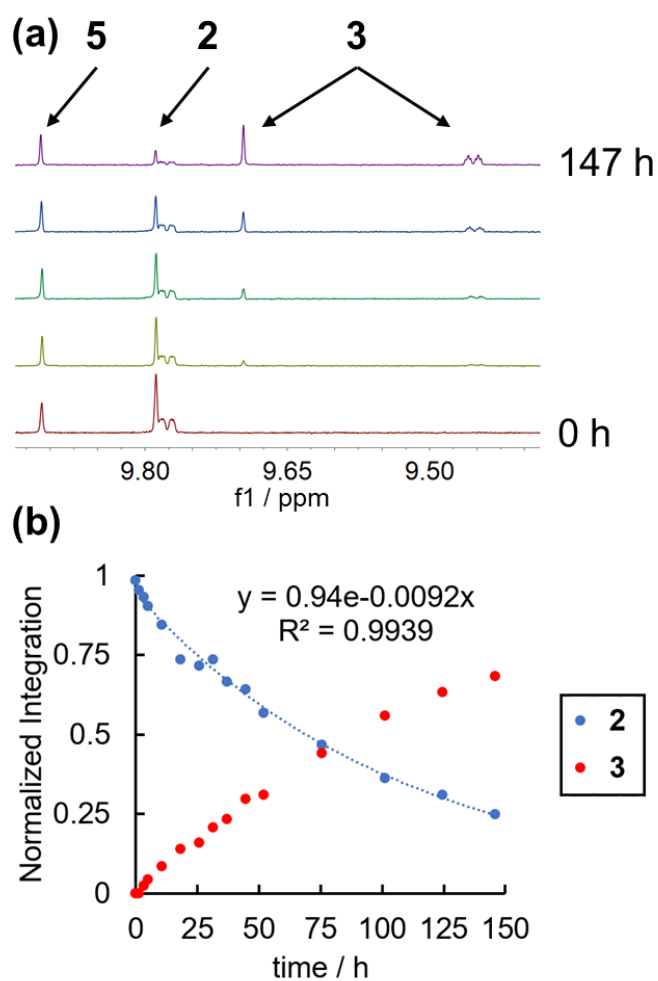


**Figure IV.16** (a) Selected <sup>1</sup>H NMR spectroscopic traces following the isomerization reaction from **IV.2** to **IV.3** and (b) monoexponential decay of the normalized integration for the conversion of **IV.2** (blue) to **IV.3** (red) at 68 °C in acetonitrile.

### *Time-Resolved Spectroscopy*

Femtosecond transient absorption spectroscopy was performed on **IV.4** to investigate the excited states properties of the two complexes, (Figure IV.17b) and compared with the results for **IV.5** (Figure IV.17a). The <sup>1</sup>ML-LCT Rh<sub>2</sub>(δ<sup>\*</sup>)/DTolF(π<sup>\*</sup>) → qxnp (π<sup>\*</sup>) excited state of **IV.4** is populated upon 600 nm excitation

(2.5  $\mu\text{J}/\text{pulse}$ , IRF = 85 fs), leading to a broad absorption at  $\sim 420$  nm. This state decays with a lifetime of 3 ps to the corresponding  $^3\text{ML-LCT}$  excited state, and the latter regenerates the ground state with  $\tau = 405$  ps in acetonitrile. The kinetic trace of the signal at 420 nm was fitted biexponentially to obtain the lifetimes of the two states (Figure IV.18). The singlet and triplet lifetimes for **IV.4**,  $\tau_S = 3$  ps and  $\tau_T = 405$  ps, respectively, are shorter than those of **IV.5**,  $\tau_S = 8$  ps and  $\tau_T = 7.2$  ns (Table IV-3). The Energy Gap Law predicts that the lower energy  $^3\text{ML-LCT}$  state in **IV.4** should lead to faster radiationless decay and a shorter  $^3\text{ML-LCT}$  lifetime as compared to **IV.5**, but the small energy difference between the two compounds would only be expected to result in a decrease to  $\sim 6$  ns in **IV.4** from 7 ns in **IV.5**. Instead, the shorter lifetimes of the excited states of **IV.4** are attributed to its longer Rh-Rh bond as compared to **IV.5**, which results in a more accessible metal-centered state that facilitates fast deactivation.

To evaluate potential application of **IV.4** and **IV.5** as dyes for DSSCs, photoinduced charge transfer from a reversible electron donor, *p*-phenylenediamine (*p*-PD) with  $E_{1/2} = + 0.28$  V vs Ag/AgCl, was examined by nanosecond transient absorption spectroscopy (Figure IV.10). Upon 600 nm excitation (5 mJ/pulse, IRF = 6 ns), a mixture of **IV.4** and *p*-PD (20 mM) displays a long-lived absorption difference spectrum consistent with the formation of the *p*-PD radical cation, with an absorption maximum at 460 nm.<sup>74</sup> This charge transfer is also observed for **IV.5** but the signal is  $\sim 30$ -fold stronger for the *p*-PD radical cation under the same experimental conditions. The differences in the efficiencies of bimolecular charge transfer between **IV.4** and **IV.5** are attributed to the shorter triplet lifetime of **IV.4**. The reductive quenching of **IV.4**, with a ground state

reduction potential of  $-0.34$  V vs Ag/AgCl (Table IV-3), by *p*-PD requires that the  $^3\text{ML-LCT}$  state,  $E_T$ , of **IV.4** lie at least  $0.62$  eV above the ground state. This value for  $E_T$  is consistent with those measured for related  $\text{Rh}_2(\text{II,II})$  complexes,  $\sim 1.1$  eV.<sup>63</sup>

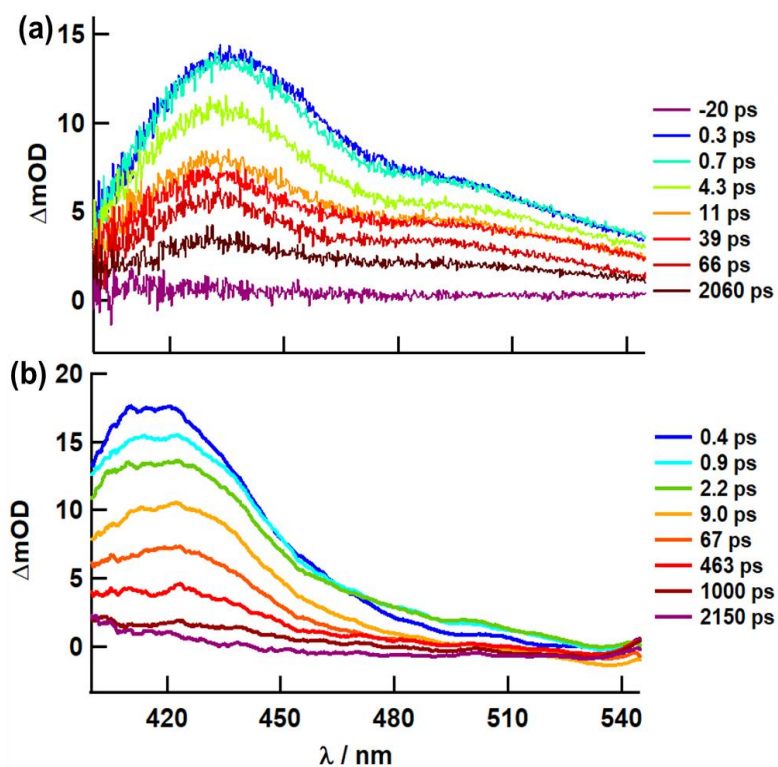


**Figure IV.17** Transient absorption spectra of (a) the *cis* isomer **IV.5** ( $\lambda_{\text{ex}} = 720$  nm,  $2.5 \mu\text{J}$ ) and (b) the *trans* isomer **IV.4** ( $\lambda_{\text{ex}} = 600$  nm,  $2.5 \mu\text{J}$ ).

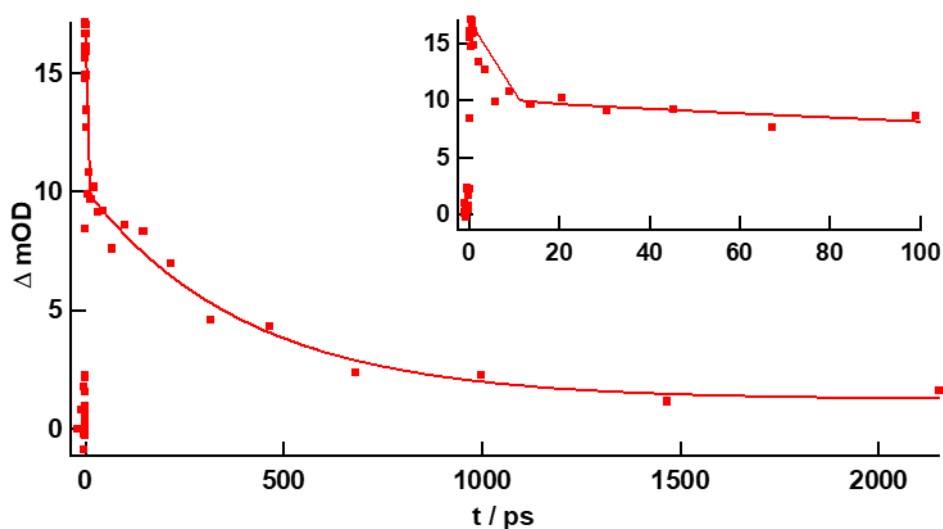


**Figure IV.18** Kinetic trace ( $\lambda_{ex} = 600$  nm,  $2.5 \mu J/pulse$ ) of **IV.4** in  $CH_3CN$  at 420 nm (at longer time); insert (at shorter time).

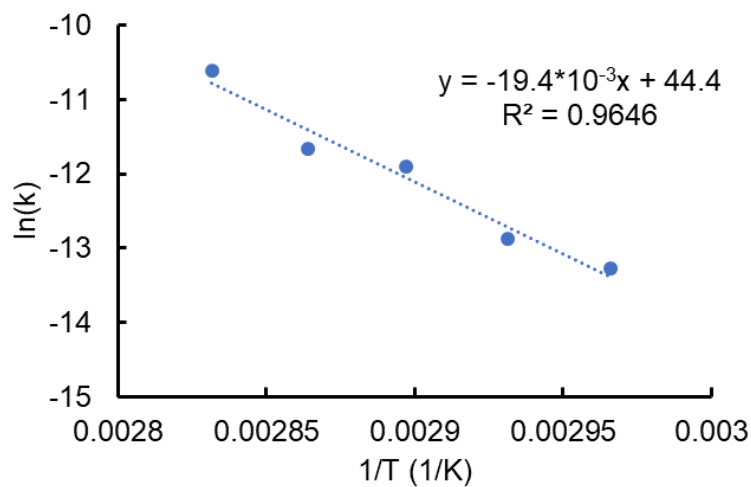


**Figure IV.19** Arrhenius plot for the calculation of the activation energy of the isomerization reaction for conversion of **IV.2** into **IV.3** in acetonitrile.

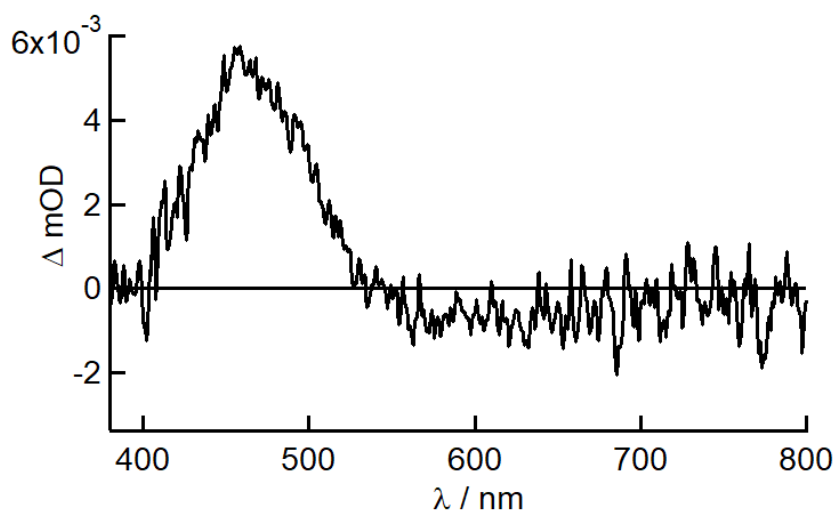


**Figure IV.20** Transient absorption spectrum of the *trans* isomer **IV.4** in acetonitrile (130  $\mu\text{M}$ ) in the presence of *p*-phenylenediamine (1:150) collected at 1  $\mu\text{s}$  after the 600 nm excitation pulse (IRF = 6 ns, 5 mJ).

## Conclusions

A series of four new dirhodium formamidinate complexes featuring  $\pi$ -accepting ligands was described in detail. A particularly important finding is the isolation of the first *trans*-formamidinate dicationic complex, **IV.4**, by careful control of the reaction conditions used to prepare the *trans* precursor, **IV.2**, in favor of the *cis* isomer. Compound **IV.4** displays a panchromatic absorption profile that extends into the near-IR region with a maximum at 832 nm that corresponds to a  $^1\text{ML-LCT}$  transition as predicted by TD-DFT. This absorption is red-shifted with respect to that of the corresponding *cis* complex **IV.5**. The  $^1\text{ML-LCT}$  and  $^3\text{ML-LCT}$  excited state lifetimes of **IV.4** were measured and found to be 3 ps and 0.4 ns, respectively, by transient absorption spectroscopy. Although these lifetimes are shorter than those of the *cis* analog, the  $^3\text{ML-LCT}$  is sufficiently long-lived to oxidize *p*-phenylenediamine in solution, leading to an excited state energy of  $\geq 0.62$  eV. The

smaller HOMO-LUMO gap of **IV.4** as compared to **IV.5** is attributed to its eclipsed configuration, which leads to better orbital overlap and a concomitant increase in energy of the Rh-containing MOs. The synthesis of **IV.4** was rendered possible by implementing the use of axial blocking ligands which trigger the migration of a bridging formamidinate ligand to yield the *trans* isomer in the presence of one equivalent of the qxnp ligand. Calculations support the feasibility of this approach as a general route to access *trans* isomers. It is especially noteworthy that a change in the arrangement of ligands in these molecules has little effect on photophysical and excited state redox properties, indeed the parentage of the transitions remains the same for the *cis* and *trans* isomers and the excited states of both species are reducing enough to allow them to participate in electron transfer reactions. The results of this study pave the way for a systematic investigation of the photophysical properties of hitherto unexplored *trans* isomers for potential sensitization of p-type semiconductors with low energy light in DSSCs and related solar energy conversion applications. Moreover, these new geometries can be used as new formamidinate-containing scaffolds as building blocks for supramolecular architectures with potentially interesting photophysical properties.

CHAPTER V  
ASYMMETRIC DIRHODIUM COMPLEXES AS PHOTOCATALYSTS FOR H<sub>2</sub>  
PRODCUTION WITH LOW-ENERGY LIGHT

**Introduction**

A series In order to address the increasing global energy demands, the quest for new and more efficient carbon-neutral fuels and renewable energy sources is of paramount importance.<sup>45, 153-157</sup> Over the last several decades, the use of solar energy has risen to the top of the approaches to tackle this challenge. Solar energy can be used for the production of electricity as well as to catalyze reactions, such as H<sub>2</sub> generation, by injecting a holes or electrons into semiconductors through absorption of light by a sensitizer or chromophore-catalyst assembly. These technologies, however, present several drawbacks, a major one of which is the lack of absorption of the sensitizers in the low-energy region of the solar spectrum which limits the efficiencies of dye-sensitized solar cells (DSSCs)<sup>57, 92-95</sup> and dye-sensitized photoelectrosynthesis cells (DSPEC).<sup>96-98</sup>

Standard n-type DSSCs have theoretical efficiencies of 33% whereas n- and p-type tandem cells have theoretical efficiencies of 43%; the highest efficiencies that have been achieved, however, are well below those values.<sup>103, 114, 115</sup> This is partly due to the inability of the dyes to absorb light in the red and near-IR regions. The archetypal n-type sensitizer N3 dye, Ru(bpy)<sub>3</sub><sup>2+</sup> (bpy = 2,2'-biyridine), does not absorb significantly past 600 nm and yields devices with efficiencies that are on the order of 10-12%.<sup>59, 163</sup> The dye with the highest current device is the SM315 porphyrin coupled to a Co(II/III) redox shuttle which



has an photocurrent efficiency (PCE) of 13%.<sup>60</sup> Since the PCE of current devices is rather low compared to the theoretical limits, an attractive alternative is the use of these devices for photoelectrosynthesis by employing a chromophore-catalyst assembly instead of a sensitizer. The first example of a hybrid molecular-semiconductor system for water splitting was developed in 1970 and consists of a TiO<sub>2</sub> semiconductor and an N3 dye as the sensitizer.<sup>187, 188</sup> Upon irradiation, the sensitizer in the presence of the dication methyl viologen (MV) transfers an electron to the semiconductor and oxidize water while catalyzing proton reduction at a separate platinum electrode in the presence of acid. A reasonable approach to improving the efficiency of these devices is to use chromophore-catalyst assemblies that have the ability to capture light while catalyzing H<sub>2</sub> production. There are many different approaches to form these types of assemblies. The cationic complex [(4,4'-(PO<sub>3</sub>H<sub>2</sub>)<sub>2</sub>bpy)<sub>2</sub>Ru(4-Mebpy-4'-bimpy)Ru(tpy)(OH<sub>2</sub>)]<sup>4+</sup> is an example of a typical covalently bonded assembly.<sup>65</sup> This compound can catalyze water splitting to form O<sub>2</sub> and H<sub>2</sub>, but it requires high energy irradiation ( $\lambda_{\text{irr}} = 455 \text{ nm}$ ) and does not take advantage of the full solar spectrum thereby decreasing its overall efficiency. In addition, pre-organized, covalently linked assemblies, although useful as a proof of concept, are synthetically challenging due to multi-step synthesis requirements and are produced in low yields. For these reasons, compounds that display panchromatic absorption profiles and which exhibit catalytic activity are very attractive candidates for these applications.

Dirhodium complexes are excellent candidates for these applications since they display panchromatic absorption profiles, are water and air stable, and are known to catalyze a myriad of reactions including proton reduction. Nocera and coworkers reported

several dirhodium complexes in which the catalytic center and the sensitizer are installed in the same unit.<sup>67, 69, 189-191</sup> As an example, the two-electron mixed-valence complex  $\text{Rh}_2^{0,\text{II}}(\text{tfepma})_2(\text{CNAd})_2\text{Cl}_2$  (CNAd = 1-adamantylisocyanide) produces  $\text{H}_2$  upon irradiation with a TON of 7 after 144 hours of irradiation ( $\lambda_{\text{irr}} > 305 \text{ nm}$ ).<sup>68</sup> This compound, however, does not absorb past 550 nm and requires UV light irradiation to produce a significant quantity of hydrogen gas. Recently, our groups developed the series of axially-blocked dirhodium sensitizers *cis*- $[\text{Rh}_2(\text{DTolF})_2(\text{L})_2][\text{BF}_4]_2$  (L = pynp (2-(pyridin-2-yl)-1,8-naphthyridine), qxnp (2-(1,8-naphthyridin-2-yl)quinoxaline) or qnnp (2-(quinolin-2-yl)-1,8-naphthyridine) that display panchromatic absorption profiles which extend into the near-IR.<sup>74</sup> Owing to the rigidity imparted by the axial blocking ligands and deactivation of solvent-assisted non-radiative decay pathways, these compounds display relatively long-lived excited state lifetimes. In addition, they are able to participate in electron transfer reactions with electron donors from their excited states upon low energy light irradiation ( $\lambda_{\text{irr}} = 600 \text{ nm}$ ). These molecules, however, are not capable of catalyzing reactions due to the blockage of the axial sites by the  $\pi$ -accepting ligands which renders the bimetallic core inaccessible. Therefore, complexes with panchromatic absorption profiles with accessible metal sites for catalysis constitute an attractive and unexplored area of research.

The present study focuses on the synthesis and characterization of two new asymmetric cationic dirhodium complexes with improved panchromatic absorption that extends into the near-IR and excited state properties that make them suitable for photocatalytic hydrogen production. The compounds *cis*- $[\text{Rh}_2(\text{DTolF})_2(\text{L})(\text{np})][\text{BF}_4]_2$  (L

= qxnp (**V.1**) and qnnp (**V.2**)) were prepared and their properties were compared to *cis*-[Rh<sub>2</sub>(DTolF)<sub>2</sub>(qxnp)<sub>2</sub>][BF<sub>4</sub>]<sub>2</sub> and *cis*-[Rh<sub>2</sub>(DTolF)<sub>2</sub>(np)<sub>2</sub>][BF<sub>4</sub>]<sub>2</sub> (Figure V.1). The axially blocking ligands, namely qxnp and qnnp, impart rigidity to the complexes and restrain the Rh-Rh bond in the excited state while blocking access to solvent molecules. The axial blockage of the complexes can, therefore, lengthen the lifetime of their excited state through deactivation of non-radiative decay pathways. In addition, a second, non-axially blocking  $\pi$ -accepting ligand np was selected to allow for one accessible axial position which can participate in catalytic reactions.

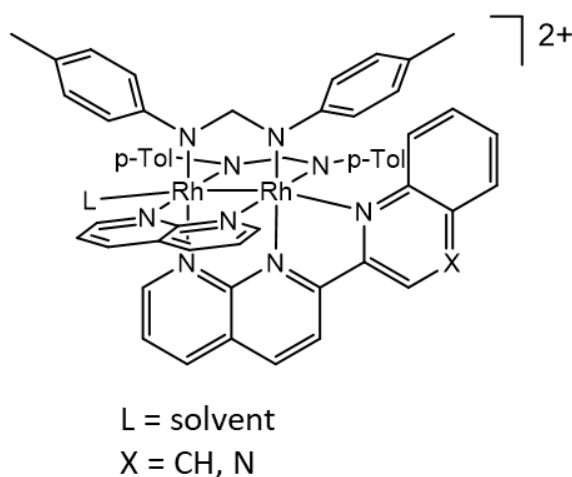


**Figure V.1** Schematic representation of the molecular structures of complexes **V.1** and **V.2**.

## Experimental Section

### Materials

The starting material  $[\text{RhCl}(\text{COD})]_2$  was purchased from Pressure Chemicals and used as received. The partially solvated compound  $\text{cis}-[\text{Rh}_2(\text{DTolF})_2(\text{MeCN})_6][\text{BF}_4]_2$  was synthesized by addition of two equivalents of the formamidinate ligand to  $[\text{RhCl}(\text{COD})]_2$  followed by oxidation with  $\text{AgBF}_4$  according to reported procedures.<sup>34</sup> Tetrabutylammonium hexafluorophosphate ( $\text{TBAPF}_6$ ) was purchased from Alfa Aesar. The ligands 2-(1,8-naphthyridin-2-yl)quinoxaline (qxnp) and 2-(quinolin-2-yl)-1,8-naphthyridine (qnp) were prepared according to reported procedures.<sup>74, 178</sup> The solvent acetonitrile was dried over 3 Å molecular sieves and distilled under a  $\text{N}_2$  atmosphere. The complexes were synthesized under a  $\text{N}_2$  atmosphere using standard Schlenk techniques. Additional manipulations of the products were performed in air.

$\text{cis}-[\text{Rh}_2(\mu\text{-DTolF})_2(\mu\text{-np})(\mu\text{-qxnp})][\text{BF}_4]_2$  (**V.1**). Equimolar quantities of  $\text{cis}-[\text{Rh}_2(\mu\text{-DTolF})_2(\mu\text{-np})(\mu\text{-qxnp})][\text{BF}_4]_2$  (101.6 mg, 0.095 mmol), np (12.2 mg, 0.094 mmol), and qxnp (24.4 mg, 0.094 mmol) were suspended in 20 mL of acetonitrile and refluxed for 24 hours in an oil bath at 90 °C. The resulting dark purple solution was concentrated to ~5 mL and copious amounts of diethyl ether were added to precipitate the product. The product was filtered through a fine frit and washed three times with 5 mL of diethyl ether. The product was obtained as a 110.3 mg mixture of **V.1**,  $\text{cis}-[\text{Rh}_2(\mu\text{-DTolF})_2(\mu\text{-np})_2][\text{BF}_4]_2$  and  $\text{cis}-[\text{Rh}_2(\mu\text{-DTolF})_2(\mu\text{-qxnp})_2][\text{BF}_4]_2$  which were separated by column chromatography using neutral alumina as the stationary phase and a gradient of 2 – 5% methanol in dichloromethane. The desired compound was collected in the second

band and evaporated to dryness to yield 39.7 mg (34.4% yield) of a purple powder.  $^1\text{H}$  NMR (499 MHz,  $\text{CD}_3\text{CN}$ )  $\delta$  10.72 (d,  $J = 40.2$  Hz, 2H), 9.67 (s, 1H), 8.72 (dd,  $J = 5.3$ , 1.3 Hz, 1H), 8.70 – 8.65 (m, 2H), 8.54 (ddd,  $J = 8.2$ , 6.9, 1.6 Hz, 2H), 8.49 (dd,  $J = 8.3$ , 1.6 Hz, 1H), 8.02 (dd,  $J = 8.4$ , 1.3 Hz, 1H), 7.87 (dd,  $J = 8.3$ , 5.3 Hz, 1H), 7.83 (ddd,  $J = 8.3$ , 6.8, 1.2 Hz, 1H), 7.71 – 7.65 (m, 2H), 7.33 – 7.29 (m, 2H), 7.17 (ddd,  $J = 8.4$ , 6.8, 1.4 Hz, 1H), 7.10 (d,  $J = 8.1$  Hz, 2H), 7.03 (dd,  $J = 8.8$ , 1.0 Hz, 1H), 6.95 – 6.89 (m, 4H), 6.71 (d,  $J = 8.2$  Hz, 2H), 6.27 (d,  $J = 8.2$  Hz, 2H), 6.20 (d,  $J = 8.2$  Hz, 2H), 6.12 (dd,  $J = 19.1$ , 7.1 Hz, 4H), 2.40 (s, 3H), 2.24 (s, 3H), 2.14 (s, 3H), 1.85 (s, 3H). HRMS (ESI-MS)  $m/z$ :  $[\text{M}]^{2+}$  ( $\text{C}_{54}\text{H}_{46}\text{N}_{10}\text{Rh}_2$ ) 520.0999 calc.  $[\text{M}]^{2+}$  ( $\text{C}_{54}\text{H}_{46}\text{N}_{10}\text{Rh}_2$ ) 520.1003.

*cis*- $[\text{Rh}_2(\mu\text{-DTolF})_2(\mu\text{-np})(\mu\text{-qnnp})][\text{BF}_4]_2$  (**V.2**). Quantities of *cis*- $[\text{Rh}_2(\mu\text{-DTolF})_2(\mu\text{-np})(\mu\text{-qxnnp})][\text{BF}_4]_2$  (100.3 mg, 0.094 mmol), np (12.1 mg, 0.093 mmol), and qnnp (23.9 mg, 0.093 mmol) were suspended in 20 mL of acetonitrile and refluxed in an oil bath at 90 °C for 24 hours. The dark purple solution was cooled and the solvent was evaporated to near dryness. Diethyl ether was used to precipitate the product which was collected by vacuum filtration on a fine frit to yield 98.6 mg of a dark blue powder. As in the case of **V.1**, the product was obtained as a mixture of **V.2** and the bis-substitution products *cis*- $[\text{Rh}_2(\mu\text{-DTolF})_2(\mu\text{-np})_2][\text{BF}_4]_2$  and *cis*- $[\text{Rh}_2(\mu\text{-DTolF})_2(\mu\text{-qnnp})_2][\text{BF}_4]_2$ . The desired product was obtained from evaporation of the second fraction from column chromatography using neutral alumina and 2–5% methanol in dichloromethane; 42.1 mg of **V.2** (36.9 % yield).  $^1\text{H}$  NMR (499 MHz,  $\text{cd}_3\text{cn}$ )  $\delta$  10.67 (d,  $J = 16.4$  Hz, 2H), 8.81 (dd,  $J = 5.3$ , 1.4 Hz, 1H), 8.58 (d,  $J = 8.8$  Hz, 1H), 8.51 (d,  $J = 7.7$  Hz, 2H), 8.46 (dd,  $J = 8.3$ , 1.7 Hz, 1H), 8.41 (dd,  $J = 8.6$ , 3.1 Hz, 2H), 8.20 (d,  $J = 8.7$  Hz, 1H), 7.90 (dd,  $J = 8.2$ , 1.2

Hz, 1H), 7.80 (dd,  $J = 8.2, 5.3$  Hz, 1H), 7.70 (dd,  $J = 8.1, 5.4$  Hz, 1H), 7.64 – 7.59 (m, 2H), 7.36 (dd,  $J = 8.1, 4.8$  Hz, 2H), 7.26 (dd,  $J = 8.2, 5.3$  Hz, 1H), 7.11 (ddd,  $J = 8.5, 5.1, 1.7$  Hz, 3H), 6.85 (d,  $J = 8.0$  Hz, 2H), 6.75 (d,  $J = 8.0$  Hz, 2H), 6.70 (d,  $J = 8.3$  Hz, 2H), 6.36 (d,  $J = 8.3$  Hz, 2H), 6.29 – 6.23 (m, 4H), 6.12 (d,  $J = 8.0$  Hz, 2H), 2.41 (s, 3H), 2.21 (s, 3H), 2.16 (s, 3H), 1.87 (s, 3H). HRMS (ESI-MS)  $m/z$ :  $[M]^{2+}$  ( $C_{54}H_{46}N_{10}Rh_2$ ) 519.6026 calc.  $[M]^{2+}$  ( $C_{55}H_{47}N_9Rh_2$ ) 519.6027.

#### *Instrumentation and methods*

$^1H$  NMR spectra were obtained on an Inova 500 MHz spectrometer; the chemical shifts were referenced to the residual peak of the residual  $CD_3CN-d_3$  deuterated solvent signal at 1.96 ppm. In addition, acid titrations with dilute DCl in  $D_2O$  were followed by  $^1H$  NMR for solutions of both complexes in  $CD_3CN-d_3$ . Electronic spectroscopy was performed on a Shimadzu UV-1601PC spectrophotometer in  $1 \times 1$  cm quartz cuvettes. Extinction coefficients in acetonitrile were determined in triplicate. An acid titration of a solution of the compounds in acetonitrile was followed by UV-Vis spectroscopy with a solution of TsOH in acetonitrile. The acid was added in amounts of 0.3 equivalents and the absorption profile was recorded. The equivalents of acid required to fully protonate the complex were determined from a plot of the absorbance at 581 nm as a function of the amount of acid added.

Electrochemical measurements for **V.1** and **V.2** ( $1 \times 10^{-3}$  M) were recorded under an inert atmosphere using dry acetonitrile and 0.1 M  $[n-Bu_4N][PF_6]$  as the supporting electrolyte with a CH Instruments electrochemical analyzer model CH1620A. A three-electrode cell was used with a Ag/AgCl reference electrode standardized to ferrocene ( $E_{1/2}$

= +0.55 V vs Ag/ AgCl), a Pt wire as the counter electrode, and a glassy carbon disk as the working electrode. High-resolution Electrospray Ionization mass spectrometry (ESI-MS) data were obtained in the Laboratory for Biological Mass Spectrometry at Texas A&M University using a Thermo Scientific Q Exactive Focus. The sample was directly infused at a flow rate of 10  $\mu$ L/min. The Q Exactive Focus HESI source was operated in full MS in positive mode. The mass resolution was tuned to 17500 FWHM at  $m/z$  200, the spray voltage was set to 3.75 kV, and the sheath gas and auxiliary gas flow rates were set to 7 and 0 arbitrary units, respectively. The transfer capillary temperature was held at 250 °C and the S-Lens RF level was set at 50 v. Exactive Series 2.8 SP1/Xcalibur 4.0 software was used for data acquisition and processing.

Nanosecond transient absorption spectra were obtained on a setup that was previously reported.<sup>180</sup> The pump beam (~ 5 mJ) was generated using a BasiScan OPO (Spectra Physics) pumped with the third harmonic of an Nd:YAG laser (Spectra Physics, INDI-40) at a rate of 10 Hz and power of 130 mJ. The output of a continuous 150 W xenon arc lamp gated using a Uniblitz shutter was used as the probe. The pump and probe pulse were overlapped at a 90° geometry at the sample. Time-resolved absorption spectra were obtained on an Edinburgh LP980 spectrometer with an ICCD-based broadband camera. The kinetic traces were collected with a PMT and an oscilloscope. All transient absorption samples were deoxygenated prior to study and UV-Vis spectra were collected before and after to ensure no sample degradation occurred upon irradiation. All samples were prepared to an optical density of ~ 0.5 OD in acetonitrile at the 650 nm excitation in a 1

by 1 cm cell and all fits were performed as the sum of exponentials using Igor Pro (6.3) software with instrument response deconvolution.

Ultrafast transient absorption (fsTA) experiments were performed on a system previously described in detail.<sup>179</sup> Briefly, the output of a Ti:sapphire regenerative amplifier (Astrella 1K-USP, Coherent) was split to generate the white light probe through rotating CaF<sub>2</sub> crystal and to pump an OPA (OPerA Solo, Coherent/Positive Light) to generate the pump pulse at 720 nm. A thermally cooled CCD camera and home-built software written in LabVIEW 2015 were used to collect and manipulate data. The sample solution was prepared with ~ 0.5 OD in acetonitrile at the excitation wavelength and ~ 5 mL of the solution containing the sample was flowed through a 1 mm path-length Harrick Scientific flow cell (1 mm thick CaF<sub>2</sub> windows) and excited with ~ 2.5  $\mu$ J at the pump wavelength. The protonated samples were prepared in acetonitrile with the addition of p-toluenesulfonic acid (TsOH) until no blue shift was observed in the spectra. An instrument response of fwhm ~ 85 fs was measured using the Kerr effect in cyclohexane. The polarization angle between the pump and probe was set to 54.7° to avoid the rotational diffusion effects. All fits were performed as the sum of exponentials using Igor Pro (6.3) software with instrument response deconvolution.

All irradiation studies were performed using light emitting diodes (Luxeon Star), where 655 nm irradiation was performed with 2 LEDs on a homebuilt irradiation apparatus, where the sum of all the LED output was found to be 500 mW. Acrylic plates were designed to hold a 1 cm cuvette in the center of the LEDs, each at a 1.6 cm distance from the photolysis vials. All samples were prepared with ~ 0.5 OD at a 655 nm irradiation



wavelength in DMF with the addition of 120 mM BNAH as the electron donor and 100 mM TsOH as the acid source. All samples were purged under N<sub>2</sub> for 15 min before irradiation. Dark controls were performed by irradiating the samples in an aluminum foil sleeve to ensure that the effect was not merely temperature dependent. Quantification of hydrogen was performed by irradiation in septum capped vials. Volume measurements of vials were performed by weight when filled with deionized water with all measurements being made in triplicate.

Gaseous products were qualified and quantified with a Shimadzu GC-2014 gas chromatograph (GC). Aliquots of headspace were removed using a Hamilton gastight syringe and injected into a GC (He carrier gas for H<sub>2</sub> generation) with a ShinCarbon column (2 m long × 1/8 in. OD × 2.0 mm ID) and a Shimadzu TCD-2014 thermal conductivity detector. The GC conditions were as follows: injector temperature, 41.0 °C; column temperature, 30 °C; detector temperature, 150 °C; and gas flow, 25 mL/min. The calibration curve was constructed by injecting a series of known amounts of 5% H<sub>2</sub>/N<sub>2</sub> mixture in triplicate.

Density Functional Theory (DFT) calculations were performed to calculate the molecular orbital contributions to the molecular orbitals using the Gaussian (09) package.<sup>131</sup> For the Rh atoms, The Stuttgart RSC 1997 Electron Core Potential (ECP)<sup>181</sup> basis set was used, and the 6-31G† basis set was used for the C, N, and H atoms.<sup>134</sup> The B3LYP correlation and exchange functional was used.<sup>132, 133</sup> The geometric parameters of a low-resolution crystal structure obtained for **V.1**, omitting interstitial solvent molecules and counterions, was used as a starting point for the gas optimization of this compound.

In addition, this optimized structure was employed as a starting point to model the structure of **V.2**, as well as the structures of the intermediates of the proposed photocatalytic cycle for H<sub>2</sub> production using ‘GaussView’. Time-Dependent Density Functional Theory (TD-DFT) calculations were performed following the gas-phase optimizations using the polarized continuum model (PCM) with acetonitrile as the solvent. The first sixty lowest singlet-to-singlet excited states were calculated from the first ground states calculated for these complexes.

Single crystals of **V.1** + HCl and **V.1** in HBF<sub>4</sub> were selected from mineral oil under ambient conditions using a MiTeGen microloop or a nylon loop. Crystals were placed in a cold N<sub>2</sub> stream at 110 K on a Bruker D8-QUEST diffractometer equipped with a I $\mu$ S Mo microsource ( $\lambda = 0.71073$  Å). Initial unit cells were determined using SAINT from a set of three  $\omega$ -scans consisting of 0.5° frames and a sweep width of 15°. For each structure, the data were corrected for absorption using SADABS and the space group was determined from analysis of the systematic absences using XPREP.<sup>128</sup> The structures were solved using the intrinsic phasing routine in SHELXT or by direct methods implemented in SHELXS. The diffraction of both crystals, however, was rather poor which precluded anisotropic refinement of the data.

## Results and Discussion

### *Synthesis and Characterization*

Compounds **V.1** and **V.2** were synthesized following the scheme presented in Figure V.2. The partially solvated complex *cis*-[Rh<sub>2</sub>(DTolF)<sub>2</sub>(MeCN)<sub>6</sub>][BF<sub>4</sub>]<sub>2</sub> was refluxed in acetonitrile in the presence of one equivalent of 1,8-naphthyridine (np) and

one equivalent of 2-(1,8-naphthyridin-2-yl)quinoxaline (qxnp) or 2-(quinolin-2-yl)-1,8-naphthyridine (qnp) for **V.1** and **V.2** respectively. Not surprisingly, the reaction yielded a mixture of three products, namely the bis-substituted np compound, the bis-substituted axially blocked species, and the desired asymmetric complex. The target complexes were separated from these mixtures using column chromatography as cationic  $[\text{BF}_4]^-$  salts and characterized by HRMS and  $^1\text{H}$  NMR. Both compounds exhibit an intense signal for the parent ion  $[\text{M}]^{2+}$  in their mass spectrum and a variety of signals in the aromatic region of the  $^1\text{H}$  NMR spectrum due to the asymmetric nature of the complexes (Figures V.3 and 4).

#### *X-ray crystal structures*

The molecular structure of **V.1** was confirmed by low resolution X-ray crystallography and is shown in Figure V.5. Crystals for **V.1** were obtained in the presence of HCl which lead to the protonation of the compound with a concomitant blue-shift of its absorption profile (vide infra). In addition, crystals of a decomposition product in the presence of  $\text{HBF}_4$  were also obtained (Figure V.6). Due to the low-resolution nature of these structures, no comments can be made about the bond lengths and angles as the structures were not able to be refined anisotropically. Nevertheless, the structure of **V.1** in the presence of HCl indicates that the ligands are connected to the metal core as expected leaving only one axial site open for catalytic applications. Long-term exposure to an excess of  $\text{HBF}_4$  leads to the cleavage of one of the formamidinate bridging ligands, consistent with the computational calculations that suggest that the N atom of the formamidinate ligand is the most basic site of the molecule.

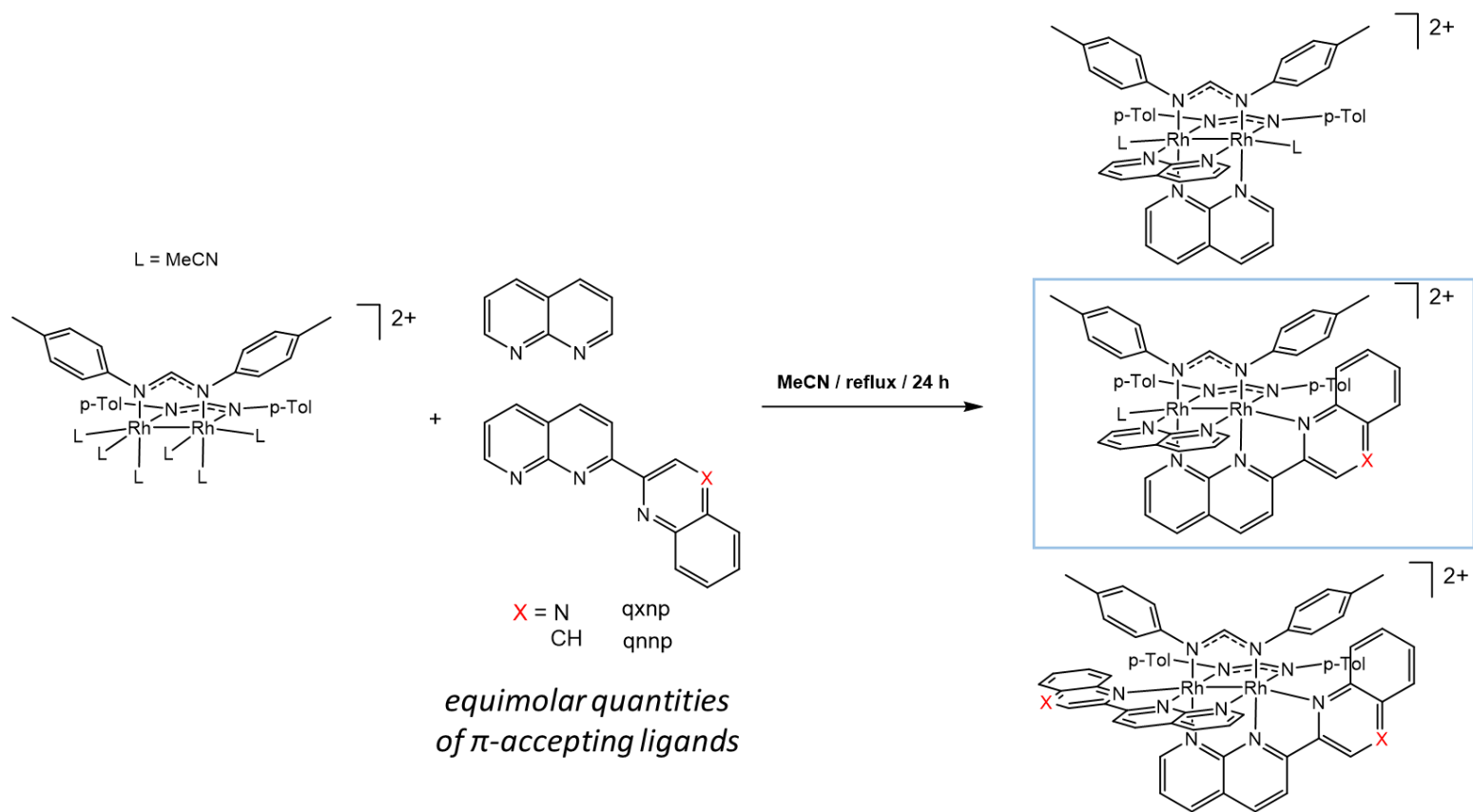


**Figure V.2** Synthetic scheme for the synthesis of **V.1** and **V.2**.

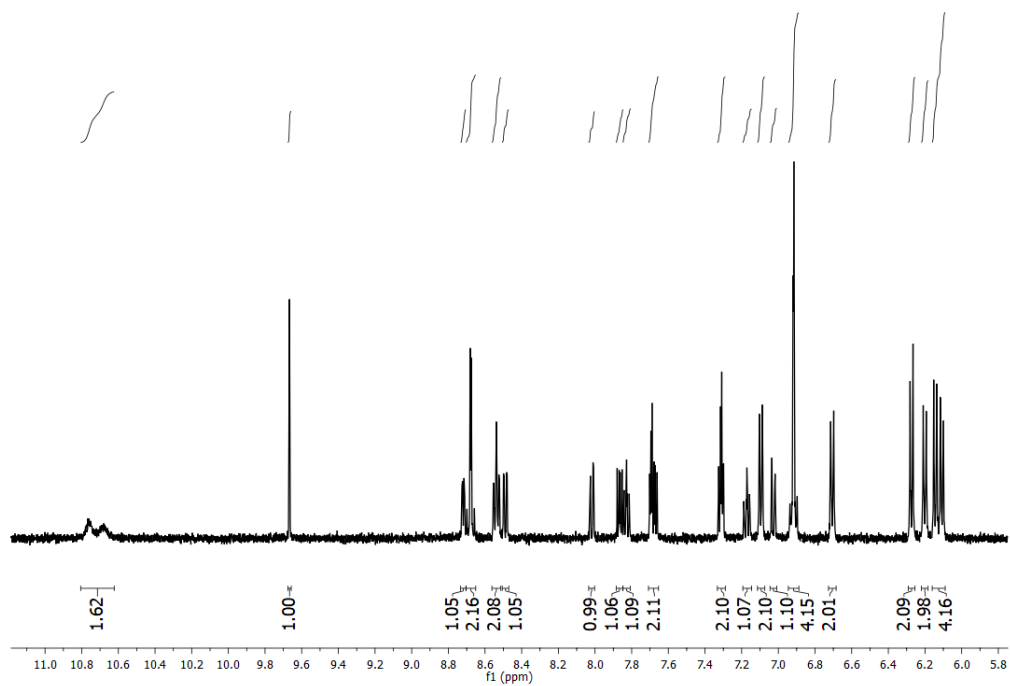


**Figure V.3** Aromatic region of the  $^1\text{H}$  NMR for **V.1** in acetonitrile- $\text{d}_3$ .

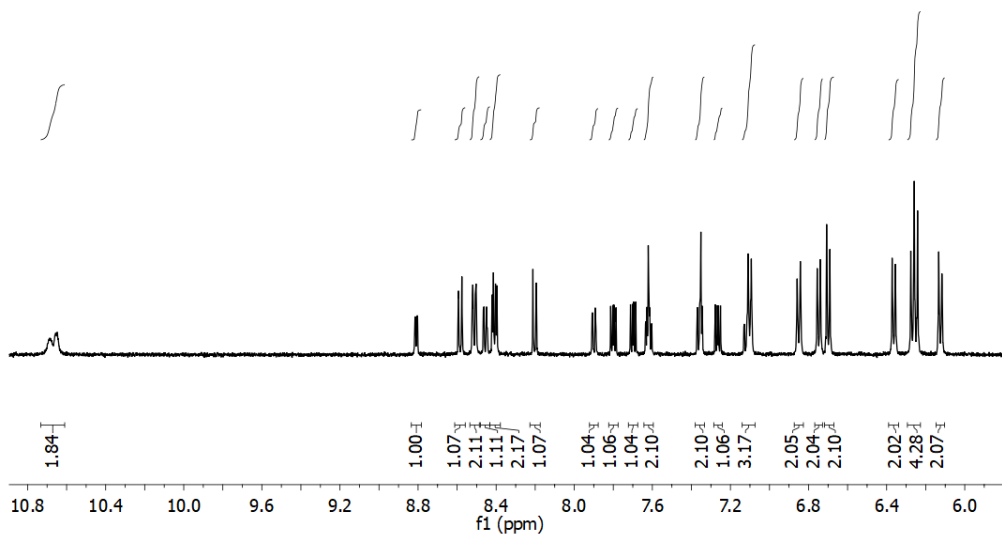


**Figure V.4** Aromatic region of the  $^1\text{H}$  NMR for **V.2** in acetonitrile- $\text{d}_3$ .

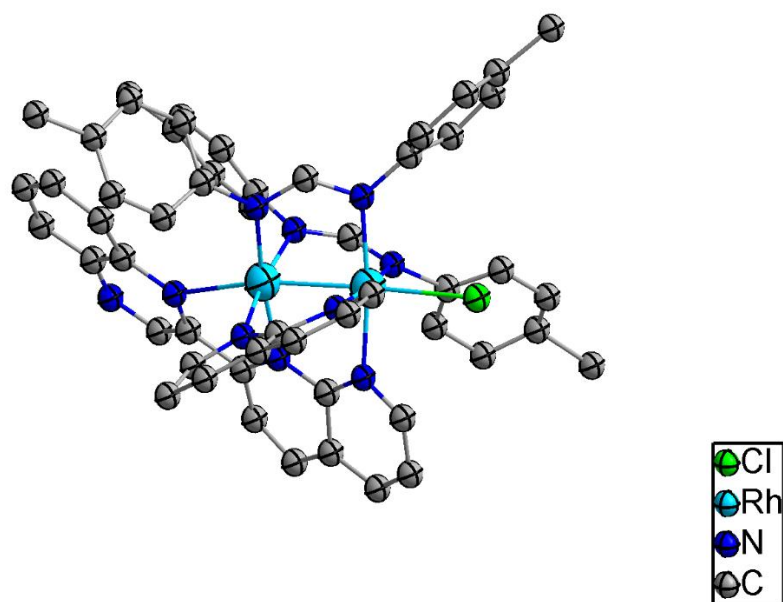


**Figure V.5** Low resolution X-ray data refined isotropically for *cis*-[Rh<sub>2</sub>(DTolF)<sub>2</sub>(qxnp)(np)][BF<sub>4</sub>]<sub>2</sub> in the presence of HCl.

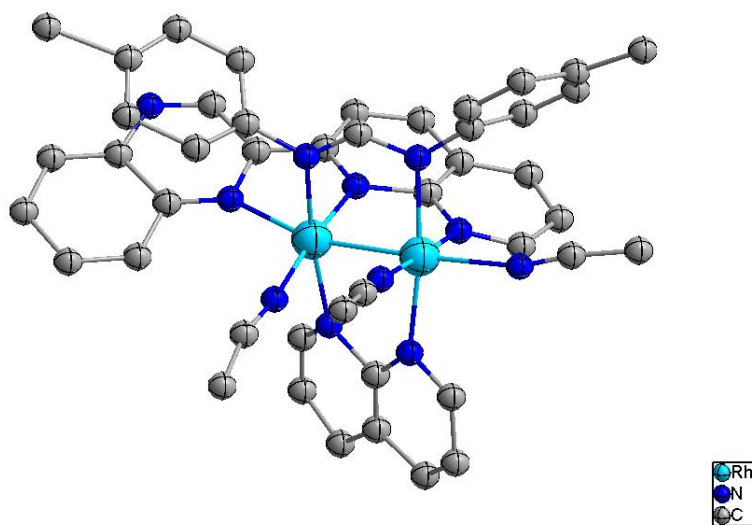


**Figure V.6** Low resolution X-ray crystal data of **V.1** after a two-week exposure to HBF<sub>4</sub> at room temperature.

### *Electrochemistry and Electronic Absorption Spectroscopy*

Table V-1. summarizes the electrochemical data and the steady state absorption spectra for **V.1** and **V.2**. Compounds **V.1** and **V.2** exhibit a one-electron oxidation in 0.1 M Bu<sub>4</sub>NPF<sub>6</sub> CH<sub>3</sub>CN with E<sub>1/2</sub> values of +0.82 and +0.80 V vs Ag/AgCl, respectively (Figure V.7). These first oxidation couples are assigned as Rh-formamidinate in character as reported for other formamidinate complexes.<sup>63, 74</sup> Upon scanning cathodically, **V.1** and **V.2** were observed to exhibit three one-electron reduction events, in contrast to related complexes such as *cis*-[Rh<sub>2</sub>(DTolF)<sub>2</sub>(qxnp)<sub>2</sub>][BF<sub>4</sub>]<sub>2</sub> which display four one-electron reduction events. This can be explained by the fact that the qxnp ligands undergo two electrons reductions whereas the np ligand is reduced by one electron. The first reduction event is assigned to the qxnp/qnnp ligands and their shift in potential is consistent with the shift in the ML-LCT band observed in the absorption spectrum for **V.2** as compared to **V.1**. That is, the more red-shifted compound **V.1** is easier one to reduce due to the presence of a quinoxaliny moiety in contrast with **V.2** which contains a quinolinyl moiety.

The steady state absorption spectra of complexes **V.1** and **V.2** are shown in Figure V.8 and their maxima and molar extinction coefficients are listed in Table V-1. Both compounds exhibit ligand-centered  $\pi\pi^*$  transitions in the ultraviolet (UV) region at 252 nm. In addition, the spectra display Rh<sub>2</sub>/DTolF $\rightarrow$ np charge transfer transitions at ~ 365 and 584 which is similar to previously assigned transitions for related complexes.<sup>127</sup> Due to the b<sub>1u</sub> symmetry of the  $\pi^*$  orbitals of the formamidinate bridging ligands, they can interact with the  $\delta^*$  orbitals of the same symmetry of the dirhodium core imparting DTolF( $\pi^*$ )/Rh<sub>2</sub>( $\delta^*$ ) character to the HOMO of these complexes in contrast with the

archetypal electronic configuration of  $(\sigma)^2(\pi)^4(\delta)^2(\delta^*)^2(\pi^*)^4(\sigma^*)^0$  for other  $d^7-d^7$  paddlewheel complexes. Interestingly, the presence of two distinct  $\pi$ -accepting ligands yields two low-energy ML-LCT bands which are  $Rh_2/DTolF \rightarrow np$  and  $Rh_2/DTolF \rightarrow qnnp/qxnp$  in nature which increases the absorption coefficients of these complexes throughout the visible region into the near-IR. This situation is an improvement over their bis-substituted counterparts which display only one low-energy ML-LCT band making them less effective panchromatic absorbers compared to the asymmetric complexes. In addition, **V.1** is red-shifted by 32 nm ( $535 \text{ cm}^{-1}$ ) with respect to *cis*- $[Rh_2(DTolF)_2(qxnp)_2][BF_4]_2$  making it a better candidate for DSSC applications for which the use of a low-energy sensitizer is required.

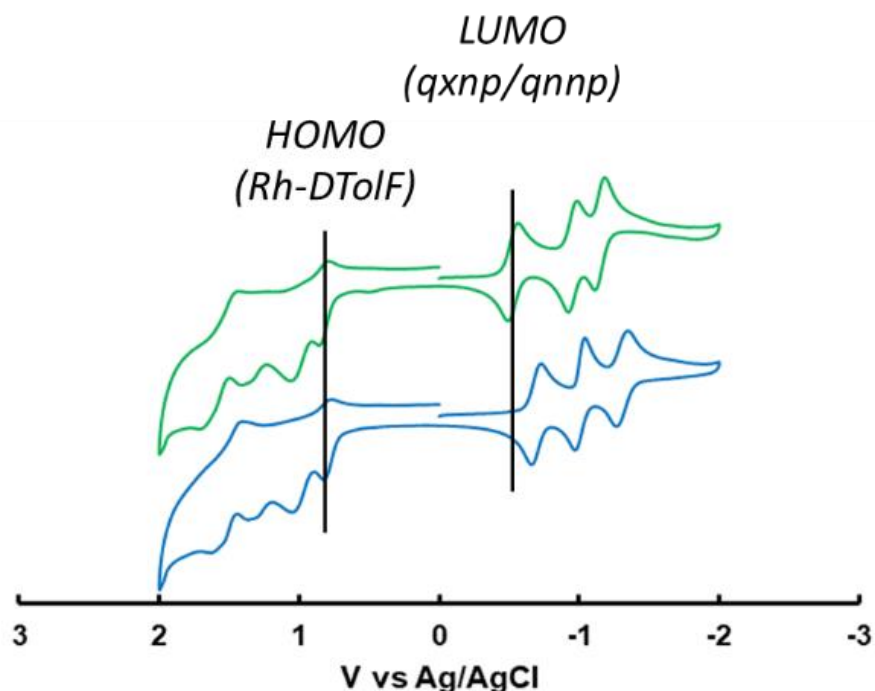


**Figure V.7** Cyclic voltammograms of **V.1** (green) and **V.2** (blue).



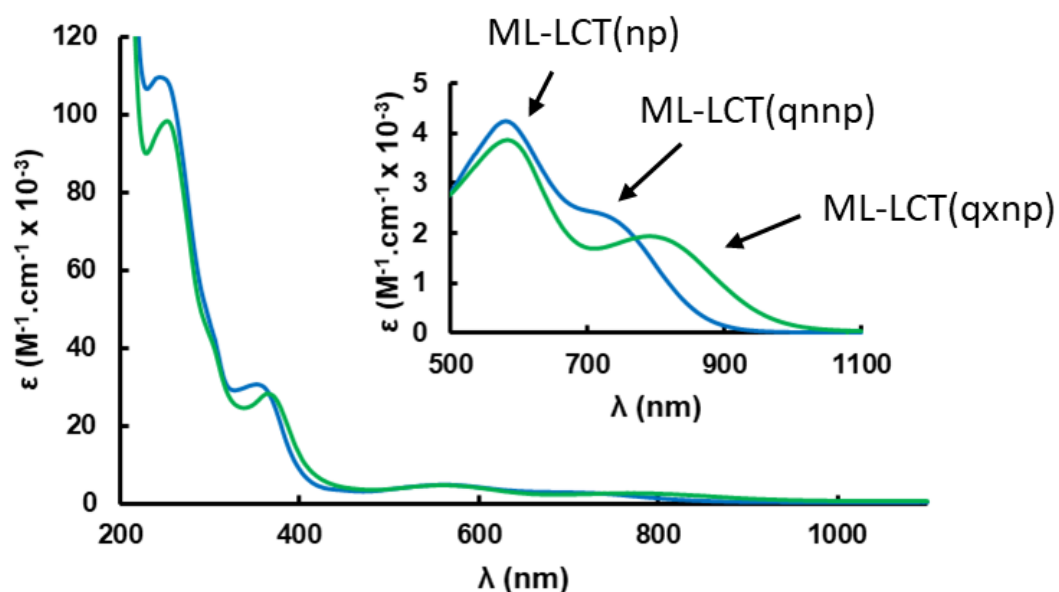


**Figure V.8** Electronic absorption spectra for **V.1** (green) and **V.2** (blue).

**Table V-1** Electronic Absorption Maxima with Molar Absorptivities in Acetonitrile, Reduction Potentials, Singlet ( $\tau_S$ ) and Triplet ( $\tau_T$ ) Lifetimes for **V.1** and **V.2**.

Complex	$\lambda_{\text{abs}} / \text{nm}$ ( $\epsilon / \times 10^3 \text{ M}^{-1} \text{ cm}^{-1}$ )	$E_{1/2} / \text{V}^a$	$t_1/\text{ps}^b$	$t_2/\text{ns}^b$
<b>V.1</b>	252 (98), 365 (29), 584 (3.9), 790 (1.9)	+0.82, -0.60	6	1.5
<b>V.2</b>	252 (109), 352 (31), 582 (4.3), 712 (2.4)	+0.80, -0.69	10	4

<sup>a</sup> $v_s$  Ag/AgCl in 0.1 M Bu<sub>4</sub>NPF<sub>6</sub>/CH<sub>3</sub>CN. <sup>b</sup>From transient absorption

experiments in acetonitrile at 298 K ( $\square_{\text{exc}} = 720 \text{ nm}, 2.5 \mu\text{J}$ ).

### Ground State Protonation

The complexes undergo protonation in the presence of a strong acid such as TsOH (Figure V.9) that leads to a blue-shift of the absorption profile as evidenced by the steady state absorption spectra presented in Figure V.10. This phenomenon has not been observed before by our groups with formamidinate bridged complexes exposed to acid in the course of studying their electrocatalytic and photocatalytic properties. In order to elucidate the number of equivalents required to fully protonate this complex, a titration experiment was carried out by sequential addition of TsOH followed by steady state absorption. The maximum at 581 nm for **2** was plotted as a function of the number of equivalents of TsOH added to the solution. Least-squares linear regression analysis of the data indicates that there is a 1:1 ratio of proton to complex as shown in Figure V.11. These data, however, do not provide insight as to where this proton is located in the complexes, that is, what is the most basic site.

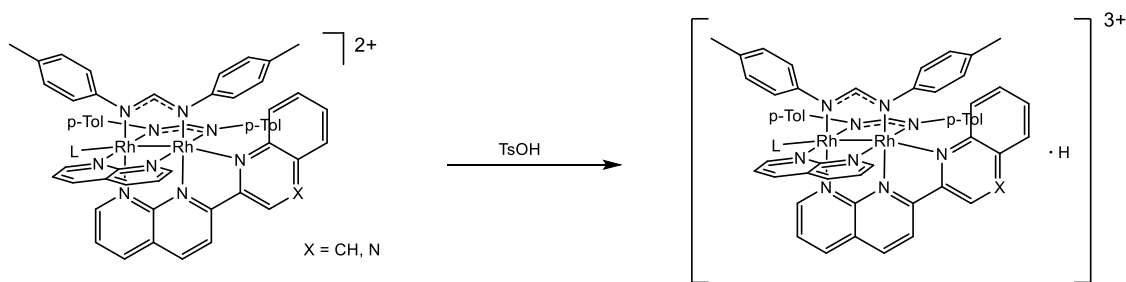


**Figure V.9** Protonation of **V.1** and **V.2** in the presence of TsOH.

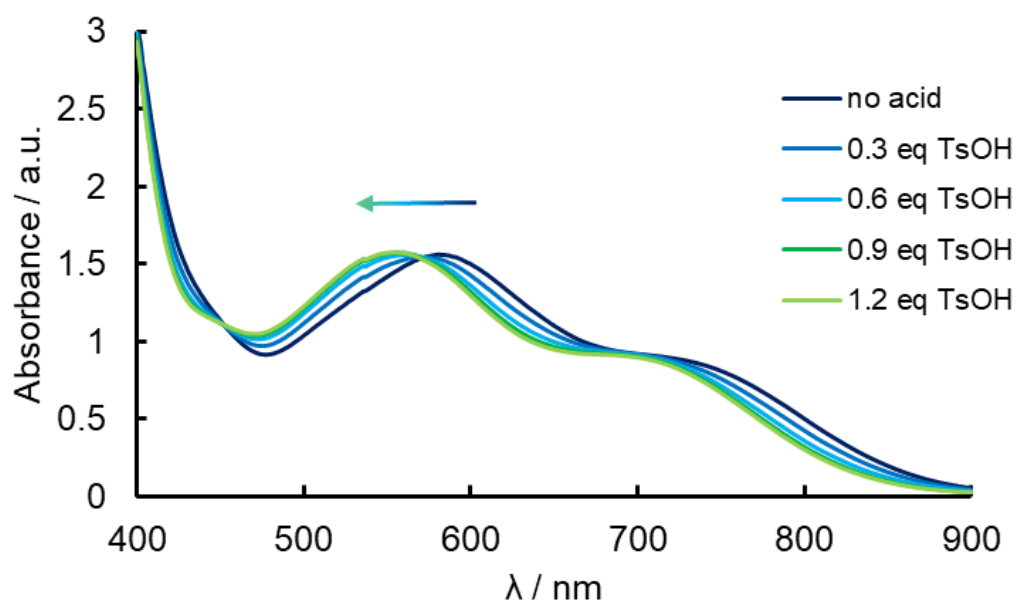


**Figure V.10** Electronic absorption spectra of **V.1** as a function of TsOH equivalents.

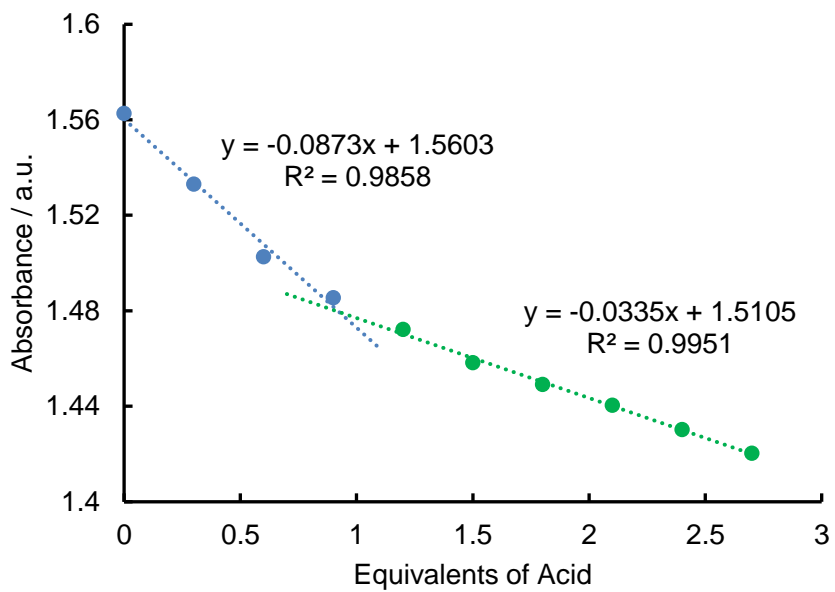


**Figure V.11** Acid titration of **V.2** with a solution of TsOH in acetonitrile followed by UV-vis spectroscopy at 581 nm.

In order to characterize the protonated complexes, a series of measurements and computational studies were performed. The protonation was also followed by  $^1\text{H}$  NMR spectroscopy for both complexes as shown in Figures V.12 and 13. To a solution of the complexes in acetonitrile- $d_3$  a solution of DCl in  $\text{D}_2\text{O}$  was added increments of 1 equivalent of acid. The shift of the signals observed at higher fields is consistent with the protonation of the complex which leads to a reduction of the electron donation of the formamidinate ligand. In addition, the spectra reveal that the signal which shifts more significantly with the addition of acid is the doublet of doublets corresponding to the  $\alpha\text{-H}$  of the naphthyridine moieties of the  $\pi$ -accepting ligands. These ligands are located *trans* to the formamidinate bridging ligands which exert a marked *trans* effect and protonation of the formamidinate ligand leads to a decrease in the *trans* effect which results a shielding of the signals that correspond to the protons of the  $\pi$ -accepting ligands across the Rh-Rh bond. These data are also consistent with what is observed in the low-resolution X-ray data obtained for the product of **V.1** after a two-week exposure to  $\text{HBF}_4$  at room temperature. The structure revealed that there is one less formamidinate bridging ligand in the complex which is consistent with it being the most nucleophilic site in the complexes and that it dissociates.

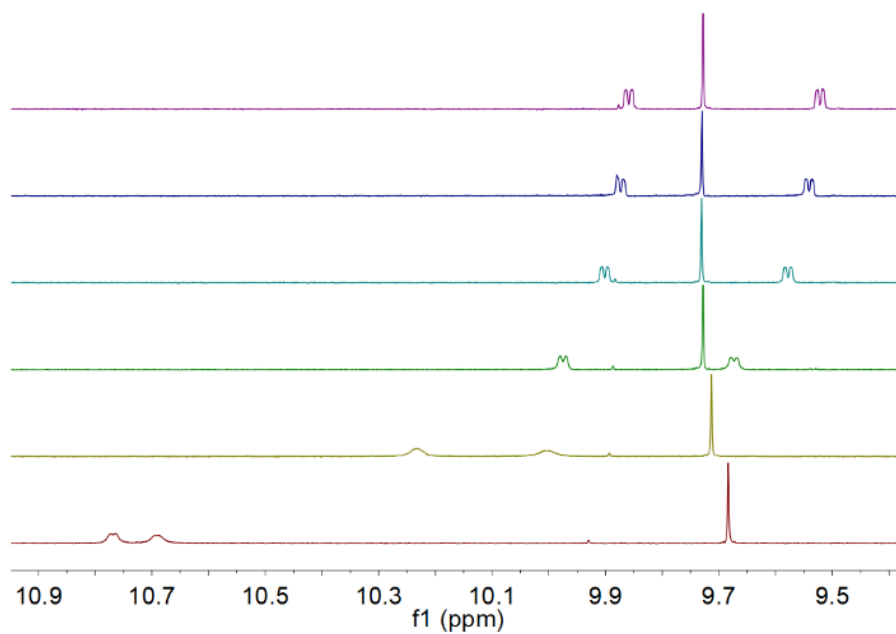


**Figure V.12** Aromatic region of the  $^1\text{H}$  NMR for **V.1** in acetonitrily- $d_3$  after protonation with DCl in  $\text{D}_2\text{O}$ .

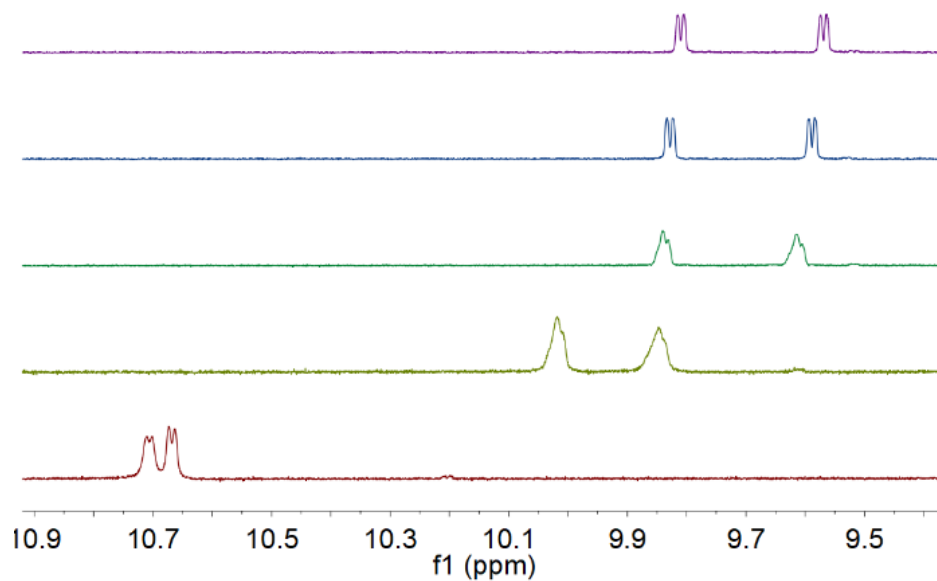


**Figure V.13** Aromatic region of the  $^1\text{H}$  NMR for **V.2** in acetonitrily- $d_3$  after protonation with DCl in  $\text{D}_2\text{O}$ .

Computational studies were performed to provide further evidence to support the conclusion that the protonation occurs at the formamidinate ligand. In this approach, a proton was added to the gas-phase optimized structures of the complexes at different positions and the effect on the resulting UV-vis absorption spectra was studied *via* TD-DFT calculations. In addition, the possibility of axial coordination of an anion as the source of the blue-shift was also investigated (*vide infra*). The results shown in Figure V.20 indicate that only protonation at the N atom of the formamidinate ligand produces a blue shift in the absorption profile. These results further support the results of  $^1\text{H}$  NMR and low-resolution X-ray crystallography.

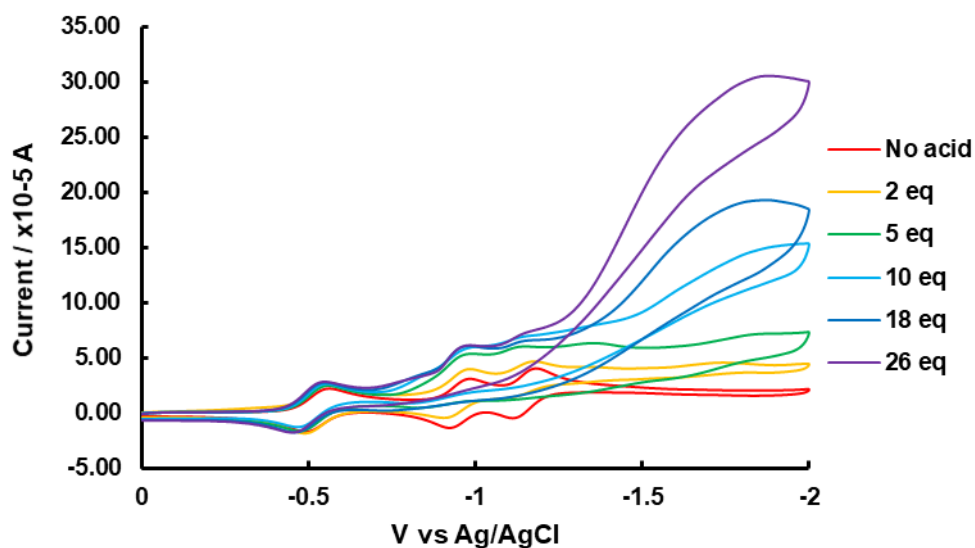
#### *Electrocatalytic H<sub>2</sub> Production*

In order to assess the electrocatalytic activity of these complexes, cyclic voltammetry experiments were performed in the presence of AcOH as an acid source. Solutions of AcOH in acetonitrile were prepared and added to the complexes in the electrochemical cell in small increments as a function of the quantity of compound. The cathodic potential was scanned for increasing amounts of acid and then recorded, and plotted against the current generated (Figures V.14 and 15). The studies reveal that both compounds have the ability to electrocatalytically produce H<sub>2</sub> in the presence of an acid source. Although AcOH is not strong enough to fully protonate the complex in the amounts added, a small shift in the first reduction potential was observed for both compounds which is taken as an indication of a minor degree of protonation. Compounds **V.1** and **V.2** respond very similarly to the addition of acid although the onset of catalytic activity for **V.2** occurs after the second reduction event whereas for **V.1** it occurs after the

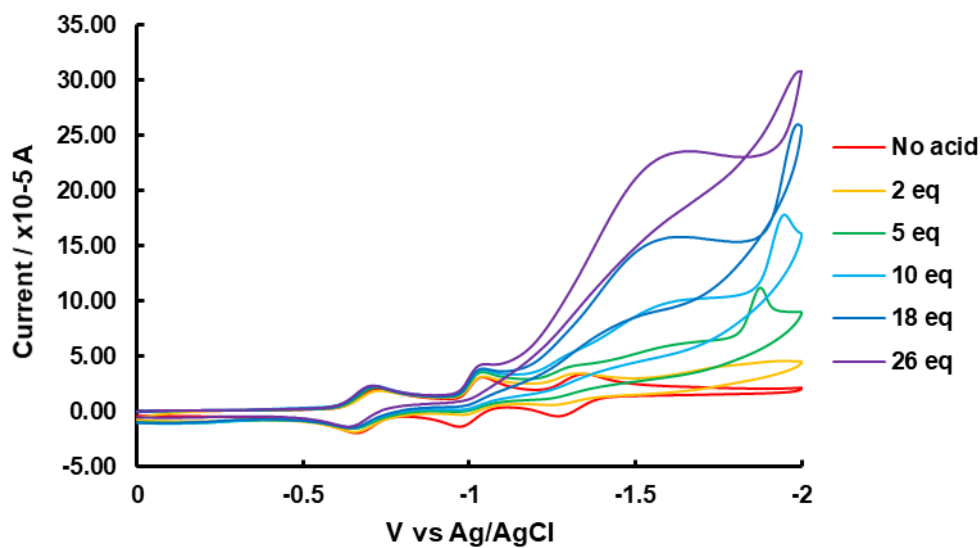
first one-electron reduction event. These observations are attributed to the difference in the axial blocking moiety for both complexes. Although qxnp is easier to reduce than the qnnp ligand, the electron donation through the Rh-Rh has a larger effect on the nucleophilicity of the remaining unoccupied axial position which leads to **V.2** being a better catalyst.

#### *Electronic Structure Calculations*

In order to better understand the origin of the electronic transitions for these complexes, density functional theory (DFT) computational calculations were performed. DFT calculations were carried out using the geometrical parameters of a low-resolution crystal structure obtained for complex **V.1** as a starting point. This structure was optimized in the gas-phase and used to model the structure of **V.2** as well (Figure V.16, Table V.2). The results show that the HOMO for complexes **V.1** and **V.2** are 31% Rh( $\pi^*$ ) in character with a large contribution of 64% of the formamidinate ligands. On the other hand, the LUMOs are 90% qxnp and qnnp in character for complexes **V.1** and **V.2** respectively (Tables V.3 and 4). The MO diagram shown in Figure V.17 highlights a major difference in the asymmetric complexes with respect to their symmetric bis-counterparts, namely that the first two LUMOs are no longer degenerate. Since **V.1** and **V.2** contain two different  $\pi$ -accepting ligands each, the first two LUMOs now have markedly different energies due to the orbital contributions of the np to the LUMO+1 and qxnp or qnnp to the LUMO. Lastly, asymmetric axial chelation leads to Rh( $\sigma^*$ ) orbitals that have energies that are intermediate between those of the fully blocked and the axially free complexes.



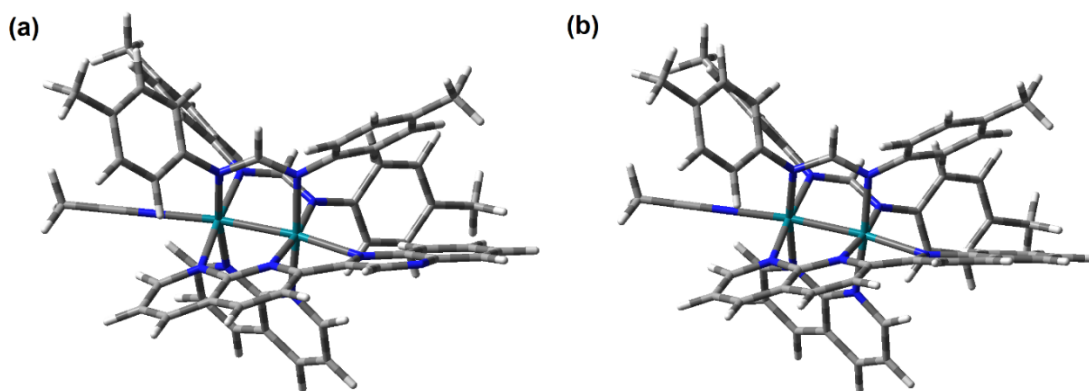
**Figure V.14** Cyclic voltammograms of **V.1** in the presence of AcOH



**Figure V.15** Cyclic voltammograms of **V.2** in the presence of AcOH.



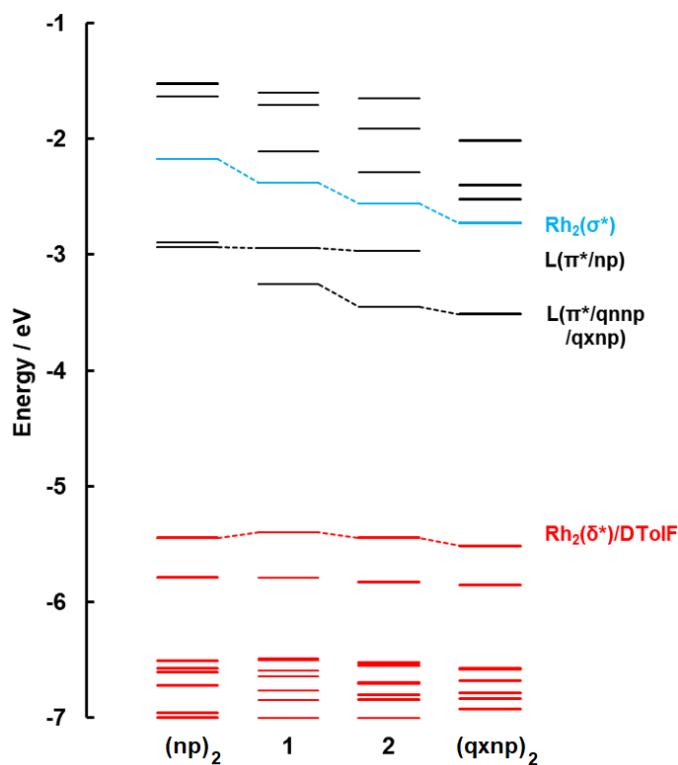
The lowest energy transitions for the compounds appear in the visible region and extend into the near-IR region; TD-DFT calculations were performed to assign the nature of these transitions (Figure V.18 and Table V.5). The lowest energy transitions for **V.1** are assigned to ML-LCT transitions that are  $\text{Rh}_2(\pi^*)/\text{DTolF} \rightarrow \text{qxnP}$  and  $\text{Rh}_2(\pi^*)/\text{DTolF} \rightarrow \text{np}$  in nature and are assigned to the lowest and second lowest energy transitions respectively. Similarly, **V.2** displays two ML-LCT transitions that are  $\text{Rh}_2(\pi^*)/\text{DTolF} \rightarrow \text{qnp}$  and  $\text{Rh}_2(\pi^*)/\text{DTolF} \rightarrow \text{np}$  in character. The difference in energy between the lowest energy transitions for **V.1** and **V.2** can be attributed to the difference in energies of the qxnP and qnp ligands which are the major contributors to the LUMOs, leading to a smaller energy gap for **V.1** compared to **V.2**.



**Figure V.16** Gas-phase optimized structures for **V.1** (a) and **V.2** (b).

**Table V-2** Calculated bond distances and dihedral angles for **V.1** and **V.2**.

Bond distance (Å) / dihedral angle (°)	V.1	V.2
Rh1-Rh2	2.49259	2.49317
Rh1-N1	2.09727	2.10413
Rh1-N3	2.07174	2.07296
Rh1-N5	2.11259	2.10990
Rh1-N7	2.12883	2.12632
Rh1-N9	2.54907	2.54529
Rh2-N2	2.06565	2.06540
Rh2-N4	2.08002	2.08080
Rh2-N6	2.13669	2.13453
Rh2-N8	2.13666	2.13462
Rh2-N10	2.25871	2.26470
N1-Rh1-Rh2-N2	-14.40571	-14.73908
N7-Rh1-Rh2-N8	-15.74080	-15.92198

**Figure V.17** A comparison of the calculated MO diagrams for **V.1** and **V.2** with the bis substituted *cis*-[Rh<sub>2</sub>(DTolF)<sub>2</sub>(np)<sub>2</sub>(MeCN)<sub>2</sub>][BF<sub>4</sub>]<sub>2</sub> and *cis*-[Rh<sub>2</sub>(Dtolf)<sub>2</sub>(qxnp)<sub>2</sub>][BF<sub>4</sub>]<sub>2</sub> complexes.

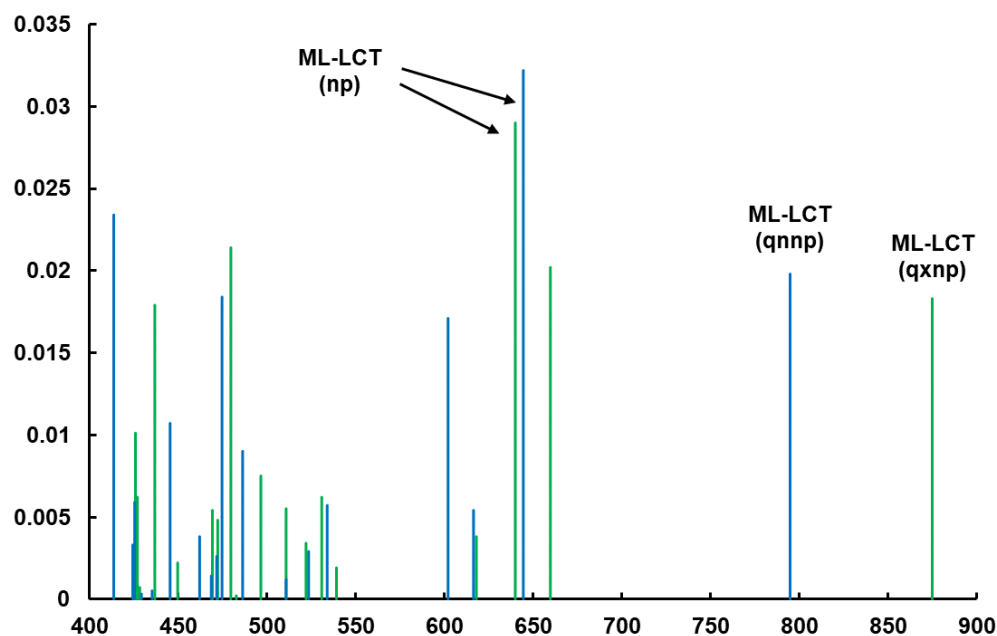


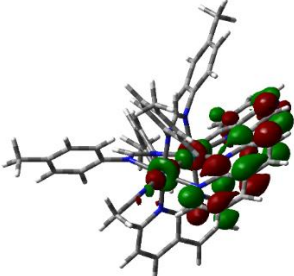
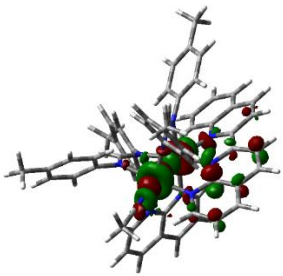
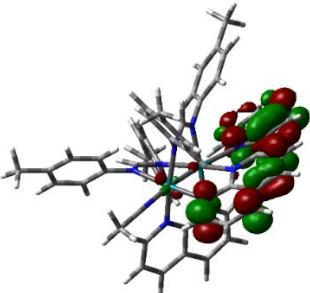
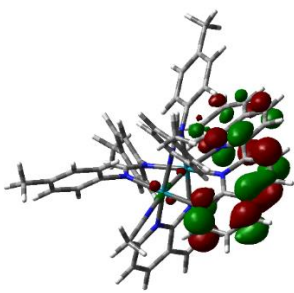
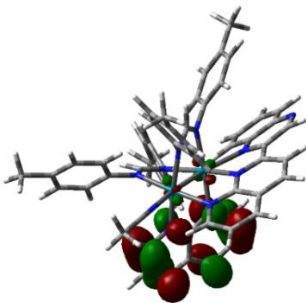
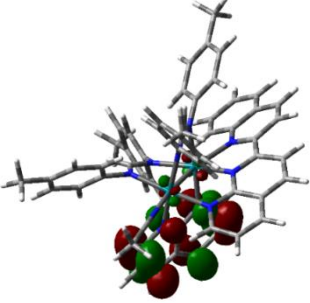
**Figure V.18** TD-DFT calculated oscillator frequencies for **V.1** (green) and **V.2** (blue).

**Table V-3** Orbital contributions for **V.1** and **V.2** as predicted by TD-DFT calculations in acetonitrile (HOMO-5 through LUMO+6).<sup>a</sup>

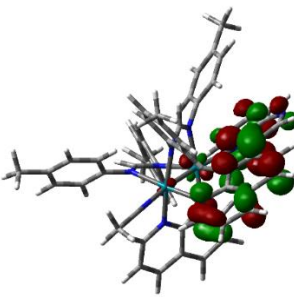
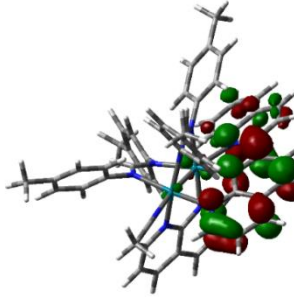
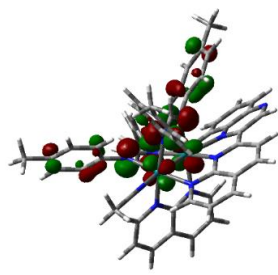
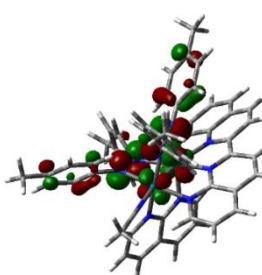
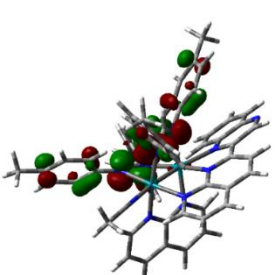
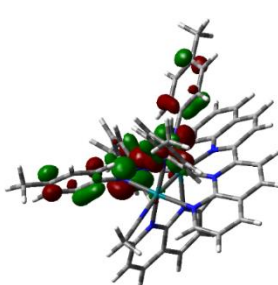
Orbital	V.1	V.2
HOMO-5	83% Rh, 11% DtoIF	67% Rh, 28% DtoIF
HOMO-4	68% Rh, 25% DtoIF	59% Rh, 18% DtoIF, 20% qnp
HOMO-3	44% Rh, 51% DtoIF	47% Rh, 49% DtoIF
HOMO-2	38% Rh, 58% DtoIF	53% Rh, 41% DtoIF
HOMO-1	9% Rh, 89% DtoIF	10% Rh, 88% DtoIF
HOMO	31% Rh, 64% DtoIF	31% Rh, 64% DtoIF
LUMO	7% Rh, 90% qxnp	7% Rh, 90% qnp
LUMO+1	10% Rh, 86% np	11% Rh, 85% np
LUMO+2	26% Rh, 65% qxnp	56% Rh, 8% DtoIF, 27% qnp
LUMO+3	53% Rh, 7% DtoIF, 30% qxnp	24% Rh, 68% qnp
LUMO+4	10% Rh, 84% qxnp	11% Rh, 68% qnp
LUMO+5	26% Rh, 15% DtoIF, 50% np	17% Rh, 7% DtoIF, 56% np, 19% qnp
LUMO+6	32% Rh, 16% DtoIF, 36% np, 16% qxnp	39% Rh, 22% DtoIF, 22% np, 16% qnp

<sup>a</sup>Only ontributions higher than 5% are listed.

**Table V-4** Electron density maps for **V.1** and **V.2** from its HOMO-1 to its LUMO+3 with an isovalue = 0.04.

Orbital	V.1	V.2
LUMO+3		
LUMO+2		
LUMO+1		

**Table V-4** Continued.

LUMO		
HOMO		
HOMO-1		

**Table V-5** Vertical energies of the singlet excited states, oscillator strengths,  $f$ , and major orbital contributions<sup>a</sup> calculated for **V.1** and **V.2** in acetonitrile (H = HOMO; L = LUMO).<sup>b</sup>

Excited State	V.1	V.2
1	11,442 cm <sup>-1</sup> (874 nm), $f = 0.018$ , H → L (98.0%)	12,579 cm <sup>-1</sup> (795 nm), $f = 0.020$ , H → L (98.0%)
2	15,152 cm <sup>-1</sup> (660 nm), $f = 0.020$ , H-1 → L (94.1%)	15,504 cm <sup>-1</sup> (645 nm), $f = 0.032$ , H → L+1 (94.1%)
3	15,625 cm <sup>-1</sup> (640 nm), $f = 0.029$ , H → L+1 (88.1%)	16,207 cm <sup>-1</sup> (617 nm), $f = 0.005$ , H → L+2 (54.8%) H-1 → L (32.5%)
4	16,181 cm <sup>-1</sup> (618 nm), $f = 0.004$ , H → L+2 (47.6%) H → L+3 (37.2%)	16,611 cm <sup>-1</sup> (602 nm), $f = 0.017$ , H-1 → L (64.0%) H → L+2 (27.0%)
5	18,553 cm <sup>-1</sup> (539 nm), $f = 0.002$ , H-3 → L (33.6%) H-4 → L (27.0%)	18,727 cm <sup>-1</sup> (534 nm), $f = 0.006$ , H-1 → L+1 (96.0%)
6	18,832 cm <sup>-1</sup> (531 nm), $f = 0.006$ , H-1 → L+1 (96.0%)	19,084 cm <sup>-1</sup> (524 nm), $f = 0.003$ , H-3 → L+2 (15.2%)
7	19,157 cm <sup>-1</sup> (522 nm), $f = 0.003$ , H-5 → L (34.1%) H-2 → L (24.0%)	19,569 cm <sup>-1</sup> (511 nm), $f = 0.001$ , H-4 → L+2 (22.1%)
8	19,569 cm <sup>-1</sup> (511 nm), $f = 0.005$ , H → L+3 (44.0%) H → L+2 (41.0%)	20,576 cm <sup>-1</sup> (486 nm), $f = 0.009$ , H-2 → L (46.2%)

<sup>a</sup>Only contributions of  $\geq 20\%$  are listed. <sup>b</sup>Yellow = ML-LCT (Rh/DtolF → qxnnp), blue = LLCT (DtolF → qxnnp), green = <sup>1</sup>MC (Rh<sub>2</sub>( $\pi^*$ ) → Rh<sub>2</sub>( $\sigma^*$ )).

Computational calculations were also performed in order to elucidate the site for protonation of these complexes. To do this, a proton was placed on different N atoms in the ligands and their predicted absorption profiles were compared to the experimentally observed blue-shift in the presence of acid. Compound **V.2** was protonated at the qnnp ligand and two possible products were proposed, namely one that includes ligand dissociation from the axial position and a second one that involves the formation of a

cyclometalated complex with the qnnp ligand (Figure V.19). The calculated spectra for both proposed protonated complexes leads to a red-shift which is not consistent with what is observed experimentally. This is a reasonable finding, since protonation of the  $\pi$ -accepting ligand would decrease the energy of the LUMO leading to a lower energy gap and a concomitant decrease in the energy of the lowest energy ML-LCT band. In contrast, protonation of **V.1** at the N atom of one of the formamidinate ligands leads to a predicted red-shift, in accord with the experimental results (Figure V.20). Protonation at this site would be expected to reduce the electron donating capabilities of the formamidinate ligand which has a large contribution to the HOMO of these complexes. This effect would lead to a decrease in the energy of the HOMO with an overall increase in the HOMO-LUMO gap which causes a blue-shift of the lowest energy ML-LCT band. In addition, changing the identity of the axial ligand from acetonitrile to chloride does not have a marked effect on the resulting spectra which supports the notion that the explanation for the observed blue-shift is protonation and not axial chelation of the counterion.

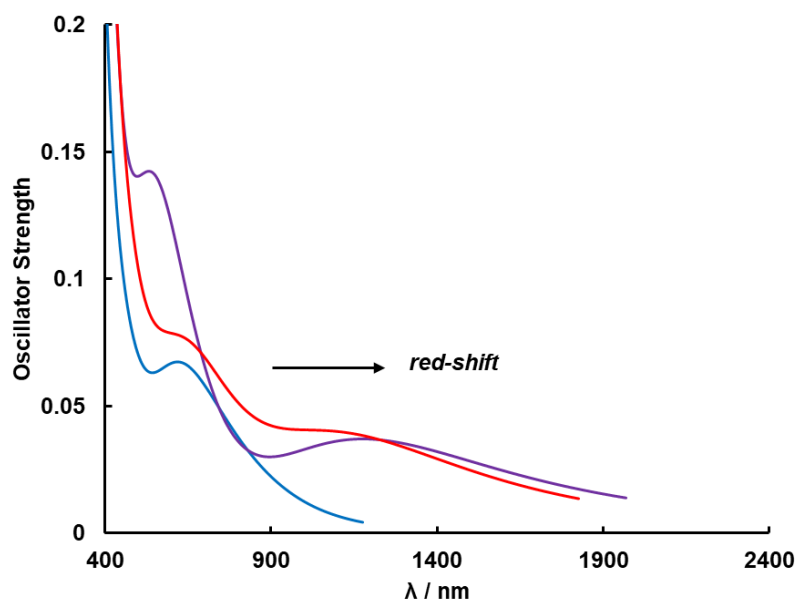


**Figure V.19** Calculated oscillator strengths for **V.2** (blue), for the complex protonated at the qnp ligand (purple), and the protonated cyclometalated qnp ligand on the dirhodium unit (red).

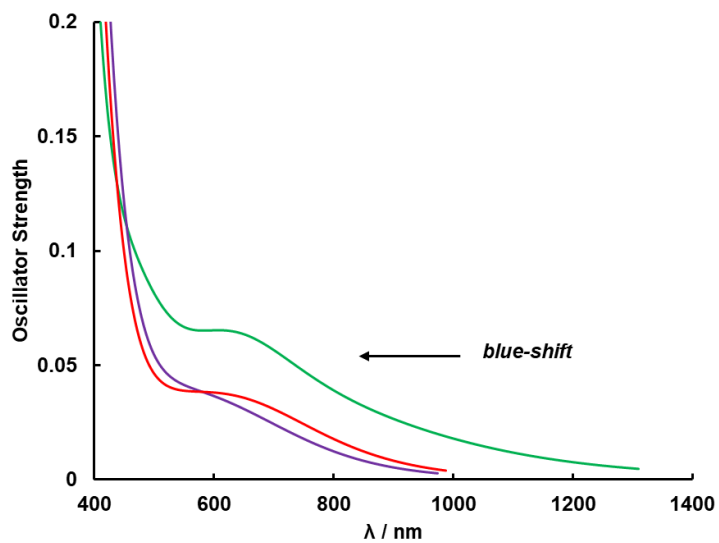


**Figure V.20** Calculated oscillator strengths for **V.1** (green) and the protonated analogues with acetonitrile (purple) or a chloride ion (red) in the axial positions respectively.



### *Time-Resolved Spectroscopy*

Femtosecond transient absorption (fsTA) spectra were collected at a 720 nm excitation for **V.1** (Figure V.21). A peak centered at 450 nm was observed with a lower intensity feature at ~ 590 nm which is the result of the subtraction of the ground state absorption maximum at 590 nm. A kinetic trace at 450 nm was fitted biexponentially with  $\tau_1 = 5.6$  ps (68%) and  $\tau_2 \sim 1.5$  ns (32%); these lifetimes are assigned to  $^1\text{ML-LCT}$  and  $^3\text{ML-LCT}$  as their symmetric analogues *cis*-[Rh<sub>2</sub>(DTolF)<sub>2</sub>(qxnp)<sub>2</sub>][BF<sub>4</sub>]<sub>2</sub> and *cis*-[Rh<sub>2</sub>(DTolF)<sub>2</sub>(qnp)<sub>2</sub>][BF<sub>4</sub>]<sub>2</sub>. Similar results were observed for **V.2**, with the lower intensity ~ 550 nm feature being due to the ground state absorption maximum bleach (Figure V.22). The singlet excited state lifetime,  $\tau_1$ , was fitted to ~ 10 ps (47%). The triplet excited state is beyond the scope of the fsTA measurement and were obtained from nanosecond transient absorption (nsTA, Figures V.23 and 24). Upon 650 nm excitation, the kinetic trace at 450 nm was deconvoluted from the instrument response function with a lifetime ~ 4 ns (53%) which is assigned to the  $^3\text{ML-LCT}$  decay. The shorter triplet lifetimes of **V.1** and **V.2** compared to their fully blocked symmetric analogues is due to the lengthening and concomitant weakening of the Rh-Rh  $\sigma^*$  interaction due to the lack of one axial blocking ligand which results in more accessible metal center ( $^3\text{MC}$ ) excited states that facilitate excited state deactivation mechanisms.

Similarly, fsTA and nsTA experiments were performed for the protonated complexes in the presence of TsOH as the proton source. Acid was added to solutions of the complexes in acetonitrile until the spectra were no longer shifting to higher energies. The fully protonated compounds **V.1** and **V.2** exhibit the same excited state kinetics

compared to the original complexes, namely they have the same lifetimes for their excited states and the same energies of the  $^1\text{ML-LCT}$  and  $^3\text{ML-LCT}$  bands. These results indicate that protonation at the formamidinate bridging ligand does not disturb the excited state properties of the complexes, and, therefore, does not interfere with their electron-transfer capabilities.

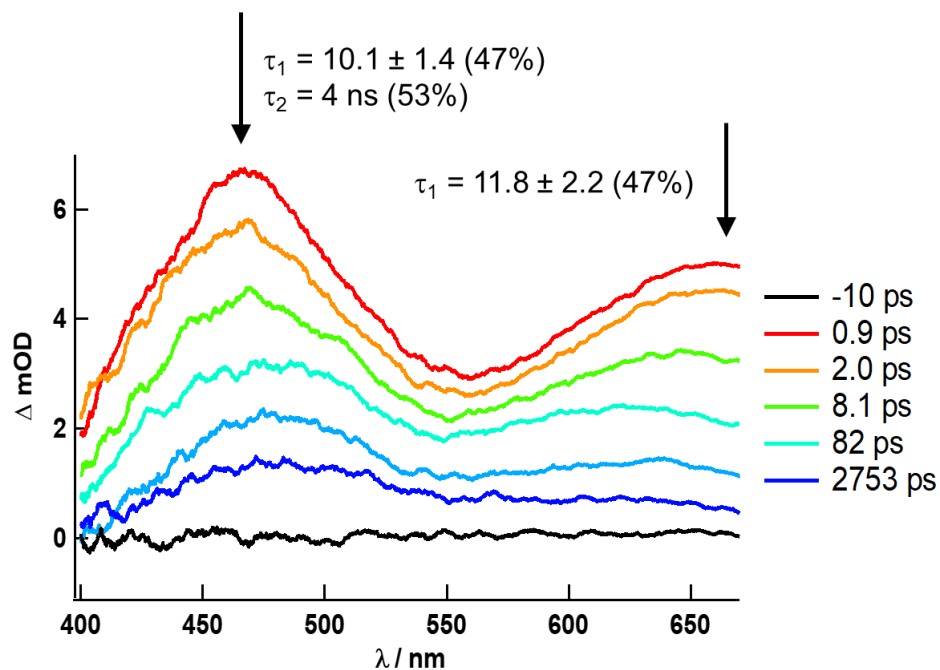


**Figure V.21** fsTA of V.1 in CH<sub>3</sub>CN ( $\lambda_{\text{ex}} = 720$  nm, 2.5  $\mu\text{J}$ ).

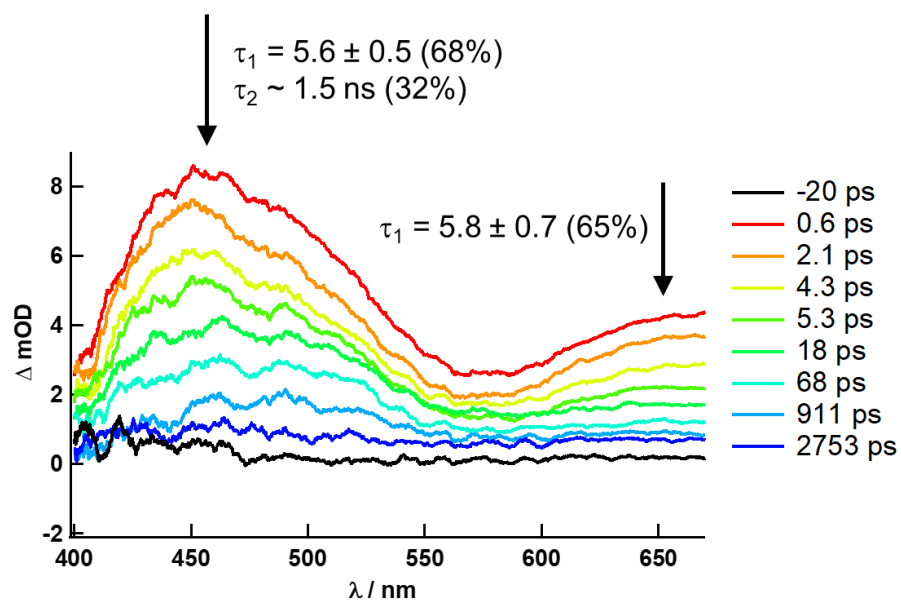


**Figure V.22** fsTA of **V.2** in  $\text{CH}_3\text{CN}$  ( $\lambda_{\text{ex}} = 720 \text{ nm}$ ,  $2.5 \mu\text{J}$ ).

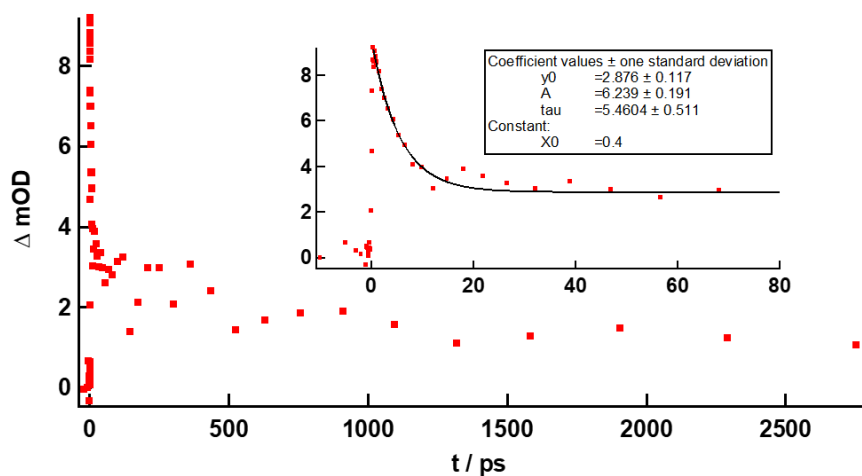


**Figure V.23** Nanosecond transient absorption spectrum of **V.1** in  $\text{CH}_3\text{CN}$  after excitation with  $650 \text{ nm}$  light ( $5 \mu\text{J}$ ) with the trace measured at  $460 \text{ nm}$ .

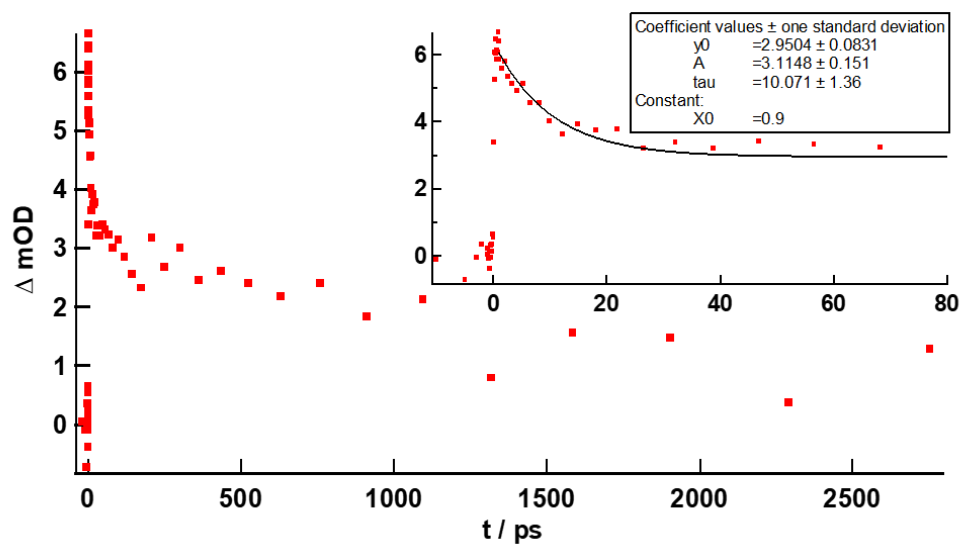


**Figure V.24** Nanosecond transient absorption spectrum of **V.2** in CH<sub>3</sub>CN after excitation with 650 nm light (5 μJ) with the trace taken at 470 nm.

### *Photocatalytic Activity*

The photocatalytic performance for hydrogen production of **V.1** and **V.2** were evaluated and a summary for these experiments can be found in Table V-6. The compounds were dissolved in acetonitrile and irradiated with low energy light ( $\lambda_{\text{irr}} = 655$  nm) in the presence of *p*-toluenesulfonic acid as the proton source and BNAH as the sacrificial donor. The compounds were initially irradiated for 4 hours and the headspace of the cell was measured for H<sub>2</sub> content using gas chromatography. Compound **V.2** had a TON of ~ 4 which represents a notable improvement given that the previously reported two-electron mixed-valence dirhodium complexes such as Rh<sub>2</sub><sup>0,II</sup>(tfepma)<sub>2</sub>(CN<sup>t</sup>Bu)<sub>2</sub>Cl<sub>2</sub> (tfepma = CH<sub>3</sub>N[P(OCH<sub>2</sub>CF<sub>3</sub>)<sub>2</sub>]<sub>2</sub>) exhibits a TON of 7 after 144 h with  $\lambda_{\text{exc}} > 305$  nm.<sup>68</sup> In contrast, **V.1** does not produce a significant amount of H<sub>2</sub>

after a 4 h irradiation period which is attributed to the shorter lifetimes of the excited states compared to **V.1**. These short lifetimes suppress the ability of the compound to participate in electron transfer reactions with the electron donor BNAH and therefore hinder the formation of the reduced bimetallic species which is most likely the catalytically active species. After 23 hours, however, some H<sub>2</sub> production is detected, which suggests that **V.1** is capable of reducing a proton that it does not have the necessary lifetime to do it efficiently. The controls that were performed indicate that all the components are necessary for H<sub>2</sub> production and that the compounds cannot reduce a proton without an appropriate source of light and an electron donor.

**Table V-6** Photocatalytic H<sub>2</sub> production of **V.1** and **V.2**.

Rh2	BNAH	TsOH	Light	TON (4 h)	TON (23 h) <sup>a</sup>
1 (22mM)	120mM	100mM	655nm	-	1.1
1	120mM	100mM	-	-	-
1	-	100mM	655nm	-	-
2 (19mM)	120mM	100mM	655nm	3.9	N/A
2	120mM	100mM	-	-	N/A
X	120mM	100mM	655nm	-	N/A
4	120mM	100mM	655nm	-	N/A

<sup>a</sup>Complex **V.1** showed very minimal H<sub>2</sub> peak after 4 h irradiation as determined by GC, so extended irradiation for 23 h was examined.

## Conclusions

Two new asymmetric dirhodium complexes, *cis*-[Rh<sub>2</sub>(DTolF)<sub>2</sub>(qxnp)(np)][BF<sub>4</sub>]<sub>2</sub> and *cis*-[Rh<sub>2</sub>(DTolF)<sub>2</sub>(qnnp)(np)][BF<sub>4</sub>]<sub>2</sub>, were prepared and their ability to photocatalyze H<sub>2</sub> production with low energy light was evaluated. Steady state absorption experiments revealed that the compounds display a panchromatic absorption profile that extends into the near-IR with two low energy features that cover the entire visible region. Computational calculations indicate that these features can be assigned to ML-LCT transitions which are Rh<sub>2</sub>(π<sup>\*</sup>)/DTolF → qxnp/qnnp and Rh<sub>2</sub>(π<sup>\*</sup>)/DTolF → np in nature for **V.1** and **V.2** respectively. Cyclic voltammetry experiments in the presence of acid showed that both compounds are capable of electrocatalytically reducing a proton to form H<sub>2</sub>. It was shown experimentally that, upon addition of acid, the compounds are protonated which leads to a blue-shift of their absorption profile. The results of low-resolution X-ray data, UV-vis titrations, and computational calculations, taken together, point to the conclusion that the protonation takes place at a bridging formamidinate ligand. This protonation reduces the donor properties of the ligand (makes it a weaker ligand) which is consistent with a shift of the absorption spectra to higher energies. In addition, **V.2** features relatively long-lived <sup>1</sup>ML-LCT and <sup>3</sup>ML-LCT states accessible with low energy light in contrast to **V.1** which has significantly shorter excited state lifetimes as concluded from transient absorption experiments. The excited state lifetimes of complex **V.2** are suitable for electron transfer reactions which makes it a good candidate for photocatalysis. In the presence of a sacrificial donor, an acid source, and light (λ<sub>irr</sub> = 655 nm) **V.2** is capable of reducing protons to form H<sub>2</sub> with a TON of ~ 4. The new aspects of this new class of

photocatalysts are the presence of an axial chelating moiety which imparts rigidity to the molecule, leading to a lengthening of excited states lifetimes, and the availability of an open axial position for catalytic activity. In contrast, fully blocked complexes with inaccessible metal sites do not display photocatalytic activity even though their excited state lifetimes are considerably longer. This work highlights how a careful choice of ligands around the dirhodium core can impart lifetimes suitable for electron transfer reactions while allowing the core to be accessed by a substrate. This new approach aimed at introducing two different acceptors into the coordination sphere opens up unexplored possibilities for the design of more efficient asymmetric dirhodium molecules for photocatalytic H<sub>2</sub> production with low energy light.

## CHAPTER VI

### CONCLUSIONS AND FUTURE DIRECTIONS

The synthesis of new and improved sensitizers is of paramount importance in a variety of diverse fields that include photodynamic therapy (PDT) and photoactivated chemotherapy (PCT) for anticancer treatment, as well as dye-sensitized solar cells (DSSCs) as a renewable source of energy, and photocatalysis for carbon-neutral fuel production among others. The highly tunable excited and ground states of dirhodium complexes which can be achieved by modifying the ligand field around the metal centers, as well as their stability under ambient conditions and solubility in a variety of solvents including water, makes these types of complexes great candidates for such applications. In this dissertation research, a new family of dirhodium complexes as potential PCT drugs and the role of the equatorial positions in the photoinduced biological activity was explored. In addition, a new class of p-type sensitizers was designed and characterized and the first reported example of a *trans*-formamidinate complex was obtained following a new synthetic methodology. Lastly, careful and judicious ligand design around the bimetallic core led to the synthesis of a new class of low energy photocatalysts for H<sub>2</sub> production that represent a leap forward in the efficiency of these types of complexes.

In Chapter II, the two new dirhodium complexes *cis*-[Rh<sub>2</sub>(AcO)<sub>2</sub>(qxnp)(MeCN)<sub>3</sub>][BF<sub>4</sub>]<sub>2</sub> and *cis*-[Rh<sub>2</sub>(AcO)<sub>2</sub>(qxnp)<sub>2</sub>][BF<sub>4</sub>]<sub>2</sub> were synthesized and characterized. The ligands were chosen in order to tune the electronic absorption properties of these complexes while retaining equatorial ligands to improve the



photoinduced biological activity of the previously published *cis*-[Rh<sub>2</sub>(AcO)<sub>2</sub>(MeCN)<sub>6</sub>][BF<sub>4</sub>]<sub>2</sub> analogue.<sup>11</sup> The incorporation of the qxnp ligand proved to be an effective way to modify the absorption profile which led to the appearance of a low-lying MLCT band. There was also a concomitant increase of the absorption coefficient by 20-fold compared to the partially solvated complex as a result of the incorporation of highly conjugated ligands that yield low-lying LUMO orbitals that are π-accepting in character. These complexes are also highly water soluble and stable in the dark as demonstrated by steady state absorption experiments in aqueous media. The fully blocked complex, *cis*-[Rh<sub>2</sub>(AcO)<sub>2</sub>(qxnp)<sub>2</sub>][BF<sub>4</sub>]<sub>2</sub>, does not bind to DNA as evidenced by gel electrophoresis experiments in the presence of the pUC-18 plasmid. This result is not surprising given that the complex is fully blocked and the qxnp ligands cannot be photohydrolyzed. The *cis*-[Rh<sub>2</sub>(AcO)<sub>2</sub>(qxnp)(MeCN)<sub>3</sub>][BF<sub>4</sub>]<sub>2</sub> compound, however, can undergo photoaquation yielding a species that is capable of binding to DNA and behaves similarly to the previously published *cis*-[Rh<sub>2</sub>(AcO)<sub>2</sub>(MeCN)<sub>6</sub>][BF<sub>4</sub>]<sub>2</sub> compound. These experiments revealed that there must be at least one open equatorial position available after irradiation to imbue relevant biological activity to the desired complexes.

In order to further red-shift the absorption profile of these complexes to achieve photoaquation with light that falls in the PDT window, a series of modifications to the bridging ligands was undertaken. The first attempt was substitution of the acetate bridging ligands for the highly electron donating formamidinate ligands. Photoaquation of the *trans*-[Rh<sub>2</sub>(DTolF)<sub>2</sub>(qxnp)(MeCN)<sub>3</sub>][BF<sub>4</sub>]<sub>2</sub> complex showed that the high electronic donation of these new bridging ligands makes the resulting complexes capable of

exchanging acetonitrile molecules even without irradiation and renders them unstable when irradiated (Figure VI.1). These undesirable features indicate that there is a balance required between electron donation and the stability in water of the complexes. To address this issue, a compound with supporting bridging ligands of intermediate electron donation capabilities such as 6-chloro-2-oxypyridine (chp) was considered (Figure VI.2). The partially solvated complex *cis*-[Rh<sub>2</sub>(chp)<sub>2</sub>(MeCN)<sub>6</sub>][BF<sub>4</sub>]<sub>2</sub> had already been reported and showed a 16.4-fold increase in cytotoxicity against HeLa cells upon irradiation when compared to the dark.<sup>9</sup> This, however, was achieved only with high energy light ( $\lambda_{\text{irr}} > 400$  nm) and it was proposed that the incorporation of one equivalent of qxnp could potentially shift the absorption and improve the photoinduced biological activity of these complexes in the PDT window.

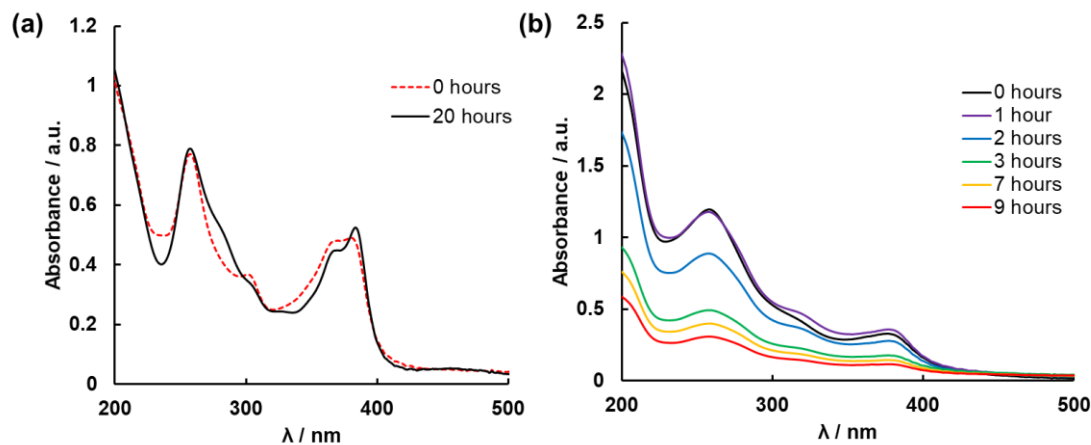


**Figure VI.1** Electronic absorption spectra for *trans*-[Rh<sub>2</sub>(DTolF)<sub>2</sub>(qxnp)(MeCN)<sub>3</sub>][BF<sub>4</sub>]<sub>2</sub> (3.X) in water in the dark (a) and upon irradiation (b).

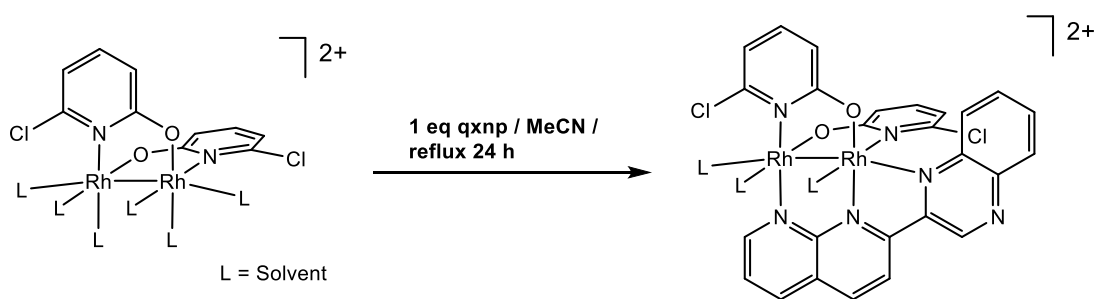


**Figure VI.2** Synthetic route to generate the proposed complex *cis*-[Rh<sub>2</sub>(mhp)<sub>2</sub>(qxnp)(MeCN)<sub>3</sub>][BF<sub>4</sub>]<sub>2</sub>.

The fully blocked complex *cis*-[Rh<sub>2</sub>(AcO)<sub>2</sub>(qxnp)<sub>2</sub>][BF<sub>4</sub>]<sub>2</sub>, although unremarkable for biological applications, inspired the design, synthesis, and characterization of a new family of formamidinate-bridged axially-blocked dirhodium complexes that was described in Chapter III. The complexes of general formula *cis*-[Rh<sub>2</sub>(DTolF)<sub>2</sub>(L)<sub>2</sub>][BF<sub>4</sub>]<sub>2</sub> (where L = pynp, qnnp, and qxnp) exhibited an extraordinary red-shift of their absorption profiles into the near-IR compared to the 1,8-naphthyridine analogue which does not absorb beyond 700 nm. More importantly, the lifetimes of the excited states of the axially blocked complexes were found to be markedly longer than the axially free analogue due to the rigidity imparted by the  $\pi$ -accepting ligands. Moreover, the excited states of these complexes are sufficiently oxidizing to transfer a hole to an electron donor such as *p*-phenylenediamine upon irradiation with low-energy light ( $\lambda_{\text{irr}} = 600$  nm). In the case of the pynp complex, the excited states are also capable of transferring an electron to the methyl viologen dication upon irradiation. This family of dirhodium dyes represents the first example of bimetallic complexes reported in the literature capable of accepting an electron from an electron donor with low energy light with an estimated redox potential

that makes them ideal candidates for p-types sensitization of NiO semiconductors for DSSC applications.

These complexes, albeit great sensitizers, do not possess the ability to bind to a semiconductor due to the lack of anchoring groups. A series of ligands was proposed for n- and p-type sensitization in the case of *cis*-[Rh<sub>2</sub>(DTolF)<sub>2</sub>(pynp)<sub>2</sub>][BF<sub>4</sub>]<sub>2</sub> that can transfer electrons or holes to electron acceptors and donors respectively from its excited state. Two possible binding modes to semiconductors are possible, namely, through the formamidinate or the axially-blocking ligand. An anchoring group on the formamidinate bridging ligand would lead to a complex that could potentially sensitized NiO since the hole localizes in the formamidinate moiety upon excitation. On the other hand, placing the anchoring group on the  $\pi$ -accepting ligand would yield a species potentially capable of transferring an electron to a n-type semiconductor such as TiO<sub>2</sub>. Figure VI.3 depicts the synthetic scheme for the proposed ligands; the <sup>1</sup>H-NMR of the Form-COOEt molecule is displayed in Figure VI.4. Schematic diagrams of the route to the dirhodium complexes are depicted in Figure VI.5. The pynp-COOEt ligands were used to synthesized two types of complexes that would allow us to investigate if anchoring through the equatorial moiety of the pynp ligand leads to more efficient electron transfer reactions than the axially bound one (Figure VI.6). To assess the ability of these complexes to transfer electrons to a semiconductor, the ester groups will be hydrolyzed with tetrabutylammonium hydroxide (TBAOH) in the presence of TiO<sub>2</sub> or NiO nanoparticles (NP) for n- and p-type sensitization respectively to generate the Rh-NP complexes. TA experiments will be carried out to assess the electron transfer properties of the Rh-NP complexes.

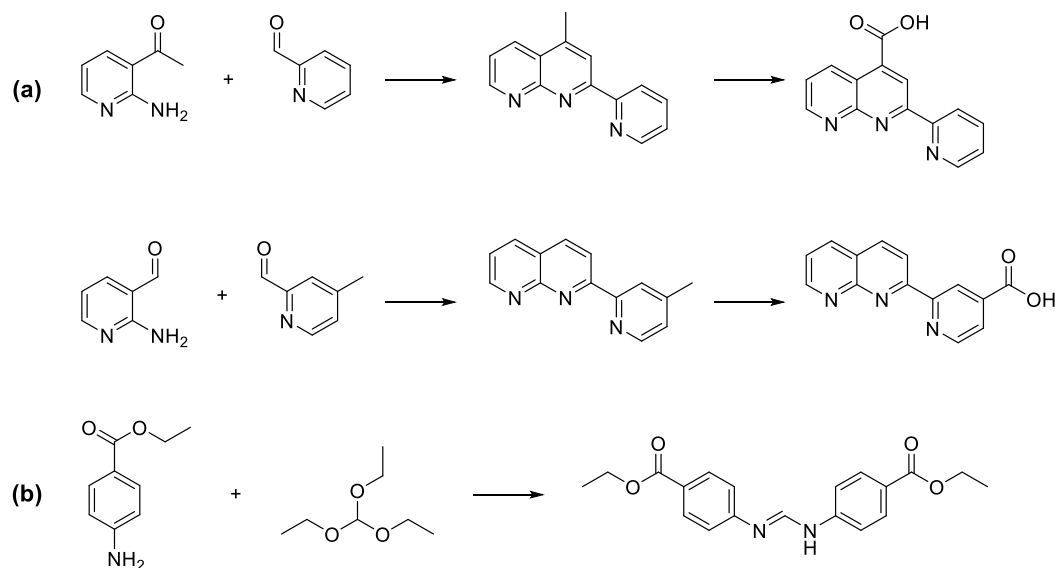


**Figure VI.3** Synthetic scheme for the  $\pi$ -accepting and axially blocking ligands with anchoring groups (a) and the formamidine electron donating bridging ligand with protected anchoring groups (b).

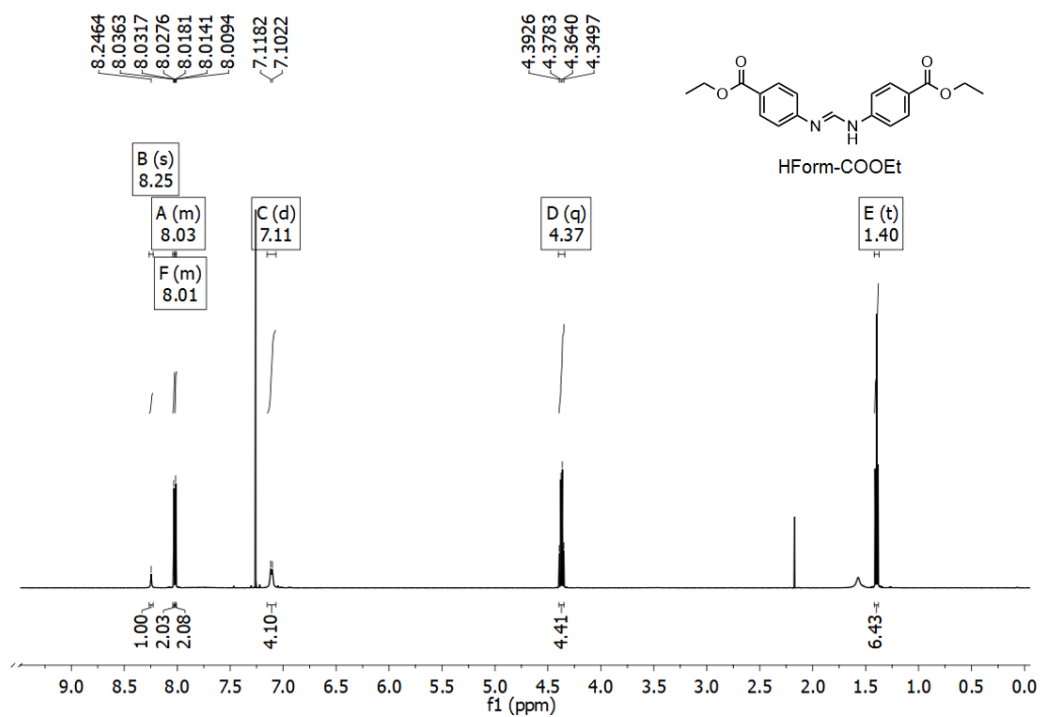


**Figure VI.4** Aromatic region of the  $^1\text{H}$  NMR for the Form-COOEt ligand.

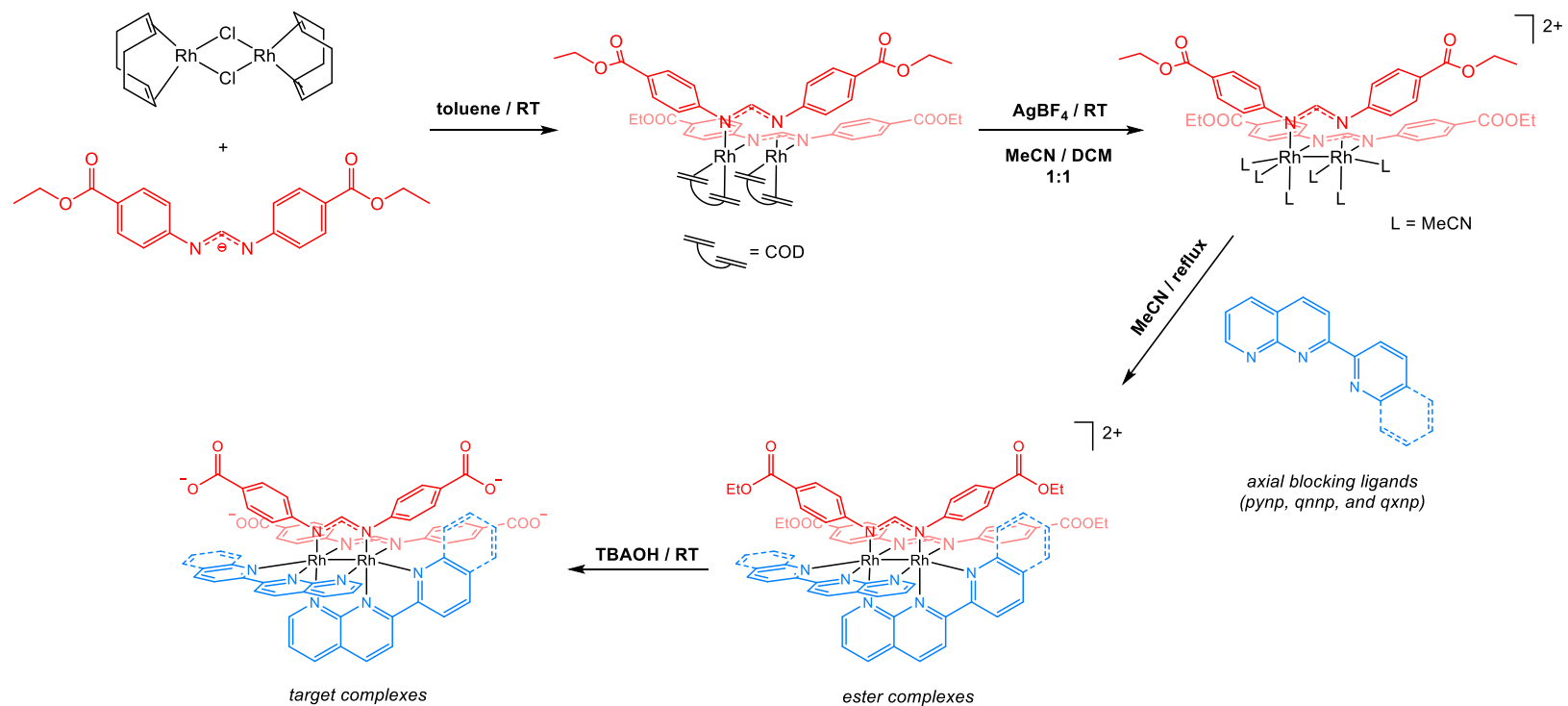


**Figure VI.5** Proposed synthetic scheme for the synthesis of a series of potential p-type dirhodium sensitizers of the type *cis*- $[\text{Rh}_2(\text{Form-COO})_2(\text{L})_2]^{2-}$  where L = pynp, qnnp, and qxnp.

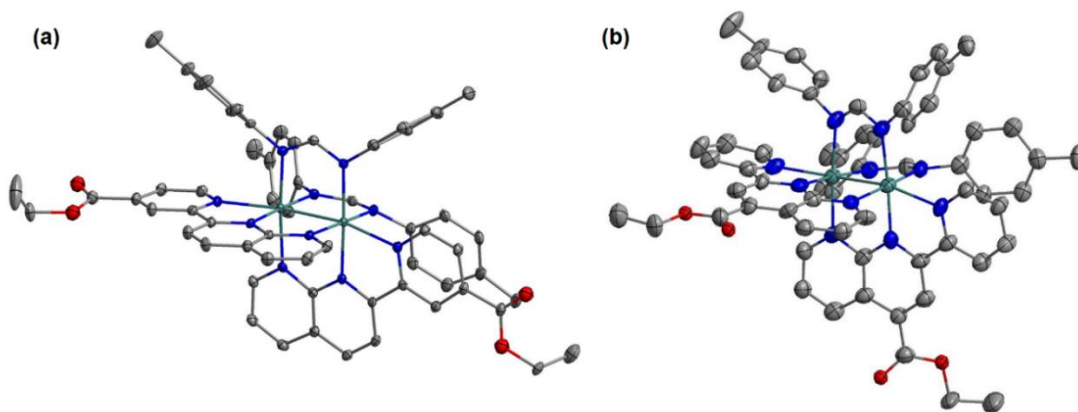


**Figure VI.6** Thermal ellipsoid plots for the compounds *cis*-[Rh<sub>2</sub>(DTolF)<sub>2</sub>(2COOEt-pynp)<sub>2</sub>][BF<sub>4</sub>]<sub>2</sub> (a) and *cis*-[Rh<sub>2</sub>(DTolF)<sub>2</sub>(4COOEt-pynp)<sub>2</sub>][BF<sub>4</sub>]<sub>2</sub> (b) at the 50% probability level. Counterions, hydrogen atoms, and solvent molecules were omitted for the sake of clarity.

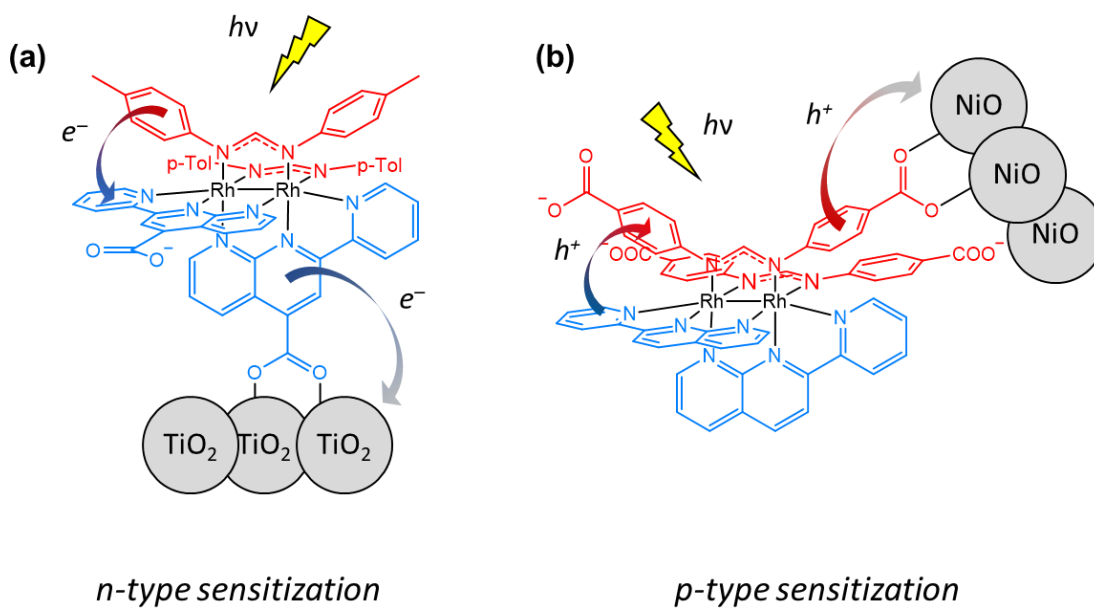


**Figure VI.7** Schematic representations of *cis*-[Rh<sub>2</sub>(DTolF)<sub>2</sub>(4COO-pynp)<sub>2</sub>][BF<sub>4</sub>]<sub>2</sub> (a) and *cis*-[Rh<sub>2</sub>(COO-Form)<sub>2</sub>(pynp)<sub>2</sub>][BF<sub>4</sub>]<sub>2</sub> (b) bound to TiO<sub>2</sub> for *n*-type sensitization and NiO for *p*-type sensitization respectively.

The vast majority of bis-substituted dirhodium partial paddlewheel complexes reported in the literature are of the *cis* configuration. Of specific note with respect to the work presented in this dissertation, there are no examples in the literature of *trans*-dirhodium formamidinate compounds due to the marked trans effect that these ligands exert across the Rh atoms which determines the geometric arrangement of the final products. In Chapter IV, a carefully designed synthetic methodology, supported by DFT calculations, led to the synthesis of the first example of a bis-substituted *trans*-dirhodium complex with two formamidinate bridging ligands. The *trans*-[Rh<sub>2</sub>(DTolF)<sub>2</sub>(qxnp)<sub>2</sub>][BF<sub>4</sub>]<sub>2</sub> complex was synthesized by addition of a single equivalent of the axially-blocking qxnp ligand which facilitates the migration of a formamidinate ligand to a *trans* intermediate as supported by DFT calculations. This intermediate, *trans*-[Rh<sub>2</sub>(DTolF)<sub>2</sub>(qxnp)(MeCN)<sub>3</sub>][BF<sub>4</sub>]<sub>2</sub>, can subsequently accept a second equivalent of qxnp to yield the final product. This compound, as shown by TA spectroscopy experiments, can also transfer a hole to an electron acceptor when irradiated with low energy light. This result is important because it opens a new avenue of exploration for different types or architectures that have been unexplored. In particular, as shown in Figure VI.8, the development of a variety supramolecular architectures is possible with the use of the newly discovered *trans* isomer as the ~ 180° between ligands allows for the formation of several different types of polygonal structures such as triangles, squares, and hexagons, among others. In contrast, the *cis* analogs are limited to the synthesis of squares and highly distorted triangles due to the ~ 90° between ligands.



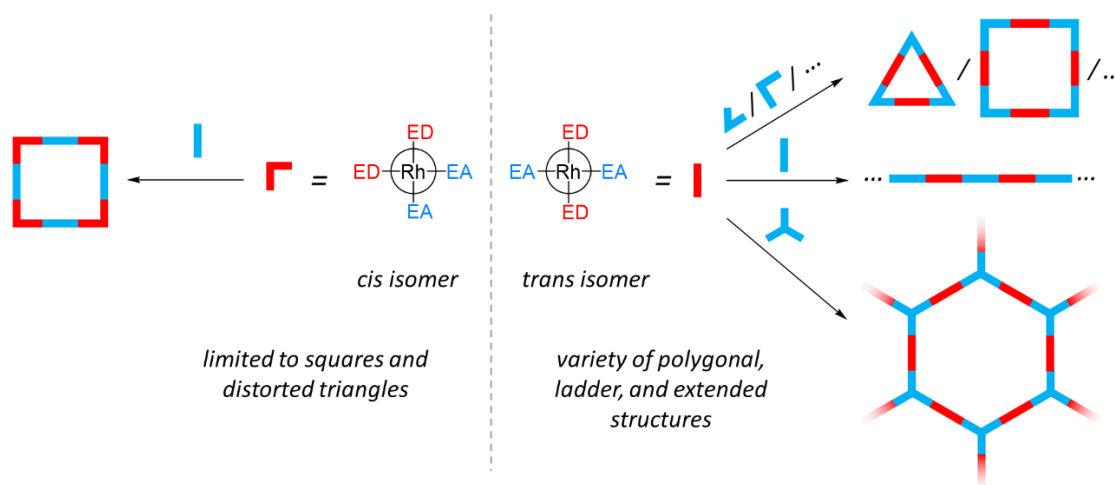


**Figure VI.8** Schematic representation of *cis* and *trans* dirhodium complexes as building blocks for supramolecular architectures.

Motivated by these findings, we proposed the synthesis of the partially solvated *trans*- $[\text{Rh}_2(\text{DTolF})_2(\text{MeCN})_6][\text{BF}_4]_2$  precursor. The reaction scheme presented in Figure VI.9 would lead to the desired *trans* building block. The critical step is the synthesis of the mono-substituted  $[\text{Rh}_2(\text{DTolF})(\text{MeCN})_8][\text{BF}_4]_3$  complex from protonation of *cis*- $[\text{Rh}_2(\text{DTolF})_2(\text{MeCN})_6][\text{BF}_4]_2$  with  $\text{HBF}_4$ , followed by the addition of a second equivalent of a formamidinate ligand to yield the desired *trans* product. This approach is entirely feasible due to the *trans* effect exerted by the strong electron donor DTolF bridging ligand that weakens the  $\text{Rh}-\text{MeCN}_{\text{eq}}$  bonds of the solvent molecules opposite to the N donors of the formamidinate which makes the formation of the *trans* isomer favored over the *cis* analog. This new building block would open new synthetic possibilities such as the synthesis of polygonal, extended, or ladder structures with potentially interesting photophysical properties (Figure VI.9).

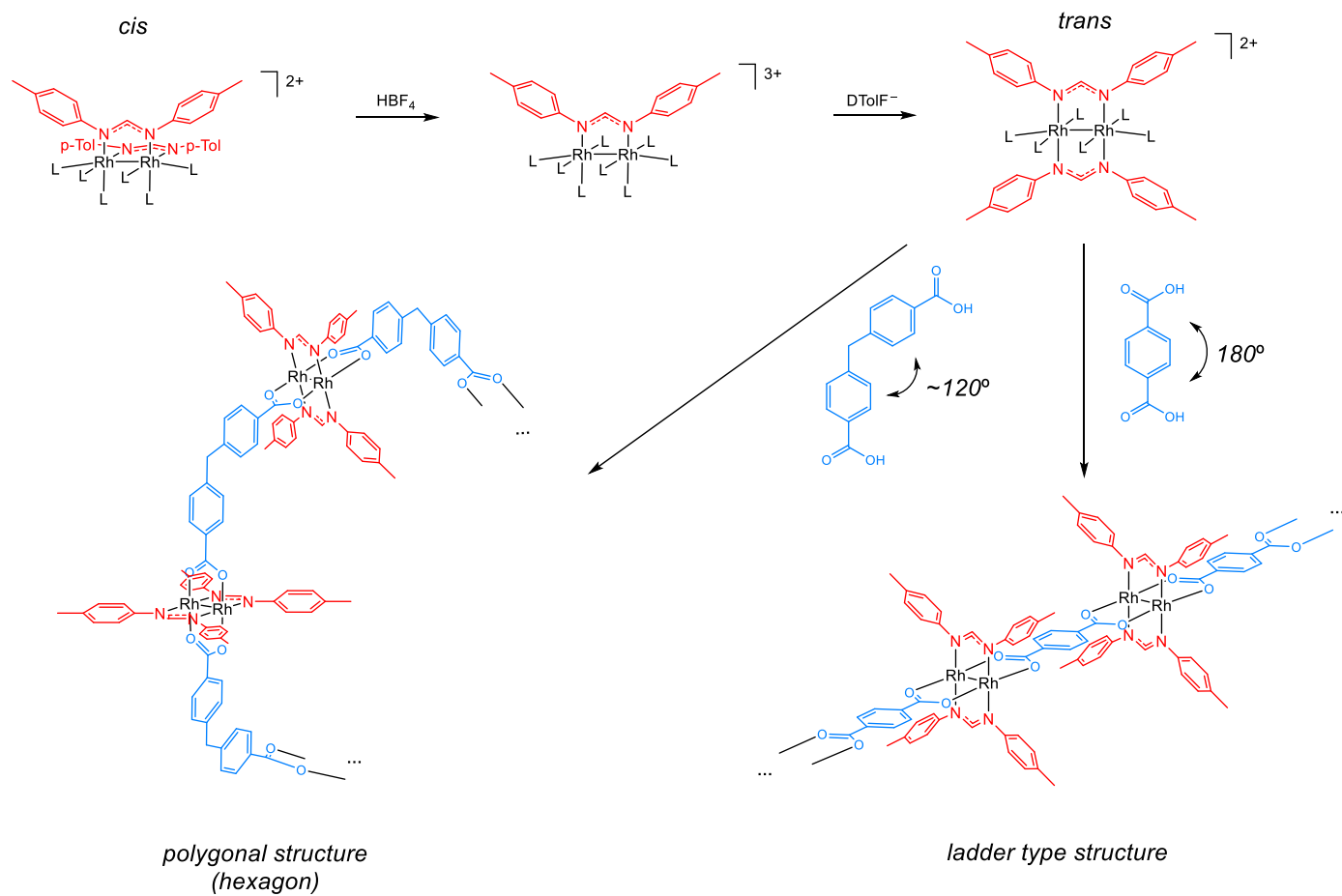


**Figure VI.9** Synthetic scheme to generate  $trans$ -[Rh<sub>2</sub>(DTolF)<sub>2</sub>(MeCN)<sub>6</sub>][BF<sub>4</sub>]<sub>2</sub> as a building block for hexagonal supramolecular architectures and ladder-type structures in the presence of appropriate linkers.

The synthesis of the novel class of sensitizers discussed in Chapter IV led to the design, synthesis, and characterization of a new class of photocatalysts that was discussed in Chapter V. The sensitizers from Chapter IV, although ideal for electron transfer reactions, are not catalytically active due to the metal centers being fully blocked. On the other hand, compounds such as *cis*-[Rh<sub>2</sub>(DTolF)<sub>2</sub>(np)<sub>2</sub>(MeCN)<sub>2</sub>][BF<sub>4</sub>]<sub>2</sub> with two labile axial positions and which are electrocatalytically active, do not have excited states that are sufficiently long-lived to participate in electron transfer reactions. Therefore, in the search for better photosensitizers, a new class of compounds was designed that supports two different types of  $\pi$ -accepting ligands, namely one that can block an axial position to impart rigidity to the complex and another that leaves an axial position free to engage in catalytic processes. The compounds *cis*-[Rh<sub>2</sub>(DTolF)<sub>2</sub>(L)(np)][BF<sub>4</sub>]<sub>2</sub> (L = qxnp or qnnp) were prepared and found to exhibit two ML-LCT features in their electronic spectra that extend into the near-IR. Their panchromatic absorption profiles poise them as excellent candidates as sensitizers. In addition, both compounds are electrocatalytically active as was evidenced by CV experiments in the presence of acid. Most importantly, the excited state lifetimes of the qnnp-bearing complexes are suitable for electron transfer reactions that are crucial for photocatalytic processes. The complexes were irradiated with low energy light ( $\lambda_{\text{irr}} > 655$  nm) in the presence of the sacrificial donor BNAH and TsOH as the acid source and the H<sub>2</sub> efficiency was evaluated. The compound with suitable excited state lifetimes, *cis*-[Rh<sub>2</sub>(DTolF)<sub>2</sub>(qnnp)(np)][BF<sub>4</sub>]<sub>2</sub>, had a TON of ~ 4 for H<sub>2</sub> production after 3 hours of irradiation. This result represents a great improvement over previously

reported complexes that had similar TONs but which required UV-light for the production of H<sub>2</sub>.<sup>67, 191, 192</sup> The mechanism for H<sub>2</sub> production has not been elucidated and a series of experiments is proposed to gain information. Cyclic voltammetry experiments in the presence of a strong acid should confirm the protonation of the complex in the formamidinate ligand by observation of a shift in the potential of the first oxidation that is Rh/Form in character. In addition, chemical reduction by one or two electrons followed by irradiation in the presence of acid should provide insight as to which species is photocatalytically active. These experiments, along with intensive DFT calculations, will provide valuable information to rule out some possible mechanisms of H<sub>2</sub> production.

Apart from the elucidation of the mechanism, these compounds present some drawbacks which serve to lower the TON for H<sub>2</sub> production. Since the complexes only contain one axial site occupied by a chelating donor, the Rh-Rh bond lengthens making metal-centered states more accessible which causes a shortening in the lifetimes of the excited states and lower efficiencies. To overcome this issue, the use of the ligand bncn (benzo[c]cinnoline) is proposed as a substitute for the bridging np ligand. This new ligand has a much shorter N-N bite distance which should lead to a target complex (Figure VI.10) with a shorter Rh-Rh bond and longer excited state lifetimes with respect to the np analog.

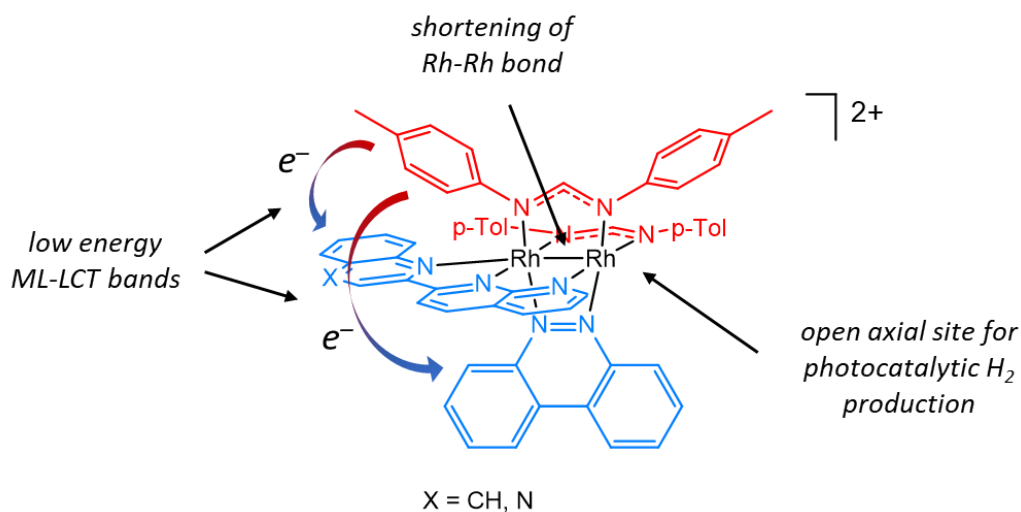


**Figure VI.10** Schematic representation of the target complexes *cis*-[Rh<sub>2</sub>(DTolF)<sub>2</sub>(qxnp)(bncn)][BF<sub>4</sub>]<sub>2</sub> and *cis*-[Rh<sub>2</sub>(DTolF)<sub>2</sub>(qnp)(bncn)][BF<sub>4</sub>]<sub>2</sub> for photocatalytic H<sub>2</sub> production with low-energy light.

The synthetic route proposed for these target complexes is presented in Figure VI.11 and involves the reaction of the partially solvated *cis*-[Rh<sub>2</sub>(DTolF)<sub>2</sub>(MeCN)<sub>6</sub>][BF<sub>4</sub>]<sub>2</sub> complex with one equivalent of the bncn ligand and one equivalent of the axial blocking ligand (qnp or qxnp). This synthetic scheme is expected to lead to the formation of a mixture of products with the major product being the target complexes. The desired final products should be easily separated using column chromatography. Similar studies must be carried out to determine the lifetime of the excited states, the electrocatalytic activity, and the photocatalytic properties of the resulting complexes that should, in principle, display higher TON for H<sub>2</sub> production with low energy light.

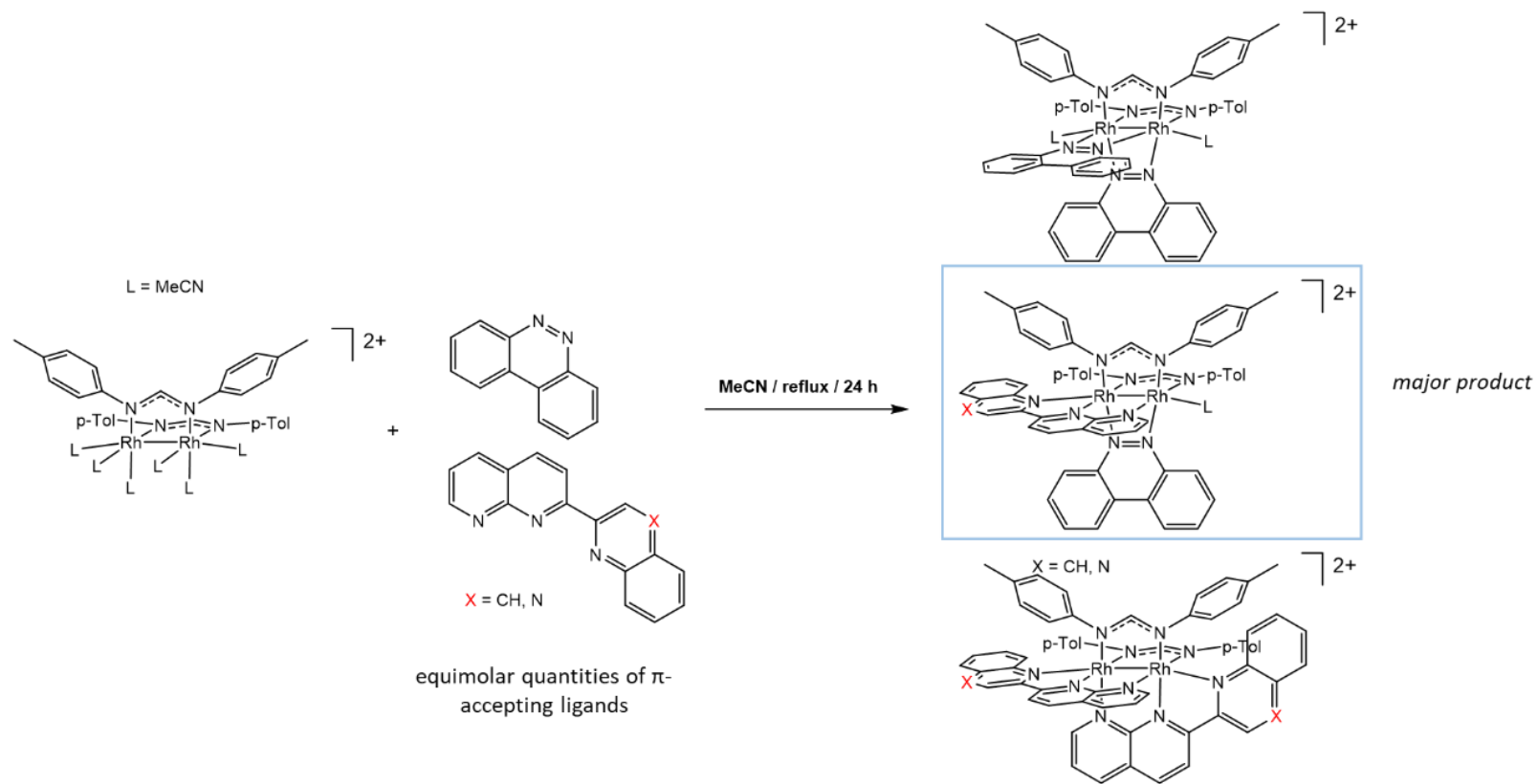


**Figure VI.11** Synthetic route proposed for the syntheses of *cis*- $[\text{Rh}_2(\text{DTolF})_2(\text{qxnp})(\text{bncn})][\text{BF}_4]_2$  and *cis*- $[\text{Rh}_2(\text{DTolF})_2(\text{qnnp})(\text{bncn})][\text{BF}_4]_2$ .

The new compounds presented in this dissertation were found to be viable for a variety of applications including photoactivated chemotherapy, p-type sensitization for DSSCs, and as photocatalysts for H<sub>2</sub> production. This body of work, as a whole, highlights the importance of ligand design for inorganic complexes and the prominent impact that the coordination sphere has over the final properties of the complexes. The work presented in this dissertation includes the synthesis of the first family of dinuclear metal-metal bonded complexes capable of p-type sensitization, the first example of *trans*-formamidinate bridged dirhodium complexes which can be used in future work as building blocks for supramolecular assemblies, and the first example of low energy light dirhodium photocatalysts for H<sub>2</sub> production. These projects expand on the dirhodium tool library and open new doors for novel and interesting applications.

## REFERENCES

1. Cotton, F. A.; Lin, C.; Murillo, C. A., Supramolecular Arrays Based on Dimetal Building Units. *Acc. Chem. Res.* **2001**, *34* (10), 759-771.
2. Kumar, D. K.; Filatov, A. S.; Napier, M.; Sun, J.; Dikarev, E. V.; Petrukhina, M. A., Dirhodium Paddlewheel with Functionalized Carboxylate Bridges: New Building Block for Self-Assembly and Immobilization on Solid Support. *Inorg. Chem.* **2012**, *51* (8), 4855-4861.
3. Chifotides, H. T.; Koshlap, K. M.; Pérez, L. M.; Dunbar, K. R., Unprecedented Head-to-Head Conformers of d(GpG) Bound to the Antitumor Active Compound Tetrakis( $\mu$ -carboxylato)dirhodium(II,II). *J. Am. Chem. Soc.* **2003**, *125* (35), 10703-10713.
4. Chifotides, H. T.; Koshlap, K. M.; Pérez, L. M.; Dunbar, K. R., Novel Binding Interactions of the DNA Fragment d(pGpG) Cross-Linked by the Antitumor Active Compound Tetrakis( $\mu$ -carboxylato)dirhodium(II,II). *J. Am. Chem. Soc.* **2003**, *125* (35), 10714-10724.
5. Chifotides, H. T.; Dunbar, K. R., Unprecedented Head-to-Head Right-Handed Cross-Links between the Antitumor Bis( $\mu$ -N,N'-di-p-tolylformamidinate) Dirhodium(II,II) Core and the Dinucleotide d(ApA) with the Adenine Bases in the Rare Imino Form. *J. Am. Chem. Soc.* **2007**, *129* (41), 12480-12490.
6. Kang, M.; Chouai, A.; Chifotides, H. T.; Dunbar, K. R., 2D NMR Spectroscopic Evidence for Unprecedented Interactions of cis-[Rh<sub>2</sub>(dap)( $\mu$ -O<sub>2</sub>CCH<sub>3</sub>)<sub>2</sub>( $\eta$ 1-



O2CCH3)(CH3OH)](O2CCH3) with a DNA Oligonucleotide: Combination of Intercalative and Coordinative Binding. *Angew. Chem. Int. Ed.* **2006**, *45* (37), 6148-6151.

7. Chifotides, H. T.; Dunbar, K. R., Interactions of Metal–Metal-Bonded Antitumor Active Complexes with DNA Fragments and DNA. *Acc. Chem. Res.* **2005**, *38* (2), 146-156.

8. Chifotides, H. T.; Lutterman, D. A.; Dunbar, K. R.; Turro, C., Insight into the Photoinduced Ligand Exchange Reaction Pathway of cis-[Rh2( $\mu$ -O2CCH3)2(CH3CN)6]2+ with a DNA Model Chelate. *Inorg. Chem.* **2011**, *50* (23), 12099-12107.

9. Li, Z.; David, A.; Albani, B. A.; Pellois, J.-P.; Turro, C.; Dunbar, K. R., Optimizing the Electronic Properties of Photoactive Anticancer Oxypyridine-Bridged Dirhodium(II,II) Complexes. *J. Am. Chem. Soc.* **2014**, *136* (49), 17058-17070.

10. Burya, S. J.; Palmer, A. M.; Gallucci, J. C.; Turro, C., Photoinduced Ligand Exchange and Covalent DNA Binding by Two New Dirhodium Bis-Amidato Complexes. *Inorg. Chem.* **2012**, *51* (21), 11882-11890.

11. Lutterman, D. A.; Fu, P. K. L.; Turro, C., cis-[Rh2( $\mu$ -O2CCH3)2(CH3CN)6]2+ as a Photoactivated Cisplatin Analog. *J. Am. Chem. Soc.* **2006**, *128* (3), 738-739.

12. Cotton, F. A.; Murillo, C. A.; Walton, R. A., *Multiple bonds between metal atoms*. 3rd ed. edited by F. Albert Cotton, Carlos A. Murillo and Richard A. Walton. New York : Springer Science and Business Media, Inc., 2005.

3rd ed.: 2005.

13. Rizzi, G. A.; Casarin, M.; Tondello, E.; Piraino, P.; Granozzi, G., UV photoelectron spectra and DV-X.alpha. calculations on diatomic rhodium formamidinate complexes. *Inorg. Chem.* **1987**, *26* (20), 3406-3409.
14. Garner, R. N.; Gallucci, J. C.; Dunbar, K. R.; Turro, C., [Ru(bpy)<sub>2</sub>(5-cyanouracil)<sub>2</sub>]<sup>2+</sup> as a Potential Light-Activated Dual-Action Therapeutic Agent. *Inorg. Chem.* **2011**, *50* (19), 9213-9215.
15. World Health Organization <https://www.who.int/news-room/fact-sheets/detail/cancer> (accessed August 13, 2019).
16. Siegel, R. L.; Miller, K. D.; Jemal, A., Cancer statistics, 2019. *CA: A Cancer Journal for Clinicians* **2019**, *69* (1), 7-34.
17. Kidani, Y.; Inagaki, K.; Iigo, M.; Hoshi, A.; Kuretani, K., Antitumor activity of 1,2-diaminocyclohexaneplatinum complexes against Sarcoma-180 ascites form. *J. Med. Chem.* **1978**, *21* (12), 1315-1318.
18. Rixe, O.; Ortuzar, W.; Alvarez, M.; Parker, R.; Reed, E.; Paull, K.; Fojo, T., Oxaliplatin, tetraplatin, cisplatin, and carboplatin: Spectrum of activity in drug-resistant cell lines and in the cell lines of the national cancer institute's anticancer drug screen panel. *Biochem. Pharmacol.* **1996**, *52* (12), 1855-1865.
19. Kelland, L., The resurgence of platinum-based cancer chemotherapy. *Nature Reviews Cancer* **2007**, *7* (8), 573-584.
20. Erck, A.; Rainen, L.; Whileyman, J.; Chang, I.-M.; Kimball, A. P.; Bear, J., Studies of Rhodium(II) Carboxylates as Potential Antitumor Agents. *Proceedings of the Society for Experimental Biology and Medicine* **1974**, *145* (4), 1278-1283.

21. Bear, J. L.; Gray, H. B.; Rainen, L.; Chang, I. M.; Howard, R.; Serio, G.; Kimball, A. P., Interaction of Rhodium(II) carboxylates with molecules of biologic importance. *Cancer Chemother Rep* **1975**, *59* (3), 611-620.
22. Howard, R. A.; Spring, T. G.; Bear, J. L., The Interaction of Rhodium(II) Carboxylates with Enzymes. *Cancer Research* **1976**, *36* (12), 4402-4405.
23. Howard, R. A.; Sherwood, E.; Erck, A.; Kimball, A. P.; Bear, J. L., Hydrophobicity of several rhodium(II) carboxylates correlated with their biologic activity. *J. Med. Chem.* **1977**, *20* (7), 943-946.
24. Howard, R. A.; Kimball, A. P.; Bear, J. L., Mechanism of Action of Tetra- $\mu$ -carboxylatodirrhodium(II) in L1210 Tumor Suspension Culture. *Cancer Research* **1979**, *39* (7 Part 1), 2568-2573.
25. Rao, P. N.; Smith, M. L.; Pathak, S.; Howard, R. A.; Bear, J. L., Rhodium (II) Butyrate: A Potential Anticancer Drug With Cell Cycle Phase-Specific Effects in HeLa Cells. *JNCI: Journal of the National Cancer Institute* **1980**, *64* (4), 905-912.
26. Chifotides, H. T.; Hess, J. S.; Angeles-Boza, A. M.; Ramón Galán-Mascarós, J.; Sorasaenee, K.; Dunbar, K. R., Structural evidence for monodentate binding of guanine to the dirrhodium(ii,ii) core in a manner akin to that of cisplatin. *Dalton Trans.* **2003**, (23), 4426-4430.
27. Aoki, K.; Salam, M. A., Interligand interactions affecting specific metal bonding to nucleic acid bases. A case of  $[\text{Rh}_2(\text{OAc})_4]$ ,  $[\text{Rh}_2(\text{HNOCCF}_3)_4]$ , and  $[\text{Rh}_2(\text{OAc})_2(\text{HNOCCF}_3)_2]$  toward purine nucleobases and nucleosides. *Inorg. Chim. Acta* **2002**, *339*, 427-437.

28. Chifotides, H. T.; Catalan, K. V.; Dunbar, K. R., Dirhodium Formamidinate Compounds with Bidentate Nitrogen Chelating Ligands. *Inorg. Chem.* **2003**, *42* (26), 8739-8747.
29. Chifotides, H. T.; Fu, P. K. L.; Dunbar, K. R.; Turro, C., Effect of Equatorial Ligands of Dirhodium(II,II) Complexes on the Efficiency and Mechanism of Transcription Inhibition in Vitro. *Inorg. Chem.* **2004**, *43* (3), 1175-1183.
30. Dunham, S. U.; Chifotides, H. T.; Mikulski, S.; Burr, A. E.; Dunbar, K. R., Covalent Binding and Interstrand Cross-Linking of Duplex DNA by Dirhodium(II,II) Carboxylate Compounds. *Biochemistry* **2005**, *44* (3), 996-1003.
31. Aguirre, J. D.; Lutterman, D. A.; Angeles-Boza, A. M.; Dunbar, K. R.; Turro, C., Effect of Axial Coordination on the Electronic Structure and Biological Activity of Dirhodium(II,II) Complexes. *Inorg. Chem.* **2007**, *46* (18), 7494-7502.
32. Angeles-Boza, A. M.; Bradley, P. M.; Fu, P. K. L.; Shatruck, M.; Hilfiger, M. G.; Dunbar, K. R.; Turro, C., Photocytotoxicity of a New Rh<sub>2</sub>(II,II) Complex: Increase in Cytotoxicity upon Irradiation Similar to That of PDT Agent Hematoporphyrin. *Inorg. Chem.* **2005**, *44* (21), 7262-7264.
33. Bradley, P. M.; Angeles-Boza, A. M.; Dunbar, K. R.; Turro, C., Direct DNA Photocleavage by a New Intercalating Dirhodium(II/II) Complex: Comparison to Rh<sub>2</sub>(μ-O<sub>2</sub>CCH<sub>3</sub>)<sub>4</sub>. *Inorg. Chem.* **2004**, *43* (8), 2450-2452.
34. Catalan, K. V.; Mindiola, D. J.; Ward, D. L.; Dunbar, K. R., A Novel Dirhodium Compound with Neutral, Bridging 9-Ethyladenine Ligands. *Inorg. Chem.* **1997**, *36* (11), 2458-2460.

35. Joyce, L. E.; Aguirre, J. D.; Angeles-Boza, A. M.; Chouai, A.; Fu, P. K.; Dunbar, K. R.; Turro, C., Photophysical properties, DNA photocleavage, and photocytotoxicity of a series of dppn dirhodium(II,II) complexes. *Inorg. Chem.* **2010**, *49* (12), 5371-6.
36. Aguirre, J. D.; Angeles-Boza, A. M.; Chouai, A.; Pellois, J.-P.; Turro, C.; Dunbar, K. R., Live Cell Cytotoxicity Studies: Documentation of the Interactions of Antitumor Active Dirhodium Compounds with Nuclear DNA. *J. Am. Chem. Soc.* **2009**, *131* (32), 11353-11360.
37. Dolmans, D. E. J. G. J.; Fukumura, D.; Jain, R. K., Photodynamic therapy for cancer. *Nature Reviews Cancer* **2003**, *3* (5), 380-387.
38. Agostinis, P.; Berg, K.; Cengel, K. A.; Foster, T. H.; Girotti, A. W.; Gollnick, S. O.; Hahn, S. M.; Hamblin, M. R.; Juzeniene, A.; Kessel, D.; Korbelik, M.; Moan, J.; Mroz, P.; Nowis, D.; Piette, J.; Wilson, B. C.; Golab, J., Photodynamic therapy of cancer: An update. *CA: A Cancer Journal for Clinicians* **2011**, *61* (4), 250-281.
39. Juarranz, Á.; Jaén, P.; Sanz-Rodríguez, F.; Cuevas, J.; González, S., Photodynamic therapy of cancer. Basic principles and applications. *Clinical and Translational Oncology* **2008**, *10* (3), 148-154.
40. Smith, N. A.; Sadler, P. J., Photoactivatable metal complexes: from theory to applications in biotechnology and medicine. *Philosophical Transactions of the Royal Society A: Mathematical, Physical and Engineering Sciences* **2013**, *371* (1995), 20120519.

41. Bonnet, S., Shifting the Light Activation of Metallodrugs to the Red and Near-Infrared Region in Anticancer Phototherapy. *Comments Inorg. Chem.* **2015**, *35* (4), 179-213.
42. Imberti, C.; Zhang, P.; Huang, H.; Sadler, P. J., New Designs for Phototherapeutic Transition Metal Complexes. *Angew. Chem. Int. Ed.* *0* (0).
43. Monro, S.; Colón, K. L.; Yin, H.; Roque, J.; Konda, P.; Gujar, S.; Thummel, R. P.; Lilge, L.; Cameron, C. G.; McFarland, S. A., Transition Metal Complexes and Photodynamic Therapy from a Tumor-Centered Approach: Challenges, Opportunities, and Highlights from the Development of TLD1433. *Chem. Rev.* **2019**, *119* (2), 797-828.
44. Orenstein, A.; Kostenich, G.; Roitman, L.; Shechtman, Y.; Kopolovic, Y.; Ehrenberg, B.; Malik, Z., A comparative study of tissue distribution and photodynamic therapy selectivity of chlorin e6, Photofrin II and ALA-induced protoporphyrin IX in a colon carcinoma model. *British Journal of Cancer* **1996**, *73* (8), 937-944.
45. Administration, U. S. E. I. Today in Energy. (accessed April 17).
46. Sampaio, P. G. V.; González, M. O. A., Photovoltaic solar energy: Conceptual framework. *Renew. Sust. Energ. Rev.* **2017**, *74*, 590-601.
47. McConnell, R. D., Assessment of the dye-sensitized solar cell. *Renew. Sust. Energ. Rev.* **2002**, *6* (3), 271-293.
48. Odobel, F.; Le Pleux, L.; Pellegrin, Y.; Blart, E., New Photovoltaic Devices Based on the Sensitization of p-type Semiconductors: Challenges and Opportunities. *Acc. Chem. Res.* **2010**, *43* (8), 1063-1071.

49. Vittal, R.; Ho, K.-C., Zinc oxide based dye-sensitized solar cells: A review. *Renew. Sust. Energ. Rev.* **2017**, *70*, 920-935.
50. Wali, Q.; Fakharuddin, A.; Jose, R., Tin oxide as a photoanode for dye-sensitised solar cells: Current progress and future challenges. *J. Power Sources* **2015**, *293*, 1039-1052.
51. Shakeel Ahmad, M.; Pandey, A. K.; Abd Rahim, N., Advancements in the development of TiO<sub>2</sub> photoanodes and its fabrication methods for dye sensitized solar cell (DSSC) applications. A review. *Renew. Sust. Energ. Rev.* **2017**, *77*, 89-108.
52. Tang, Q.; Duan, J.; Duan, Y.; He, B.; Yu, L., Recent advances in alloy counter electrodes for dye-sensitized solar cells. A critical review. *Electrochim. Acta* **2015**, *178*, 886-899.
53. Nath, N. C. D.; Lee, J.-J., Binary redox electrolytes used in dye-sensitized solar cells. *Journal of Industrial and Engineering Chemistry* **2019**, *78*, 53-65.
54. Carella, A.; Borbone, F.; Centore, R., Research Progress on Photosensitizers for DSSC. *Frontiers in Chemistry* **2018**, *6* (481).
55. Hardin, B. E.; Snaith, H. J.; McGehee, M. D., The renaissance of dye-sensitized solar cells. *Nature Photonics* **2012**, *6* (3), 162-169.
56. Cole, J. M.; Pepe, G.; Al Bahri, O. K.; Cooper, C. B., Cosensitization in Dye-Sensitized Solar Cells. *Chem. Rev.* **2019**, *119* (12), 7279-7327.
57. Wood, C. J.; Summers, G. H.; Clark, C. A.; Kaeffer, N.; Braeutigam, M.; Carbone, L. R.; D'Amario, L.; Fan, K.; Farré, Y.; Narbey, S.; Oswald, F.; Stevens, L. A.; Parmenter, C. D. J.; Fay, M. W.; La Torre, A.; Snape, C. E.; Dietzek, B.; Dini, D.;

- Hammarström, L.; Pellegrin, Y.; Odobel, F.; Sun, L.; Artero, V.; Gibson, E. A., A comprehensive comparison of dye-sensitized NiO photocathodes for solar energy conversion. *PCCP* **2016**, *18* (16), 10727-10738.
58. Grätzel, M., Dye-sensitized solar cells. *J. Photochem. Photobiol. C* **2003**, *4* (2), 145-153.
59. Nazeeruddin, M. K.; Kay, A.; Rodicio, I.; Humphry-Baker, R.; Mueller, E.; Liska, P.; Vlachopoulos, N.; Graetzel, M., Conversion of light to electricity by cis-X<sub>2</sub>bis(2,2'-bipyridyl-4,4'-dicarboxylate)ruthenium(II) charge-transfer sensitizers (X = Cl-, Br-, I-, CN-, and SCN-) on nanocrystalline titanium dioxide electrodes. *J. Am. Chem. Soc.* **1993**, *115* (14), 6382-6390.
60. Mathew, S.; Yella, A.; Gao, P.; Humphry-Baker, R.; Curchod, B. F. E.; Ashari-Astani, N.; Tavernelli, I.; Rothlisberger, U.; Nazeeruddin, M. K.; Grätzel, M., Dye-sensitized solar cells with 13% efficiency achieved through the molecular engineering of porphyrin sensitizers. *Nat. Chem.* **2014**, *6*, 242.
61. Kakiage, K.; Aoyama, Y.; Yano, T.; Otsuka, T.; Kyomen, T.; Unno, M.; Hanaya, M., An achievement of over 12 percent efficiency in an organic dye-sensitized solar cell. *Chem. Commun.* **2014**, *50* (48), 6379-6381.
62. Pastore, M.; De Angelis, F., Aggregation of Organic Dyes on TiO<sub>2</sub> in Dye-Sensitized Solar Cells Models: An ab Initio Investigation. *ACS Nano* **2010**, *4* (1), 556-562.



63. Whittemore, T. J.; Sayre, H. J.; Xue, C.; White, T. A.; Gallucci, J. C.; Turro, C., New Rh<sub>2</sub>(II,II) Complexes for Solar Energy Applications: Panchromatic Absorption and Excited-State Reactivity. *J. Am. Chem. Soc.* **2017**, *139* (41), 14724-14732.
64. Ashford, D. L.; Gish, M. K.; Vannucci, A. K.; Brennaman, M. K.; Templeton, J. L.; Papanikolas, J. M.; Meyer, T. J., Molecular Chromophore–Catalyst Assemblies for Solar Fuel Applications. *Chem. Rev.* **2015**, *115* (23), 13006-13049.
65. Alibabaei, L.; Sherman, B. D.; Norris, M. R.; Brennaman, M. K.; Meyer, T. J., Visible photoelectrochemical water splitting into H<sub>2</sub> and O<sub>2</sub> in a dye-sensitized photoelectrosynthesis cell. *Proceedings of the National Academy of Sciences* **2015**, *112* (19), 5899-5902.
66. Ashford, D. L.; Sherman, B. D.; Binstead, R. A.; Templeton, J. L.; Meyer, T. J., Electro-assembly of a Chromophore–Catalyst Bilayer for Water Oxidation and Photocatalytic Water Splitting. *Angew. Chem. Int. Ed.* **2015**, *54* (16), 4778-4781.
67. Teets, T. S.; Nocera, D. G., Photocatalytic hydrogen production. *Chem. Commun.* **2011**, *47* (33), 9268-9274.
68. Elgrishi, N.; Teets, T. S.; Chambers, M. B.; Nocera, D. G., Stability-enhanced hydrogen-evolving dirhodium photocatalysts through ligand modification. *Chem. Commun.* **2012**, *48* (76), 9474-9476.
69. Esswein, A. J.; Veige, A. S.; Nocera, D. G., A Photocycle for Hydrogen Production from Two-Electron Mixed-Valence Complexes. *J. Am. Chem. Soc.* **2005**, *127* (47), 16641-16651.

70. Lee, C. H.; Cook, T. R.; Nocera, D. G., HX Addition and Photochemical H<sub>2</sub> Elimination by Ni NHC Complexes. *Inorg. Chem.* **2011**, *50* (3), 714-716.
71. Takahara, P. M.; Rosenzweig, A. C.; Frederick, C. A.; Lippard, S. J., Crystal structure of double-stranded DNA containing the major adduct of the anticancer drug cisplatin. *Nature* **1995**, *377* (6550), 649-652.
72. Farrer, N. J.; Salassa, L.; Sadler, P. J., Photoactivated chemotherapy (PACT): the potential of excited-state d-block metals in medicine. *Dalton Trans.* **2009**, (48), 10690-10701.
73. Betanzos-Lara, S.; Salassa, L.; Habtemariam, A.; Sadler, P. J., Photocontrolled nucleobase binding to an organometallic RuII arene complex. *Chem. Commun.* **2009**, (43), 6622-6624.
74. Whittemore, T. J.; Millet, A.; Sayre, H. J.; Xue, C.; Dolinar, B. S.; White, E. G.; Dunbar, K. R.; Turro, C., Tunable Rh<sub>2</sub>(II,II) Light Absorbers as Excited-State Electron Donors and Acceptors Accessible with Red/Near-Infrared Irradiation. *J. Am. Chem. Soc.* **2018**, *140* (15), 5161-5170.
75. Fulmer, G. R.; Miller, A. J. M.; Sherden, N. H.; Gottlieb, H. E.; Nudelman, A.; Stoltz, B. M.; Bercaw, J. E.; Goldberg, K. I., NMR Chemical Shifts of Trace Impurities: Common Laboratory Solvents, Organics, and Gases in Deuterated Solvents Relevant to the Organometallic Chemist. *Organometallics* **2010**, *29* (9), 2176-2179.
76. Adamo, C.; Barone, V., Exchange functionals with improved long-range behavior and adiabatic connection methods without adjustable parameters: The mPW and mPW1PW models. *J. Chem. Phys.* **1998**, *108* (2), 664-675.

77. Leonid, S., *Chemission 1.7* **2005-2010**.
78. Angeles-Boza, A. M.; Bradley, P. M.; Fu, P. K. L.; Wicke, S. E.; Bacsa, J.; Dunbar, K. R.; Turro, C., DNA Binding and Photocleavage in Vitro by New Dirhodium(II) dppz Complexes: Correlation to Cytotoxicity and Photocytotoxicity. *Inorg. Chem.* **2004**, *43* (26), 8510-8519.
79. Crawford, C. A.; Matonic, J. H.; Streib, W. E.; Huffman, J. C.; Dunbar, K. R.; Christou, G., Reaction of 2,2'-bipyridine (bpy) with dirhodium carboxylates: mono-bpy products with variable chelate binding modes and insights into the reaction mechanism. *Inorg. Chem.* **1993**, *32* (14), 3125-3133.
80. Calligaris, M.; Campana, L.; Mestroni, G.; Tornatore, M.; Alessio, E., Synthesis and crystal structure of dinuclear Rh(II) complexes with 1,10-phenanthroline and its 4,7- and 3,4,7,8-methyl derivatives. *Inorg. Chim. Acta* **1987**, *127* (1), 103-112.
81. Tikkanen, W. R.; Binamira-Soriaga, E.; Kaska, W. C.; Ford, P. C., Preparation and spectral and electrochemical characterization of dirhodium(II) complexes with bridging 1,8-naphthyridine ligands: 2,7-bis(2-pyridyl)-1,8-naphthyridine, 5,6-dihydrodipyrido[2,3-b:3'2'-j][1,10]phenanthroline, 2-(2-pyridyl)-1,8-naphthyridine and 1,8-naphthyridine. X-ray crystal structure of tris( $\mu$ -acetato)(2,7-bis(2-pyridyl)-1,8-naphthyridine)dirhodium(II) Hexafluorophosphate. *Inorg. Chem.* **1984**, *23* (2), 141-146.
82. Pimblett, G.; Garner, C. D.; Clegg, W., Synthesis, crystal structure, and spectroscopic properties of  $[\text{Mo}_2(\text{O}_2\text{CMe})_2(\text{MeCN})_6][\text{BF}_4]_2$ ,  $[\text{Rh}_2(\text{O}_2\text{CMe})_2(\text{MeCN})_6][\text{BF}_4]_2$ , and  $[\text{Rh}_2(\text{O}_2\text{CMe})_2(\text{MeCN})_4(\text{py})_2][\text{BF}_4]_2$ . *J. Chem. Soc., Dalton Trans.* **1986**, (6), 1257-1263.

83. Kudo, A.; Miseki, Y., Heterogeneous photocatalyst materials for water splitting. *Chem. Soc. Rev.* **2009**, *38* (1), 253-278.
84. van de Krol, R.; Liang, Y.; Schoonman, J., Solar hydrogen production with nanostructured metal oxides. *J. Mater. Chem.* **2008**, *18* (20), 2311-2320.
85. Balzani, V.; Credi, A.; Venturi, M., Photochemical Conversion of Solar Energy. *ChemSusChem* **2008**, *1* (1-2), 26-58.
86. Song, W.; Chen, Z.; Glasson, C. R. K.; Hanson, K.; Luo, H.; Norris, M. R.; Ashford, D. L.; Concepcion, J. J.; Brennaman, M. K.; Meyer, T. J., Interfacial Dynamics and Solar Fuel Formation in Dye-Sensitized Photoelectrosynthesis Cells. *ChemPhysChem* **2012**, *13* (12), 2882-2890.
87. Andreiadis, E. S.; Chavarot-Kerlidou, M.; Fontecave, M.; Artero, V., Artificial Photosynthesis: From Molecular Catalysts for Light-driven Water Splitting to Photoelectrochemical Cells. *Photochem. Photobiol.* **2011**, *87* (5), 946-964.
88. Queyriaux, N.; Jane, R. T.; Massin, J.; Artero, V.; Chavarot-Kerlidou, M., Recent developments in hydrogen evolving molecular cobalt(II)-polypyridyl catalysts. *Coord. Chem. Rev.* **2015**, *304-305*, 3-19.
89. Ma, Y.; Wang, X.; Jia, Y.; Chen, X.; Han, H.; Li, C., Titanium Dioxide-Based Nanomaterials for Photocatalytic Fuel Generations. *Chem. Rev.* **2014**, *114* (19), 9987-10043.
90. McKone, J. R.; Lewis, N. S.; Gray, H. B., Will Solar-Driven Water-Splitting Devices See the Light of Day? *Chem. Mater.* **2014**, *26* (1), 407-414.

91. Armaroli, N.; Balzani, V., Solar Electricity and Solar Fuels: Status and Perspectives in the Context of the Energy Transition. *Chemistry – A European Journal* **2016**, *22* (1), 32-57.
92. Hagfeldt, A.; Boschloo, G.; Sun, L.; Kloo, L.; Pettersson, H., Dye-Sensitized Solar Cells. *Chem. Rev.* **2010**, *110* (11), 6595-6663.
93. Robertson, N., Optimizing Dyes for Dye-Sensitized Solar Cells. *Angew. Chem. Int. Ed.* **2006**, *45* (15), 2338-2345.
94. Pashaei, B.; Shahroosvand, H.; Graetzel, M.; Nazeeruddin, M. K., Influence of Ancillary Ligands in Dye-Sensitized Solar Cells. *Chem. Rev.* **2016**, *116* (16), 9485-9564.
95. Gong, J.; Sumathy, K.; Qiao, Q.; Zhou, Z., Review on dye-sensitized solar cells (DSSCs): Advanced techniques and research trends. *Renew. Sust. Energ. Rev.* **2017**, *68*, 234-246.
96. Beiler, A. M.; Khusnutdinova, D.; Wadsworth, B. L.; Moore, G. F., Cobalt Porphyrin–Polypyridyl Surface Coatings for Photoelectrosynthetic Hydrogen Production. *Inorg. Chem.* **2017**, *56* (20), 12178-12185.
97. Brennaman, M. K.; Dillon, R. J.; Alibabaei, L.; Gish, M. K.; Dares, C. J.; Ashford, D. L.; House, R. L.; Meyer, G. J.; Papanikolas, J. M.; Meyer, T. J., Finding the Way to Solar Fuels with Dye-Sensitized Photoelectrosynthesis Cells. *J. Am. Chem. Soc.* **2016**, *138* (40), 13085-13102.
98. Antoniuk-Pablant, A.; Terazono, Y.; Brennan, B. J.; Sherman, B. D.; Megiatto, J. D.; Brudvig, G. W.; Moore, A. L.; Moore, T. A.; Gust, D., A new method for the

synthesis of  $\beta$ -cyano substituted porphyrins and their use as sensitizers in photoelectrochemical devices. *J. Mater. Chem. A* **2016**, *4* (8), 2976-2985.

99. Hamann, T. W.; Jensen, R. A.; Martinson, A. B. F.; Van Ryswyk, H.; Hupp, J. T., Advancing beyond current generation dye-sensitized solar cells. *Energy Environ. Sci.* **2008**, *1* (1), 66-78.

100. Adkins, J., Standard Tables for Reference Solar Spectral Irradiances: Direct Normal and Hemispherical on 37° Tilted Surface. American Society for Testing and Materials: West Conshohocken, PA 2012.

101. Smestad, G. P.; Krebs, F. C.; Lampert, C. M.; Granqvist, C. G.; Chopra, K. L.; Mathew, X.; Takakura, H., Reporting solar cell efficiencies in Solar Energy Materials and Solar Cells. *Sol. Energy Mater. Sol. Cells* **2008**, *92* (4), 371-373.

102. Hasselman, G. M.; Watson, D. F.; Stromberg, J. R.; Bocian, D. F.; Holten, D.; Lindsey, J. S.; Meyer, G. J., Theoretical Solar-to-Electrical Energy-Conversion Efficiencies of Perylene–Porphyrin Light-Harvesting Arrays. *The Journal of Physical Chemistry B* **2006**, *110* (50), 25430-25440.

103. Nattestad, A.; Mozer, A. J.; Fischer, M. K. R.; Cheng, Y. B.; Mishra, A.; Bäuerle, P.; Bach, U., Highly efficient photocathodes for dye-sensitized tandem solar cells. *Nat. Mater.* **2009**, *9*, 31.

104. Huang, S. Y.; Schlichthörl, G.; Nozik, A. J.; Grätzel, M.; Frank, A. J., Charge Recombination in Dye-Sensitized Nanocrystalline TiO<sub>2</sub> Solar Cells. *The Journal of Physical Chemistry B* **1997**, *101* (14), 2576-2582.

105. Qin, P.; Zhu, H.; Edvinsson, T.; Boschloo, G.; Hagfeldt, A.; Sun, L., Design of an Organic Chromophore for P-Type Dye-Sensitized Solar Cells. *J. Am. Chem. Soc.* **2008**, *130* (27), 8570-8571.
106. Sinopoli, A.; Wood, C. J.; Gibson, E. A.; Elliott, P. I. P., New cyclometalated iridium(III) dye chromophore complexes for n-type dye-sensitised solar cells. *Inorg. Chim. Acta* **2017**, *457*, 81-89.
107. Mayo, E. I.; Kilså, K.; Tirrell, T.; Djurovich, P. I.; Tamayo, A.; Thompson, M. E.; Lewis, N. S.; Gray, H. B., Cyclometalated iridium(iii)-sensitized titanium dioxide solar cells. *Photochemical & Photobiological Sciences* **2006**, *5* (10), 871-873.
108. Baranoff, E.; Yum, J.-H.; Graetzel, M.; Nazeeruddin, M. K., Cyclometallated iridium complexes for conversion of light into electricity and electricity into light. *J. Organomet. Chem.* **2009**, *694* (17), 2661-2670.
109. Sinopoli, A.; Wood, C. J.; Gibson, E. A.; Elliott, P. I. P., Hybrid Cyclometalated Iridium Coumarin Complex as a Sensitiser of Both n- and p-Type DSSCs. *Eur. J. Inorg. Chem.* **2016**, *2016* (18), 2887-2890.
110. Takizawa, S.-y.; Ikuta, N.; Zeng, F.; Komaru, S.; Sebata, S.; Murata, S., Impact of Substituents on Excited-State and Photosensitizing Properties in Cationic Iridium(III) Complexes with Ligands of Coumarin 6. *Inorg. Chem.* **2016**, *55* (17), 8723-8735.
111. Campbell, W. M.; Jolley, K. W.; Wagner, P.; Wagner, K.; Walsh, P. J.; Gordon, K. C.; Schmidt-Mende, L.; Nazeeruddin, M. K.; Wang, Q.; Grätzel, M.; Officer, D. L., Highly Efficient Porphyrin Sensitizers for Dye-Sensitized Solar Cells. *The Journal of Physical Chemistry C* **2007**, *111* (32), 11760-11762.

112. Li, L.-L.; Diau, E. W.-G., Porphyrin-sensitized solar cells. *Chem. Soc. Rev.* **2013**, *42* (1), 291-304.
113. Nattestad, A.; Mozer, A. J.; Fischer, M. K. R.; Cheng, Y. B.; Mishra, A.; Bäuerle, P.; Bach, U., Highly efficient photocathodes for dye-sensitized tandem solar cells. *Nat. Mater.* **2010**, *9* (1), 31-35.
114. Nikolaou, V.; Charisiadis, A.; Charalambidis, G.; Coutsolelos, A. G.; Odobel, F., Recent advances and insights in dye-sensitized NiO photocathodes for photovoltaic devices. *J. Mater. Chem. A* **2017**, *5* (40), 21077-21113.
115. Odobel, F.; Pellegrin, Y.; Gibson, E. A.; Hagfeldt, A.; Smeigh, A. L.; Hammarström, L., Recent advances and future directions to optimize the performances of p-type dye-sensitized solar cells. *Coord. Chem. Rev.* **2012**, *256* (21), 2414-2423.
116. Yu, M.; Draskovic, T. I.; Wu, Y., Cu(i)-based delafossite compounds as photocathodes in p-type dye-sensitized solar cells. *PCCP* **2014**, *16* (11), 5026-5033.
117. Smeigh, A. L.; Pleux, L. L.; Fortage, J.; Pellegrin, Y.; Blart, E.; Odobel, F.; Hammarström, L., Ultrafast recombination for NiO sensitized with a series of perylene imide sensitizers exhibiting Marcus normal behaviour. *Chem. Commun.* **2012**, *48* (5), 678-680.
118. D'Amario, L.; Jiang, R.; Cappel, U. B.; Gibson, E. A.; Boschloo, G.; Rensmo, H.; Sun, L.; Hammarström, L.; Tian, H., Chemical and Physical Reduction of High Valence Ni States in Mesoporous NiO Film for Solar Cell Application. *ACS Applied Materials & Interfaces* **2017**, *9* (39), 33470-33477.



119. Perera, I. R.; Daeneke, T.; Makuta, S.; Yu, Z.; Tachibana, Y.; Mishra, A.; Bäuerle, P.; Ohlin, C. A.; Bach, U.; Spiccia, L., Application of the Tris(acetylacetonato)iron(III)/(II) Redox Couple in p-Type Dye-Sensitized Solar Cells. *Angew. Chem. Int. Ed.* **2015**, *54* (12), 3758-3762.
120. Summers, G. H.; Lefebvre, J.-F.; Black, F. A.; Stephen Davies, E.; Gibson, E. A.; Pullerits, T.; Wood, C. J.; Zidek, K., Design and characterisation of bodipy sensitizers for dye-sensitized NiO solar cells. *PCCP* **2016**, *18* (2), 1059-1070.
121. Lefebvre, J.-F.; Sun, X.-Z.; Calladine, J. A.; George, M. W.; Gibson, E. A., Promoting charge-separation in p-type dye-sensitized solar cells using bodipy. *Chem. Commun.* **2014**, *50* (40), 5258-5260.
122. Tian, H.; Oscarsson, J.; Gabrielsson, E.; Eriksson, S. K.; Lindblad, R.; Xu, B.; Hao, Y.; Boschloo, G.; Johansson, E. M. J.; Gardner, J. M.; Hagfeldt, A.; Rensmo, H.; Sun, L., Enhancement of p-Type Dye-Sensitized Solar Cell Performance by Supramolecular Assembly of Electron Donor and Acceptor. *Scientific Reports* **2014**, *4*, 4282.
123. Maufroy, A.; Favereau, L.; Anne, F. B.; Pellegrin, Y.; Blart, E.; Hissler, M.; Jacquemin, D.; Odobel, F., Synthesis and properties of push-pull porphyrins as sensitizers for NiO based dye-sensitized solar cells. *J. Mater. Chem. A* **2015**, *3* (7), 3908-3917.
124. Zhang, L.; Favereau, L.; Farre, Y.; Maufroy, A.; Pellegrin, Y.; Blart, E.; Hissler, M.; Jacquemin, D.; Odobel, F.; Hammarström, L., Molecular-structure control of electron transfer dynamics of push-pull porphyrins as sensitizers for NiO based dye sensitized solar cells. *RSC Advances* **2016**, *6* (81), 77184-77194.

125. Caspar, J. V.; Meyer, T. J., Application of the energy gap law to nonradiative, excited-state decay. *J. Phys. Chem.* **1983**, *87* (6), 952-957.
126. Li, Z.; Leed, N. A.; Dickson-Karn, N. M.; Dunbar, K. R.; Turro, C., Directional charge transfer and highly reducing and oxidizing excited states of new dirhodium(ii,ii) complexes: potential applications in solar energy conversion. *Chem. Sci.* **2014**, *5* (2), 727-737.
127. White, T. A.; Dunbar, K. R.; Thummel, R. P.; Turro, C., Electronic influences of bridging and chelating diimine ligand coordination in formamidinate-bridged Rh<sub>2</sub>(II,II) dimers. *Polyhedron* **2016**, *103*, 172-177.
128. Sheldrick, G. M., SADABS. University of Gottingen: Germany, 1996.
129. Sheldrick, G., Crystal structure refinement with SHELXL. *Acta Cryst. C* **2015**, *71* (1), 3-8.
130. Burdzinski, G.; Hackett, J. C.; Wang, J.; Gustafson, T. L.; Hadad, C. M.; Platz, M. S., Early Events in the Photochemistry of Aryl Azides from Femtosecond UV/Vis Spectroscopy and Quantum Chemical Calculations. *J. Am. Chem. Soc.* **2006**, *128* (41), 13402-13411.
131. M. J. Frisch, G. T., W.; Schlegel, H. B.; Scuseria, G. E.; Robb, M. A.; Cheeseman, J. R.; Scalmani, G.; Barone, V.; Mennucci, B.; Petersson, G. A.; Nakatsuji, H.; Caricato, M.; Li, X.; Hratchian, H. P.; Izmaylov, A. F.; Bloino, J.; Zheng, G.; Sonnenberg, J.L. , *Gaussian09* **2009**, *Gaussian, Inc* (Wallingford, CT).

132. Lee, C.; Yang, W.; Parr, R. G., Development of the Colle-Salvetti correlation-energy formula into a functional of the electron density. *Physical Review B* **1988**, *37* (2), 785-789.
133. Stephens, P. J.; Devlin, F. J.; Chabalowski, C. F.; Frisch, M. J., Ab Initio Calculation of Vibrational Absorption and Circular Dichroism Spectra Using Density Functional Force Fields. *J. Phys. Chem.* **1994**, *98* (45), 11623-11627.
134. Petersson, G. A.; Al-Laham, M. A., A complete basis set model chemistry. II. Open-shell systems and the total energies of the first-row atoms. *J. Chem. Phys.* **1991**, *94* (9), 6081-6090.
135. Scalmani, G.; Frisch, M. J.; Mennucci, B.; Tomasi, J.; Cammi, R.; Barone, V., Geometries and properties of excited states in the gas phase and in solution: Theory and application of a time-dependent density functional theory polarizable continuum model. *J. Chem. Phys.* **2006**, *124* (9), 094107.
136. Tomasi, J.; Mennucci, B.; Cammi, R., Quantum Mechanical Continuum Solvation Models. *Chem. Rev.* **2005**, *105* (8), 2999-3094.
137. Keith, T. A. M., J. M., Agui. Semichem Inc.: Shawnee Mission, KS, 2008.
138. Campos-Fernández, C. S.; Ouyang, X.; Dunbar, K. R., A Homologous Series of Redox-Active, Dinuclear Cations with the Bridging Ligand 2-(2-Pyridyl)-1,8-naphthyridine. *Inorg. Chem.* **2000**, *39* (12), 2432-2433.
139. Lichtenberger, D. L.; Lynn, M. A.; Chisholm, M. H., Quadruple Metal–Metal Bonds with Strong Donor Ligands. Ultraviolet Photoelectron Spectroscopy of M<sub>2</sub>(form)<sub>4</sub>

- (M = Cr, Mo, W; form = N,N'-diphenylformamidinate). *J. Am. Chem. Soc.* **1999**, *121* (51), 12167-12176.
140. Cotton, F. A.; Ren, T., Preparation and molecular and electronic structures of a new diamagnetic diruthenium(II) complex, Ru<sub>2</sub>[(p-tol)NC(H)N(p-tol)]<sub>4</sub>. *Inorg. Chem.* **1991**, *30* (19), 3675-3679.
141. Cotton, F. A.; Ren, T.; Eglin, J. L., Synthesis and characterization of a complex with a very long osmium-osmium triple bond, dichlorotetrakis(di-p-tolylformamidinato)diosmium. *Inorg. Chem.* **1991**, *30* (11), 2559-2563.
142. Bradley, P. M.; Smith, L. T.; Eglin, J. L.; Turro, C., Direct Observation of the Luminescence from the  $3\delta\delta^*$  Excited State of Re<sub>2</sub>Cl<sub>2</sub>(p-OCH<sub>3</sub>form)<sub>4</sub>. *Inorg. Chem.* **2003**, *42* (23), 7360-7362.
143. Cotton, F. A., Metal-Metal Bonding in [Re<sub>2</sub>X<sub>8</sub>]<sup>2-</sup> Ions and Other Metal Atom Clusters. *Inorg. Chem.* **1965**, *4* (3), 334-336.
144. Cai, Z.-L.; Sendt, K.; Reimers, J. R., Failure of density-functional theory and time-dependent density-functional theory for large extended  $\pi$  systems. *J. Chem. Phys.* **2002**, *117* (12), 5543-5549.
145. Alberding, B. G.; Chisholm, M. H.; Gustafson, T. L., Detection of the Singlet and Triplet MM  $\delta\delta^*$  States in Quadruply Bonded Dimetal Tetracarboxylates (M = Mo, W) by Time-Resolved Infrared Spectroscopy. *Inorg. Chem.* **2012**, *51* (1), 491-498.
146. Fox, L. S.; Marshall, J. L.; Gray, H. B.; Winkler, J. R., Photoinduced charge separation and recombination kinetics in a dimeric iridium(I) complex with covalently bound alkyl-pyridinium acceptors. *J. Am. Chem. Soc.* **1987**, *109* (22), 6901-6902.

147. Durrell, A. C.; Keller, G. E.; Lam, Y.-C.; Sýkora, J.; Vlček, A.; Gray, H. B., Structural Control of 1A<sub>2u</sub>-to-3A<sub>2u</sub> Intersystem Crossing in Diplatinum(II,II) Complexes. *J. Am. Chem. Soc.* **2012**, *134* (34), 14201-14207.
148. Miskowski, V. M.; Rice, S. F.; Gray, H. B.; Milder, S. J., Excited-state decay processes of binuclear rhodium(I) isocyanide complexes. *J. Phys. Chem.* **1993**, *97* (17), 4277-4283.
149. Sun, Q.; Tripathi, G. N. R.; Schuler, R. H., A time-resolved Raman study of the reaction of hydroxyl radicals with p-phenylenediamine. *J. Phys. Chem.* **1990**, *94* (5), 2216-2217.
150. Buchalska, M.; Kuncewicz, J.; Świętek, E.; Łabuz, P.; Baran, T.; Stochel, G.; Macyk, W., Photoinduced hole injection in semiconductor-coordination compound systems. *Coord. Chem. Rev.* **2013**, *257* (3), 767-775.
151. Bird, C. L.; Kuhn, A. T., Electrochemistry of the viologens. *Chem. Soc. Rev.* **1981**, *10* (1), 49-82.
152. Xu, Y.; Schoonen, M. A. A., The absolute energy positions of conduction and valence bands of selected semiconducting minerals. *Am. Mineral.* **2000**, *85* (3-4), 543-556.
153. Wang, Z.; Li, C.; Domen, K., Recent developments in heterogeneous photocatalysts for solar-driven overall water splitting. *Chem. Soc. Rev.* **2019**, *48* (7), 2109-2125.

154. Su, J.; Wei, Y.; Vayssieres, L., Stability and Performance of Sulfide-, Nitride-, and Phosphide-Based Electrodes for Photocatalytic Solar Water Splitting. *J. Phys. Chem. Lett.* **2017**, *8* (20), 5228-5238.
155. Kim, J. H.; Hansora, D.; Sharma, P.; Jang, J.-W.; Lee, J. S., Toward practical solar hydrogen production – an artificial photosynthetic leaf-to-farm challenge. *Chem. Soc. Rev.* **2019**, *48* (7), 1908-1971.
156. Yuan, Y.-J.; Yu, Z.-T.; Chen, D.-Q.; Zou, Z.-G., Metal-complex chromophores for solar hydrogen generation. *Chem. Soc. Rev.* **2017**, *46* (3), 603-631.
157. Wang, Y.; Suzuki, H.; Xie, J.; Tomita, O.; Martin, D. J.; Higashi, M.; Kong, D.; Abe, R.; Tang, J., Mimicking Natural Photosynthesis: Solar to Renewable H<sub>2</sub> Fuel Synthesis by Z-Scheme Water Splitting Systems. *Chem. Rev.* **2018**, *118* (10), 5201-5241.
158. O'Regan, B.; Grätzel, M., A low-cost, high-efficiency solar cell based on dye-sensitized colloidal TiO<sub>2</sub> films. *Nature* **1991**, *353* (6346), 737-740.
159. Shah, A.; Torres, P.; Tscharnner, R.; Wyrsh, N.; Keppner, H., Photovoltaic Technology: The Case for Thin-Film Solar Cells. *Science* **1999**, *285* (5428), 692.
160. Kalyanasundaram, K., *Dye-sensitized solar cells. edited by K. Kalyanasundaram.* Boca Raton, Fla. : CRC Press, [2010]: 2010.
161. Green, M. A.; Hishikawa, Y.; Dunlop, E. D.; Levi, D. H.; Hohl-Ebinger, J.; Yoshita, M.; Ho-Baillie, A. W. Y., Solar cell efficiency tables (Version 53). *Progress in Photovoltaics: Research and Applications* **2019**, *27* (1), 3-12.
162. Komiya, R.; Fukui, A.; Murofushi, N.; Koide, N.; Yamanaka, R.; Katayama, H. In *Improvement of the conversion efficiency of a monolithic type dye-sensitized solar cell*

*module*, Technical Digest, 21st International Photovoltaic Science and Engineering Conference, 2011; pp 2C-5O.

163. Sharma, K.; Sharma, V.; Sharma, S. S., Dye-Sensitized Solar Cells: Fundamentals and Current Status. *Nanoscale Res Lett* **2018**, *13* (1), 381-381.

164. Han, L.; Islam, A.; Chen, H.; Malapaka, C.; Chiranjeevi, B.; Zhang, S.; Yang, X.; Yanagida, M., High-efficiency dye-sensitized solar cell with a novel co-adsorbent. *Energy Environ. Sci.* **2012**, *5* (3), 6057-6060.

165. Sayre, H. J.; Millet, A.; Dunbar, K. R.; Turro, C., Photocatalytic H<sub>2</sub> production by dirhodium(ii,ii) photosensitizers with red light. *Chem. Commun.* **2018**, *54* (60), 8332-8334.

166. Xue, C.; Sayre, H. J.; Turro, C., Electron injection into titanium dioxide by panchromatic dirhodium photosensitizers with low energy red light. *Chem. Commun.* **2019**.

167. Doyle, M. P.; Protopopova, M. N., New aspects of catalytic asymmetric cyclopropanation. *Tetrahedron* **1998**, *54* (28), 7919-7946.

168. Bradley, P. M.; Bursten, B. E.; Turro, C., Excited-State Properties of Rh<sub>2</sub>(O<sub>2</sub>CCH<sub>3</sub>)<sub>4</sub>(L)<sub>2</sub> (L = CH<sub>3</sub>OH, THF, PPh<sub>3</sub>, py). *Inorg. Chem.* **2001**, *40* (6), 1376-1379.

169. Lutterman, D. A.; Degtyareva, N. N.; Johnston, D. H.; Gallucci, J. C.; Eglin, J. L.; Turro, C., Photoinduced One-Electron Reduction of Alkyl Halides by Dirhodium(II,II) Tetraformamidinates and a Related Complex with Visible Light. *Inorg. Chem.* **2005**, *44* (15), 5388-5396.

170. Pena, B.; Barhoumi, R.; Burghardt, R. C.; Turro, C.; Dunbar, K. R., Confocal fluorescence microscopy studies of a fluorophore-labeled dirhodium compound: visualizing metal-metal bonded molecules in lung cancer (A549) cells. *J. Am. Chem. Soc.* **2014**, *136* (22), 7861-4.
171. Knoll, J. D.; Turro, C., Control and utilization of ruthenium and rhodium metal complex excited states for photoactivated cancer therapy. *Coord. Chem. Rev.* **2015**, *282-283*, 110-126.
172. Cotton, F. A.; Murillo, C. A.; Wang, X.; Yu, R., Chiral Organometallic Triangles with Rh–Rh Bonds. 1. Compounds Prepared from Racemic cis-Rh<sub>2</sub>(C<sub>6</sub>H<sub>4</sub>PPh<sub>2</sub>)<sub>2</sub>(OAc)<sub>2</sub>. *Inorg. Chem.* **2004**, *43* (26), 8394-8403.
173. Cotton, F. A.; Daniels, L. M.; Lin, C.; Murillo, C. A.; Yu, S.-Y., Supramolecular squares with Rh<sup>2+</sup> corners. *J. Chem. Soc., Dalton Trans.* **2001**, (5), 502-504.
174. Cook, T. R.; Zheng, Y.-R.; Stang, P. J., Metal–Organic Frameworks and Self-Assembled Supramolecular Coordination Complexes: Comparing and Contrasting the Design, Synthesis, and Functionality of Metal–Organic Materials. *Chem. Rev.* **2013**, *113* (1), 734-777.
175. Chakrabarty, R.; Mukherjee, P. S.; Stang, P. J., Supramolecular Coordination: Self-Assembly of Finite Two- and Three-Dimensional Ensembles. *Chem. Rev.* **2011**, *111* (11), 6810-6918.
176. Lou, Y.; Remarchuk, T. P.; Corey, E. J., Catalysis of Enantioselective [2+1]-Cycloaddition Reactions of Ethyl Diazoacetate and Terminal Acetylenes Using Mixed-



- Ligand Complexes of the Series  $\text{Rh}_2(\text{RCO}_2)_n$  ( $L^*4-n$ ). Stereochemical Heuristics for Ligand Exchange and Catalyst Synthesis. *J. Am. Chem. Soc.* **2005**, *127* (41), 14223-14230.
177. Anderson, B. G.; Cressy, D.; Patel, J. J.; Harris, C. F.; Yap, G. P. A.; Berry, J. F.; Darko, A., Synthesis and Catalytic Properties of Dirhodium Paddlewheel Complexes with Tethered, Axially Coordinating Thioether Ligands. *Inorg. Chem.* **2019**, *58* (3), 1728-1732.
178. Ashford, D. L.; Glasson, C. R. K.; Norris, M. R.; Concepcion, J. J.; Keinan, S.; Brennaman, M. K.; Templeton, J. L.; Meyer, T. J., Controlling Ground and Excited State Properties through Ligand Changes in Ruthenium Polypyridyl Complexes. *Inorg. Chem.* **2014**, *53* (11), 5637-5646.
179. Loftus, L. M.; Li, A.; Fillman, K. L.; Martin, P. D.; Kodanko, J. J.; Turro, C., Unusual Role of Excited State Mixing in the Enhancement of Photoinduced Ligand Exchange in Ru(II) Complexes. *J. Am. Chem. Soc.* **2017**, *139* (50), 18295-18306.
180. Rohrbaugh, T. N.; Collins, K. A.; Xue, C.; White, J. K.; Kodanko, J. J.; Turro, C., New Ru(ii) complex for dual photochemotherapy: release of cathepsin K inhibitor and  $1\text{O}_2$  production. *Dalton Trans.* **2018**, *47* (34), 11851-11858.
181. Dolg, M.; Stoll, H.; Preuss, H.; Pitzer, R. M., Relativistic and correlation effects for element 105 (hahnium, Ha): a comparative study of M and MO (M = Nb, Ta, Ha) using energy-adjusted ab initio pseudopotentials. *J. Phys. Chem.* **1993**, *97* (22), 5852-5859.
182. He, L. P.; Yao, C. L.; Naris, M.; Lee, J. C.; Korp, J. D.; Bear, J. L., Molecular structure and chemical and electrochemical reactivity of  $\text{Co}_2(\text{dpb})_4$  and  $\text{Rh}_2(\text{dpb})_4$  (dpb=N,N'-Diphenylbenzamidinate). *Inorg. Chem.* **1992**, *31* (4), 620-625.

183. Majumdar, M.; Patra, S. K.; Kannan, M.; Dunbar, K. R.; Bera, J. K., Role of Axial Donors in the Ligand Isomerization Processes of Quadruply Bonded Dimolybdenum(II) Compounds. *Inorg. Chem.* **2008**, *47* (6), 2212-2222.
184. Cotton, F. A.; Liu, C. Y.; Murillo, C. A., Systematic Preparation of Mo<sup>2+</sup> Building Blocks for Supramolecular Assemblies. *Inorg. Chem.* **2004**, *43* (7), 2267-2276.
185. Chisholm, M. H.; Huffman, J. C.; Iyer, S. S., Some studies of the substitution chemistry of [Rh<sub>2</sub>(OAc)<sub>2</sub>(CH<sub>3</sub>CN)<sub>4</sub>][BF<sub>4</sub>]<sub>2</sub> with monodentate and bidentate tertiary phosphines. *J. Chem. Soc., Dalton Trans.* **2000**, (9), 1483-1489.
186. Stoner, C. E.; Rheingold, A. L.; Brill, T. B., Thermal decomposition of energetic materials. 48. Structures and decomposition mechanisms of copper(II) complexes of furazans (1,2,5-oxadiazoles). *Inorg. Chem.* **1991**, *30* (3), 360-364.
187. Bock, C. R.; Meyer, T. J.; Whitten, D. G., Electron transfer quenching of the luminescent excited state of tris(2,2'-bipyridine)ruthenium(II). Flash photolysis relaxation technique for measuring the rates of very rapid electron transfer reactions. *J. Am. Chem. Soc.* **1974**, *96* (14), 4710-4712.
188. Durham, B.; Dressick, W. J.; Meyer, T. J., Photoelectrochemical production of hydrogen from the tris(2,2'-bipyridine) ruthenium–NN'-dimethyl-4,4'-bipyridylium (paraquat) system. *J. Chem. Soc., Chem. Commun.* **1979**, (8), 381-382.
189. Odom, A. L.; Heyduk, A. F.; Nocera, D. G., Photochemistry of dirhodium(II,II) diphosphazane tetrachloride complexes. *Inorg. Chim. Acta* **2000**, *297* (1), 330-337.

190. Heyduk, A. F.; Nocera, D. G., Hydrogen Produced from Hydrohalic Acid Solutions by a Two-Electron Mixed-Valence Photocatalyst. *Science* **2001**, *293* (5535), 1639-1641.
191. Powers, D. C.; Chambers, M. B.; Teets, T. S.; Elgrishi, N.; Anderson, B. L.; Nocera, D. G., Halogen photoelimination from dirhodium phosphazane complexes via chloride-bridged intermediates. *Chem. Sci.* **2013**, *4* (7), 2880-2885.
192. Esswein, A. J.; Nocera, D. G., Hydrogen Production by Molecular Photocatalysis. *Chem. Rev.* **2007**, *107* (10), 4022-4047.